Study on Upward Turbulent Bubbly Flow in Ducts

ZHANG HONGNA

Doctoral Dissertation

Department of Nuclear Engineering
Graduate School of Engineering
Kyoto University

September 2014

Acknowledgements

I here would like to sincerely thank many people for their kind aids and encouragements during my doctor course in Kyoto University.

Foremost, I would like to express my special appreciation and thanks to my supervisor Profess Tomaki KUNUGI, who has been a tremendous mentor of me for his patience, motivation, enthusiasm, and immense knowledge. I would like to thank him for showing me what the research is and how to enjoy it, for discussing on many scientific problems, for encouraging me, and for allowing me to grow as a research scientist freely. I have been extremely lucky to have a supervisor like him.

Special thanks are also extended to my committee members, Professor Kazuyoshi NAKABE and Associate professor Takehiko YOKOMINE for serving as my committee members and for their questions and suggestions during my defense.

I also wish to thank all the members in KUNUGI Lab for their help on my life and research in Kyoto University. Special thanks are given to Professor Jun SUGIMOTO, Lecturer Zensaku KAWARA, Dr. Li-Fang JIAO, Dr. Hao-Min SUN, Dr. Hong-Son PHAM and Dr. Yang CAO for their help on my life and their discussions on my research and Ms. Hijiri SOEJIMA for her management on my financial budget.

Thanks are also extended to Japan Society for the Promotion of Science (JSPS) Research Fellowship and Global Center of Excellence (G-COE) Program (J-051) for their financial support during my doctor course.

Finally, special thanks are given to my family and my friends. Words cannot express how grateful I am to my father Mr. Liu-Xian ZHANG, my mother Mrs. Feng-Ying LI, and my brother Mr. Chao ZHANG for all their sacrifices, encouragements and supports that they've made on my behalf. I would also like to thank all of my friends who supported me in writing, and encouraged me to strive towards my goal.

Table of Contents

List of Tables

List of Figures

Chapter 1

Introduction

1.1 Motivation

Nowadays, in a wide variety of engineering systems the upward turbulent bubbly flows play an increasingly important role such as boiling water and pressurized water nuclear reactors (BWRs and PWRs), heat exchangers, petroleum transportation systems and so on. Therein, accurate predictions of the flow characteristics are essentially required for the design, process optimization and safety control. For example, in the various subchannels of a nuclear fuel rod bundle of BWRs, the predictions of the flow especially the void lateral distribution must be accurately carried out in order to analyze the performance of the heat transfer such as local critical heat flux (CHF) which is an important thermal-hydraulic phenomenon for the safety control. During the transportation of the crude petroleum which is usually the two-phase or multiphase flow, the predictions of the flow especially the drag friction are very crucial for the pipeline design and operations such as the arrangement of the pump stations. Therefore, the reliable two-phase flow models are in urgently needs based on the well understanding of their physical processes.

So far, with the development of the experimental techniques and computational fluid dynamics (CFD), numerous researches on the turbulent bubbly flow have been carried out, on basis of which the understanding and modeling of turbulent bubbly flow have been improved. However, the existence of the multi-deformable and moving interfaces therein could induce the significant discontinuities of the fluid properties and the complex flow field near the interface, which makes it much more complicated as compared to the single-phase turbulent flow. Consequently, our current understanding

about the turbulent bubbly flows is still very limited due to its complicated properties, and thus the predictive capability of the existing modeling is still far from the level of the single-phase turbulent flow.

Due to its wide application in the various engineering systems and the lack of a satisfactory knowledge about this complicated phenomenon, more researches related with this phenomenon are necessary to be carried out in order to improve our physical understanding and the existing models.

1.2 State-of-the-art of turbulent bubbly flow

In this section, the state-of-the-art of the upward turbulent bubbly flow will be reviewed including the following topics:

(a) How were the previous researches on the turbulent bubbly flows carried out?

(b) What are the key issues in order to understand and model the turbulent bubbly flow?

(c) What have we achieved based on the previous researches?

(d) What needs to be studied on the turbulent bubbly flow in the future?

1.2.1 Background

Generally, the researches to understand and model the turbulent bubbly flow started from the single-phase turbulent flow which was considered as one of the most complicated and unsolved physical problem in the last century and taken as the background knowledge for the turbulent bubbly flow.

As for the single-phase turbulence, since the observation of the turbulence phenomenon by Reynolds's famous experiments in 1883, the innumerable researches have been carried out from the experimental, theoretical and numerical point of views. In general, the following topics were mainly focused on [1.1] including: (1) how the turbulent flows behave; (2) what kinds of the fundamental physical processes involved; (3) how to describe the turbulent flows quantitatively; (4) how to simulate and model the turbulent flows to meet the requirements of the engineering application. Owing to

the contributors, our knowledge on single-phase turbulence has been improved significantly in the past century.

As for the researches of the turbulent bubbly flows, the similar targets to that of the single-phase turbulent flow are aimed at, which are solving the above four questions. However, in the turbulent bubbly flows, there exist the multi-deformable and moving interfaces which could also be coalesced to form new interfaces or broken into more small interfaces [1.2]. Therefore, in addition to the general researches of the single-phase turbulent flow, the bubbles behavior and bubbles' effect are necessary to be considered for the turbulent bubbly flow. Comparing to the single-phase turbulent flow, the turbulent bubbly flow owns the different characteristics due to the existence of the dispersed phase such as:

(a) Discontinuities of the fluid properties: During the mathematical description of the turbulent bubbly flow, the general continuum fluid assumption used for the single-phase flow becomes invalid because of the presence of the multi-interfaces.

(b) Relative motion: Due to the density difference or the buoyancy effect, the relative motions exist between the bubbles and the liquid phase.

(c) New characteristic scale: Additional characteristic scales related with the bubble size D_B are introduced on basis of the duct geometrical size D_H and eddy scales l_v such as Kolmogorov scale and the integrated length scale l_e for the single-phase turbulent flow.

(d) Phase interaction: Due to the relative motion and the new characteristic scale, the flow characteristics in each phase could be influenced by the other phase through the interfaces between them. For example, from the micro-scale point of view, the presence of the interfaces could induce complex flow field near the interface and consequently the complex flow field could modify the interface characteristics such as bubble shape. For the turbulent bubbly flow in the pipes, from the macro-scale point of view, the phase distribution could be affected due the interaction between two phases. Consequently, the flow

field in the liquid phase such as velocities and turbulence distribution could then be modified comparing to that of the single-phase flow. For a long time, the understanding of the interfacial interaction, the phase distribution in the turbulent bubbly flow and the turbulence modulation were very important research topics and attracted numerous attentions.

(e) Complicated flow closure problem: With the interfacial interactions and difficulties of the mathematical description, the flow closure problems of the momentum and energy in the turbulent bubbly flow become more complicated comparing to that of the single-phase turbulent flow. For example, therein how to model the contributions of the phase interaction and how to numerically solve the proposed models are both important research topics.

Basically, for the turbulent bubbly flow, the existing researches from the experimental, theoretical and numerical point of views were mainly focused on the following questions aiming at accurate modeling of the turbulent bubbly flows.

(a) How does the turbulent bubbly flow behave? In addition to the general researches of the single-phase turbulent flow, herein how does the bubbles behave such as bubble distribution, deformation, coalescence and breakup are also necessary to be considered.

(b) What kinds of the fundamental physical processes are involved in the turbulent bubbly flow? In addition to the general researches of the single-phase turbulent flow, herein what kind of the fundamental physical processes responsible for the bubbles behaviors and the phase interactions are also necessary to be considered.

(c) How to describe the turbulent bubbly flows quantitatively? In addition to the general researches of the single-phase turbulent flow, herein how to solve the problem induced by discontinuities of the fluid properties and how to quantitatively describe the bubbles behaviors and phase interactions were also necessary to be considered.

(d) How to simulate and model the turbulent bubbly flows to meet the requirements of the engineering application? Additionally, how to model the phase interaction based on the understanding the physical process are also necessary to be considered.

In the following sections, what have we achieved about the above questions for the turbulent bubbly flows will be reviewed based on the existing literatures. Firstly, the establishment of the database of turbulent bubbly flow will be reviewed to answer the first two questions mentioned above and validate the later proposed models. Then, the development and implementation of the models for the turbulent bubbly flow will be summarized to answer the latter two questions mentioned above. Finally, the unsolved problems and the scope of the current dissertation will be given.

1.2.2 Review of the experimental and numerical databases

Currently, the databases for the turbulent bubbly flows are established based on the experimental measurements and the direct numerical simulations (DNSs).

1.2.2.1 Experimental measurements

To understand the physical process and develop the model of the turbulent bubbly flows, the detailed flow information such as the drag resistance, the temporal and spatial evolutions of velocities and turbulence in two phases and the detailed bubbles behaviors such as the bubble concentration, the bubble size, the bubble shape and the bubbles motion are necessary at the same time. However, so far limited by the current experimental techniques, for the turbulent bubbly flow, only several flow parameters are available such as the statistical liquid phase velocities and turbulence intensities, the void fraction, the bubble size and velocity, and the interfacial area concentrations (IAC) and so on. The experimental databases on these parameters have been established.

1.2.2.1.1 Database of turbulent bubbly flow

So far the databases of the turbulent bubbly flow have been established in the following flow types:

(i) Uniform bubbly flow

The uniform flow is a simplest flow type for the understanding of the flow characteristics and physical process and the developing the models. The studies on the uniform turbulent flows such as the homogeneous turbulent flows generated by homogeneous shear and the homogeneous isotropic turbulent flows generated by grids have played an important role for the model development in the single-phase turbulent flow [1.1]. As for the turbulent bubbly flow, so far Marie [1.3] and Lance *et al.*[1.4-1.5] developed the measurements of the liquid-phase turbulence in a grid-generated and a homogeneous shear-generated bubbly turbulent flow based on Laser-Doppler and hot-film anemometry. Therein, the following liquid turbulent characteristics were studied including the relation between the turbulent kinetic energy and the void fraction, the isotropy level of the Reynolds stress tensor and the turbulent energy spectra. According to their studies, two distinct regimes were found according to the void fraction, which are a) for the low void fraction where hydrodynamic bubbles interactions are negligible, the turbulent kinetic energy of the liquid could be considered to be just the summation of the turbulent kinetic energy generated by the grid and the motion of non-interactive bubbles; b) for the higher void fraction cases, due to the bubbles mutual interactions, the bubbles transfer a greater amount of kinetic energy to the liquid and the bubble-induced turbulence dominates the grid-generated turbulence. In addition, during the above process, the isotropy of the turbulent field was found to be not altered or improved by bubbles. The one-dimensional turbulent energy spectra of the bubble-induced wake were found to be deviated from the classical power law exponents. However, it is notable that in these experiments, the void fraction was very low less than 3% with the bubble diameter around 5mm. As for the other conditions, it still needs further investigation.

(ii) Boundary layer flow

The boundary flow is another simple flow type for the understanding of the flow characteristics and physical process and the developing the models for the single-phase turbulent flow [1.1]. For the turbulent bubbly flow, so far there are very few researches of this flow type, except Moursali *et al.*[1.6] developed the measurements in an upward turbulent bubbly boundary layer along a vertical flat plate based on LDV. Therein, they focused on the void fraction distribution, the wall shear stress, and the mean liquid velocity profiles. According to their study, the lateral bubble migration toward to the wall occurs depending on the bubble mean diameter and the void fraction similar to the duct flow. In addition, the wall skin friction coefficient was observed to increase because of the presence of the bubbles, which modifies the universal logarithmic law near the wall. In this experiment, the measured location was mainly at 1*m* from the inlet and the void fraction was less than 10% with the bubble diameter around 3.5*mm*. However, as for the other conditions and measurements such as turbulence, it still needs further investigation

(iii) Duct flow

According to the different duct geometries, several experimental databases of the upward turbulent bubbly flows have been established in the small circular and large circular pipes, and small non-circular and large noncircular ducts. The small and large ducts were distinguished by the relation between the duct size D_H and maximum bubble size D_{Max} $(=40\sqrt{\sigma/g(\rho_i-\rho_g)})$ under the tested conditions, i.e., the small duct if $D_H <$ D_{Max} and otherwise large ducts [1.7]. The detailed literature survey of this flow type could be found in [1.8]. In this section, the representative experimental studies and the observations are briefly summarized.

In the small circular pipes with pipe diameter ranging from 15*mm* and 60*mm*, the representative experimental studies were carried out by Serizawa [1.9-1.10], Theofanous and Sullivan [1.11], Wang *et al.* [1.12], Liu [1.13-1.15], and Hibiki *et al.*

[1.16-1.17] by measuring the flow patterns and local flow distributions including averaged liquid and gas velocities, void fraction, turbulence, bubble size, bubble interfacial area concentration under several flow conditions. Therein, it was observed that: for the upward turbulent bubbly flow in the small circular pipes, the pronounced wall peak of the void fraction occurs for low area-averaged void fraction flow conditions but core-peak occurs for the higher void fraction. The interesting phenomenon was attributed to the lift force exerted on the bubbles which were dependent on the bubble size [1.13]. With the wall peak of void fraction, the average axial liquid velocity (W_l) profiles were observed to be more uniform in the core region [1.9-1.17]. For higher void fraction cases, Theofanous and Sullivan [1.11] and Wang *et al.* [1.12] observed slightly shift of the location of the maximum liquid velocity profile. As for the turbulent structures, the radial distribution of the turbulence was observed to be more uniform in the core region comparing to that of the single-phase flow. Moreover, similar to the mirco-bubble case the turbulent drag reduction near the wall was also observed under the low void fraction [1.18-1.19].

For the upward turbulent bubbly flow in the large diameter circular (pipe diameter larger than 100 mm), Ohnuki and Akimoto [1.20] and Shawkat *et al.* [1.21-1.22] established the comprehensive databases including the velocity field, turbulent kinetic energy, void fraction, bubble size, bubble velocities and so on. The experiments carried out [1.23-1.29] mainly measured the bubbles information including void fraction, bubble size, bubble velocities and the interfacial area concentration without the liquid phase flow field. According to the above databases, it was obtained that the bubbles tend to migrate toward the pipe center earlier forming a core-peak of the void fraction profile rather the wall-peak void distribution under the same flow conditions even for the smaller bubbles with the bubble diameter 3-5*mm* [1.22], which is different from those in small circular pipes. The wall-peak of the void fraction was only observed for the cases with very low averaged void fraction less than 4% in the experiments carried out by [1.20, 1.22, 1.24] in a 200*mm* pipe when the bubble diameter was relatively small. No significant difference on the magnitude and shape for the

average liquid velocity was observed except the lower value in the near wall region compared to that in the small circular pipe. Besides, as compared with that in the smaller pipe, Prasser *et al.* [1.30] observed that under the same superficial velocities the bubbles with larger diameter could move more freely and become more deformed in the large pipes. The modifications of the distribution of the void fraction were attributed to the deformation of the bubbles [1.31-1.33]. As for the liquid turbulence structure was also considered to be one of the main mechanisms for the formation of the core-peak of the void fractions in the large pipes. Lahey *et al.* [1.34] and Ohnuki and Akimoto [1.35] suggested the strong turbulence diffusion effect on the bubbles is regarded as one reason for the above phenomenon. However, more experimental databases of the liquid turbulence are still necessary to validate these points.

For the upward turbulent bubbly flow in the small noncircular ducts, Lopez de Bertodano *et al.* [1.36] established the comprehensive databases of the velocity fields, Reynolds stress tensor and void fraction in the triangle duct. The other experiments in the square and rectangular ducts by [1.37-1.41], mainly measured the void fraction. According to the above databases, for noncircular ducts cases, it was observed that due to the non-homogeneous geometrical boundary bubbles tend to be accumulated more in the corner region, thus leading to the more significant corner peak of the void fraction compared to the wall peak. The average liquid velocity was also found to be more uniform comparing to the single-phase flow.

For the upward turbulent bubbly flow in the large noncircular ducts, recent experiments done by Sun *et al.* [1.42] established detailed database for large vertical square duct. Similar to the bubbly flow in other noncircular pipes [1.36-1.41], the pronounced corner and wall peaks of void fraction were observed under the low averaged void fraction cases. Due to the high local void fraction near the wall and the corner the apparent peak of average liquid velocity was also found near corner and wall. However, among the existing experiments in the circular small and large pipe and small noncircular pipe no such strong velocity peak has been observed near the wall except slightly peak near the wall [1.11-1.12]. In addition, the secondary flow in the cross

section observed in the single-phase turbulent flow in the noncircular ducts [1.43] may have an effect on the flow characteristics. However, so far there are few experimental measurements to show the existence and effect of the secondary flow.

1.2.2.1.2 Database of bubble behaviors

As mentioned above, the bubbles behavior is another key point to understand the flow characteristics, the physical process and modeling of the turbulent bubbly flow in the above flow types. So far, the basic databases of the bubble behaviors have been established in the following flow types:

(i) Stagnant system

Therein, the important parameters including the terminal velocities V_T, bubble deformation E, and the drag coefficient C_D were investigated based on the numerous experiments of the single bubble [1.44]. The correlations of the above parameters were proposed based on the following dimensionless numbers when it is dominated by different effects such as the surface tension, inertial or viscosity effects.

$$\mathrm{Eo}=\frac{\left(\rho_l-\rho_g\right)gD_B^2}{\sigma},\quad \mathrm{M}=\frac{g\mu_l^4\left(\rho_l-\rho_g\right)}{\left(\rho_l^2\sigma^3\right)},\quad \mathrm{Re}_B=\frac{\rho_l D_B V_R}{\mu_l}\quad\text{and}\quad \mathrm{We}=\frac{\rho_l D_B V_R^2}{\sigma}. \tag{1.1}$$

where Eötvös number Eo characterizes the relative importance of gravity to surface tension; Morton number M the physical properties of systems; Reynolds number Re the relative importance of inertial force to viscous force; and Weber number We the relative importance of inertial force to surface tension. For the constant the fluid properties (the constant M), the above dimensionless numbers solely depend on the bubble size D_B, since the relative velocity V_R is also determined by the bubble size and the fluid properties.

(ii) Uniform shear flow

Single-bubble experiments in the uniform shear flow were carried out by Tomiyama *et al.*[1.33], where the bubble's lateral migration was found to depend on the

bubble size D_B or Eo. For example, the migration direction for the small bubble or Eo was opposite to that for the large bubble or Eo. Besides, the well-known lift force coefficient correlation was proposed, which will be given in the later section.

(iii) Upward turbulent bubbly flow

For the upward turbulent bubbly flow, Liu [1.13] studied the bubble size effect on the flow characteristics in the small circular pipe by carefully controlling the inlet bubble size D_B. The lateral migration of bubbles and the flow regime transition were found to be very sensitive to the bubble size. Under the low void fraction for the cases of the bubble size D_B < 5~6*mm*, the wall peak of the void fraction could be obtained, while the core peak of the void fraction was observed for the large bubble size D_B >5~6*mm*. This was in consistent with the observation of Tomiyama's single bubble experiments [1.33]. In addition, the entrance length effect L/D_H was also confirmed to be an important parameter to determine the lateral void distribution due to the pressure difference which could induce the bubble expansion. Along the axial direction, the different flow regimes from the bubbly flow to slug flow are possible to be observed due to the developing of the bubble coalescence and the bubble break-up.

1.2.2.1.3 Summary on experimental measurements

In summary, based on the above experimental databases, the following main achievements were obtained for the turbulent bubbly flow:

(i) Bubble behaviors

For the upward turbulent bubbly flow in the ducts, there may exist the bubbles lateral migration due to the additional force exerted on the bubbles from the liquid phase, which could cause the phenomenon of the wall-peak, double peak or the core peak of the void fraction. The lateral migration of the bubbles depends on the bubble size, the bubble deformation, the duct size, and also the duct geometry. For the small bubbles, under the low averaged void fraction the wall peak of the void fraction distribution tends to be formed, while the core peak of the void fraction distribution tends to be

formed for the large bubbles. The duct size and geometry affects the void fraction under which the transition from the wall peak to the core peak occurs earlier. Moreover, increasing the averaged void fraction, the flow regime transition occurs which might change from the dispersed bubbly flow to the annular flows, for which several flow regime maps have been proposed [1.2].

(ii) Velocity fields in the liquid phase

The averaged liquid phase velocity and the turbulence fields were mainly focused on. For the upward turbulent bubbly flow with the wall peak of the void fraction, the liquid phase velocities were found to be more uniform in the core region. For the turbulent bubbly flow with the core peak of the void fraction, the liquid phase velocities were found to be steeper comparing to that of the single phase flow.

(iii) Turbulence modulation in the liquid phase

With the presence of the bubbles, the turbulence modulation occurs and according to the above experiments, the observation could be summarized as follows:

(a) How the turbulence of the liquid phase was modulated strongly depends on the bubble size and void fraction. Generally, with smaller particle or bubble size smaller than the eddy size, the turbulence reduction occurs, while for the large bubble size, the turbulence attenuation occurs [1.45]. However, for the turbulent bubbly flow with relative large bubble size, under very low void fraction cases such as less that 5%, the turbulence suppression could also occur [1.19, 1.21]. For higher void fraction cases, the turbulence enhancement occurs.

(b) The turbulent energy spectra in the turbulent bubbly flow were only considered under very low void fraction. Therein, it was found that the classical Kolmogorov power law (-5/3) was replaced by (-8/3) [1. 4, 1.21].

(c) Few detailed discussions of the turbulence anisotropy were carried out for the upward turbulent bubbly flow, among which it was found to be controversial. Theofanous and Sullivan showed the presence of the bubbles

didn’t alter the turbulent isotropy level [1.11]. Similar results were also reported by Lance *et al.* [1.4, 1.5]. However, Wang *et al.* [1.12] showed the bubbles modification of the local turbulence isotropy occurs which were more anisotropic turbulence in the core region but more isotropic turbulence near the wall [1.12].

1.2.2.2 Numerical simulations

Except experimental measurements, DNS has been proved to be a powerful tool and played very important role in developing the turbulent models for the single-phase turbulent flow. By directly solving the governing equations of the flow, DNS could provide us all the scales of the turbulence without resorting any empirical closure assumptions. Based on the VOF methods which are used to reconstruct the interface structures, DNSs have been carried out for the turbulent flow with single bubble or several bubble cases. However, for the cases with a large number of the bubbles, DNSs started very late and are still very limited.

For the turbulent bubbly flow, currently Tryggvason group [1.46-1.56] has constructed the numerical algorithms based on the finite difference method and the front tracking of the bubble interface. With this numerical algorithm, a series of DNS studies were performed for the homogeneous turbulent bubbly flow, vertical channel turbulent bubbly flow and so on [1.46-1.56]. Therein, the detailed flow characteristics including the flow fields, turbulence and bubbles behaviors were investigated.

For example, similar to the uniform turbulent bubbly flow carried out by Lance and Bataille [1.4], Esmaeeli and Tryggvason [1.46-1.48] carried out DNSs of two- and three- dimensional buoyant bubbles with regular array and freely array in the periodic domains for the low and moderate Reynolds numbers. The turbulence generated therein was compared the turbulence prediction based on the potential model [1.4]. The large difference was found especially for the three-dimensional flow. In addition, the inverse energy cascade of the turbulent structures was also noticed. Bunner and Tryggvason [1.49-1.51] extended the previous DNS study [1.46-1.48] to more buoyant bubbles by

focusing on the bubbles behaviors including the rising velocity, the microstructures, the dispersion and the fluctuation velocities of the bubbles and the flow fields such as the bubble-induced pseudo-turbulence. Therein, the turbulent energy spectra showed a -3.6 power-law distribution at large wave numbers in consistent with Lance's experimental observations [1.4]. Moreover, the turbulence was found to be strongly anisotropic and the anisotropy declined as the void fraction increased. The effects of the bubble deformation on the flow properties were also investigated by Bunner and Tryggvason [1.52], which showed a preference for pairs of the deformed bubbles to be vertically aligned and for pairs of spherical bubbles to be aligned horizontal. Consequently, the deformed bubbles tend to move toward the former bubbles' wake, by which the stronger velocity fluctuations could be induced by the deformed bubbles. Similar to the duct flow, Lu *et al.* [1.53-1.55] carried out DNSs of the upward and downward turbulent bubbly flows in a vertical channel with the low void fraction. Their numerical results [1.55] showed that the bubble deformation rather than bubble size dominated the bubbles lateral migration. In the upward flow, the deformed bubbles tend to migrate toward the channel center, while the spherical bubbles tend to move the channel walls. Even with relatively larger bubble size, the turbulent drag reduction was also obtained under low void fraction when the bubble size was comparable to the buffer layer. Tryggvason [1.56] addressed the multi-scale issues of the turbulent bubbly flow, and suggested the multi-scale model for the turbulent bubbly flow based on the DNS databases.

Based on the DNS of the turbulent flow in a upward vertical channel, Bolotnov [1.57] paid attention to the isotropy level of Reynolds stress distribution for the single-phase and bubbly flow in order to address whether the isotropic turbulent assumptions are suitable for the bubbly flows applications or not. His numerical results showed that the presence of the bubbles improved the turbulence isotropy for low Reynolds number flows, and didn't alter for the moderate Reynolds number cases. However, it is notable that the DNSs [1.57] only considered the extremely low void fraction cases, say less than 3%.

1.2.2.3 Summary

So far, from the literatures, the numerical databases on the turbulent bubbly flow have been established as summarized in Table 1.1, based on which our understanding on the detailed fundamental processes and mechanisms of the turbulent bubbly flow were improved. However, it is worth noting that in the above numerical simulations, only tens at most hundreds of the bubbles were simulated due to the increasing of the numerical difficulty especially the computer requirement, i.e., the numerical databases were still limited in the low void fraction cases as compared to the real experiments. There still exist some qualitatively controversial topics especially the bubble effects on the turbulent anisotropy. In the simulations of the turbulent uniform bubbly flow by Tryggvason groups [1.51-1.52], the turbulent behaves strongly anisotropic, while in Bolotnov's simulation in the vertical channel, the presence of the bubbles improve the turbulence isotropy [1.57].

Table 1.1 Numerical databases based on DNSs of the turbulent bubbly flow.

Numerical Geometry	Researchers	Void fraction α	Bubble shape S: Spherical; D: Deformed	Note
2D Uniform flow	Esmaeeli and Tryggvason [1.46-1.48]	12.56%	Eo = 1.0(S)	-
3D Uniform flow	Esmaeeli and Tryggvason [1.47-1.48] Buner and Tryggvason [1.49-1.52]	0%, 2%, 6%, 12%, 24%	Eo = 1.0(S) Eo = 1.0(S), 5.0(D)	Regular bubble array and Free bubbles
3D Vertical channel	Lu & Tryggvason [1.53-1.55] Bolotnov [1.57]	1.5%, 3.0%, 6.0% 0%, 1%	Eo = 0.45(S), 4.5(D) Eo = 0.11(S)	- -

1.2.3 Review of existing models for turbulent bubbly flow

Similar to the single-turbulent flow, though DNSs of the turbulent bubbly flow could provide us the most detailed flow information, the requirements on the computer memory and numerical time limited its application to the real industrial engineering systems, especially for the large void fraction with a large number of the bubbles. The models which could meet the requirements of the engineering application were more efficient for the turbulent bubbly flows. This section will review the state-of-the-art of the development and implementation of the models for the turbulent bubbly flows.

1.2.3.1 Model development

As mentioned before, in the turbulent bubbly flows the presence of the multi-moving and deformable interfaces leads the flow to be significant discontinuous, which brings the main numerical difficulties, i.e., resolving the fine interfacial structures. During the model development of the turbulent bubbly flow the first important issue is to eliminate the flow discontinuity and to obtain the macroscopic governing equations which should satisfy the continuum fluid assumption based on the proper averaging method.

Generally, according to the domain in the averaging method, the models for the turbulent bubbly flow could be classified into two types, i.e., the one-dimensional models and the multi-dimensional models. The one-dimensional models solve the evolution of the cross-section averaged mean flow information such as the void fraction, velocities, and pressure. The homogeneous equilibrium mixture model and the drift-flux model by Zuber and Findlay [1.58] belong to this type. It requires less computer memory and has been widely adopted in the past design calculations for the nuclear reactor [1.59]. However, the models of this type require the prior knowledge of the local distributions of phase, velocities and so on which are normally not known. As compared to the one-dimensional model, the multi-dimensional models were derived based on the time averaging, and can provide the local time-averaged flow information with the aid of the powerful computer. Thus, to improve the models of the turbulent bubbly flow, the

numerical studies based on the multi-dimensional models are necessary.

According to the methods to consider the two phases during the averaging, the models of the turbulent bubbly flow could be also classified into two types, i.e., the mixture models and two-fluid models [1.2].

The mixture models consider the flow with both the continuous liquid phase and the dispersed bubbles as a whole mixture, whose properties were determined by coupling the properties of the two phases and each phase's fraction. Consequently, the conservation equations were established for the mass, momentum and energy based on the whole mixture fluid. The homogeneous equilibrium mixture model is the simplest example, which treats the fluid of the bubbly flow as a continuous mixture just like single phase flow with modified the fluid properties. The relative motion between two phases was neglected in the homogeneous equilibrium mixture model. Nowadays, the drift-flux model proposed by Zuber and Findlay [1.58] is one widely used mixture model, in which another equation for the relative motion between two phases was included and the effects of two-phase interaction on the flow could be considered.

The two-fluid model proposed by Ishii [1.60] treats the two phases separately. For each phase, the conservation equations including the mass, momentum and energy were established based on the time averaging. Though the two-fluid model is more complicated as compared with drift-flux model, however, in this way the more detailed flow information such as the transfer processes of the mass, momentum and energy between two phases could be predicted. Nowadays, the two-fluid model has been paid lots of attentions, based on which the numerical predictions of the turbulent bubbly flow were improved, and in the present dissertation this model will also be considered.

The basic governing equations of two-fluid model were shown in Eqs. (1.2) and (1.3). Here, the flows were restricted to the adiabatic and incompressible two-phase flows without the phase change.

$$\frac{D_k \alpha_k}{Dt} + \alpha_k \nabla \cdot \overline{\mathbf{V}}_k = 0 \tag{1.2}$$

$$\alpha_k \rho_k \frac{D_k \overline{\mathbf{V}}_k}{Dt} = \nabla \cdot \left(\alpha_k \left[\mu_k \nabla \overline{\mathbf{V}}_k \right] - \rho_k \left(\overline{\mathbf{v}_k \mathbf{v}_k} \right) \right) - \alpha_k \nabla p_k - \alpha_k \rho_k \mathbf{g} + \mathbf{M}_{ik} - \mathbf{M}_{wk} - \boldsymbol{\tau}_{ki} \cdot \nabla \alpha_k + \left(p_{ki} - p_k \right) \nabla \alpha_k \tag{1.3}$$

where the subscript-*k* refers to the liquid (*l*) and gas (*g*) flow; the subscript-*i* refers to the effect of the interfaces; the overbar means the time-averaged quantities; the bold variables are the vectors or tensors; α_k is void fraction of phase-*k*; $\mathbf{V}_k$ is the corresponding phase velocity vector and could be separated by the mean value and the fluctuations $\mathbf{V}_k = \overline{\mathbf{V}_k} + \mathbf{v}_k$; $\mathbf{v}_k$ the fluctuating velocity vector; D_k / D_t indicates the material derivative; ρ_k and μ_k are the density and viscosity of the corresponding phase-*k*; p_k is the static pressure of the corresponding phase-*k*; **g** is the gradational acceleration; $\mathbf{M}_{ik}$ is the interfacial force on phase-*k*; $\mathbf{M}_{wk}$ is the wall shear force on phase-*k*; $\boldsymbol{\tau}_k = \mu_k \nabla \overline{\mathbf{V}}_k - \left(\rho_k \overline{\mathbf{v}_k \mathbf{v}_k} \right)$; $\rho_k \overline{\mathbf{v}_k \mathbf{v}_k}$ is Reynolds stress in the phase-*k*.

Comparing to the single-phase turbulent flow, the averaging process generates the new interfacial transfer terms as shown by the last four terms in Eq. (1.3). The interfacial term $\mathbf{M}_{ik}$ related with the jump condition stratify $\mathbf{M}_{il} + \mathbf{M}_{ig} = 0$. In addition, the turbulent Reynolds stresses also includes the phase interaction through the interfaces. To improve the model of the turbulent bubbly flow the current work was mainly focused on the establishment and validation of the constitutive relations for the interfacial transfer terms and the turbulent Reynolds stresses based on the established experimental databases. Some attentions were also paid to the numerical algorithms to solve the above equations. In the following, the state-of-the-art of the constitutive relations for the two-fluid model will be reviewed in brief.

1.2.3.1.1 Interfacial transfer terms

During the model development, the interfacial term $\mathbf{M}_{ik}$ was decomposed into the drag force $\mathbf{M}_{ik}^{d}$ and the non-drag force $\mathbf{M}_{ik}^{nd}$,

$$\mathbf{M}_{ik} = \mathbf{M}_{ik}^{d} + \mathbf{M}_{ik}^{nd} \tag{1.4}$$

The drag force $\mathbf{M}_{ik}^{d}$ is generally expressed by the following standard form in terms of the drag coefficient C_D, the relative velocity $\mathbf{V}_r$ between two-phases and the interfacial area concentration a_i of the bubbles [1.60]:

$$\mathbf{M}_{ig}^{d} = -\tfrac{1}{2} C_D \rho_l \mathbf{V}_r |\mathbf{V}_r| a_i . \tag{1.5}$$

The attentions were paid to establish the correlations for C_D and a_i. Several correlations for C_D have been established based on the experiments of the single solid particle, droplets, or bubbles in the infinite systems [1.44]. Ishii and Chawla [1.61] developed the correlation of C_D for the multi-particle systems considering the flow regimes and the characteristics of the particles.

As for the interfacial area concentration a_i, the simplest expression is given in terms of the Sauter mean diameter D_{SM} and the void fraction α assuming the bubbles to be spherical shape: $a_i=6\alpha/D_{SM}$, where D_{SM} is the volume equivalent bubble diameter of spheres. Ishii and Mishima [1.62] developed the correlations of the interfacial area concentration a_i considering the flow regimes as shown in Eq. (1.6).

$$a_i = \begin{cases} \frac{6\alpha}{D_{SM}} & \text{For bubbly flow} \\ \frac{4.5}{D_H}\frac{\alpha-\alpha_{gs}}{1-\alpha_{gs}} + \frac{6\alpha_{gs}}{D_H}\frac{1-\alpha}{1-\alpha_{gs}} & \text{For slug or churn turbulent flow} \end{cases}. \tag{1.6}$$

As for the non-drag force $\mathbf{M}_{ik}^{nd}$, the following forces were usually considered according to the single-particle theory.

Lahey *et al.* [1.63] studied the constitutive equations of the virtual mass force for the bubbly flow. They found that the introduction of the virtual mass force $\mathbf{M}_{ig}^{V}$ term could improve the numerical stability and efficiency, and thus was important to the two-fluid model. Ishii and Mishima [1.62] summarized and gave the correlations for $\mathbf{M}_{ig}^{V}$ in term of the virtual mass coefficient C_{VM} and the acceleration of the relative velocities according to the flow regimes as

$$\mathbf{M}_{ig}^{V} = -C_{VM}\rho_l \left(\frac{D\mathbf{V}_r}{Dt} - \mathbf{V}_r \cdot \nabla \mathbf{V}_r \right), \tag{1.7}$$

and

$$C_{VM}=\begin{cases}\frac{1}{2}\alpha\dfrac{1+2\alpha}{1-\alpha} & \text{For bubbly flow}\\ 5\alpha\left[0.66+0.34\left(\dfrac{1-D_b/L_b}{1-D_b/(3L_b)}\right)\right] & \text{For slug flow}\end{cases} \tag{1.8}$$

According to the analysis of the single-spherical particle moving in the viscous shear flow [1.44], the particle could receive the lift force $\mathbf{M}_{ig}^{L}$ from the liquid phase perpendicular to the flow direction. Similarly, for the turbulent bubbly flow with the relative velocity $\mathbf{V}_r$ and the liquid phase velocity gradient $\nabla\mathbf{V}_l$, the lift force exerted on the bubbles was also considered and expressed in term of the lift force coefficient C_{LM}, the relative velocity $\mathbf{V}_r$, and the liquid phase velocity gradient $\nabla\mathbf{V}_l$ as

$$\mathbf{M}_{ig}^{L}=-C_L\alpha\rho_l\mathbf{V}_r\times\nabla\times\mathbf{V}_l\,. \tag{1.9}$$

The lift force played a very important role to the prediction of the bubble lateral distributions [1.10-1.17]. Attentions have been paid to determine the lift force coefficient C_{LM} based on the single bubble experiments and simulations [1.33, 1.34, 1.44], which was found to be related with the bubble size and deformation. According to Tomiyama's experiments [1.33], the lift force coefficient C_{LM} was given as follows:

$$C_{LM}=-\begin{cases}\min\left[0.288\tanh(0.121\mathrm{Re}),\,f(\mathrm{Eo}_H)\right] & \text{For}\quad \mathrm{Eo_H}<4\\ f(\mathrm{Eo}_H) & \text{For}\quad 4<\mathrm{Eo_H}<10\\ -0.27 & \text{For}\quad 10<\mathrm{Eo_H}\end{cases} \tag{1.10}$$

where $f(\mathrm{Eo_H})=0.00105\mathrm{Eo_H^3}-0.0159\mathrm{Eo_H^2}-0.0204\mathrm{Eo_H}+0.474$; $\mathrm{Eo_H}=\dfrac{g(\rho_j-\rho_g)D_{HB}^2}{\sigma}$;

D_{HB} the maximum horizontal bubble dimension.

The constitutive relations of the turbulent dispersion force $\mathbf{M}_{ig}^{T}$ exerted on the bubbles were derived by Lahey [1.34], Bertodano [1.65-1.66], and Burns [1.67] respectively using different methods as follows:

$$\mathbf{M}_{ig}^{T}=-\begin{cases}-C_T\rho_l k\nabla\alpha & \text{From Lahey [1993]}\\ -C_T\rho_l\frac{\upsilon_t}{\tau_b}\nabla\alpha & \text{From Bertodano [2006]}\\ -\frac{3}{4}C_TC_D\frac{\alpha}{d}\mathbf{V}_r\rho_l\frac{\upsilon_t}{0.9}\left(\frac{\nabla\alpha}{\alpha}-\frac{\nabla(1-\alpha)}{(1-\alpha)}\right) & \text{From Burns [2004]}\end{cases} \tag{1.11}$$

where C_T is the turbulent diffusion coefficient; k is the turbulent kinetic energy; υ_t is the eddy viscosity.

Antal *et al.* [1.68] introduced and derived the wall-lubrication force $\mathbf{M}_{ig}^{w}$ exerted on the bubble into the two-fluid model to prevent the bubble from touching the wall based on the analysis of single spherical bubble moving in the laminar flow. The lateral distribution near the wall could be better predicted with this force $\mathbf{M}_{ig}^{w}$ as expressed in the following form:

$$\mathbf{M}_{ig}^{w}=\alpha\rho_l C_W\frac{2}{d}\left|\mathbf{V}_r\right|^2\mathbf{n}_w \tag{1.12}$$

where $\mathbf{n}_w$ is the wall-normal unit vector; C_W is the wall force coefficient which is related with the distance y to wall and expressed as

$$C_W(y)=\begin{cases}-0.104-0.06\mathbf{V}_r\mathbf{n}_w+0.147\frac{D_B}{2y} & \text{From Antal [1991]}\\ F(\mathrm{Eo})\left(\frac{D_B^3}{4y^2}-\frac{D_B^3}{4(D_H-y)^2}\right) & \text{From Tomiyama [1998]}\\ -0.005+0.05\frac{D_B}{2y} & \text{From ANSYS [2010]}\end{cases} \tag{1.13}$$

$$\text{with}\quad F(\mathrm{Eo})=-\begin{cases}\exp(-0.933\mathrm{Eo}+0.179) & \text{For } 1\le \mathrm{Eo_H}\le 5\\ 0.007\mathrm{Eo}+0.04 & \text{For } 5<\mathrm{Eo_H}<33\end{cases}.$$

The last two terms in Eq. (1.3) indicate the interfacial pressure and shear stress terms. Lahey [1.70] and Bertodano *et al.* [1.71] considered the same pressure in both phases $p_k=p$, $\boldsymbol{\tau}_{ik}=\boldsymbol{\tau}_k$ and introduced the following constitutive relations for interfacial pressure and shear stress terms:

$$\mathbf{M}_{ig}^{P} = \left(\bar{p}_{ig} - \bar{p}_{g}\right)\nabla\alpha = C_{p}\alpha\rho_{l}\left|\mathbf{V}_{r}\right|^{2}\nabla\alpha \tag{1.14}$$

$$\mathbf{M}_{ig}^{S} = \boldsymbol{\tau}_{ig}\nabla\alpha = \boldsymbol{\tau}_{g}\nabla\alpha \tag{1.15}$$

where C_p is the pressure coefficient and 0.25 for non-interacting spherical bubbles based on the inviscid result. Bertodano *et al.* [1.66] discussed the non-spherical cases where $C_p > 0.25$ due to the wake effect behind the bubbles.

Though several experimental and analytical efforts were carried out to improve the above correlation coefficients [1.2], so far the physical mechanism of the above forces are still poorly understood. In addition, it is also notable that the aforementioned correlations were mainly proposed based on the single particle case, for the bubbly flow with many bubbles and bubble-bubble interaction further efforts are still necessary.

1.2.3.1.2 Turbulent Reynolds stresses

Turbulence term $\boldsymbol{\tau}_{k}^{T} = \rho_{k}\overline{\mathbf{v}_{k}\mathbf{v}_{k}}$ in the above momentum equations is one of the most important key terms for the turbulent bubbly flow, which determines the prediction of the distributions of the velocities, void fraction, and interfacial term. Turbulent models for the single-phase turbulence have been widely studied and could be found everywhere in the textbooks about the turbulence [1.1]. However, for turbulent bubbly flow, the understanding and modeling of this term are still in an initial stage due to the complicated physical process. Therein, the following mechanisms for the turbulence generation coexist such as the general shear-induced turbulence, the interaction between the shear-induced turbulent structures and the bubbles, the bubbles-induced turbulence and its interaction between the different turbulent structures [1.5, 1.9]. So far, the development of the turbulent models for the turbulent bubbly flow was mainly carried out based on the analogy of the single-phase turbulent models.

Based on the phenomenological modeling where the eddy viscous assumption for the turbulent shear stress $\boldsymbol{\tau}_{S}^{T} = \rho_{k}\left(\upsilon_{l} + \upsilon_{t}\right)\left(\nabla\mathbf{V}_{l} + \nabla\mathbf{V}_{l}^{T}\right)/2$ was also adopted, Sato and Sadatomi [1.72], Drew and Lahey [1.73] and Kataoka and Serizawa [1.74] adopted

the zero or one equation model to the turbulent bubbly flow to determine the turbulent shear stress by adding the bubble-induced turbulence. Therein, the attentions were also paid to the determination of the eddy viscosity υ_t and the mixing length l_m.

$$\tau_S^T = \begin{cases} \rho_l \left(\upsilon_s + \upsilon_b\right) \dfrac{dV}{dr} & \text{From Sato, 1981} \\ \rho_l l_m^2 \left|\dfrac{dV}{dr}\right| \dfrac{dV}{dr} & \text{From Drew and Lahey, 1981} \\ \rho_l \left(l_s + l_B\right) \sqrt{\dfrac{2k}{3}} \dfrac{dV}{dr} & \text{From Kataoka and Serizawa, 1995} \end{cases} \tag{1.16}$$

where υ_s and υ_b are the eddy viscosity induced by shear and bubbles, in Sato and Sadatomi [1.72] $\upsilon_b = \alpha C_{\mu b} D_B V_{r\infty}$; l_s and l_b are the mixing lengths of the shear induced turbulence and bubble induced turbulence respectively; υ_s and l_s were decided based on the Prandtl mixing theory. However, the determinations of the eddy viscosity and mixing length are strongly dependent on their experimental data, and so far the applications of the above models were still limited and need further validation.

Theofanous and Sullivan [1.11] and Wijngaarden [1.75] theoretically and statistically discussed the bubble-induced turbulence or the pseudo-turbulence by comparing the turbulent intensities before and after the bubbles injection. Based on the potential theory Wijngaarden [1.75] derived the pseudo turbulent Reynolds stress for the rising bubbles in the laminar flow as

$$\boldsymbol{\tau}_B = \alpha \left[\frac{3}{20} \alpha \left|\overline{\mathbf{V}_r}\right|^2 I + \frac{1}{20} \alpha \left(\overline{\mathbf{V}_r} \overline{\mathbf{V}_r}\right) \right], \tag{1.17}$$

and for the uniform turbulent flow,

$$\overline{k_E^2} = \alpha \left|\overline{\mathbf{V}}_r\right|^2 \left\{ M + 6 \frac{u_0'^2}{\left|\overline{\mathbf{V}}_r\right|^2} \left[f\left(0\right) + f\left(a\right) \right] \right\} \tag{1.18}$$

For the bubbly flow in the pipe, Theofanous and Sullivan [1.11] estimated the total turbulence based on the mean flow velocity and the wall shear stress as

$$\left(\frac{\overline{vv}}{V_c}\right)=\left\{\frac{1}{2}c_f\left(1+\alpha\right)\left(1-\alpha\right)+\delta\alpha\left(1-\alpha\right)\left|1-\frac{\rho_g}{\rho_l}\right|\frac{D_H g}{4V_c^2}\right\}\left(1+1.5\alpha\frac{D_H}{D_B}\right). \quad (1.19)$$

Several more general and accurate turbulent models for turbulent bubbly flow have also been developed on basis of the two-equation model or Reynolds stress model of the single phase turbulent flow [1.1]. Kataoka *et al.* [1.76] derived the basic equations for the turbulent Reynolds stress and dissipation for the two-phase flow, where the expressions of the interfacial terms were given and discussed. So far, according to the author's knowledge, the following three different methods were used to consider the turbulence.

Lahey [1.70] developed τ-ε model for the turbulent stresses in the liquid phase of the turbulent bubbly flow by mimicking the single-phase τ-ε model as follows:

$$\alpha_l\frac{D}{Dt}\overline{\mathbf{vv}}=\nabla\cdot\left[\alpha_l\left(\upsilon_l+C_S\frac{k}{\varepsilon}\overline{\mathbf{vv}}\right)\nabla\overline{\mathbf{vv}}\right]+\alpha_l\left(\mathbf{P}+\mathbf{\Phi}-2\varepsilon\mathbf{I}+\mathbf{S}_i\right) \quad (1.20)$$

$$\alpha_l\frac{D\varepsilon}{Dt}=\nabla\cdot\left[\alpha_l\left(\upsilon_l+C_\varepsilon\frac{\varepsilon}{k}\overline{\mathbf{vv}}\right)\nabla\varepsilon\right]+\alpha_l\left(C_{\varepsilon1}\frac{\varepsilon}{k}P-C_{\varepsilon2}\frac{\varepsilon}{k}\varepsilon+C_{\varepsilon B}\frac{S_i}{t_e}\right) \quad (1.21)$$

P, **Φ**, ε and **I** are the turbulence production, redistribution, dissipation and unit tensor which are the same as the single-phase turbulent flow. C_ε, $C_{\varepsilon1}$, $C_{\varepsilon2}$ and $C_{\varepsilon B}$ are the model constants. For the turbulent bubbly flow, the additional interfacial tensor $\mathbf{S}_i$ and $C_{\varepsilon B}S_i/t_e$ are the bubble induced turbulence generation and dissipation; $S_i=\mathrm{trace}\left(\mathbf{S}_i\right)$; t_e is the characteristic time of the eddies, and the choice of t_e was discussed by Rzehak and Krepper [1.77].

By $k=\frac{1}{2}\mathrm{trace}\left(\overline{\mathbf{vv}}\right)$, the above Reynolds stress model become the k-ε model for the turbulent bubbly flow in the following form:

$$\alpha_l\frac{D}{Dt}k=\nabla\cdot\left[\alpha_l\left(\upsilon_l+\upsilon_t\right)\nabla k\right]+\alpha_l\left(P-\varepsilon+S_i\right). \quad (1.22)$$

Several studies were paid to the constitutive relations of the additional interfacial

tensor $\mathbf{S}_i$ and the additional interfacial dissipation term $C_{\varepsilon B}S_i / t_e$ [1.77].

Bertodano *et al.* [1.71] proposed another type of τ-ε model considering the transport equations for both the shear-induced turbulent and the bubble-induced turbulence:

$$\alpha_l \frac{D}{Dt} k_S = \nabla \cdot \left[\alpha_l \left(\upsilon_l + \upsilon_t \right) \nabla k_S \right] + \alpha_l \left(P_S - \varepsilon_S \right). \tag{1.23}$$

$$\alpha_l \frac{D}{Dt} k_B = \nabla \cdot \left[\alpha_l \left(\upsilon_l + \upsilon_t \right) \nabla k_B \right] + \frac{\alpha_l}{t_b} \left(k_{Bam} - k_B \right). \tag{1.24}$$

$$\alpha_l \frac{D}{Dt} \varepsilon_S = \nabla \cdot \left[\alpha_l \frac{\left(\upsilon_l + \upsilon_t \right)}{\sigma_t} \nabla \varepsilon_S \right] + \alpha_l \left(C_{\varepsilon 1} \frac{\varepsilon_S}{k} P - C_{\varepsilon 2} \frac{\varepsilon_S}{k} \varepsilon_S \right). \tag{1.25}$$

In addition, the turbulent shear stress was expressed as

$$\boldsymbol{\tau} = \rho_l \upsilon_t \left(\nabla \mathbf{V} + \nabla \mathbf{V}^T \right) / 2 - \frac{2}{3} \mathbf{A}_S \rho_l k_S + \mathbf{A}_B k_B \tag{1.26}$$

where the eddy viscosity $\upsilon_t = C_\mu \frac{k^2}{\varepsilon} + C_{\mu b} D_B \alpha \left| \mathbf{V}_r \right|$, and $\mathbf{A_S}$ and $\mathbf{A_B}$ are the tensors to show the turbulence anisotropy for the sear-induced turbulence and bubble-induced turbulence respectively.

Similar to Lahey [1.70] and Bertodano *et al.* [1.71], Chahed *et al.* [1.78-1.79] proposed another turbulent model by decomposing the turbulent Reynolds stress into turbulent dissipative part due to the velocity gradient and the pseudo-turbulent non-dissipative part due to the interfacial drag. Therein, the turbulent anisotropy was considered by introducing the bubble characteristics time following the experimental results and initial model of Lance [1.4-1.6].

On the other hand, as observed in the experimental and numerical databases, the bubbles size and deformation could strongly affect the flow characteristics. The aforementioned models were developed based on a prior knowledge of the bubbles size and deformation such as the averaged bubble Sauter mean diameter D_{SM}. However, in the real systems, there exist a broad range of the bubble sizes, and the bubbles could

experience the coalescence with other bubbles and also breakup, which were not shown in the above models at all. Recently, to improve the models for the turbulent bubbly flow, the attentions were also paid to the bubble behaviors such as distributions of the bubble size or interfacial area concentration (IAC) [1.2]. Generally, the models to predict the bubble behaviors are based on Boltzman statistical averaging method and Boltzman equation for the dispersed bubbles. Correspondingly, the dispersed gas phase was separated into several groups according to the interested properties of the dispersed bubbles such as bubble size and IAC. For each group of the dispersed phase, the conservations equations of the mass, momentum, and energy were established considering the birth and death of the each group. For the continuous phase, the interfacial effects from the dispersed phase are the sum of all groups. With this method, it aimed at predicting the behaviors of the dispersed gas phase such as the distributions of the bubble size or interfacial area concentration which are crucial to the flow characteristics. Currently, the population balance model [1.80], the one-group and two-group interfacial transport model [1.2] and multi-fluid model [1.81] belong to the model of this type. Therein, the attentions were mainly paid to model the birth and death of the each group which depend on the bubble coalescence and breakup. The corresponding detailed reviews could be found in [1.82-1.83]. Due to the complicated nature of the bubble coalescence and breakup, these models are still in an initial stage and the more efforts are required in the future work.

1.2.3.2 Model implementation and validation

As mentioned in Section 1.2.2, the current experimental databases of the turbulent bubbly flow were mainly established in the following flow types: uniform bubbly flow, bubbly boundary layer flow, the bubbly flow in the small and large circular pipes and small and large noncircular ducts. With the aid of these databases, the implementations and validations of the two-fluid model were carried out such as in [1.70-1.85]. At this stage, most of the attentions were focused on the prediction of the phase distributions by considering the interfacial terms in the momentum transport

equations [1.70-1.74]. However, for the prediction of the characteristics of the turbulent structures such as intensities and anisotropic properties, even several models have been proposed [1.75, 1.78-1.79], they were limited for very low void fraction or not satisfactory due to our limited knowledge on the bubble-induced turbulence. Moreover, the previous implementation and validation of models were mainly carried out in the small circular pipes [1.70-1.71, 1.84]. For the bubbly flow in the large circular and noncircular ducts where the flow were strongly affected by the duct geometry and showed different characteristics, there were still very few detailed validation work [1.34-1.35, 1.85]. In addition, with the above models only the drag enhancement could be predicted due to the superposition of the shear-induced turbulence and bubble-induced turbulence, whereas the turbulent drag reduction were also observed in the experiments [1.19]. Therefore, whether the models proposed and validate before are suitable for the different conditions still needs further studies based on the new experimental databases. And the new models for other flow properties such as turbulence are also required.

1.2.4 Summary on review of databases and models

In section 1.2.2-1.2.3, the state-of-the-art of the turbulent bubbly flow was briefly reviewed including the existing databases and models. So far, the experimental databases of the turbulent bubbly flow have been developed for several flow types including uniform bubbly flow, circular pipe flow, and noncircular duct flow. The flow characteristics such as phase distribution and turbulence were mainly analyzed and modeled for the turbulent bubbly flow in the small circular pipes and noncircular ducts. However, for the turbulent bubbly flow in the large and non-circular ducts which could be often met in the engineering applications, it is still lack of the experimental database and the model evaluations. The previous developed models were focused on the prediction of the phase distributions, but about the turbulent characteristics such as intensities, turbulence generation process and anisotropic properties the current understandings are still far from the satisfactory and limited for very low void fraction.

1.3 Scope and layout of the dissertation

On basis of the background of the turbulent bubbly flow mentioned above, the present dissertation is aimed at the following aspects to improve the understanding and modeling of the turbulent bubbly flow especially in the large noncircular duct:

(1) Evaluating the models proposed for the turbulent bubbly flow in the small circular and noncircular ducts to that in the large noncircular duct;

(2) Further analyzing the flow characteristics of the turbulent bubbly flow in the large noncircular ducts especially the liquid phase velocities and turbulence;

(3) Improving the current models for the prediction of the turbulent bubbly flow in the large noncircular ducts especially for the turbulence structures based on the proposed analysis above.

The dissertation is composed by 8 chapters and arranged as follows: Chapter 1 mainly introduces the motivation, the current research status and the purpose of this study. Chapter 2 describes the experimental database including the experimental apparatus, flow conditions and some experimental results. Chapter 3 describes the numerical methodologies based on the two-fluid model for the turbulent bubbly flow in the large square duct, numerical results and discussions. To improve the modeling of the turbulent bubbly flow in the large noncircular ducts, the further analysis and modeling improvement are carried out for flow characteristics in the later four chapters. Chapter 4 discusses the developing process in the turbulent bubbly flow. Chapter 5 is focused on the characteristics and modeling of the liquid phase velocities. Chapter 6 proposes a new correlation for the bubble deformation and describes the numerical validation of the void fraction. Chapter 7 describes the turbulence modulation due to the presence of the bubbles. Finally, the summary of this dissertation and the recommendation of the future work will be given in Chapter 8.

Reference

[1.1] Pope, S. B., 2000, Turbulent flows, Cambridge University Press.

[1.2] Ishii, M., Hibiki, T., 2011, Thermo-fluid dynamics of two-phase flow. 2nd ed. New York: Springer.

[1.3] Marié, J. L., 1983, Investigation of two-phase bubbly flows using Laser Doppler Anemometry, PCH Physico Chemical Hydrodynamics 4, 103-118.

[1.4] Lance, M. , Bataille, J., 1991, Turbulence in the liquid phase of a uniform bubbly air-water flow, J. Fluid Mechanics 222, 95-118.

[1.5] Lance, M. , Bataille, J., 1991, Homogeneous turbulence in bubbly flows, J. Fluids, Engineerig 113, 295-300.

[1.6] Moursali, E., Bataille, J., Marié, J. L., 1995, An upward turbulent bubbly boundary layer along a vertical flat plate, Int. J. Multiphase Flow 21, 107-117.

[1.7] Isao, K., Mamoru, I., 1987, Drift flux model for large diameter pipe and new correlation for pool void fraction, Int. J. Heat Mass Transfer 30, 1927–1939.

[1.8] Sun, H. M., 2014, Study on upward air-water two-phase flow characteristics in a vertical large square duct, Doctor Thesis, Kyoto University.

[1.9] Serizawa, A., 1974, Fluid dynamics characteristics of two-phase flow, Doctor Thesis, Kyoto University.

[1.10] Serizawa, A., Kataoka, I., Michiyoshi, I., 1975, Turbulence structure of air - water bubbly flow—II. local properties, Int. J. Multiphase Flow 2, 235–246.

[1.11] Theofanous, T. G., Sullivan, J., 1982, Turbulence in two-phase dispersed flows, J. Fluid Mechanics 116, 343-362.

[1.12] Wang, S., Lee, S., Jones, O., Lahey, R., 1987, 3-D turbulence structure and phase distribution measurements in bubbly two-phase flows, Int. J. Multiphase Flow 13, 327–343.

[1.13] Liu, T. J., 1993, Bubble size and entrance length effects on void development in a vertical channel, Int. J. Multiphase Flow 19, 99–113.

[1.14] Liu, T. J., Bankoff, S. G., 1993, Structure of air-water bubbly flow in a vertical

pipe—I. liquid mean velocity and turbulence measurements, Int. J. Heat Mass Transfer 36, 1049–1060.

[1.15] Liu, T. J., Bankoff, S. G., 1993, Structure of air-water bubbly flow in a vertical pipe—I. bubble void fraction, bubble velocity and bubble size distribution, Int. J. Heat Mass Transfer 36, 1061–1072.

[1.16] Hibiki, T., Ishii, M., 1999, Experimental study on interfacial area transport in bubbly two-phase flows, In. J. Heat Mass Transfer 42, 3019–3035.

[1.17] Hibiki, T., Ishii, M., Xiao Z., 2001, Axial interfacial area transport of vertical bubbly flows, In. J. Heat Mass Transfer 44, 1869–1888.

[1.18] Michiyoshi, I., Serizawa, A., 1986, Turbulence in two-phase bubble flow, Nucl. Eng. Des. 95, 253-267

[1.19] Serizawa, A., Kataoka, I., 1990, Turbulence suppression in bubbly two-phase flow, Nucl. Eng. Des. 122, 1–16.

[1.20] Ohnuki, A., Akimoto, H., 2000, Experimental study on transition of flow pattern and phase distribution in upward air–water two-phase flow along a large vertical pipe, Int. J. Multiphase Flow. 26, 367–386.

[1.21] Shawakat, M. E., Ching, C. Y., Shoukri, M., 2007, On the liquid turbulence energy spectra in two-phase bubbly flow in a large diameter vertical pipe, Int. J. Multiphase Flow 33, 300-316.

[1.22] Shawakat, M. E., Ching, C. Y., Shoukri, M., 2008, Bubble and liquid turbulence characteristics of bubbly flow in a large diameter vertical pipe, Int. J. Multiphase Flow 34, 767-785.

[1.23] Sun, X., Smith, T. R., Kim, S., Ishii, M., Uhle, J., 2003, Interfacial structure of air-water flow in a relatively large pipe. Exp. Fluids 34, 206-219.

[1.24] Shoukri, M., Hassan, I., Gerges, I., 2003, Two-phase bubbly flow structure in large-diameter vertical pipes, The Canadian J. Chem. Eng. 1 205-211.

[1.25] Shen, X., Mishima, K., Nakamura, H., 2005, Two-phase phase distribution in a vertical large diameter pipe, Int. J. Heat Mass Transfer 48, 211–225.

[1.26] Schlegel, J.P., Sawant, P., Paranjape, S., Ozar, B., Hibiki, T., Ishii, M., 2009, Void fraction and flow regime in adiabatic upward two-phase flow in large diameter vertical pipes, Nucl. Eng. Des. 239, 2864–2874.

[1.27] Smith, T.R., Schlegel, J.P., Hibiki, T., Ishii, M., 2012, Two-phase flow structure in large diameter pipes, Int. J. Heat Fluid Flow 33, 156–167.

[1.28] Shen, X., Hibiki, T., Nakamura, H., Developing structure of two-phase flow in a large diameter pipe at low liquid flow rate, Int. J. Heat Fluid Flow. 34 (2012) 70–84.

[1.29] Schlegel, J.P., Miwa, S., Chen, S., Hibiki, T., Ishii, M., 2012, Experimental study of two-phase flow structure in large diameter pipes, Exp. Thermal Fluid Sci. 4, 12–22.

[1.30] Prasser, H. M., Beyer, M., Boettger, A., Carl, H., Lucas, D., Schaffrath, A., Schuetz, P., Weiss, F. P., Zschau, J., 2005, Influence of the Pipe Diameter on the Structure of the Gas-Liquid Interface in a Vertical Two-Phase Pipe Flow, Nucl. Tech. 152, 3-22

[1.31] Esmaeeli, E. A., Tryggvason, G., 1994, Numerical simulations of rising bubbles in bubbles dynamics and interface phenomena, Kluwer Academic, Dordrecht.

[1.32] Ervin, E. A., Tryggvason, G., 1997, The rise of bubbles in a vertical shear flow. J. Fluids Eng. 119, 443-449.

[1.33] Tomiyama, A., Tamai, H., Zun, I., Hosokawa, S., 2002, Transverse migration of single bubbles in simple shear flows, Chem. Eng. Sci. 57, 1849-1858.

[1.34] Lahey, Jr R. T., Bertodano, de M. L., Jones, Jr O. C., 1993, Phase distribution in complex geometry conduits, Nucl. Eng, Des. 141, 177-201.

[1.35] Ohnuki, A., Akimoto, H., 2001, Model development for bubble turbulent diffusion and bubble diameter in large vertical pipes. J. Nucl. Sci. Technol. 38, 1074-1080.

[1.36] Bertodano, de M. L., 1992, Turbulent bubbly two-phase flow in a triangular duct. Doctoral Thesis, Resselaer Polytechnic Institute.

[1.37] Launder, B.E., Ying, W.M., 2006, Secondary flows in ducts of square cross-section, J. Fluid Mech. 54, 289.

[1.38] Ohba, K., Yuhara, T., 1982, Study on vertical bubbly flows using laser doppler measurements: 2nd report, turbulence structure in square duct flow. Trans. Japan Society of Mech. Eng. 48, 78-87

[1.39] Ohba, K., Yuhara, T., 1985, Matsuyama H. Study on vertical bubbly flows using laser doppler measurements: 3rd report, simultaneous measurement of bubble and liquid. Trans. Japan Society Mech. Eng. 51, 4194-4200.

[1.40] Zun, I., 1990, The mechanism of bubble non-homogeneous distribution in two-phase shear flow. Nucl. Eng. Des. 118, 155-162.

[1.41] Sadatomi, M., Sato, Y., Saruwatari, S., 1982, Two-phase flow in vertical noncircular channels. Int. J. Multiphase Flow 8, 641–655.

[1.42] Sun, H. M., Kunugi, T., Shen, X. Z., Wu, D. Z. and Nakamura, H., Upward air-water bubbly flow characteristics in a vertical square duct, J. Nucl. Sci. Tech., Vol. 51, 267–281(2014).

[1.43] Hoagland, L. L., 1960, Fully Developed Turbulent Flow in Straight Rectangular Ducts - Secondary Flow, Its Cause and Effect on the Primary Flow, Ph.D. thesis, Department of Mechanical Engineering, MIT.

[1.44] Clift, R., Grace, J.R., Weber M.E., 1972, Bubbles, drops, and particles, Science.

[1.45] Gore, R. A., Crowe, C. T., 1989, Effect of particle size on modulating turbulent intensity, Int. J. Multiphase Flow 15, 279-285.

[1.46] Esmaeeli, A., Tryggvason, G., 1996, An inverse energy cascade in two-dimensional low Reynolds number bubbly flows, J. Fluid Mech. 314, 315-330

[1.47] Esmaeeli, A., Tryggvason, G., 1998, Direct numerical simulations of bubbly flows Part 1. Low Reynolds number arrays, J. Fluid Mech. 377, 313-345.

[1.48] Esmaeeli, A., Tryggvason, G., 1999, Direct numerical simulations of bubbly flows Part 1. Moderate Reynolds number arrays, J. Fluid Mech. 385, 325-358.

[1.49] Bunner, B., Tryggvason, G., 1999, Direct numerical simulations of three-dimensional bubbly flows, Phys. Fluids 11, 1967-1969.

[1.50] Bunner, B., Tryggvason, G., 2002, Dynamics of homogeneous bubbly flows Part 2: Rise velocity and microstructure of the bubbles, J. Fluid Mech. 466, 17-52.

[1.51] Bunner, B., Tryggvason, G., 2002, Dynamics of homogeneous bubbly flows Part 2: velocity fluctuations, J. Fluid Mech. 466, 53-84.

[1.52] Bunner, B., Tryggvason, G., 2003, Effect of bubble deformation on the properties of bubbly flows, J. Fluid Mech. 495, 77-118.

[1.53] Lu, J., Fernández, A., Tryggvason, G., 2005, The effects of bubbles on the wall drag in a turbulent channel flow, Phys. Fluids 17, 095102.

[1.54] Lu, J., Tryggvason, G., 2006, Numerical study of turbulent bubbly downflows in a vertical channel, Phys., Fluids 18, 103302.

[1.55] Lu, J., Tryggvason, G., 2008, Effect of bubble deformability in turbulent bubbly upflow in a vertical channels, Phys. Fluids 20, 040701.

[1.56] Tryggvason, G., 2013, Multiscale issues in DNS of multiphase flows, 8th International Conference on Multiphase Flow, 2013, Jeju, Korea.

[1.57] Bolotnov, Igor A., 2013, Influence of bubbles on the turbulence anisotropy, J. Fluids Eng. 135, 051301.

[1.58] Zuber, N., Findlay, J. A., 1965, Average volumetric concentration in two-phase flow systems, J. Heat Transfer, 453-468.

[1.59] Wheeler, C. L., 1986, COBRA-NC: a thermal-hydraulic code of transient analysis of nuclear reactor components: equations and constitutive models. NUREG/CCR-3262.

[1.60] Ishii, M., 1975, Thermo-fluid Dynamic Theory of Two-phase Flow, Eyrolles.

[1.61] Ishii, M., Chawla, T. C., Local drag laws in dispersed two-phase flows, Argonne Nation Lab Report, ANL-79-105.

[1.62] Ishii, M., Mishima, K., 1984, Two-Fluid model and hydrodynamics constitutive relations, Nucl. Eng. Des. 82, 107-126.

[1.63] Lahey, Jr. R.T., Cheng, L. Y., Drew, D. A.,, Flaherty, J. E., 1980, The effects of virtual mass on the numerical stability of accelerating two-phase flows, Int. J. Multiphase flow 6, 281-294.

[1.64] Tomiyama, A., Sou, A., Zun, I., Kanami, N., Sakaguchi, T., 1995, Effects of Eötvös number and dimensionless liquid volumetric flux on local motion of a bubble in a laminar duct flow, Advance In Multiphase Flow, Elsevier, 3-15.

[1.65] Bertodano, Lopez M., 1998, Two fluid model for two-phase turbulent jets, Nucl. Eng. Des. 179, 65-74.

[1.66] Bertodano, Lopez M., Sun, X., Ishii, M., Ulke, A., 2006, Phase distribution in the cap bubble regime in a duct, J. Fluids Eng. 977-1001.

[1.67] Burns, D., Frank, T., Hamill, I., Shi, J. M., 2004, The Favre averaged drag model for turbulent dispersion in Eulerian multi-phase flow. In: 5th International Conference on Multiphase Flow, Yokohama, Japan, 392.

[1.68] Antal, S.P., Lahey, Jr R. T., Flaherty, J. E., 1991, Analysis of phase distribution in fully developed laminar bubbly two-phase flow, Int. Multiphase Flow 13, 309-326.

[1.69] Tomiyama, A., 1998, Struggle with computational bubble dynamics. In: 3rd International Conference on Multiphase Flow, ICMF'98, Lyon, France.

[1.70] Lahey Jr. R.T., 1990, The analysis of phase separation and phase distribution phenomena using two-fluid models, Nucl. Eng. Des. 122, 17-40.

[1.71] Bertodano, Lopez M., Lahey, Jr. R.T., Jones, O. C., 1994, Phase distribution in bubbly two-phase flow in vertical ducts, Int. J. Multiphase Flow 20, 805-818.

[1.72] Sato, Y., Sadatomi, M., 1981, Momentum and heat transfer in two-phase bubble flow—I. Theory, Int. J. Multiphase Flow 7, 167-177.

[1.73] Drew, D. A., Lahey, Jr. R.T., 1982, Phase distribution mechanisms in turbulent low-quality two-phase flow in a circular pipe, J. Fluid Mech. 117, 91-106.

[1.74] Kataoka, I., Serizawa, A., 1995, Modeling and prediction of turbulence in bubbly two-phase flow, Proc. 2nd Int. Conf. Multiphase Flow, Kyoto, MO2:11-16

[1.75] Wijngaarden, van L., 1998, On pseudo turbulence, Theoret. Comput. Fluid Dynamics 10, 449-458.

[1.76] Kataoka, I., Serizawa, A., 1989, Basic equations of turbulence in gas-liquid two-phase flow, Int. Multiphase Flow 5, 843-855.

[1.77] Rzehak, R., Krepper, E., 2013, Bubble-induced turbulence: Comparison of CFD models, Nucl. Eng. Des. 258, 57-65.

[1.78] Chahed, J., Roig, V., Masbernat, L., 2003, Eulerian-Eulerian two-fluid model for turbulent gas-liquid bubbly flows, Int. J. Multiphase Flow 29, 23-49.

[1.79] Bellakhel, G., Chahed, J., Masbernat, L., 2004, Analysis of the turbulence statistics and anisotropy in homogeneous shear bubbly flow using a turbulent viscosity model, Journal of Turbulence 5, 036

[1.80] Das, A. K., Das, P. K., 2010, Modeling bubbly flow and its transitions in vertical annuli using population balance technique, Int. J. Heat Fluid Flow 31, 101-104.

[1.81] Politano, M. S., Carrica, P. M., Converti, J., 2003, A model for turbulent polydisperse two-phase flow in vertical channels, Int. J. Multiphase Flow 19, 1153-1182.

[1.82] Liao, Y., Lucas, D., 2009, A literature review of theoretical models for drop and bubble breakup in turbulent dispersions, Chem. Eng. Sci. 64, 3389-3406.

[1.83] Liao, Y., Lucas, D., 2010, A literature review on mechanisms and models for the coalescence process of fluid particles, Chem. Eng. Sci. 65, 2851-2864.

[1.84] Bertodano, M. L., Lahey Jr, R. T. and Jones Jr, O. C., 1994, Development of a k-ε model for bubbly two-phase flow. J. Fluids Engineering 116, 128-134.

[1.85] Lucas, D., Tomiyama, A., 2011, On the lateral lift force in poly-dispersed bubbly flows, Int. J. Multiphase Flow 37, 1178-1190.

Chapter 2

Experimental databases of upward turbulent bubbly flow

2.1 Introduction

Before evaluating the existed models of the turbulent bubbly flow in the large noncircular ducts, a comprehensive database is necessary to be collected. Table 2.1 summarized the database information according to its duct geometry, which will be used in the present dissertation. Sun's experimental result in the large noncircular ducts [2.10] will be chosen as the main database in the following chapters. In the following, the experimental database will be reviewed and collected including the experimental techniques and apparatus, the flow conditions and the experimental results.

2.2 Experimental techniques

To measure the velocity and turbulence fields, nowadays several experimental techniques have been developed and could be classified into contact type and contactless type according to whether inserting the probes into the flow or not. The contact type techniques insert the probes into the flow and thus there may exist some effects of the inserted probes on the flow. Therefore, nowadays for the single-phase turbulent flow measurement, the contactless measurement techniques such as laser Doppler velocimetry (LDV), particle tracking velocimetry (PTV) and the particle image velocimetry (PIV) played more and more important role in the understanding and modeling of the single-phase turbulence. Generally, the above contactless techniques are based on the optical techniques and require the transparent fluids property. However, unlike the single-phase turbulent flow, due to the low visibility the above optical

measurement techniques failed for the turbulent bubbly flow except for the cases with the few bubbles and in the near-wall region. The velocities and turbulence in the turbulent bubbly flow were mainly measured by the contact type technique such as the hot-film probe, based on which the velocity and the turbulent kinetic energy could be measured at single point. However, it is notable that for the flow with large void fraction the hot film is easy to be burn out due to the inefficient cooling by gas phase. These phenomena also limit the application of hot film to the turbulent bubbly flow measurements. Nonetheless, it has provided us many useful databases to understand the physics and develop the model of turbulent bubbly flow.

As for the measurement of the bubbles' behaviors, generally the flow visualization is a useful way which also requires high visibility of the fluid properties and thus could only be adopted in few bubbles cases. At present, for the turbulent bubbly flow with many bubbles, the bubbles' behaviors are mainly measured by probes such as optical-sensor probes and conductive-sensor probes, based on which the bubble number, concentration and the bubble geometry could be measured at the single point. Fig. 2.1 summarizes the applications of the current experimental techniques for the turbulent bubbly flow measurement.

2.3 Experimental apparatus

The experimental apparatus for the upward turbulent bubbly flow generally contains five systems including the liquid phase circulation loop, the gas phase supplying system, the inlet two phase mixing or bubble generation system, the phase separation system and the test section with the measurement systems. Fig. 2.2 shows a simplified schematic diagram of the experimental apparatus.

For the single phase flow, when the flows are introduced to the ducts there exist two stages including the developing region with the entrance effects and the developed region far from the inlet and without the entrance effects. In order to establish and validate the models, the universal databases are necessary, which requires the

experimental measurements to be carried out in the fully developed region or developing region with accurate control of the inlet flow. However, unlike the single phase flow where the fully developed flow status could be reached with the long enough pipes, for the turbulent bubbly flow the following problems make it difficult to establish the universal database for the model development.

(a) Inlet flow control: not only the flow velocities, but also the distributions of the void fraction and the bubble diameters should be considered.

(b) Bubble coalescence and breakup: they could change the bubbles properties but their measurements and mechanisms are still in an initial stage.

(c) Bubble expansion: the bubbles properties could be changed for the high and long ducts so that the fully-developed turbulent bubbly flow is difficult to reach.

In summary, for the upward turbulent bubbly flow, after it is introduced to the ducts, the flow includes the developing of the liquid phase flow field and the dispersed bubbles distributions or flow regimes which couples together and determines the final flow characteristics. It is more complicated for the flow to reach the fully-developed status for both the liquid phase flow field and the dispersed bubbles distributions. During the establishment and validation the turbulent bubbly flow models, the developing status is necessary to be examined with the carefully controlled and measured inlet parameters such as the distributions of void fractions, the bubble diameters, and the velocities of liquid phase and bubbles. Table 2.1 shows the locations of the experimental measurements in the current used databases which are still very limited to understand the flow developing process.

Table 2.1 Experimental databases in different duct geometries. B: Base; H: Height

Duct shape	Experimental database	Duct size $D_H(mm)$	Experimental techniques	Measured locations z/ D_H	Measurements
Small Circular Pipe	Serizawa *et al.* [2.1-2.2]	60	Dual-senor Conductive & Hot-film probes	10, 20, 30	α, v_b, f_b W, w_{rms}
	Wang *et al.* [2.3]	57.15	Hot-film probe	35	α, W, w_{rms}, v_{rms}, $<vw>$
	Liu *et al.* [2.4-2.5]	38 57.2	Dual-senor Conductive & Hot-film probes	36 30, 60, 90, 120	α, v_b, f_b, D_b, W, w_{rms}, v_{rms}, $<vw>$
	Hibiki *et al.* [2.6]	25.4 50.8	Dual-senor Conductive & Hot-film probes	12, 65, 125 6, 30.3, 53.5	α, v_b, D_b, a_i W, w_{rms}
Small Triangle Duct	Bertodano *et al.* [2.7]	B: 50 H: 100	Hot-film probe	73	α, W, w_{rms}, v_{rms}, $<vw>$
Large Circular pipe	Shawkat *et al.* [2.8]	200	Dual-senor optical & Hot-film probes	42	α, v_b, f_b, D_b, W, w_{rms}, v_{rms}, $<vw>$
	Sun *et al.* [2.9]	100	Multi-senor Optical & Hot-film probe	3, 18, 33	α, v_b, D_b, a_i
Large Square Duct	Sun [2.10]	136×136	Multi-senor Optical & Hot-film probe	4.5, 10.1, 16	α, v_b, f_b, D_b, a_i W, w_{rms}, v_{rms}, $<vw>$

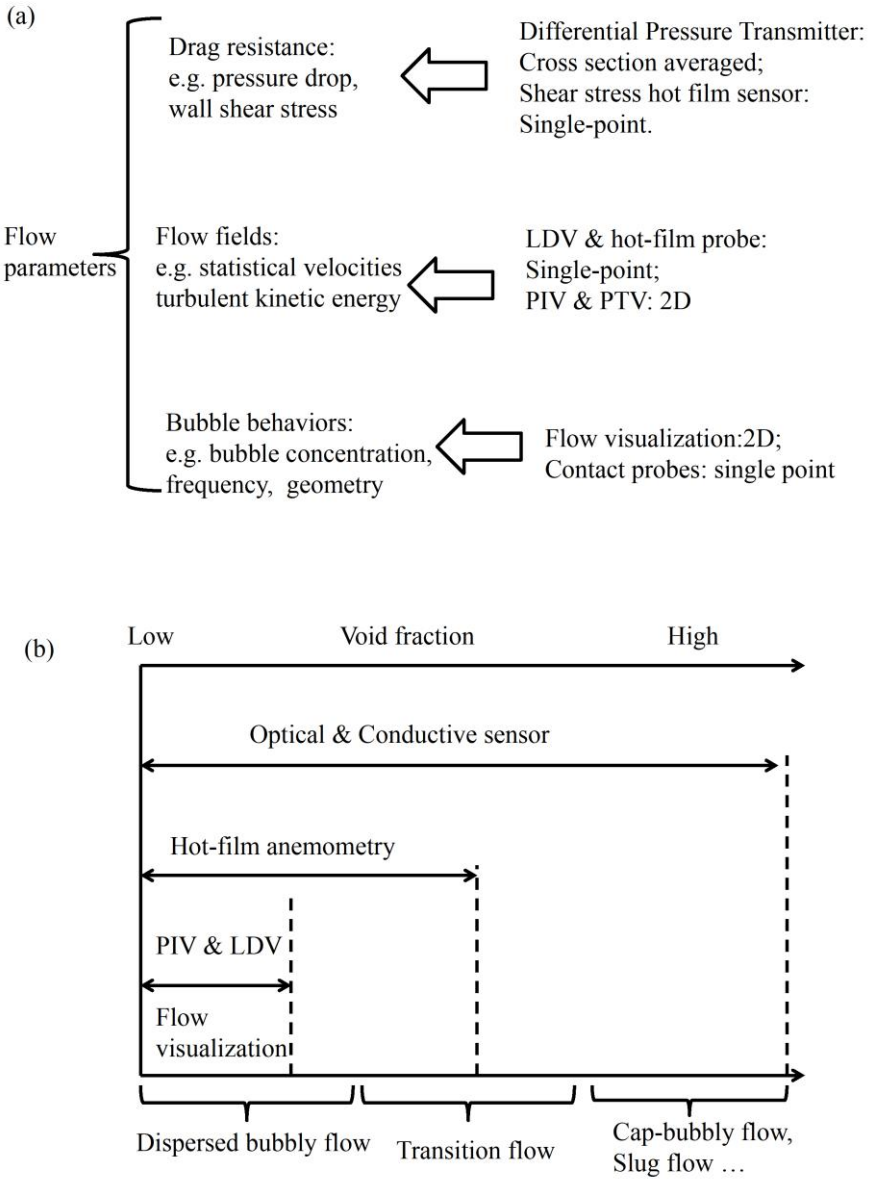

Fig. 2.1 (a) Experimental techniques for the flow measurements and (b) its applications in the turbulent bubbly flow.

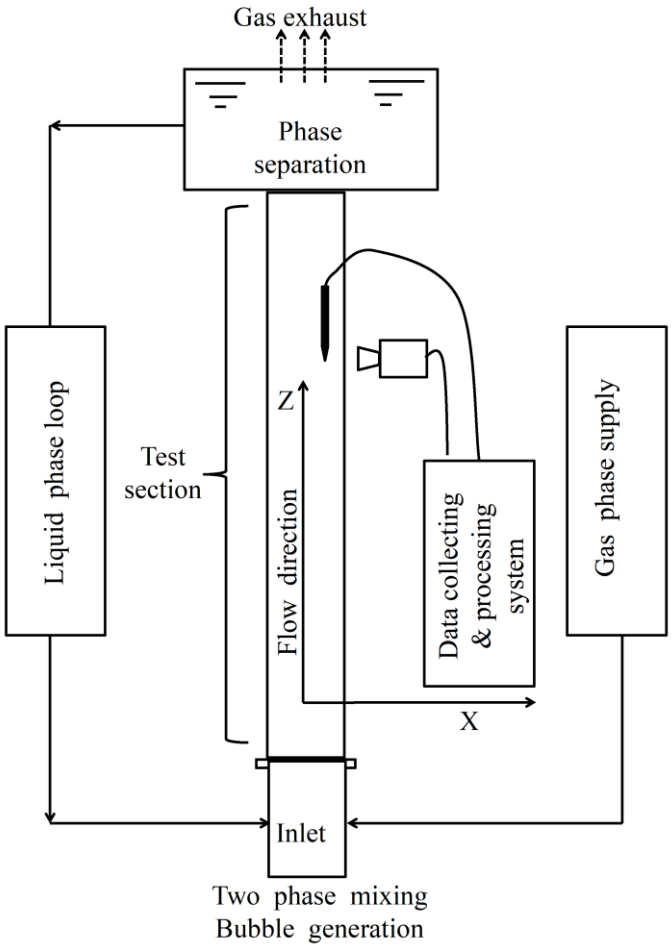

Fig. 2.2 Simplified schematic diagram of the experimental apparatus.

2.4 Experimental results

Firstly, the flow conditions of the collected databases were shown in Tables 2.2 based on the area-averaged superficial liquid velocity J_l and gas velocity J_g for different geometries. Meanwhile, the range of the flow regime is also shown.

For simplicity, only several representative sets of experimental results were shown here in Figs. 2.3–2.11 including the axial liquid phase velocities W_l, void fraction α, the turbulent intensities k or turbulent components $\langle uu \rangle$ or $\langle vv \rangle$ and the measured bubble diameter D_B. For the other sets used in the dissertation, it could be found in the corresponding references.

As shown from Figs. 2.3–2.11 and mentioned in Chapter 1, for the upward

turbulent bubbly flow in the small circular pipes, the pronounced wall peak of the void fraction could be observed for low area-averaged void fraction flow conditions. With the wall peak of void fraction, the average axial liquid velocity (W_l) and turbulence profiles are more uniform in the core region. For the turbulent bubbly in the large circular pipes, the void fraction profile tends to be flatter as compared to the turbulent bubbly flow in the small circular pipes. The wall-peak of the void fraction could only be observed for the cases with extremely low averaged void fraction. Generally, in the both the small and large circular pipes, comparing to the upward single-phase flow the steeper ∩-shape with flatter velocity profile in the core region could be observed with the wall peak of the void fraction. However, in the large square duct, not only the pronounced wall and corner peaks of the void fraction, but also the significant peaks of W_l could be observed near the corner and wall which form like the typical M-shaped velocity distribution between two parallel walls and two diagonal corners. Hence, here the apparent M-shaped W_l profile is regarded as one of typical characteristics of the upward turbulent bubbly flow in this large noncircular duct. The detailed mechanism will be considered in the Chapter 5.

2.5 Summary

In this chapter, the experimental databases used in the present dissertation were collected including the flow conditions and the representative experimental results. In the following chapters, the numerical evaluation and further analysis will be carried out based on these experimental databases. It is notable that, in this chapter, generally two sets of the experimental results were shown for simplicity. The more detailed database could be found in the corresponding references.

Table 2.2 Experimental flow conditions in different duct geometries. B: Bubbly flow; T: Transition regime.

Duct shape	Experimental database	Flow conditions		Flow regime
		$<J_l>$	$<J_g>$, χ (For Serizawa [2.1-2.2])	
Small Circular Pipe	Serizawa *et al.* [2.1-2.2]	0.74 0.88 1.03	0, 0.0119, 0.0240, 0.0358 0, 0.0099, 0.0198, 0.03 0, 0.0085, 0.0170, 0.0258, 0.0341	B
	Wang *et al.* [2.3]	0.43	0, 0.1, 0.27, 0.4	B to T
	Liu *et al.* [2.4-2.5]	0.376 0.535 0.753	0.0, 0.18 0.18 0, 0.18	B to T
	Hibiki *et al.* [2.6]	0.491 0.986	0, 0.0275, 0.0556, 0.129, 0.190 0, 0.0473, 0.0113, 0.242, 0.321	B to T
Small Triangle Duct	Bertodano *et al.* [2.7]	1.0	0.1	B
Large Circular Pipe	Shawkat *et al.* [2.8]	0.45 0.58 0.68	0.015, 0.03,0.05, 0.065, 0.085, 0.1 0.015, 0.03, 0.065, 0.085, 0.1, 0.18 0.015, 0.03, 0.065, 0.085, 0.1, 0.18	B to T
	Sun *et al.* [2.9]	1.021	0.1	B
Large square duct	Sun *et al.* [2.10]	0.50	0.0, 0.068, 0.090, 0.135	B to T
		0.75	0.0, 0.068,0.090, 0.135, 0.180	B to T
		1.00	0.0, 0.090, 0.135, 0.180, 0.225	B to T
		1.25	0.0, 0.135, 0.180, 0.225, 0.270	B to T

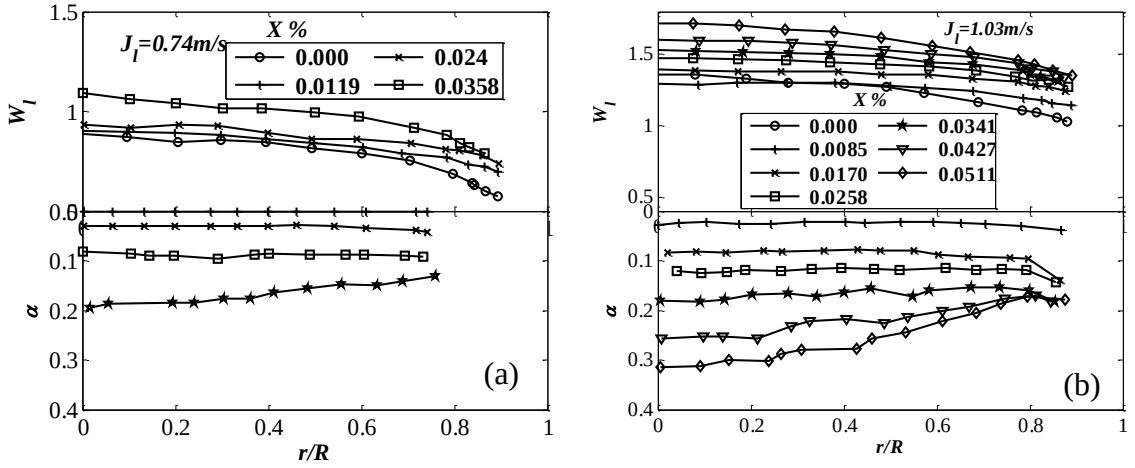

Fig. 2.3 Lateral distributions of axial liquid phase velocities W_l and void fraction α in the small circular pipe with D_H=60*mm* under (a) J_l =0.74 *m/s* and (b) J_l =1.03 *m/s* based on Serizawa's experimental database [2.1].

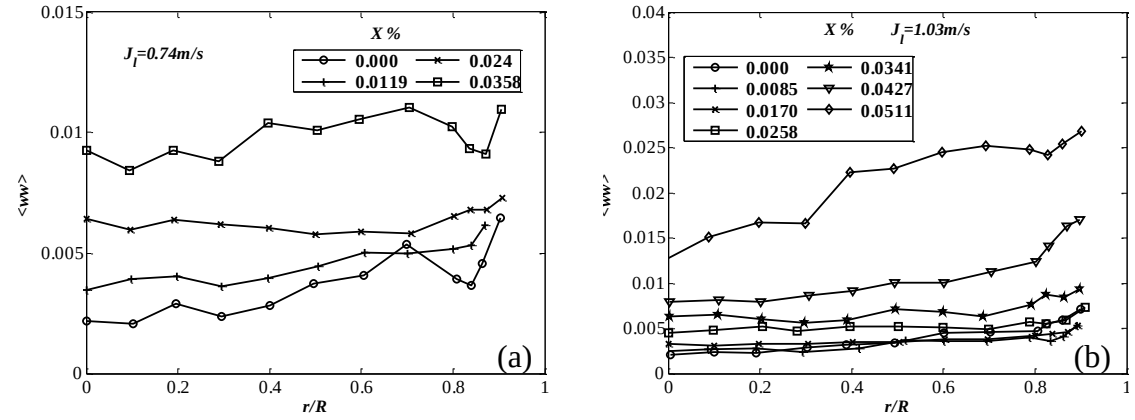

Fig. 2.4 Lateral distributions of axial turbulent intensities <*ww*> in the small circular pipe with D_H=60*mm* under (a) J_l =0.74*m/s* and (b) J_l =1.03*m/s* based on Serizawa's experimental database [2.1].

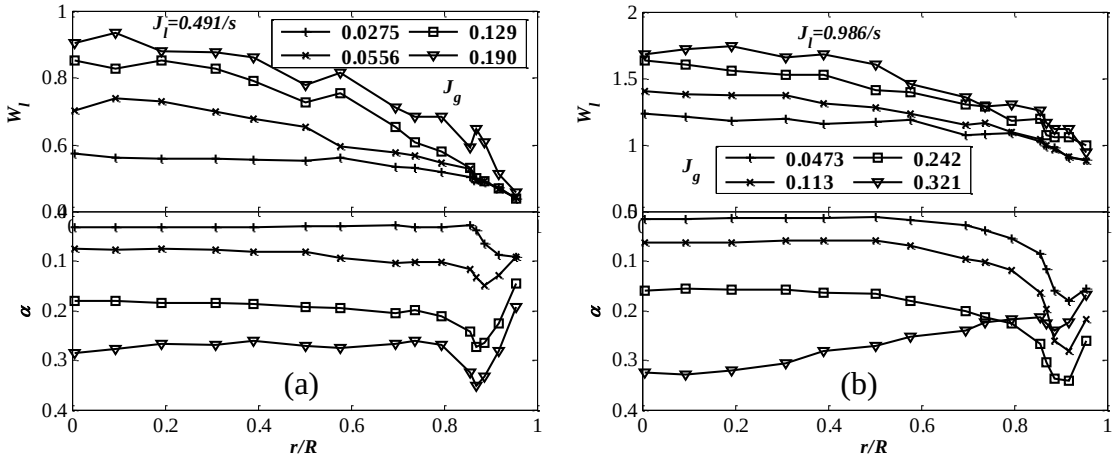

Fig. 2.5 Lateral distributions of axial liquid phase velocities W_l and void fraction α in the small circular pipe with D_H=50.8*mm* under (a) J_l =0.491*m/s* and (b) J_l =0.986*m/s* based on Hibiki's experimental database [2.6].

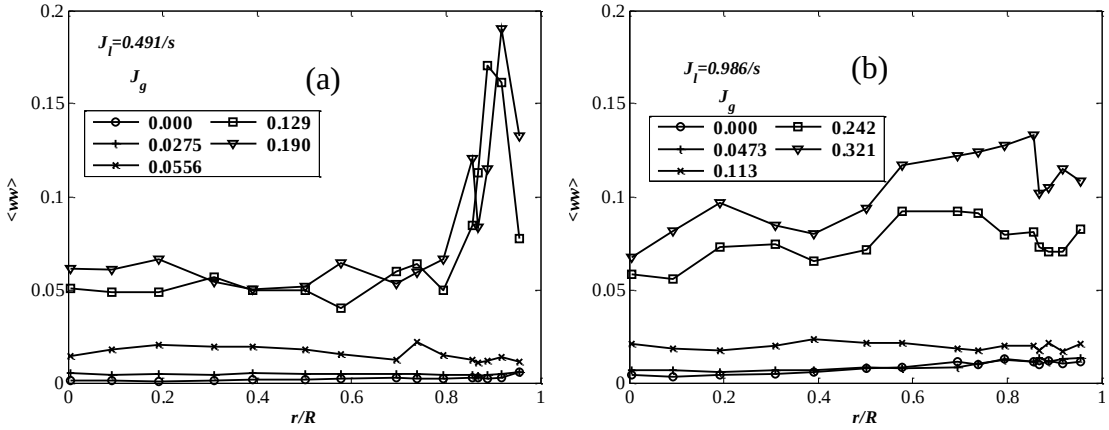

Fig. 2.6 Lateral distributions of axial turbulent intensities <*ww*> in the small circular pipe with D_H=50.8*mm* under (a) J_l =0.491*m/s* and (b) J_l =0.986*m/s* based on Hibiki's experimental database [2.6].

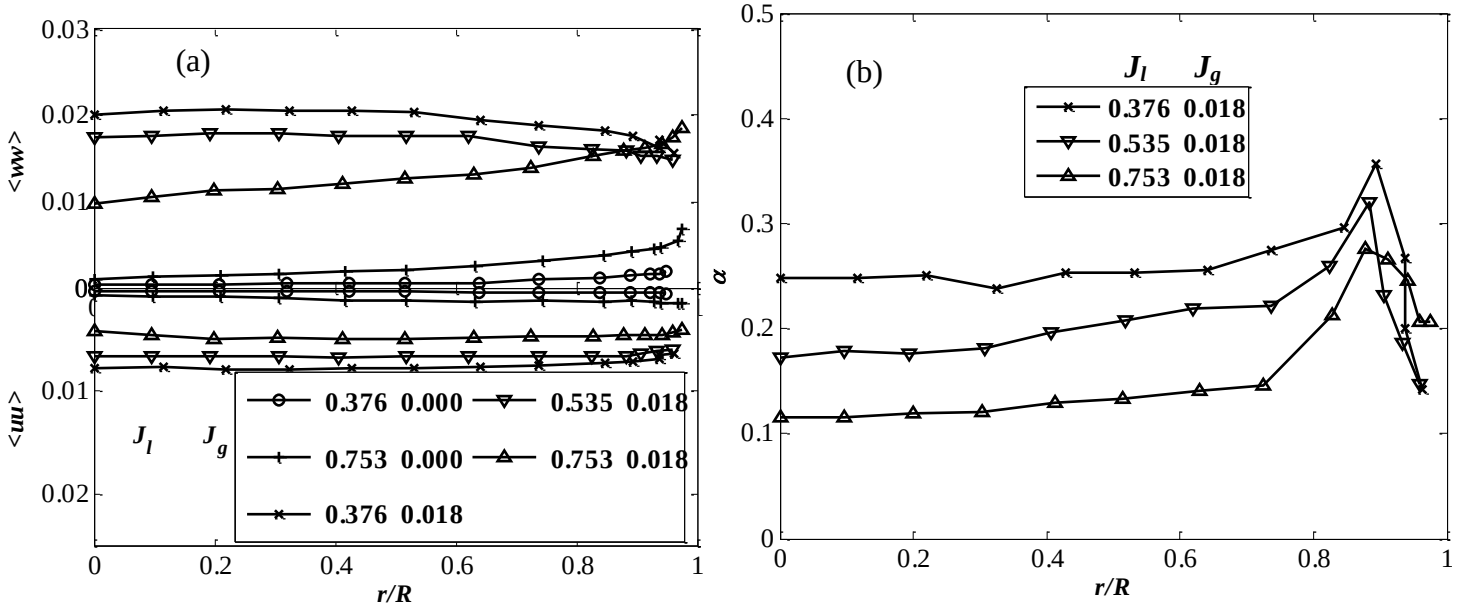

Fig. 2.7 Lateral distributions of (a) axial turbulent kinetic energy <*ww*> and lateral turbulent kinetic energy <*uu*> and (b) void fraction α in the small circular pipe with D_H=60*mm* based on Liu's experimental database [2.3-2.4].

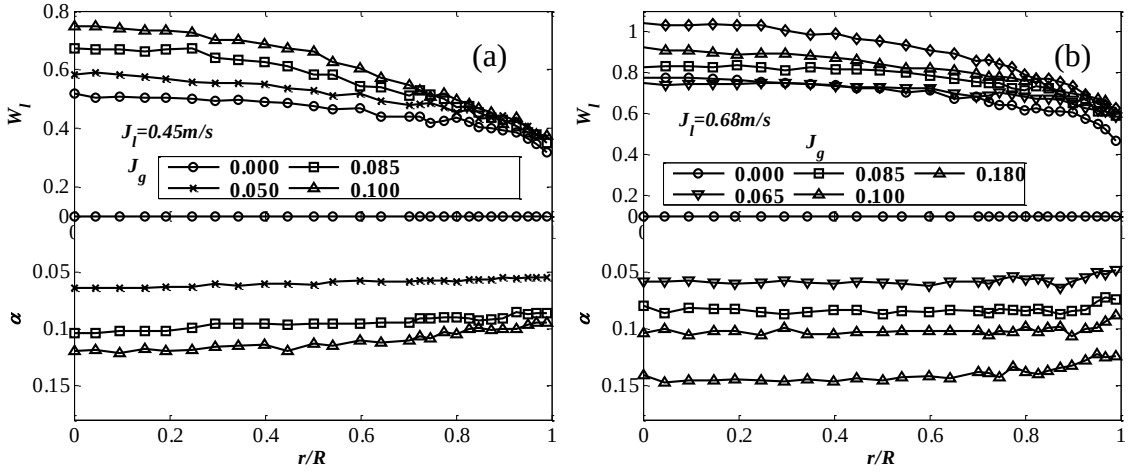

Fig. 2.8 Lateral distributions of axial liquid phase velocities W_l and void fraction α in the large circular pipe with D_H=200*mm* under (a) J_l =0.45*m/s* and (b) J_l =0.68*m/s* based on Shakwat's experimental database [2.7].

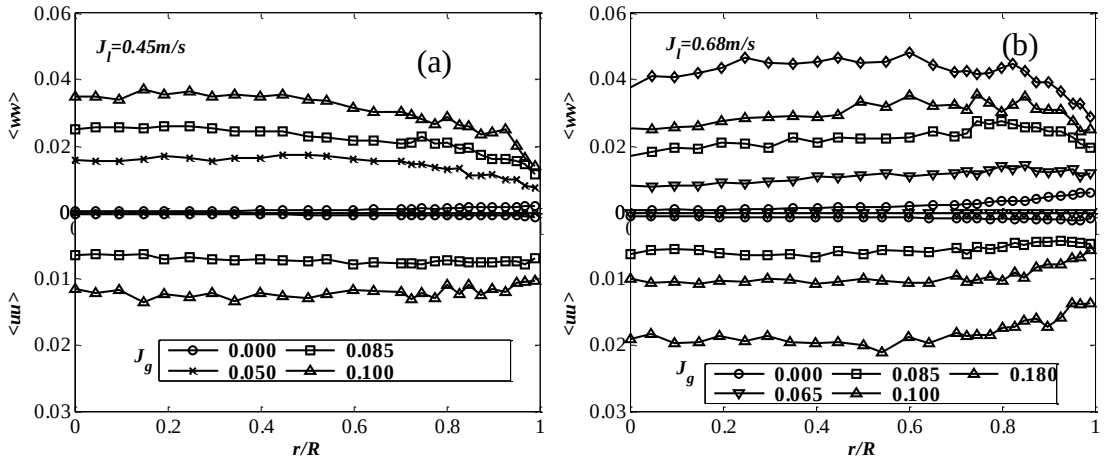

Fig. 2.9 Lateral distributions of axial turbulent kinetic energy <*ww*> and lateral turbulent kinetic energy <*uu*> in the large circular pipe with D_H=200*mm* under (a) J_l =0.45*m/s* and (b) J_l =0.68*m/s* based on Shakwat's experimental database [2.7].

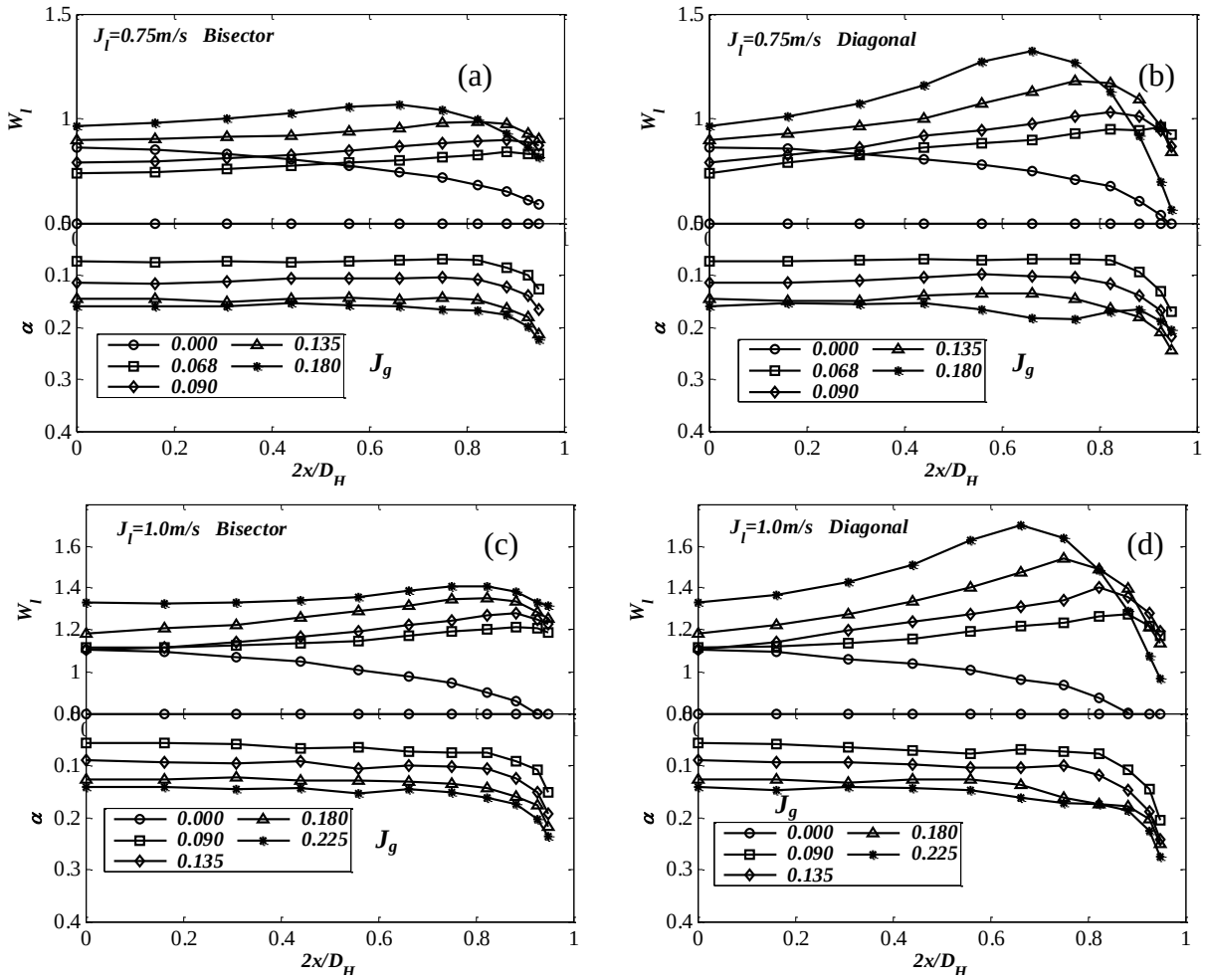

Fig. 2.10 Lateral distributions of axial liquid phase velocities W_l and void fraction α in the large circular pipe with D_H=136mm: under J_l =0.75m/s (a) along the bisector line; (b) along the diagonal line; under J_l =1.00m/s (c) along the bisector line; (b) along the diagonal line based on Sun's experimental database [2.10].

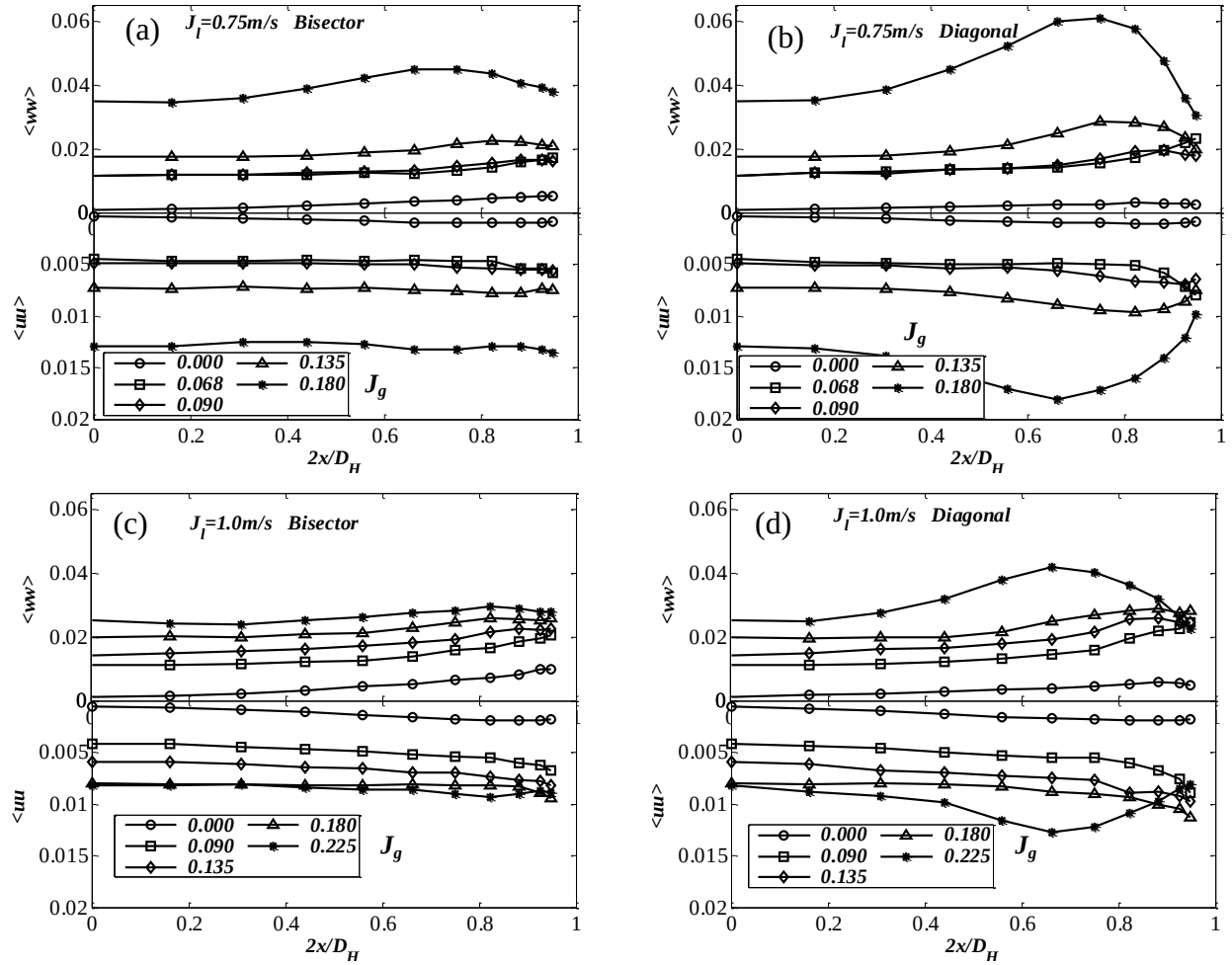

Fig. 2.11 Lateral distributions of axial turbulent kinetic energy <*ww*> and lateral turbulent kinetic energy <*uu*> in the large circular pipe with D_H=136*mm* under J_l =0.75*m/s* (a) along the bisector line; (b) along the diagonal line; under J_l =1.00*m/s* (c) along the bisector line; (d) along the diagonal line based on Sun's experimental database [2.10].

Reference

[2.1] Serizawa, A., 1974, Fluid dynamics characteristics of two-phase flow, Doctor Thesis, Kyoto University.

[2.2] Serizawa, A., Kataoka, I., Michiyoshi, I., 1975, Turbulence structure of air-water bubbly flow—II. local properties, Int. J. Multiphase Flow 2, 235–246.

[2.3] Wang, S., Lee, S., Jones, O., Lahey, Jr R. T., 1987, 3-D turbulence structure and phase distribution measurements in bubbly two-phase flows, Int. J. Multiphase Flow 13, 327–343.

[2.4] Liu, T. J., Bankoff, S. G., 1993, Structure of air-water bubbly flow in a vertical pipe—I. bubble void fraction, bubble velocity and bubble size distribution, Int. J. Heat Mass Transfer 36, 1061–1072.

[2.5] Liu, T. J., Bankoff, S. G., 1993, Structure of air-water bubbly flow in a vertical pipe—I. liquid mean velocity and turbulence measurements, Int. J. Heat Mass Transfer 36, 1049–1060.

[2.6] Hibiki, T., Ishii, M., Z. Xiao, 2001, Axial interfacial area transport of vertical bubbly flows, Int. J. Heat Mass Transfer 44, 1869-1888.

[2.7] Bertodano, de M. L., 1992, Turbulent bubbly two-phase flow in a triangular duct. Doctoral Thesis, Resselaer Polytechnic Institute.

[2.8] Shawakat, M. E., Ching, C. Y., Shoukri, M., 2008, Bubble and liquid turbulence characteristics of bubbly flow in a large diameter vertical pipe, Int. J. Multiphase Flow 34, 767-785.

[2.9] Sun, X., Smith, T. R., Kim, S., Ishii, M., Uhle, J., 2003, Interfacial structure of air-water flow in a relatively large pipe. Exp. Fluids 34, 206-219.

[2.10] Sun, H. M., 2014, Study on upward air-water two-phase flow characteristics in a vertical large square duct, Doctor Thesis, Kyoto University.

Chapter 3

Numerical evaluation of two-fluid model of turbulent bubbly flow in large square duct

3.1 Introduction

As reviewed in Chapter 1, numerical efforts on turbulence modeling of bubbly flow have been made based on an assumption of isotropic turbulence, such as k-ε model. Moreover, the numerical evaluations of the previous models were mainly carried out based on the experimental database in the small circular and noncircular ducts. However, for the single-phase turbulent flow in the noncircular ducts, the secondary flow exists in the cross-section due to the anisotropic turbulence, which has strong effects on the flow characteristics such as distorting the local mean velocity distribution. Therefore, for the turbulent bubbly flow in the noncircular ducts, the interaction between the secondary flow and the bubbles could exist. In addition, the turbulent bubbly flow in the large duct shows different flow characteristics from that in the small ducts. Thus, the models mentioned above need to be evaluated for the turbulent bubbly flow in the large and noncircular ducts. In this chapter, the numerical evaluation of the existed two-fluid model will be carried out for the turbulent bubbly flow in the large square duct based on the recently established database by Sun [3.1].

3.2 Numerical methodology

3.2.1 Problem description

The numerical evaluation here is carried out by mimicking previous simulation

of the turbulent bubbly flow in the circular pipe by changing the shape of the duct geometry as shown in Fig. 3.1. Similar to that in [3.1], the duct size is chosen to be 0.136m×0.136m×3m. The bubble size D_B is chosen according to the different experimental conditions.

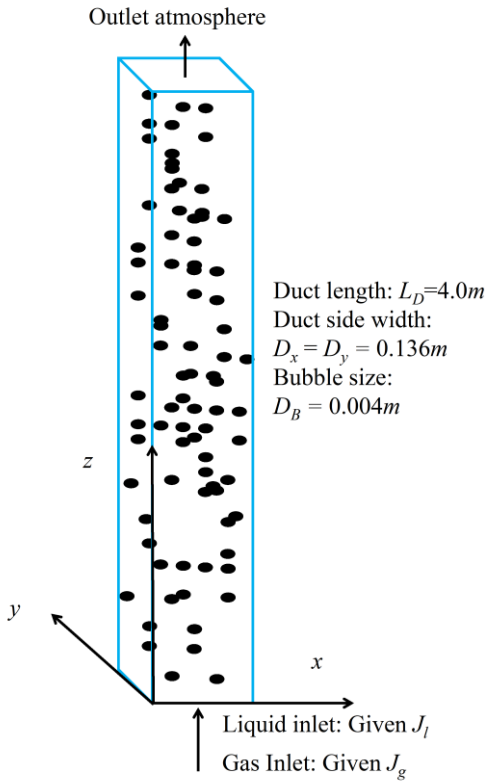

Fig. 3.1 Schematic diagram of the numerical problem.

3.2.2 Numerical methods

3.2.2.1 Governing equations

Considering the incompressible liquid and gas phase without phase change, the governing equations of the turbulent bubbly flow based on Eulerian-Eulerian two-fluid model [3.2] could be given as follows including the mass and momentum conservation.

$$\partial \alpha_g / \partial t + \nabla \cdot \left(\alpha_g \overline{\mathbf{V}}_g \right) = 0 , \tag{3.1}$$

$$\partial\alpha_l / \partial t + \nabla \cdot \left(\alpha_l \overline{\mathbf{V}}_l \right) = 0 , \tag{3.2}$$

$$\begin{aligned} \rho_g \alpha_g \partial \overline{\mathbf{V}}_g / \partial t + \rho_g \alpha_g \overline{\mathbf{V}}_g \cdot \nabla \overline{\mathbf{V}}_g = & -\alpha_g \nabla p + \nabla \cdot \alpha_g \mu_g \left(\nabla \overline{\mathbf{V}}_g + \nabla \overline{\mathbf{V}}_g^{\,T} \right), \\ & + \rho_g \alpha_g \boldsymbol{\tau}_{\mathrm{Re}g} + \rho_g \alpha_g \mathbf{g} + \mathbf{M}_{ig} \end{aligned} \tag{3.3}$$

$$\begin{aligned} \rho_l \alpha_l \partial \overline{\mathbf{V}}_l / \partial t + \rho_l \alpha_l \overline{\mathbf{V}}_l \cdot \nabla \overline{\mathbf{V}}_l = & -\alpha_l \nabla p + \nabla \cdot \alpha_l \mu_l \left(\nabla \overline{\mathbf{V}}_l + \nabla \overline{\mathbf{V}}_l^{\,T} \right), \\ & + \rho_l \alpha_l \boldsymbol{\tau}_{\mathrm{Re}l} + \rho_l \alpha_l \mathbf{g} + \mathbf{M}_{il} \end{aligned} \tag{3.4}$$

where the definitions of the variables are the same as that defined in Chapter 1. In addition, the void fraction satisfies $\alpha_l + \alpha_g = 1$; the phase interaction through the interfaces satisfies $\mathbf{M}_{il} + \mathbf{M}_{ig} = 0$; the Reynolds stress term $\rho_g \alpha_g \boldsymbol{\tau}_{\mathrm{Re}g}$ in the gas phase could be neglected due to $\rho_g << \rho_l$.

3.2.2.2 Constitutive relations

The following constitutive relations were adopted for the interfacial and turbulence terms to close the above equations:

For the interfacial term $\mathbf{M}_{il}$, the phase interaction was considered by a drag force $\mathbf{M}_D$ [3.2], a virtual mass force $\mathbf{M}_{Vm}$ [3.3], a lift force $\mathbf{M}_L$ [3.4], a turbulent dispersion force $\mathbf{M}_T$ [3.5], a wall force $\mathbf{M}_w$ [3.6], and a pressure force $\mathbf{M}_p$[3.7].

$$\mathbf{M}_{il} = -\mathbf{M}_{ig} = \mathbf{M}_D + \mathbf{M}_{VM} + \mathbf{M}_L + \mathbf{M}_T + \mathbf{M}_W + \mathbf{M}_p . \tag{3.5}$$

The following constitutive relations were adopted for each force:

$$\mathbf{M}_D = \frac{3}{4D_B} C_D \rho_l \alpha_g \left| \overline{\mathbf{V}}_g - \overline{\mathbf{V}}_l \right| \left(\overline{\mathbf{V}}_g - \overline{\mathbf{V}}_l \right), \tag{3.6}$$

$$\mathbf{M}_L = \alpha_g C_L \rho_l \left(\left(\overline{\mathbf{V}}_g - \overline{\mathbf{V}}_l \right) \times \nabla \times \overline{\mathbf{V}}_l \right), \tag{3.7}$$

$$\mathbf{M}_{VM} = \alpha_g \rho_l C_{VM} \tfrac{D}{Dt} \left(\overline{\mathbf{V}}_g - \overline{\mathbf{V}}_l \right), \tag{3.8}$$

$$\mathbf{M}_T = -C_{TD} C_D \frac{\upsilon_t}{\sigma_\alpha} \left(\frac{\nabla \alpha_g}{\alpha_g} - \frac{\nabla \alpha_l}{\alpha_l} \right), \tag{3.9}$$

$$\mathbf{M}_{\mathrm{W}} = C_W \alpha_g \rho_l \left(\left| \overline{\mathbf{V}}_g - \overline{\mathbf{V}}_l \right|^2 \right) \mathbf{n}_w , \tag{3.10}$$

$$\mathbf{M}_{\mathrm{p}} = C_p \alpha_g \rho_l \left(\left| \overline{\mathbf{V}}_g - \overline{\mathbf{V}}_l \right|^2 \right) \mathbf{n}_i , \tag{3.11}$$

where C_D, C_L , C_{VM}, C_{TD}, C_W , and C_p are the coefficients for each force and were chosen as follows:

$$C_D = \max\left[\min\left[\frac{24}{\mathrm{Re}}\left(1 + 0.15\,\mathrm{Re}^{0.687}\right), \frac{72}{\mathrm{Re}} \right], \frac{8}{3}\frac{\mathrm{Eo}}{\mathrm{Eo}+4} \right];$$

$$C_L = \begin{cases} \min\left(0.288\tanh\left(0.121\,\mathrm{Re}_m\right), f\left(\mathrm{Eo}'\right)\right) & \text{For} \quad \mathrm{Eo}' < 4 \\ f\left(\mathrm{Eo}'\right) & \text{For} \quad 4 < \mathrm{Eo}' < 10 \\ -0.29\mathrm{Eo}' & \text{For} \quad 10 < \mathrm{Eo}' \end{cases};$$

$$C_{VM} = 1/2\,, \quad C_W = \max\left(0, \frac{0.01}{D_B} + \frac{-0.05}{y_w}\right); C_{TD} = 0.1\,; C_p = 1.0$$

For the turbulence term $\boldsymbol{\tau}_{\mathrm{Re}l}$ in Eq. (3.4), the τ-ε model proposed by Lopez Bertodano *et al.* [3.7] was adopted, which considers the turbulence in the liquid phase $\boldsymbol{\tau}_{\mathrm{Re}l}$ separately including the shear-induced turbulence $\boldsymbol{\tau}_s$ and bubble induced turbulence $\boldsymbol{\tau}_B$.

$$\boldsymbol{\tau}_{\mathrm{Re}} = \boldsymbol{\tau}_S + \boldsymbol{\tau}_B \ . \tag{3.12}$$

The shear-induced turbulence $\boldsymbol{\tau}_s$ and bubble-induced turbulence $\boldsymbol{\tau}_B$ are respectively given by

$$\boldsymbol{\tau}_S = \mu_{eff,l}\left(\nabla\mathbf{V}_l + \left(\nabla\mathbf{V}_l\right)^T\right) + \frac{2}{3}\rho_l \mathbf{A}_S k_S \,, \tag{3.13}$$

$$\boldsymbol{\tau}_B = \frac{2}{3}\rho_l \mathbf{A}_B k_B \,, \tag{3.14}$$

where $\mathbf{A}_{\mathrm{S}}$ and $\mathbf{A}_B$ are the anisotropy matrices. $\mu_{eff,l}$ is the effective eddy viscosity and was chosen based on the k-ε model and Sato model [3.8] as

$$\mu_{eff,l} = \mu_{t,l} + \mu_{tb} = C_{\mu l} k_S^2 / \varepsilon + C_{\mu b}\rho_l \alpha_g D_b \left| u_g - u_l \right| \ , \tag{3.15}$$

where $C_{\mu l}$ and $C_{\mu b}$ are the model constants and chosen to 0.09 and 0.6 respectively.

To close Eq. (3.13) and (3.15), the shear-induced turbulent kinetic energy k_S was considered by the well-known k-ε model for the single-phase turbulent flow as

$$\alpha_l\left(\frac{\partial k_S}{\partial t}+\overline{\mathbf{V}}_l\cdot\nabla k_S\right)=\nabla\cdot\left(\alpha_l\upsilon_t\nabla k_S\right)+\alpha_l\left(P\text{-}\varepsilon\right), \tag{3.16}$$

$$\alpha_l\left(\frac{\partial \varepsilon}{\partial t}+\overline{\mathbf{V}}_l\cdot\nabla \varepsilon\right)=\nabla\cdot\left(\alpha_l\frac{\upsilon_t}{\sigma_\varepsilon}\nabla\varepsilon\right)+\alpha_l\left(C_{\varepsilon 1}\frac{\varepsilon P}{k_S}\text{-}C_{\varepsilon 2}\frac{\varepsilon^2}{k_S}\right), \tag{3.17}$$

where $P=\mu_{eff,l}\nabla\overline{\mathbf{V}}_l\cdot\left[\left(\nabla\overline{\mathbf{V}}_l+\left(\nabla\overline{\mathbf{V}}_l\right)^T\right)\right]$; σ_ε, $C_{\varepsilon 1}$ and $C_{\varepsilon 2}$ are model constants and are the same as that in the single-phase k-ε model with σ_ε=1.3, $C_{\varepsilon 1}$=1.44, and $C_{\varepsilon 1}$=1.92, respectively.

Considering the bubble-induced turbulent kinetic energy k_B as a scalar, the transport equations could be given as

$$\alpha_l\left(\frac{\partial k_B}{\partial t}+\overline{\mathbf{V}}_l\cdot\nabla k_B\right)=\nabla\cdot\left(\alpha_l\upsilon_t\nabla k_B\right)+\frac{\alpha_l V_T}{D_B}\left(k_{Ba}\text{-}k_B\right) \tag{3.18}$$

where V_T is the terminal velocity of a single bubble and k_{Ba} is the asymptotic value of the bubble-induced kinetic energy $k_{Ba}=\frac{1}{2}\alpha_g\widehat{C}_{VM}\left|\overline{\mathbf{V}}_g-\overline{\mathbf{V}}_l\right|^2$ and $\widehat{C}_{VM}=2$.

3.2.2.3 Boundary conditions

The boundary conditions especially at the wall are essential for the numerical simulation and given as follows: In the inlet, the uniform boundary conditions were adopted including uniform liquid and gas superficial velocities J_l and J_g and turbulence. In the outlet, the natural flow conditions were adopted by giving the outlet pressure as the atmosphere. At the wall, for the liquid phase, similar to the single-phase turbulent flow, the wall function was used for the velocity and turbulence [3.9]. For the gas phase, the void fraction at the wall was set to be $\alpha_g\big|_{Wall}=0$ indicating the bubble can't enter the wall.

3.2.2.4 Numerical procedures

In the present dissertation, the governing equations were numerically solved by finite differential method, which could be briefly summarized as follows: Firstly, the discretization of the above equations could be rearranged as

$$\mathbf{A}_{\alpha g}^{n}\alpha_{g}^{n+1}=\mathbf{G}_{\alpha g}^{n}\left(\alpha_{g}^{n}\right)\overline{\mathbf{V}}_{g}^{n+1}+\mathbf{A}_{\alpha g}^{n}\alpha_{g}^{n}, \tag{3.19}$$

$$\mathbf{A}_{\alpha l}^{n}\alpha_{l}^{n+1}=\mathbf{G}_{\alpha l}^{n}\left(\alpha_{l}^{n}\right)\overline{\mathbf{V}}_{l}^{n+1}+\mathbf{A}_{\alpha l}^{n}\alpha_{l}^{n}, \tag{3.20}$$

$$\mathbf{A}_{Vg}^{n}\left(\alpha_{g}^{n}\right)\overline{\mathbf{V}}_{g}^{n+1}=\mathbf{H}_{Vg}^{n}\left(p^{n+1}\right)+\mathbf{G}_{Vg}^{n}\left(\alpha_{g}^{n}\right)\overline{\mathbf{V}}_{g}^{n}+\mathbf{A}_{Vg}^{n}\overline{\mathbf{V}}_{g}^{n}, \tag{3.21}$$

$$\mathbf{A}_{Vl}^{n}\left(\alpha_{l}^{n}\right)\mathbf{V}_{l}^{n+1}=\mathbf{H}_{Vl}^{n}\left(p^{n+1}\right)+\mathbf{G}_{Vl}^{n}\left(\alpha_{l}^{n}\right)\overline{\mathbf{V}}_{l}^{n}+\mathbf{A}_{Vl}^{n}\overline{\mathbf{V}}_{l}^{n}, \tag{3.22}$$

$$\mathbf{A}_{ks}^{n}\left(\alpha_{l}^{n}\right)k_{S}^{n+1}=\mathbf{G}_{ks}^{n}k_{S}^{n}+\mathbf{A}_{ks}^{n}\left(\alpha_{l}^{n}\right)k_{S}^{n}, \tag{3.23}$$

$$\mathbf{A}_{\varepsilon s}^{n}\left(\alpha_{l}^{n}\right)\varepsilon_{S}^{n+1}=\mathbf{G}_{\varepsilon s}^{n}\varepsilon_{S}^{n}+\mathbf{A}_{ks}^{n}\left(\alpha_{l}^{n}\right)\varepsilon_{S}^{n}, \tag{3.24}$$

$$\mathbf{A}_{kB}^{n}\left(\alpha_{l}^{n}\right)k_{B}^{n+1}=\mathbf{G}_{kB}^{n}k_{B}^{n}+\mathbf{A}_{kB}^{n}\left(\alpha_{l}^{n}\right)k_{B}^{n}, \tag{3.25}$$

where **A**, **H** and **G** are matrices related with the discretization of the time-derivative, pressure term and the other terms including convection, diffusion, interfacial interaction, turbulence and source terms.

Then, the projection method was used to solve the pressure filed *p* and update the velocity field **V** as follows:

$$\mathbf{V}_{g}^{*}=\left(\mathbf{G}_{Vg}^{n}\left(\alpha_{g}^{n}\right)\overline{\mathbf{V}}_{g}^{n}+\mathbf{A}_{Vg}^{n}\overline{\mathbf{V}}_{g}^{n}\right)/\mathbf{A}_{Vg}^{n}\alpha, \tag{3.26}$$

$$\mathbf{V}_{l}^{*}=\left(\mathbf{G}_{Vl}^{n}\left(\alpha_{l}^{n}\right)\overline{\mathbf{V}}_{l}^{n}+\mathbf{A}_{Vl}^{n}\overline{\mathbf{V}}_{l}^{n}\right)/\mathbf{A}_{Vl}^{n}\left(\alpha_{l}^{n}\right), \tag{3.27}$$

$$\overline{\mathbf{V}}_{g}^{n+1}=\mathbf{V}_{g}^{*}+\mathbf{H}_{Vg}^{n}\left(p^{n+1}\right)/\mathbf{A}_{Vg}^{n}\left(\alpha_{g}^{n}\right), \tag{3.28}$$

$$\overline{\mathbf{V}}_{l}^{n+1}=\mathbf{V}_{l}^{*}+\mathbf{H}_{Vl}^{n}\left(p^{n+1}\right)/\mathbf{A}_{Vl}^{n}\left(\alpha_{l}^{n}\right), \tag{3.29}$$

Substituting Eqs. (3.28) and (3.29) to the summation of Eqs. (3.19) and (3.20) with the constraint of $\alpha_g+\alpha_l=1$ and rearranging, the pressure filed could be solved by

$$\mathbf{B}^n\left(p^{n+1}\right)=\mathbf{C}^n\left(\mathbf{V}_l^*\right)+\mathbf{D}^n\left(\mathbf{V}_g^*\right), \tag{3.30}$$

where **B**, **C** and **D** are matrices related with grid size.

With the new pressure field, the fields of velocities in liquid and gas phases, void fraction and turbulence could be updated. Fig. 3.2 shows the flow chart which was used to solve the governing equations.

3.3 Results and discussion

During the numerical calculation, the inlet flow rates and bubble size were set to be similar to that in the experiments [3.1]. Figs 3.4 show the comparisons of the void fraction, liquid phase velocities and turbulence between the experimental measurements and predictions under J_l =0.75*m/s* and J_g =0.09*m/s*. For simplicity, the comparisons of the other cases were not shown here since they showed the similar tendency. It is obtained that the current *k*-*ε* model could predict the corner peak phenomenon of void fraction and local liquid velocity. However, the predicted values of the peak void fraction and velocity showed much smaller as compared with experiments, especially, the turbulence fields.

The following factors are considered to be responsible for the above insufficient prediction. (1) As compared with the experiments, the existing model predicted the almost constant relative velocity W_r around 0.23*m/s*. However, in the experiments, the relative velocity W_r was related with the void fraction and shows smaller than the prediction. (2) Based on the *k*-*ε* model, the secondary flow effect was neglected, which could affect the bubbles motion and push the bubbles to the corner. In addition, unlike the circular pipe with a homogeneous boundary, the small bubbles could be trapped in the corner region because of the non-homogeneous boundary. (3) The model constants were mainly proposed and validated based on the experiments in

the small ducts. It might not be suitable in the large ducts however so far our current understandings of the physical process therein are limited. Therefore, to improve the model for the turbulent bubbly flow in the large noncircular ducts, firstly the understanding of the physical process in the large noncircular ducts is urgently in need, which is the target in the following four chapters.

3.4 Summary

In this Chapter, the numerical evaluations of the current two-fluid model of the turbulent bubbly flow were carried out in the large square duct based on the recently established database. It showed that the current model might not be suitable for the prediction of the turbulent bubbly flow in the large noncircular ducts because of the different physical processes therein as compared to that in the small circular pipes. In order to improve the model therein, the further detailed analysis of the physical process of the turbulent bubbly flow in the large noncircular ducts will be suggested such as the liquid phase velocity peak near the wall, the significant corner peak of the void fraction, and strong turbulence.

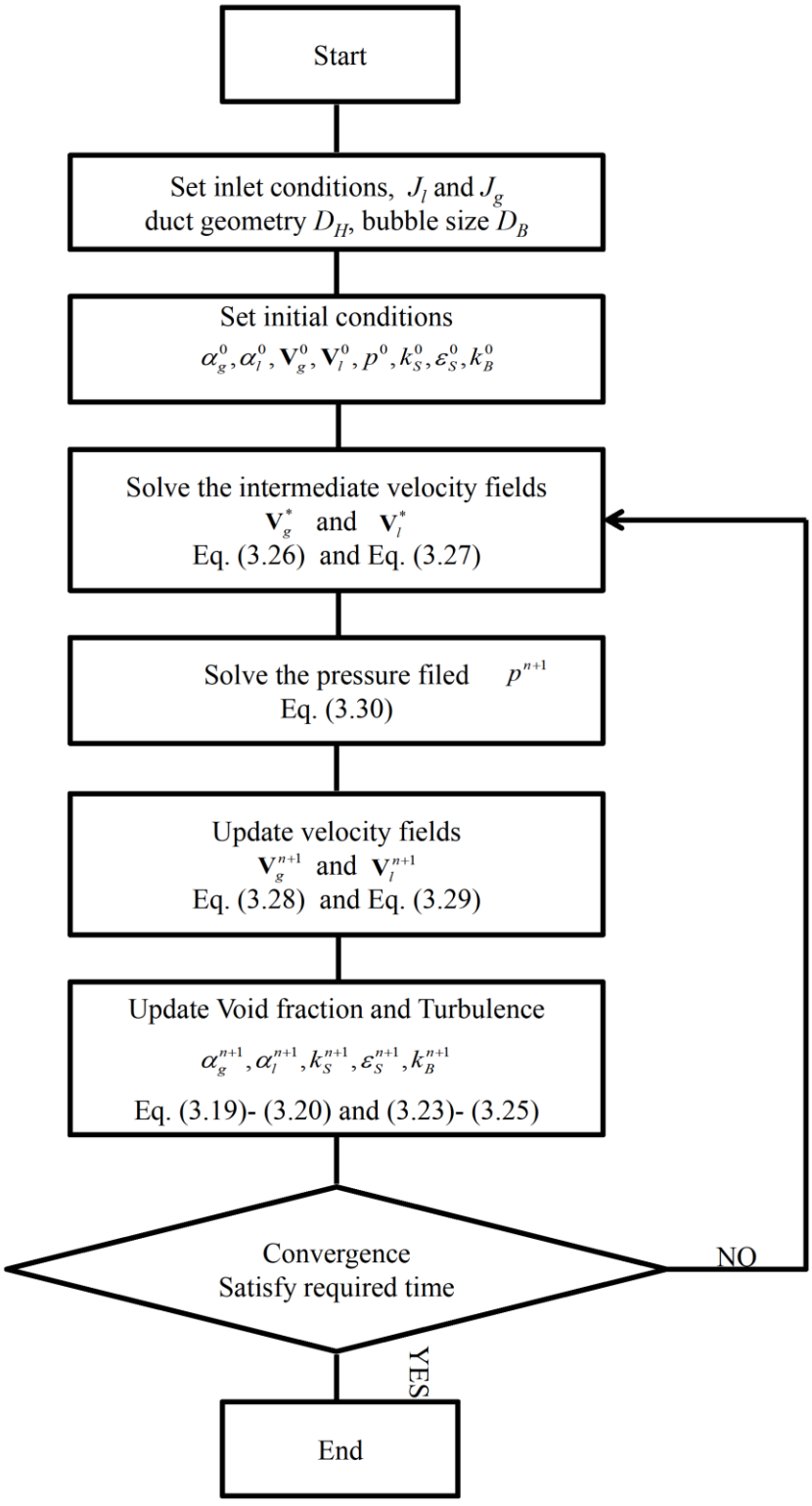

Fig. 3.2 Flow charts of numerical calculation.

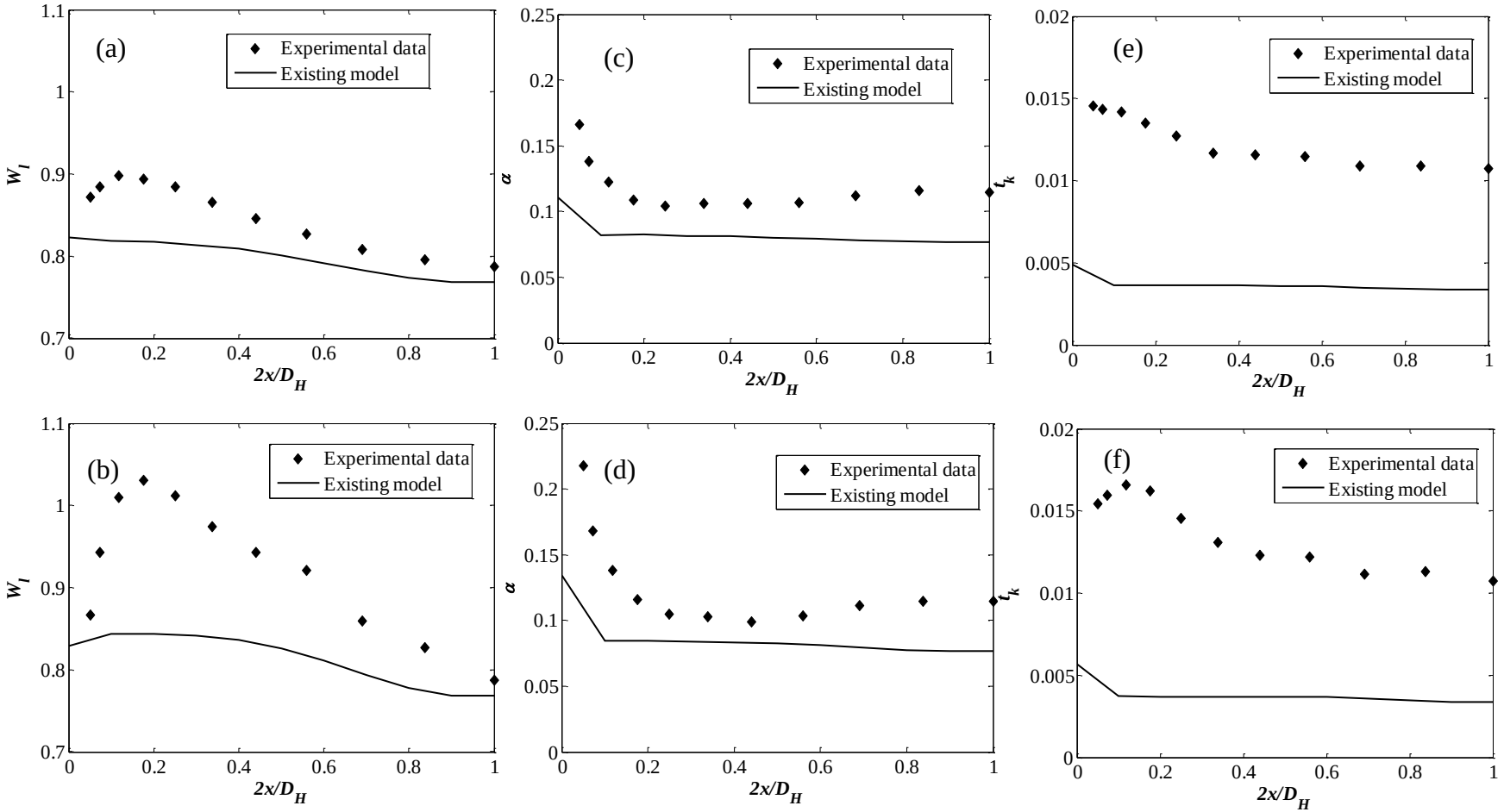

Fig. 3.3 Comparisons of the experimental measurements and numerical model under J_l =0.75*m/s* and J_g =0.09*m/s*:
for the liquid phase velocity (a) along the bisector line and (b) along diagonal line; for the void fraction (c) along the bisector line and (d) along diagonal line; for turbulence (e) along the bisector line and (f) along diagonal line.

Reference

[3.1] Sun, H. M., 2014, Study on upward air-water two-phase flow characteristics in a vertical large square duct, Doctor Thesis, Kyoto University.

[3.2] Ishii, M., Hibiki, T., 2011, Thermo-fluid dynamics of two-phase flow. 2nd ed. New York: Springer.

[3.3] Lahey Jr. R.T., 1990, The analysis of phase separation and phase distribution phenomena using two-fluid models, Nucl. Eng. Des. 122, 17-40.

[3.4] Tomiyama, A., Tamai, H., Zun, I., Hosokawa, S., 2002, Transverse migration of single bubbles in simple shear flows, Chem. Eng. Sci. 57, 1849-1858.

[3.5] Burns, D., Frank, T., Hamill, I., Shi, J. M., 2004, The Favre averaged drag model for turbulent dispersion in Eulerian multi-phase flow, Proc. 5th International Conference on Multiphase Flow, Yokohama, Japan, 392.

[3.6] Antal, S.P., Lahey, Jr R. T., Flaherty, J. E., 1991, Analysis of phase distribution in fully developed laminar bubbly two-phase flow, Int. Multiphase Flow 13, 309-326.

[3.7] Bertodano, Lopez M., Lahey, Jr. R.T., Jones, O. C., 1994, Phase distribution in bubbly two-phase flow in vertical ducts, Int. J. Multiphase Flow 20, 805-818.

[3.8] Sato, Y., Sadatomi, M., 1981, Momentum and heat transfer in two-phase bubble flow—I. Theory, Int. J. Multiphase Flow 7, 167-177.

[3.9] Pope, S. B., 2000, Turbulent flows, Cambridge University Press.

Chapter 4

Developing process of turbulent bubbly flow

4.1 Introduction

Several researches have discussed the developing of the turbulent bubbly flow but mainly focused on the general flow pattern transition from the bubbly flow to the slug flow [4.1-4.3]. Few researches were focused on the detailed developing process based on the bubble motion. Consequently, there does not exist any detailed model about the formation of the bubble layer, the velocity and the turbulence distribution during the developing process. Similar to the single-phase turbulent flow, in order to develop the developing models for the turbulent bubbly flow, the experimental databases are essentially required with the well-controlled inlet flow conditions including not only velocity distributions but also the bubble distribution. However, for the circular pipes the experimental databases could not satisfy the requirements which were either with complicated inlet flow conditions [4.4-4.5] or measured far from the inlet [4.6]. In Sun's experiments [4.7], the experimental measurements were carried out at different locations during the flow developing with well-controlled inlet flow conditions, which provides us the possibility to consider the developing process. In this chapter, the developing process in the turbulent bubbly flow will be discussed based on the database in [4.7].

4.2 Experimental observations

Firstly, based on Sun [4.7] Figs. 4.1-4.4 show the experimental results of the

liquid phase velocities and the corresponding void fractions at different locations for the different flow conditions summarized in Table 4.1. From the inlet to the measured location, generally two stages could be observed during the developing including the formation of the bubble layer near the wall and the developing the liquid phase with this bubble layer the image of which was shown in Fig. 4.5. Moreover, the developing processes for the small void and large void fraction cases in the transition region showed quite different characteristics. For the cases with large void fraction, after the formation of the bubble layer, the further rearrangement of the bubbles could be observed due to the coalescence of the bubbles occur near the wall, which made the bubble lateral migration from the wall to the center. This process dominates the second stage of the developing process and was more complicated. In this chapter, we will discuss the developing processes during these two stages especially for the small void fraction. The following topics will be focused on. In the first stage, the formation of the bubble layer will be discussed by considering how long it needs to form the developed bubble layer. In the second stage, the length required to lift up the liquid phase velocity will be discussed.

Table 4.1 Experimental conditions for the developing process.

J_l (m/s)	0.5		0.75			1.0			1.25		
J_g (m/s)	0.09	0.135	0.09	0.135	0.18	0.09	0.135	0.18	0.135	0.18	0.225

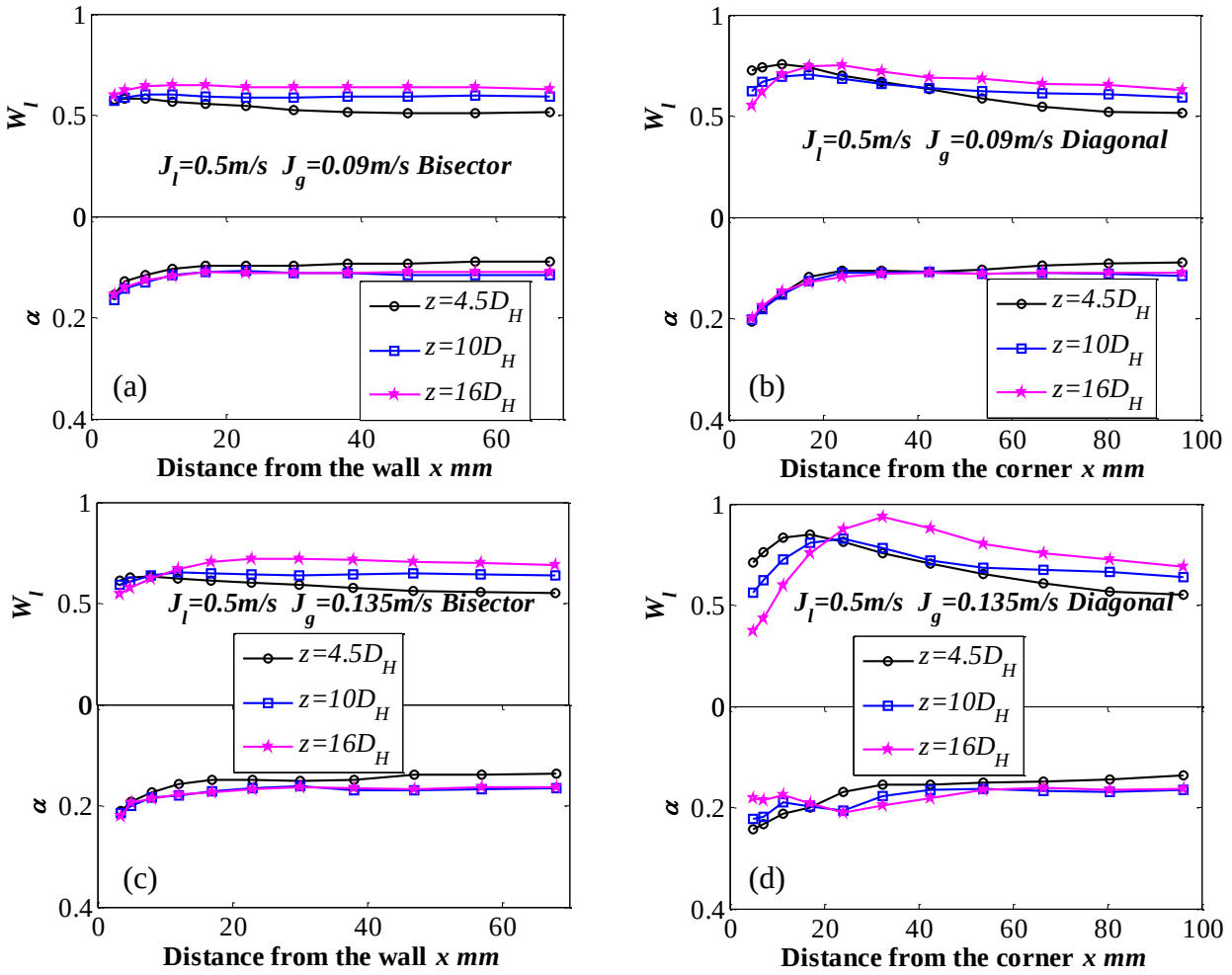

Fig. 4.1 Liquid phase velocities W_l and the corresponding void fractions α at z=4.5 D_H, 10 D_H and 16D_H for J_l=0.5*m/s*: with J_g=0.09*m/s* along (a) the bisector line; (b) the diagonal line; with J_g=0.135*m/s* along (c) the bisector line; (d) the diagonal line [4.7].

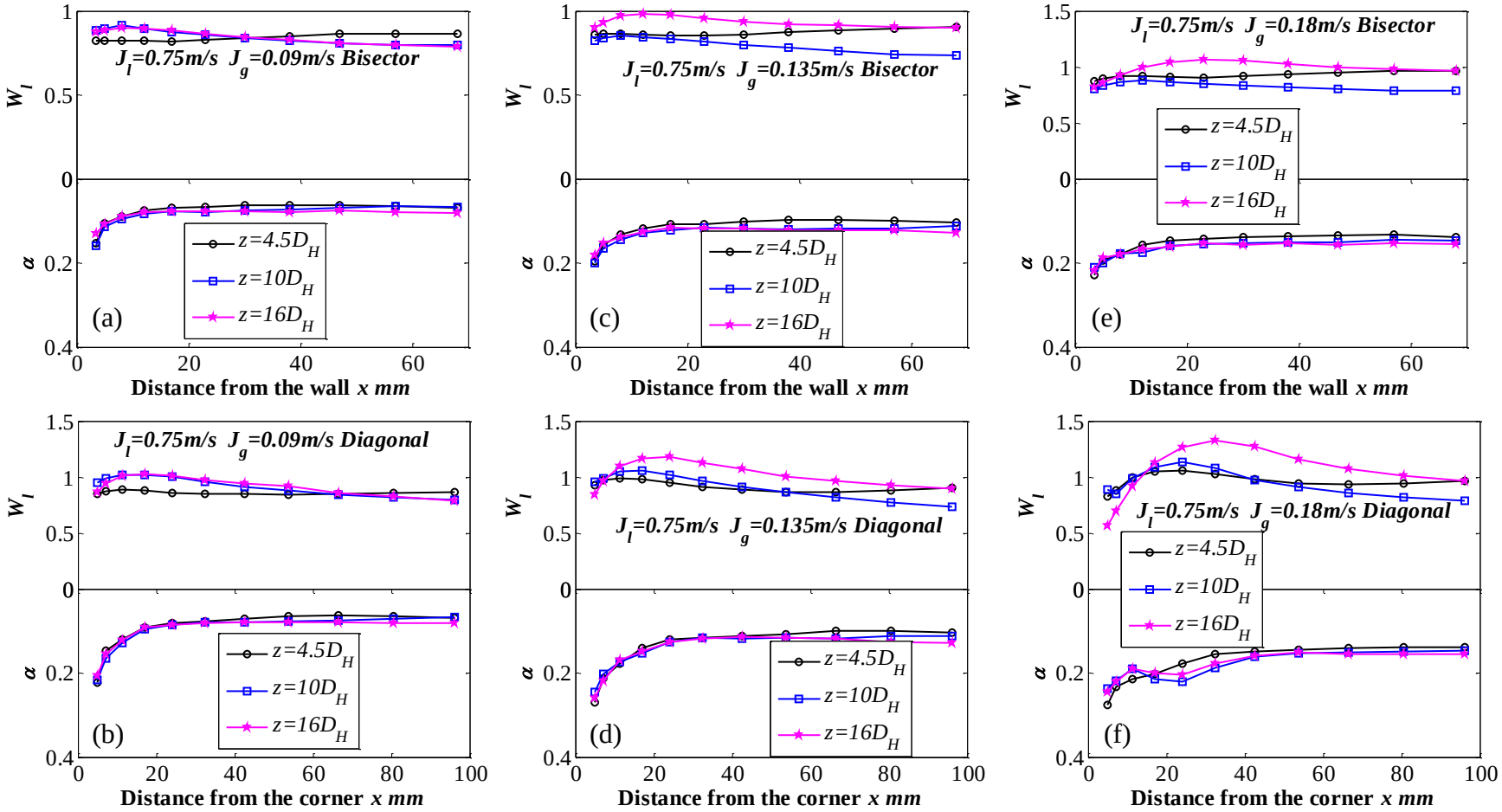

Fig. 4.2 Liquid phase velocities W_l and the corresponding void fractions α at z=4.5 D_H, 10 D_H and 16D_H for J_l=0.75m/s: with J_g=0.09m/s along (a) the bisector line; (b) the diagonal line; with J_g=0.135m/s along (c) the bisector line; (d) the diagonal line; with J_g=0.18m/s along (e) the bisector line; (f) the diagonal line [4.7].

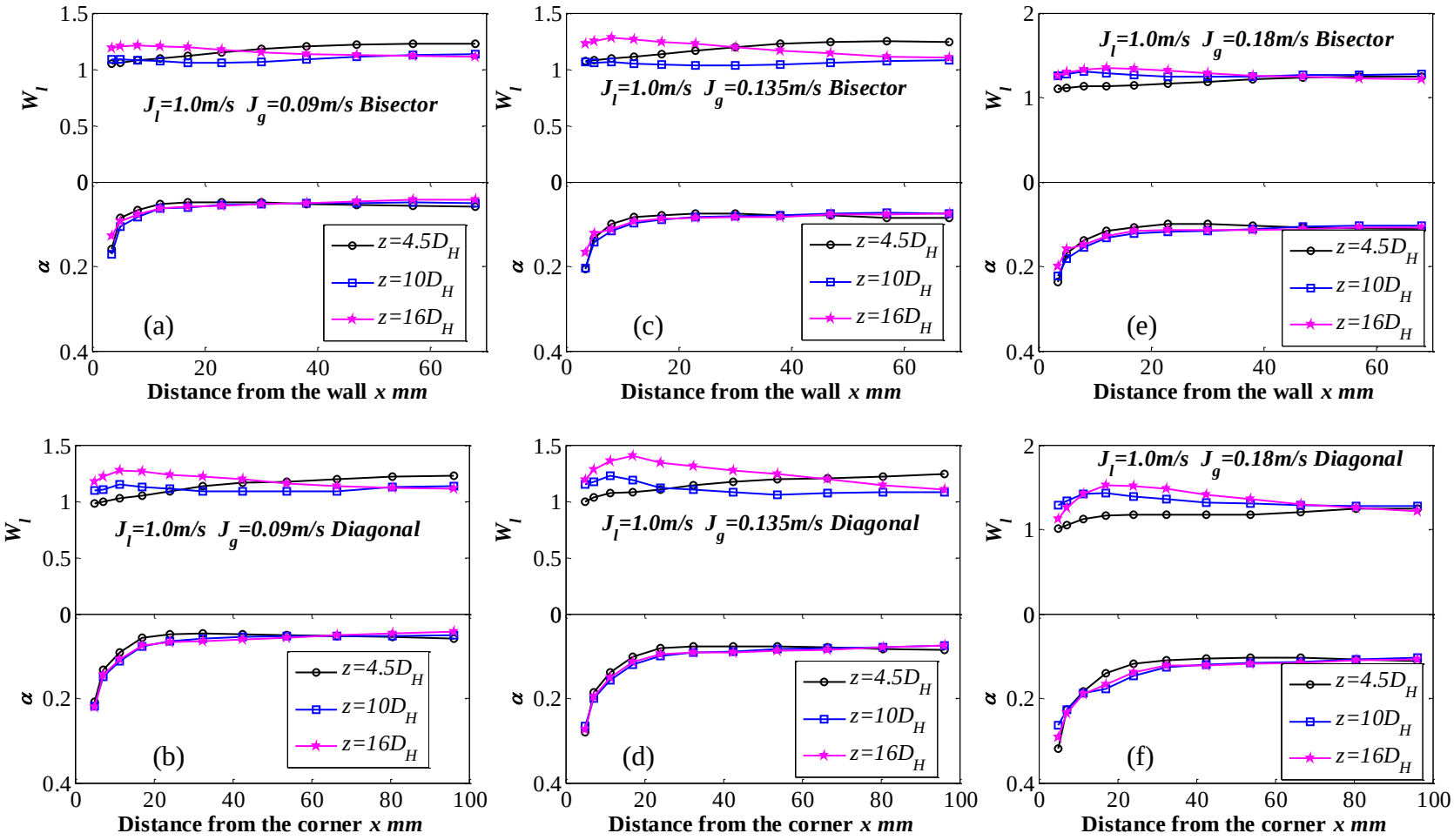

Fig. 4.3 Liquid phase velocities W_l and the corresponding void fractions α at z=4.5 D_H, 10 D_H and 16D_H for J_l=1.0 *m/s*: With J_g=0.09*m/s* along (a) the bisector line; (b) the diagonal line; with J_g=0.135*m/s* along (c) the bisector line; (d) the diagonal line; with J_g=0.18*m/s* along (e) the bisector line; (f) the diagonal line [4.7].

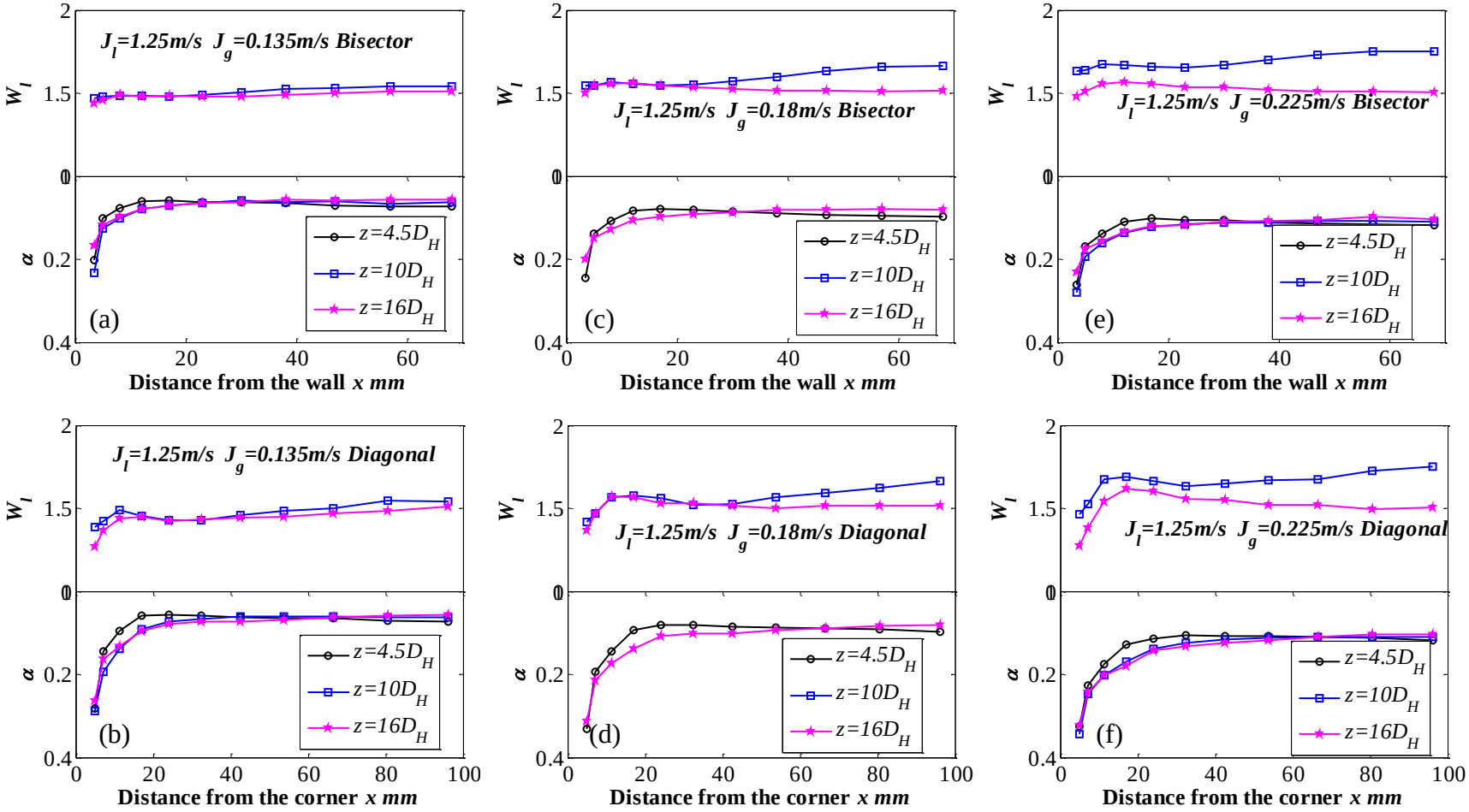

Fig. 4.4 Liquid phase velocities W_l and the corresponding void fractions α at z=4.5 D_H, 10 D_H and 16D_H for J_l=1.25*m/s*: with J_g=0.135*m/s* along (a) the bisector line; (b) the diagonal line; with J_g=0.18*m/s* along (c) the bisector line; (d) the diagonal line; with J_g=0.225*m/s* along (e) the bisector line; (f) the diagonal line [4.7].

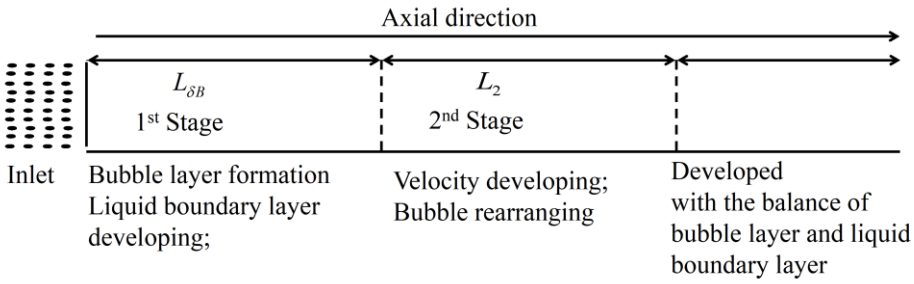

Fig. 4.5 Schematic diagram of the developing process of the upward turbulent bubbly flow in the large square duct.

4.3 Modeling of developing process

4.3.1 Formation of bubble layer in the first stage

In order to determine the length required for the formation of the bubble layer $L_{\delta B}$, the following two questions are necessary to be considered, i.e., why the lateral migration of the bubbles occurs and when the stable bubble layer could be formed. As mentioned in Chapter 1, the bubble lateral accumulation in the duct flow results from the lift force because of the liquid phase velocity gradient in the lateral direction which is dominated by the viscosity and the wall effect. Therefore, the process of the bubble layer formation could be modeled as follows. Given the bubbly flow with perfect inlet boundary conditions which are the uniform distributions of the bubbles liquid phase velocity and turbulence, two processes coupled together during the flow developing process including the developing of the liquid boundary layer and the bubble layer. Then, when the bubble layer could be formed? The lateral force balance exerted on the bubbles as shown in Fig. 4.6 dominates the bubbles lateral migration and the formation of the bubble layer. In addition to the wall lubrication force [4.8], the turbulence developing near the wall due to the shear and bubbles could induce the lateral turbulent dispersion force [4.9] toward the center. Moreover, the coalescence of the bubbles due

to accumulation of the bubbles near the wall will also occur, which increased the bubble size and decreased the lift force. When the lateral forces reached the balanced status, the bubble layer could be formed. Herein, the flow with the small void fraction without the bubble coalescence effect will be only considered. Therefore, the developing process of the bubble layer is dominated by the developing of the liquid phase boundary layer including the liquid phase velocity which generated the lateral lift force and the turbulence near the wall which generated the turbulent dispersion force balanced with the lift force. The length required to form the bubble layer $L_{\delta B}$ then depends on the developing process of the liquid phase boundary layer.

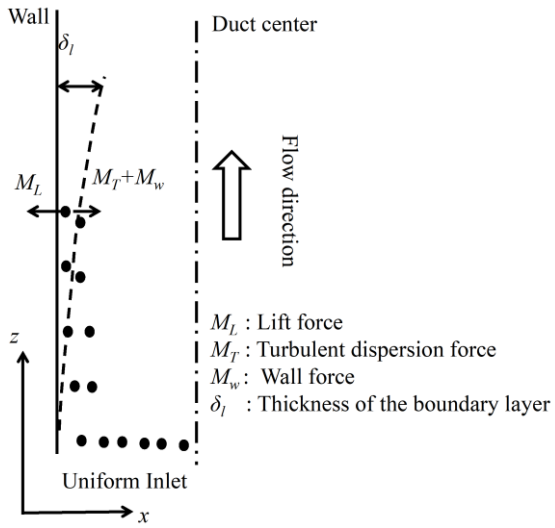

Fig. 4.6 Schematic diagram of the formation of the bubble layer due to the lift force exerted on the bubbles and the developing of the boundary layer in the liquid phase.

The following method is used to determine the developing length of the bubble layer $L_{\delta B}$. Firstly, the following assumptions are considered: (1) The uniform velocity and bubble distribution in the inlet; (2) The little bubble effect on the liquid flow developing during the lateral accumulation of the bubbles; (3) Neglecting the turbulent

dispersion force; (4) During the formation of boundary layer, only the neighbor bubble could enter this layer immediately and other bubbles will also be mixed immediately. With the above assumptions, the formation of the bubble layer with the thickness δ_B at least requires the existence of the liquid phase boundary layer with the thickness $\delta_l = \delta_B$, i.e., the length from the inlet for the bubble layer formation L_B could be reflected by the length from the inlet for liquid-phase boundary layer formation with the thickness $L_{\delta l}$.

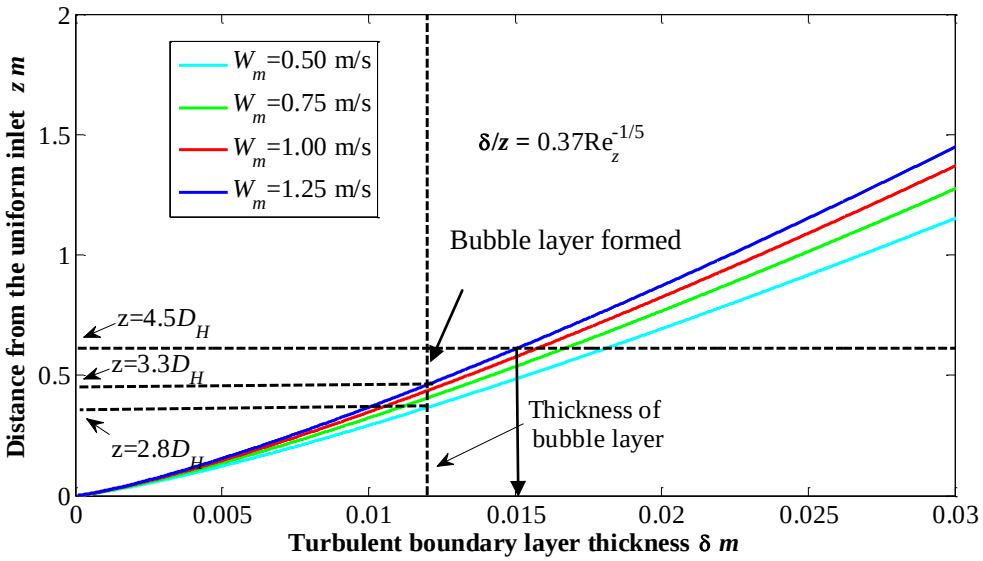

Fig. 4.7 Comparison between the thickness of the boundary layer δ_l and the bubble layer δ_B at the measurement location z=4.5D_H.

Then, the bubble effect on the flow developing and the turbulent dispersion force effect will be considered. As compared to the single-phase flow, the liquid phase velocity in the boundary layer will be lifted up by the bubble accumulation and buoyancy effect therein, which will lead to reduction of the lift force. The turbulent dispersion force exerted on the bubbles will resist the bubbles moving into the boundary layer. Therefore, the thickness of the bubble layer δ_B will be smaller than that of the boundary layer δ_l, or the developing length L_B will be shortened by these two effects,

i.e., $L_B > L_{\delta l}$. Here, the developing process of the liquid phase boundary layer will be considered based on the single-phase turbulent boundary layer theory [4.10]: $\delta_l / z = 0.371 \mathrm{Re}_z^{-1/5}$, where $\mathrm{Re}_z = Vz/\upsilon$. Fig. 4.7 shows the thickness of the boundary layer δ_l during the developing and the bubble layer δ_B at the measurement location z=4.5D_H. It could be observed that based on the above assumptions $\delta_l > \delta_B$ at the measurement location z=4.5D_H, indicating the bubble layer could be already formed before entering the measurement location.

4.3.2 Liquid phase velocity lifting in the second stage

Due to the formation of the bubble layer near the wall which made the fluid lighter than that in the core region, the liquid phase velocity near the wall will be lifted up by the bubbles. Fig. 4.8 shows the schematic diagram of liquid phase velocity lifting up in the second stages as shown in Fig. 4.5. In the part, the length required to lift up the liquid phase velocity L_p will be discussed based on the dimensional analysis as follows.

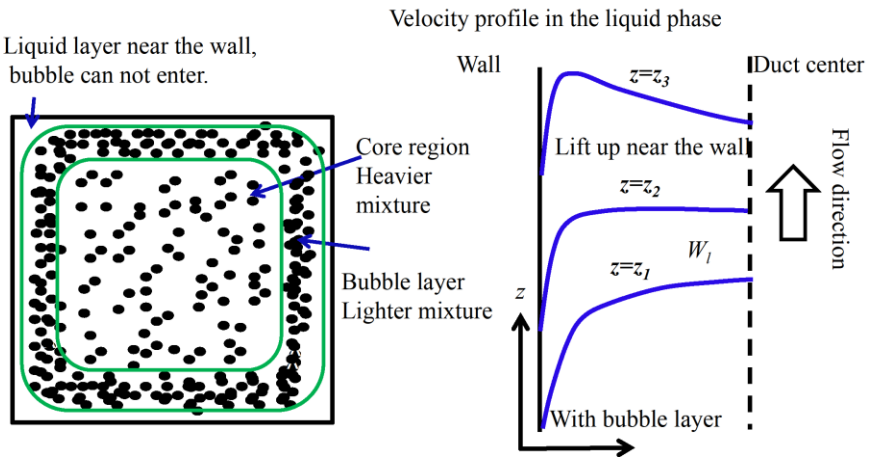

Fig. 4.8 Schematic diagram of liquid phase velocity lifting up in the second stage.

After forming the bubble layer near the wall, the liquid phase therein will be accelerated due to the buoyancy effect. Here, considering the force balance on the liquid

phase, the acceleration rate a_l could be estimated as

$$a_l \propto \alpha g /(1-\alpha). \tag{4.1}$$

For different mean liquid phase velocity W, the time t_l required to lift the velocity near the wall from $h_1 \times W$ to $h_2 \times W$ could be estimated as

$$t_l \propto (h_2 - h_1) W (1-\alpha) / (\alpha g). \tag{4.2}$$

Then the length L_p required to lift the velocity near the wall from 0 to $h \times W$ could be estimated as considering the acceleration

$$L_p \propto (h_2^2 - h_1^2) W^2 (1-\alpha) / (2\alpha g). \tag{4.3}$$

The dimensionless parameter A is defined as follows which shows the developing status of the liquid phase velocity and ratio between the measured location z_p and L_p:

$$A = 2 z_p \alpha g / \left[(h_2^2 - h_1^2) W^2 (1-\alpha) \right] \propto \frac{z_p}{L_p}, \tag{4.4}$$

Fig. 4.7 shows the ratio A based on the experimental results corresponding to the cases as shown in Table 4.1. For these cases, the measurements were carried out for three locations z_p =4.5D_H, 10D_H and 16D_H. There might exist a critical value A_C, according to which, the velocity developing status could be judged by

$$\begin{cases} A < A_C & \text{For not lifted up} \\ A < A_C & \text{For lifted up} \end{cases}. \tag{4.5}$$

According to the experimental results shown in Fig. 4.2, it could be obtained that for the cases with J_l = 0.75*m/s* and J_l = 0.09*m/s*, the liquid phase velocities near the wall shows still flat at 4.5D_H and then were lifted up at z=10D_H and stable until 16D_H. Thus, the dimensionless parameter A for this case at z=10D_H is chosen as a criterion A_C.

Correspondingly, the following conjectures for the other cases could be obtained: For the cases with J_l = 0.5*m/s*, the liquid phase velocities could be lifted up before 4.5D_H. For the cases with J_l = 1.0*m/s*, the liquid phase velocities could be lifted up around or after 10D_H. For example, it is around 10 D_H for J_g = 0.18*m/s*, 16 D_H for J_g = 0.135*m/s*, but more than 16 D_H for J_g = 0.09*m/s*. For the cases with J_l = 1.25*m/s*, except J_g = 0.225*m/s*, more than 16 D_H is required to lift up the liquid phase velocities near the wall. By comparing with Figs. 4.1 -4.4 the above conjectures could be well confirmed, which indicates the dimensionless parameter *A* could be a proper criterion to judge the flow developing status.

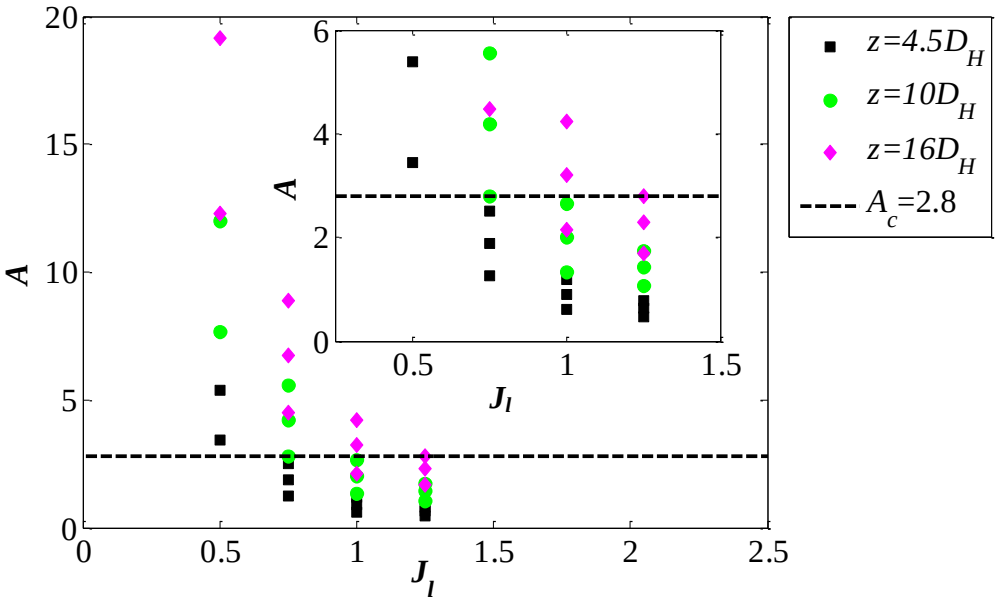

Fig. 4.9 Comparison of dimensionless parameter $A = L_p \alpha g / \left[W^2 (1-\alpha) \right]$ for different superficial liquid and gas phase velocities J_l and J_g and measurement locations.

4.4 Summary and Discussion

In Section 4.2-4.3, the developing processes of the turbulent bubbly flow were analyzed based on Sun's experimental results [4.7]. Two stages were observed during the flow developing which are forming the bubble layer and the velocity developing based on the formed bubble layer. At the first stage of the bubble layer formation, the length required to form the bubble layer was analyzed, which was found to be less than that required to develop the liquid phase boundary layer with the similar thickness. At the second stage of the velocity developing, the length required to lift up the liquid phase velocity near the wall was analyzed, based on which the criterion to judge the flow developing status was suggested.

However, so far the lack of the detailed experimental databases during the flow developing process strongly limited us to verify the above analysis and to further understand and model of this process. Many interesting questions and modeling are still unable to be considered including:

(1) For the turbulent bubbly flow the thickness of the bubble layer δ_B was observed to around $2\delta_B/D_H \approx 0.2$. And why the bubble layer was formed with thickness? During the formation of the bubble layer, how do the distributions of the phase, liquid velocity and turbulence evolve?

(2) At second stage where the velocity develops with bubble layer, how much does it need to develop the velocity such as lift up the local liquid velocity? After lifting up the liquid phase velocity near the wall, how are the bubbles and liquid phase velocity rearranged?

Therefore, in order to understand the developing process of the turbulent bubbly flow, the boundary layer flow type with careful design and detailed measurements are suggested.

Reference

[4-1] Kaichiro, M., Ishii, M., 1984, Flow regime transition criteria for upward two-phase flow in vertical tubes, Int. J. Heat Mass Transfer 27, 723–737.

[4-2] Schlegel, J.P., Sawant, P., Paranjape, S., Ozar, B., Hibiki, T., Ishii, M., 2009, Void fraction and flow regime in adiabatic upward two-phase flow in large diameter vertical pipes, Nucl. Eng. Des. 239, 2864–2874.

[4-3] Ohnuki, A., Akimoto, H., 2000, Experimental study on transition of flow pattern and phase distribution in upward air–water two-phase flow along a large vertical pipe, Int. J. Multiphase Flow. 26, 367–386.

[4-4] Serizawa, A., 1974, Fluid dynamics characteristics of two-phase flow, Doctor Thesis, Kyoto University.

[4-5] Wang, S., Lee, S., Jones, O., Lahey, Jr R. T., 1987, 3-D turbulence structure and phase distribution measurements in bubbly two-phase flows, Int. J. Multiphase Flow 13, 327–343.

[4-6] Shawakat, M. E., Ching, C. Y., Shoukri, M., 2008, Bubble and liquid turbulence characteristics of bubbly flow in a large diameter vertical pipe, Int. J. Multiphase Flow 34, 767-785.

[4-7] Sun, H. M., 2014, Study on upward air-water two-phase flow characteristics in a vertical large square duct, Doctor Thesis, Kyoto University.

[4-8] Antal, S.P., Lahey, Jr R. T., Flaherty, J. E., 1991, Analysis of phase distribution in fully developed laminar bubbly two-phase flow, Int. Multiphase Flow 13, 309-326.

[4-9] Lahey, Jr R. T., , Bertodano, de M. L., Jones, O. C., 1993, Phase distribution in complex geometry conduits, Nucl. Eng. Des. 141,177-201.

[4-10] Schlichting, H., Gersten, K., 2008, Boundary layer theory, 8th ed., Springer.

Chapter 5

Axial liquid-phase velocity of turbulent bubbly flow

5.1 Introduction

As shown in Fig. 2.9, for the turbulent bubbly flow in the large square duct [5.1], not only the pronounced wall and corner peaks of void fraction, but also the significant peaks of liquid phase velocities were observed near the corner and wall which form like the typical M-shaped velocity distribution as shown in Fig. 5.1(a) between two parallel walls, especially two diagonal corners. Generally, for the upward turbulent bubbly flow in the small and large circular pipe, the steeper ∩-shape with flatter velocity profile in the core region as compared with the upward single-phase flow was observed [5.2-5.6] even with the significant wall peak of the void fraction. Therefore, the apparent M-shaped W_l profile could be regarded as one of typical characteristics of the upward turbulent bubbly flow in this large square duct where both the scale and the non-homogeneous geometrical boundary effects are important. In this chapter, we firstly discussed the mechanisms for formation of typical M-shaped W_l profile observed in the previous upward turbulent bubbly flow experiments [5.1]. Here, three topics about the formation of this typical velocity profile will be firstly discussed including the index of flow type, the conditions for the formation of the M-shaped W_l profile and the peak location of W_l. Based on that, the duct geometry effects on the void fraction profile and wall shear stress will be considered. Then, the flow characteristics will be discussed in two layers based on the normalization of obtained axial liquid phase velocity. Finally, the numerical validation of the axial liquid phase velocity will be carried out.

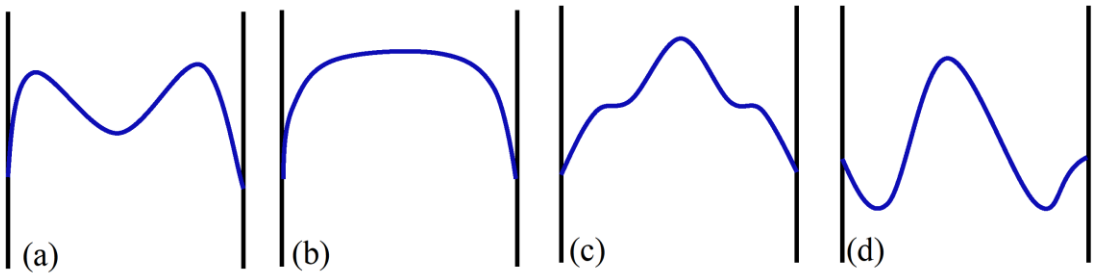

Fig. 5.1 Schematic diagram of the type of the velocity profile of the upward flow:

(a) M-shape; (b) ∩-shape; (c) Cuspid-shape; (d) W-shape

5.2 Index of flow type

In this part, the index of the flow type as shown in Fig. 5.1 will be focused on in order to consider the formation conditions of M-shaped W_l profile. Generally the formation of different velocity profile in the upward turbulent bubbly flow could be attributed to the counteraction between the wall and bubble effect which exert retarding and pushing effect on the liquid flow, respectively.

To begin with, the wall effects on upward flow driven by pressure drop were considered. Generally, the wall retards the main flow because of the nonslip condition at the wall and fluid viscosity. For the single-phase upward flow with the constant density the wall retarding effect is exerted on the whole area, so the ∩-shaped velocity profile shown in Fig. 5.2(b) could be formed. However, for the upward turbulent bubbly flow, the bubbles lateral migration due to the lift force result in the non-uniform density of the fluid $\rho_f = \alpha_l \rho_l + \alpha_g \rho_g$. Hereafter, the symbols α and ρ are the void fraction and density, and the subscripts "l" and "g" indicate the liquid and gas phase, respectively. The area with wall retarding effect could be modified by the non-uniform density distribution.

To show the coupling interaction between the wall and non-uniform density effect, the local net driving force F was evaluated. Considering the mixture of the gas and liquid phases, the averaged local net driving force F directed to the upward in the

cross section could be calculated by

$$F = -dP/dz + \alpha_l \rho_l g + \alpha_g \rho_g g \ , \tag{5.1}$$

where *dp/dz* is the mean pressure gradient of the mixture and the main driving force coming from the pump and compressor; *g* is gravity acceleration: -9.81m^2/s. The gas phase could be neglected since $\rho_g << \rho_l$. Here assuming fully-developed flow status and neglecting the flow acceleration and secondary flow, the net driving force *F* is balanced with the local net viscous force dτ_v/d*s* (τ_v: local viscous force and *s*: coordinate direction, *x* or *y*) from the neighbor fluid elements due to the molecular and turbulent eddy viscosities.

Next, we consider the indications of physical process between the wall and center by the sign of local net driving force *F*. If locally $F > 0$, it indicates the pressure gradient is able to overcome the local gravity, and the flow could be pushed upward driven by the pressure gradient. The local net viscous force from the neighbor fluid element is downward and retards the local flow as a flow resistance. But if locally $F < 0$, it indicates the pressure gradient is unable to overcome the local gravity. The fluids tend to fall downward and keep the flow upward because the local net viscous force is upward which pulls the flow as the additional driving force. In this case, the flow is driven by the viscous shear force.

For the fully-developed turbulent flow, we assume the pressure gradient *dp/dz* to be uniform among the cross sections. With the above indication, for the upward single-phase flow driven by the pressure gradient, the net driving force *F* is uniform and positive. Due to the wall, the local net viscous force always acts as the flow resistance and the ∩-shaped velocity profile is formed. However, for the upward turbulent bubbly flow, the net driving force *F* is non-uniform due to the non-uniform density among the cross sections. According to the sign of *F*, the formation of different shape velocity

profile could be implied.

In [5.1], the mean pressure gradient *dp/dz* and α_g distributions were measured simultaneously and assuming *dp/dz* to be uniform among cross sections, the lateral distributions of *F* were calculated and shown along the bisector and the diagonal lines, respectively in Figs. 5.2-5.3. Table 5.1 shows the experimental data of the mean pressure gradient *dp/dz* for different flow conditions at $z=16D_H$ based on the pressure and height difference between $z=15D_H$ and $z=19D_H$ measured by the differential pressure transmitters. Besides, the void fraction distribution at $z=10.1D_H$ was used since the flow at $z=16D_H$ was developed based on void fraction distribution before entering this part such as $z=10.1D_H$. Besides, the void fraction distribution has already reached the developed status at $z=4.5D_H$ as discussed in Section 4.2, so the choice of void fraction distribution at different locations have no effect on the following analysis.

Table 5.1 Experimental data of *dp/dz* (*kPa/m*).

J_l (*m/s*) \ J_g (*m/s*)	0.090	0.135	0.180	0.225	0.315
0.75	8.90	8.50	8.12	7.86	-
1.00	9.10	8.78	8.48	8.19	7.98

As shown in the above figures, the obvious sign changing of *F* at point x_p near the wall and corner could be observed for the turbulent bubbly flow in the large square duct. Moreover, completely different behaviors were observed for the small, intermediate and large void fraction cases. For the small void fraction case, the local net driving force *F* is positive between x_p and the wall, but negative between x_p and the duct center, indicating that the local net viscous force behaves as flow resistance between x_p

and wall but driving force between the point x_p and the duct center. Because of the wall retarding effect, for the small void fraction cases the viscous force drags the flow near the wall. After x_p, the flow is driven by the local viscous force due to the high velocity near the wall, indicating the wall retarding effect disappears or is blocked by the bubbles accumulated between the wall and x_p. It is notable that when F has a sign changing point, the cuspid-shaped velocity profile shown in Fig. 5.1(c) also implying the role of local net viscous force changes from the drag force to the driving force. However, since there is no driving force in the duct center, this flow type could not be formed. Therefore, the flow in this area is pulled upward by the flow near the wall from falling down and driven by the shear. Therefore, with this distribution of F, it implies the liquid phase velocity peak could be observed around the point x_p where the sign change of F occurs, and the M-shaped W_l profile. The following flow types were also inferred for the upward turbulent bubbly flow in the large square duct as shown in Fig. 5.4. Due to the bubbles accumulation near the wall, the lighter mixture layer was formed and pushed upward faster by the pressure gradient. In the core region, the liquid is heavier and the flow is pulled upward by the faster layer near the wall. In other words, two layers with the different flow types are formed between the wall to the duct center including the upward pressure driven flow near the wall, and the viscous shear driven flow in the core region. Wall retarding effect was confined in the lighter mixture layer or blocked from transferring into bulk region. Moreover, if x_p gets closer to the wall, the wall effect is confined in a smaller area and blocked more.

To verify the above viewpoints, the corresponding lateral distributions of liquid phase velocity were shown in Fig. 5.2(b) and Fig. 5.3(b) along the bisector line and diagonal line for the bubbly flow, respectively. It is confirmed that once the local net driving force F has an obvious sign changing near the wall, the lateral distribution of the

axial liquid-phase velocity W_l behaves as M-shaped. Besides, the location of the velocity peak is observed to be lied close to x_p according to the current experimental data. Therefore it is suitable to choose F as an index of the flow type.

For the cases with the larger void fraction, since the bubbles coalescence occurs and the bubbles were migrated to the core region, the net driving force F is negative between x_p and the wall, but positive between x_p and the duct center. It indicates the net viscous force acts as the driving force upward between the point x_p and the wall, but the flow resistance between x_p and the duct center. Similarly, two layers with different flow types as shown in Fig. 5.5 were also formed between the wall to the duct center but with the viscous shear driven flow near the wall pulled by the faster flow in the duct center. With further increasing the void fraction, more bubbles moved to the core region which led to the heavier fluid near the wall. Once the viscous shear force is not strong enough to overcome the local gravity, the W-shaped velocity profile with the downward flow near the wall as shown in Fig. 5.1(d) is possible to be observed. However, so far the current experimental technique (the X type hot-film anemometry used here) can't measure the liquid phase velocities under these flow conditions due to the limitations of the hot-film anemometry measurement due to the high void fraction. Therefore, currently it is lack of the experimental data of liquid velocities to validate the W-shaped velocity profile.

In addition, for the intermediate void fraction cases in the transition regime such as J_l=0.75*m/s* and J_g=0.18*m/s* and J_l = 1.0*m/s*, J_g = 0.27*m/s*, it is notable that along the diagonal line, double peaks of F were observed as shown in Fig.5.3 (a) and 5.3(c) due to the double void peak. For these cases, the peak locations of the liquid velocities tend to migrate to the duct center especially along the diagonal line. Along the bisector line, the peak locations of liquid velocities deviate more from x_p due to the following reasons. As

we have confirmed, for the bubbly flow in this large square duct under certain condition, peaks of void fraction and liquid phase velocity could be observed near the wall center and corner with more apparent peak near the corner. For the small void fraction cases, the locations of F=0 along the diagonal X_{p1} and bisector X_p lines are close to each other. However, for the cases in the transition regime such as J_l = 0.75m/s, J_g = 0.18m/s and at J_l = 1.0m/s, J_g = 0.225m/s, X_{p1} and X_p tends to be farther to each other, with X_{p1} closer to the duct center as shown in Fig. 5.6. And thus the location of the velocity peak along the bisector line might be affected by that along the diagonal line and gets closer to the duct center.

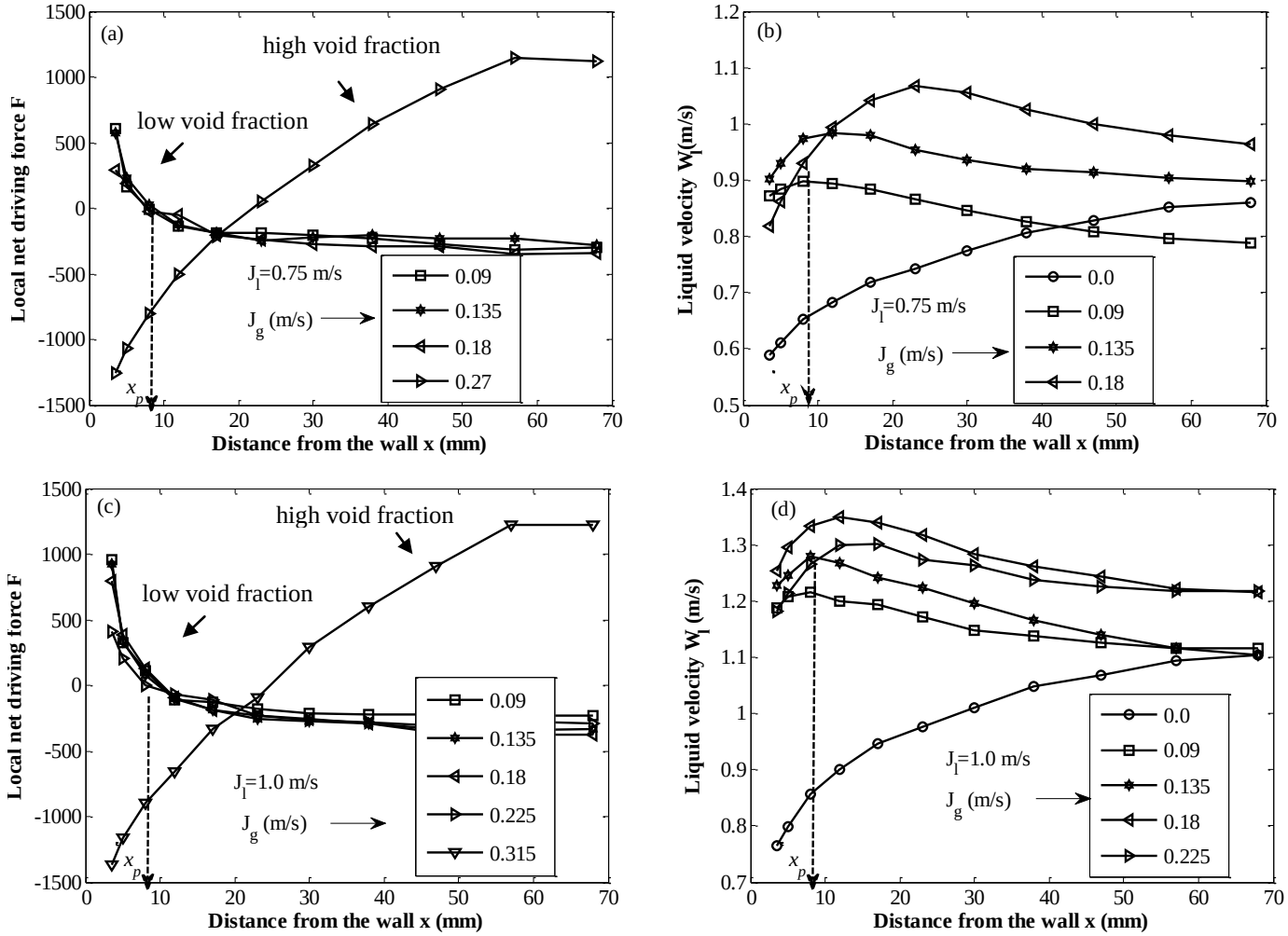

Fig. 5.2 Distributions of the local net driving force F for (a) J_l=0.75m/s and (c) J_l=1.0m/s and corresponding liquid velocities W_l for (b) J_l=0.75m/s and (d) J_l=1.0m/s along the bisector line.

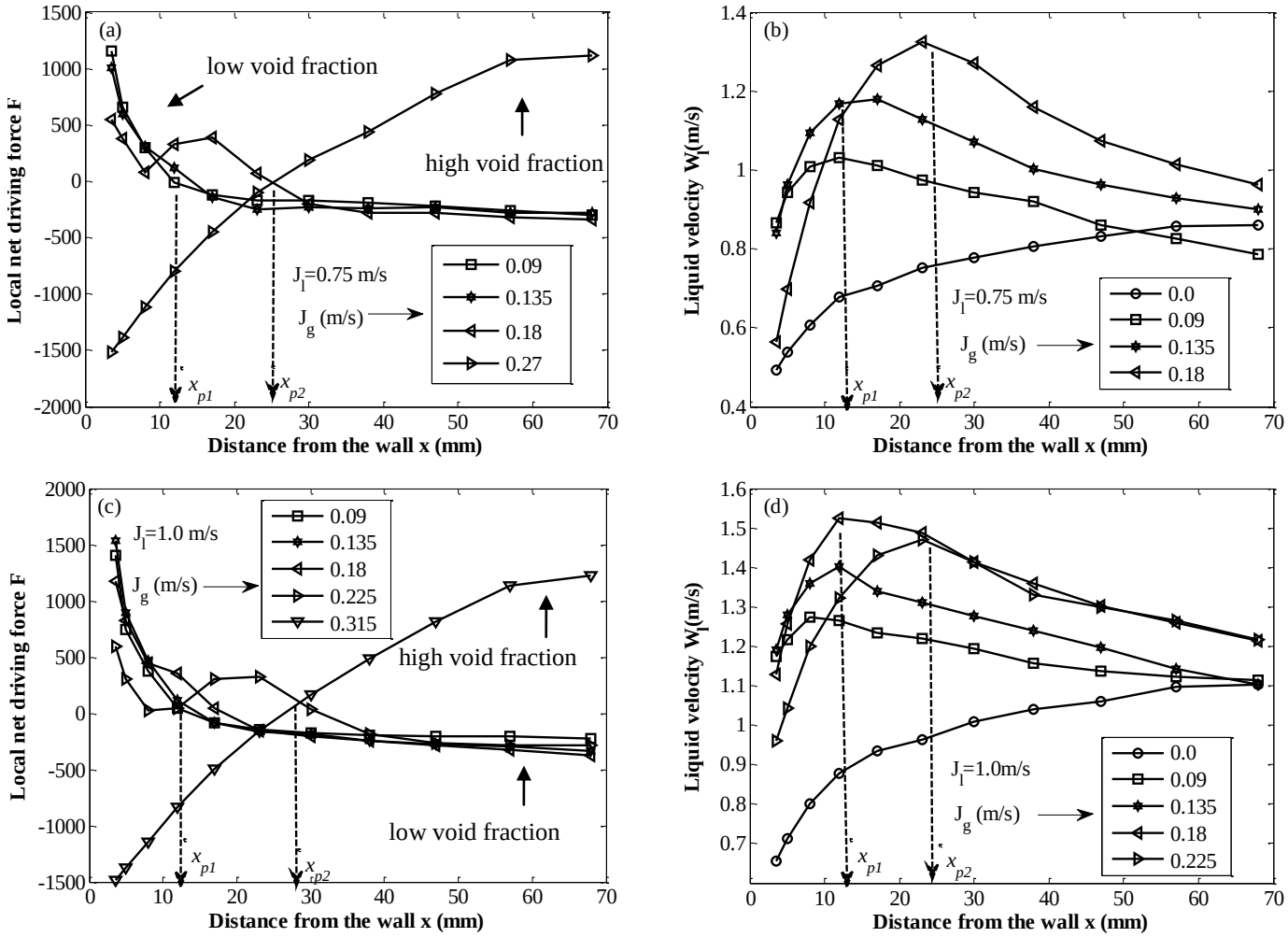

Fig. 5.3 Distributions of the local net driving force F for (a) J_l=0.75m/s and (c) J_l=1.0m/s and corresponding liquid velocities W_l for (b) J_l=0.75m/s and (d) J_l=1.0m/s along the diagonal line.

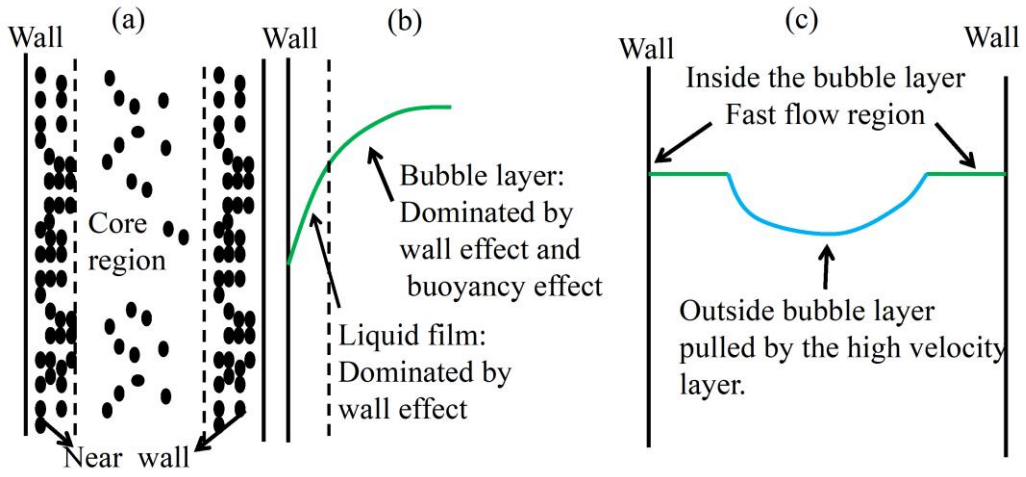

Fig. 5.4 Schematic diagram of flow image for the small void fraction: (a) Bubble lateral distribution; (b) Inside the bubble layer near wall; (c) Outside the bubble layer.

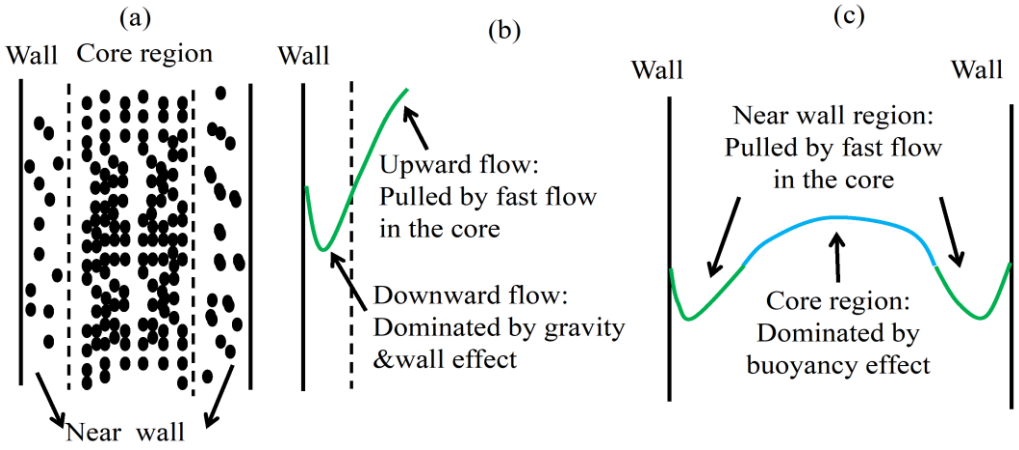

Fig. 5.5 Schematic diagram of flow image for the large void fraction: (a) Bubble lateral distribution; (b) Flow near the wall; (c) Flow in the core region.

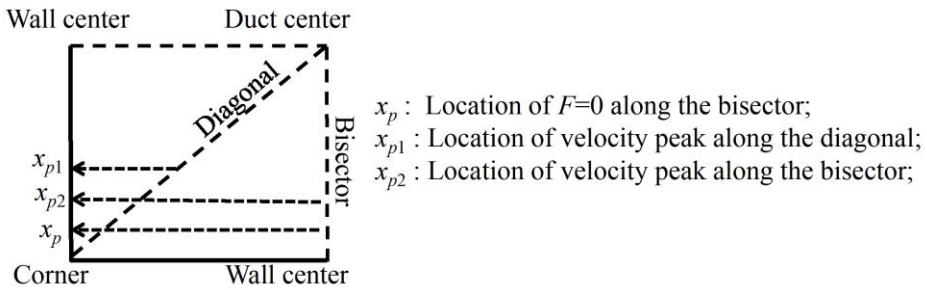

Fig. 5.6 Schematic diagram of velocity peak location.

5.3 Conditions for M-shaped W_l profile

As mentioned previously, except in the large square duct, in the existed database of upward turbulent bubbly flow, there were very few observations of such significant liquid-phase velocity peak near the wall region except that slightly peak or slightly shift of velocity peak from the pipe center which is termed as "chimney effects"[5.3]. In the small pipe, generally the steeper "∩" shape or slightly shift of velocity peak was observed even with significant wall peak of void fraction. Following the analysis in section 4.3.1, in this section the conditions required for the formation of M-shaped W_l profile will be discussed.

Firstly, based on the fully-developed flow the time averaged force balance globally, we have

$$-dP/dz = -\rho_l \alpha_{lm} g - \rho_g \alpha_{gm} g - \tau_w / H \,, \tag{5.2}$$

where α_{lm}=1-α_{gm} and α_{gm} are the mean volume fraction of the liquid and gas phases, respectively. τ_w is the wall shear stress per unit area exerted on the flow and is negative if the wall drags the flow, and is also important to determine the internal flow structures. H is the geometry dimension depending on the different geometry, and given for several geometry in Table 5.2.

Table 5.2 Geometry dimension H to determine the wall shear stress

Duct Geometry	Circular pipe D_H: pipe diameter	Channel D_H: Channel width	Square duct D_H: Duct width	Triangle D_H: Side length
H	D_H /4	D_H /2	D_H /4	D_H /12

Substituting Eq. (5.2) to Eq. (5.1), the local net driving force F could be rearranged as follows:

$$F = \left(\rho_l - \rho_G\right)\left(\alpha_{gm} - \alpha_g\right) g - \tau_w / H \,. \tag{5.3}$$

By setting Eq. (5.3) equals to zero, the sign changing point of F satisfies

$$\alpha_g^0 = \alpha_{gm} - \tau_w / \left[(\rho_l - \rho_G) g H \right] \ , \tag{5.4}$$

where $\alpha_g{}^0$ is the void fraction at the position where F changes the sign. Since $\alpha_g{}^0 > 0$, it also requires

$$\alpha_{gm} \geq \tau_w / \left[(\rho_l - \rho_G) g H \right]. \tag{5.5}$$

According to the previous analysis in Section 4.3.1, the M-shaped W_l profile is possible to be formed when

$$x \in (0, x_p), \alpha_g > \alpha_g^0 \ \text{ and } \ x \in (x_p, x_c), \alpha_g < \alpha_g^0, \tag{5.6}$$

where x_p is the distance between the location of the sign changing point of F and the wall x=0. Besides, it is easier to observe M-shaped velocity profile if x_p is closer to be zero, since the wall effect was confined in a narrower region near the wall.

Eqs. (5.5) and (5.6) indicate that under the similar wall shear stress τ_w/H, the cases with larger α_{gm} and steeper profile of the void fraction is easier to form M-shaped velocity profile. Under the similar void fraction distribution, the cases with the smaller wall shear stress τ_w/H are easier to form the M-shaped velocity profile. The final flow type is determined by the lateral void fraction distribution and the wall drag resistance. Under the same flow conditions, duct geometry plays a dominated effect on determining these two factors.

5.4 Duct geometry effect

To answer the reason why the typical M-shaped velocity profile is observed in the large square duct rather than the small circular and non-circular ducts and also the large circular pipe, the duct geometry effect on the void fraction distribution and the wall shear stress is discussed in this section by examining the ability of gathering bubbles to near the wall region and the wall shear stress under the similar liquid and gas

flow rate J_l and J_g.

For the upward turbulent bubbly flow with the wall peak of the void fraction, the ratio γ between the maximum void fraction near the wall α_{gmax} and that in duct center α_{gc} is defined as the peaking factor of the bubble gathering.

$$\gamma = \alpha_{g\max} / \alpha_{gc} . \tag{5.7}$$

The larger γ indicates stronger bubble gathering near the wall. Generally, γ is determined by the flow rate, bubble size, and duct geometry and so on. To show the geometry effect, the flow conditions with the similar flow rates and bubble size were chosen for the different experiments as shown in Table 5.3. Fig. 5.7 shows the comparison of γ for the different duct geometries including small and large circular ducts and noncircular ducts. The following results are obtained: (1) for the upward turbulent bubbly flow in the circular ducts, γ for the small pipes γ_{sc} is larger than that for the large pipes γ_{lc}, indicating stronger bubbles gathering ability in the smaller pipes; (2) γ_{ln} in the large noncircular duct is larger than that the large pipes γ_{lc} and especially near the corner, where γ_{ln} gets close to that for the small circular pipes γ_{sc}, indicating stronger bubble gathering ability as compared to that in the large circular pipe due to the corner.

The duct geometry effect on the wall shear stress for two-phase flows is examined by the well-known Lockhart-Martinelli correlation [5.9]. It shows the duct geometry effect on the wall shear stress for the upward turbulent bubbly flow could be estimated based on the single-phase flow under the same flow rate and a multiplier as follows:

$$\tau_{w,t} = \phi_L^2 \tau_{w,l} , \tag{5.8}$$

where ϕ_L^2 is the frictional multiplier for two-phase flow and $\tau_{w,l}$ is the single-phase wall shear stress resulting from the liquid phase flow rate of J_l/α_l. Next the duct geometry effect on ϕ_L^2 and $\tau_{w,l}$ will be considered respectively to show its effect on the wall shear stress for two-phase flows.

For the upward turbulent bubbly flow in the smooth pipe, according to

Chisholm-Larid correlation [5.9],

$$\phi_L^2 = \left(1 + 21/X + 1/X^2\right) \tag{5.9}$$

$$\text{and} \quad X = \sqrt{\tau_{w,l} / \tau_{w,g}}\,, \tag{5.10}$$

where $\tau_{w,g}$ is the single-phase wall shear stress resulting from the gas phase flow rate of J_g/α_g.

For the single-phase flow in the pipe, the wall shear stress $\tau_{w,l}$ is usually predicted based on the following empirical correlation:

$$\tau_{w,l} = f_l \rho_l W_l^2 / 2\,, \tag{5.11}$$

where W_l is the mean flow rate of the single-phase flow; f_l is the friction factor, and could be estimated by f_l=16/Re$_l$ and f_l=0.0791/Re$_l^{0.25}$ for laminar and turbulent flow respectively; Re$_l$ is Reynolds number, Re$_l$=$\rho_l V_l D_H/\mu_l$.

For the upward turbulent bubbly flow, substituting Eq. (5.11) into Eqs. (5.9) and (5.10) for the liquid and gas phases to calculate the multiplier, it shows the duct geometry has no effect on ϕ_L^2. Therefore, the duct geometry effect on the wall shear stress for the upward turbulent bubbly flow could be estimated based on the single-phase flow under the same flow rate where the larger duct corresponds to the smaller wall shear stress. It means that the large square duct owns not only the stronger bubble gathering ability to the wall and corner as compared with other large circular ducts but also less wall shear stress compared with other smaller ducts. According to the analysis in Section 5.2, it showed the flow with smaller wall shear stress, and steeper void fraction profile is easier to form M-shaped velocity profile. Therefore, the observation of the significant M-shaped W_l profile in the large square duct could be well understood.

Table 5.3 Experimental conditions to for different geometries in the literatures. In the table, C: circular duct; T: triangle duct; S: square duct; B: base length; H: height.

Exps. / Authors	Duct shape	D_H (*mm*)	J_l (*m/s*)	D_B (*mm*)	z (D_H)
Serizawa *et al.*[5.2]	C	60	1.03	3.5~4	20
Liu *et al.*[5.5]	C	57.2	0.75 1.083	2~4	36
Wang *et al.*[5.4]	C	57.15	0.71 0.94	×	35
Shawkat *et al.*[5.6]	C	200	0.68	3~6	42
Sun *et al.*[5.7]	C	101.6	1.021	4~5	18
Lahey *et al.*[5.8]	T	50(B) 100(H)	1.0	5	73
Sun[5.1]	S	136	0.75 1.0	3~5	16

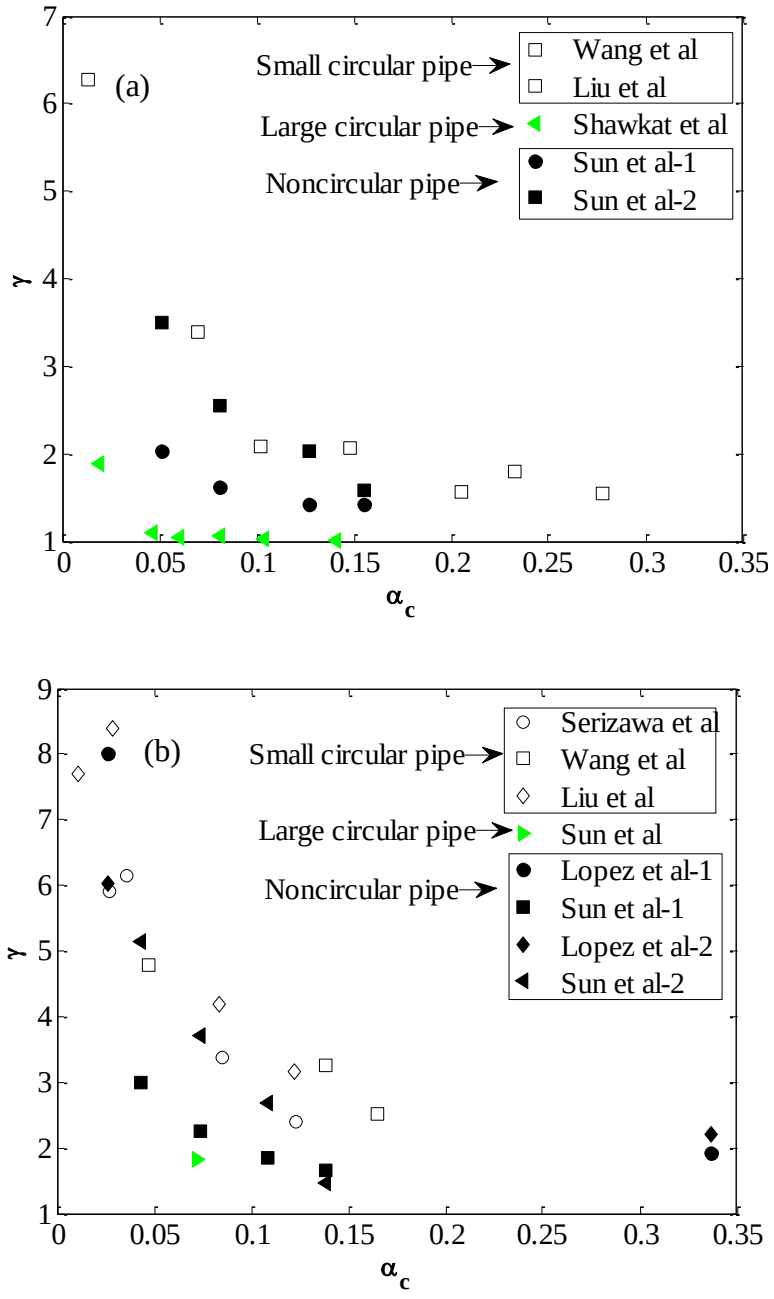

Fig. 5.7 Comparison of γ for different duct geometries for J_l around (a) 0.75*m/s* and (b) 1.0*m/s*. For noncircular geometry, "-1" and "-2" indicate data obtained near the wall center and corner, respectively.

5.5 Peak location of W_l near the wall

This section will discuss the peak location x_l of the liquid phase velocity W_l near the wall. At the peak location x_l, the viscous force τ_v is zero. To get x_l, the lateral distribution of τ_v could be calculated on the bisector line by integrating of $-F$ from the wall or the duct center to the specified location x, respectively.

$$\tau_v = \tau_w + \int_0^x (-F)dx' = \tau_{D_H/2} - \int_x^{D_H/2} (-F)dx' . \tag{5.12}$$

For the fully-developed flow, $\tau_{v,D/2} = 0$ due to the flow symmetry in the duct center. Substituting Eqs. (5.1) and (5.3) to Eq. (5.12), and after rearranging, the lateral distribution of τ_v could be obtained as

$$\begin{aligned} \tau_v &= \tau_w (1 - 2x / D_H) + \underbrace{\rho_l g \alpha_{lm} (\alpha_{lm1} / \alpha_{lm} - 1)}_{\text{the bubble blocking effect}}, \\ &= (\nabla P + \rho_l g \alpha_{lm2})(x - D_H / 2), \end{aligned} \tag{5.13}$$

where α_{lm1} is mean void fraction between location x and wall; α_{lm2} is mean void fraction between location x and center. The second term on the right hand shows the blocking effect of bubble layer near the wall on wall retarding effect from transferring into the core region. With M-shape velocity profile, for the fully developed flow, zero local viscous force τ_v is reached at the location x_l due to the zero velocity gradients. According to Eq. (5.13), at the location x_l, we have $\alpha_{lm2} = -\nabla P / (\rho_l g)$ indicating it lies between the wall and that of sign changing point of F. However, as shown from Figs. 5.2 and 5.3, the velocity peak was between the sign changing point of F and the duct center, which is not consistent with this analysis.

5.6 Flow characteristics in two layers

With the M-shaped liquid phase velocity profile, two layers with the different flow types (pressure driven and shear driven flows) could be formed. In this section, the flow characteristics in these two layers are presented based on the normalization of

liquid phase velocity.

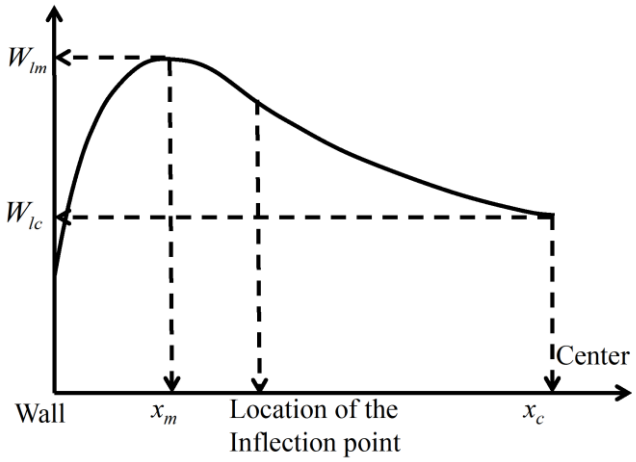

Fig. 5.8 Definition of two layers.

5.6.1 Definition of two layers

Fig. 5.8 shows the definition of two layers divided by the peak of W_l. In the inner layer where the wall strongly affects the entire region, the following dimensionless quantities are defined,

$$W_{in}^{*} = W / W_{lm}, \text{ and } X_{in}^{*} = x / x_m . \tag{5.14}$$

The maximum magnitude of the velocity W_{lm} and the distance of this point to the wall x_m were chosen as the characteristic velocity and length for the different flow conditions, respectively. As for the single-phase pipe flow driven by the constant pressure gradient, the quadratic relation W^{*}_{in} =1- $(X^{*}_{in}$ -1)^2 could be derived in between W^{*}_{in} and X^{*}_{in} for the fully-developed laminar flow regime.

In the outer layer, due to symmetry at the center of the wall where the velocity gradient is zero, there might exist an inflection point in the liquid velocity profile between x_m and x_c as shown in Fig. 5.8. In the present study this feature will be not focused due to the lack of the experimental data. In the outer layer where the wall effects were blocked by the bubble layer, the following dimensionless quantities are

defined,

$$W^*_{out} = (W - W_{lc})/(W_{lm} - W_{lc}), \text{ and } \quad X^*_{out} = (x - x_m)/(x_c - x_m). \qquad (5.15)$$

Herein the flow is driven by the local viscous shear generated by the faster inner layer. The velocity difference (W_{lm}-W_c) and the distance (x_c-x_m) between the velocity peak location and the duct center were chosen as the characteristic velocity and the length for the different flow conditions, respectively. For the single-phase pipe flow completely driven by the constant local net viscous shear dτ_v/ds (τ_v: local viscous force and s: coordinate direction, x or y), the quadratic relation W^*_{out} =(X^*_{out} -1)^2 could be derived in between W^*_{out} and X^*_{out} for the fully-developed laminar flow regime. If the flow is completely driven by the velocity difference like the Couette flow, the linear relation W^*_{out} =1-X^*_{out} could be derived for the fully-developed flow regime.

5.6.2 Velocity characteristics

By using the above normalization quantities and the measured experimental data of the bubbly flow in the square duct [5.1], the velocity characteristics in the inner and outer layers are shown along both the bisector and the diagonal lines in Fig. 5.9. Because of the limitation of the pipe length in the experiments, the experimental cases with the better developed M-shaped W_l profile was chosen. Besides since in Sun's experiments only a few points were measured in the inner layer, the cases of the upward turbulent bubbly flow in the transition region were chosen. Considering the features of the single-phase flow, it is treated all in the inner layer. In order to have an intuitive understanding, the distributions of void fraction along both the bisector and the diagonal lines could be found in Fig. 2.10 in Chapter 2.

In the inner layer, the velocity profile deviates from the quadratic function due to the turbulent effects as shown in Figs. 5.9(a) and 5.9(b). Along the bisector line, it is noted that W^* under J_l=1.25*m/s* and J_g=0.27*m/s* becomes lager than the other cases. It might be attributed to the following two reasons. Due to the high liquid superficial velocity of this case, (1) the location of the velocity peak is closer to the wall; (2) the

flow might be less developed based on the uniform inlet flow distribution. In addition, along the diagonal line near the corner it is observed that the velocity profile returns to the quadratic function with the increase of the void fraction as shown in Fig 5.9(b). Two possible reasons could be considered for this phenomenon. One is that the bubble clustering region in these cases could be considered as a boundary which confined the liquid flow between the wall and itself. It results in the smaller characteristic length as compared with the single-phase flow. Therefore, the inertial effects in this layer will be suppressed and the flow tends to be relaminarized. The other is that with the increase of the void fraction, the flow in the inner layer also gets closer to the Couette flow, which is completely driven by the velocity difference.

In the outer layer, the velocity profile is observed between the quadratic function and the linear function as shown in Figs. 5.9(c) and 5.9(d). If much more bubbles are accumulated near the wall and/or the corner as compared to the core region (steeper void fraction distribution from the wall to the duct center), the velocity profile gets closer to the Couette flow as shown in Fig. 5.9(d). It could be imagined that the asymptote of the Couette flow could be reached for completely stratified flow of the gas and liquid with the gas flow near the wall and the liquid flow in the duct center. In the real situation, with the increase of the void fraction, the coalescence of the bubbles occurs which makes the bubble migrate to the duct center region. Under the large enough void fraction, considering the mixture of the fluids, the similar tendency to the Couette flow will be formed between the duct center and near the wall region. Therefore, it further confirms that for the upward turbulent bubbly flow in this large square duct, two layers with the different flow types were easy to be formed. According to these characteristics, the two-layer model which models the turbulent bubbly flow seperatedly in different regions according to the different flow types was suggested to improve the modeling of the upward turbulent bubbly flow therein.

In addition, unlike the flows in the circular pipes with the axisymmetric flow distribution, for the single-phase turbulent flow in square duct there exists the secondary flow in cross section due to the non-axisymmetric lateral turbulent intensities [5.10].

For the turbulent bubbly flow in the square duct, the non-axisymmetric void distribution may also induce the horizontal secondary flow due to non-axisymmetric buoyancy effect. The existence of the secondary flow could have a strong effect on flow characteristics such as distorting the local mean velocity distribution. As shown in Fig. 5.9(d), it was observed that W^*_{out} in the middle region, which might be related to the convective transport of the axial liquid momentum due to the existence of secondary flow. Therefore, in order to improve the model of the turbulent bubbly flow in the non-circular ducts, the secondary flow effect should be considered. However, currently there are no experimental information about the secondary flow of turbulent bubbly flow therein, so the experimental measurements about the secondary flow is suggested to carry out in the future work.

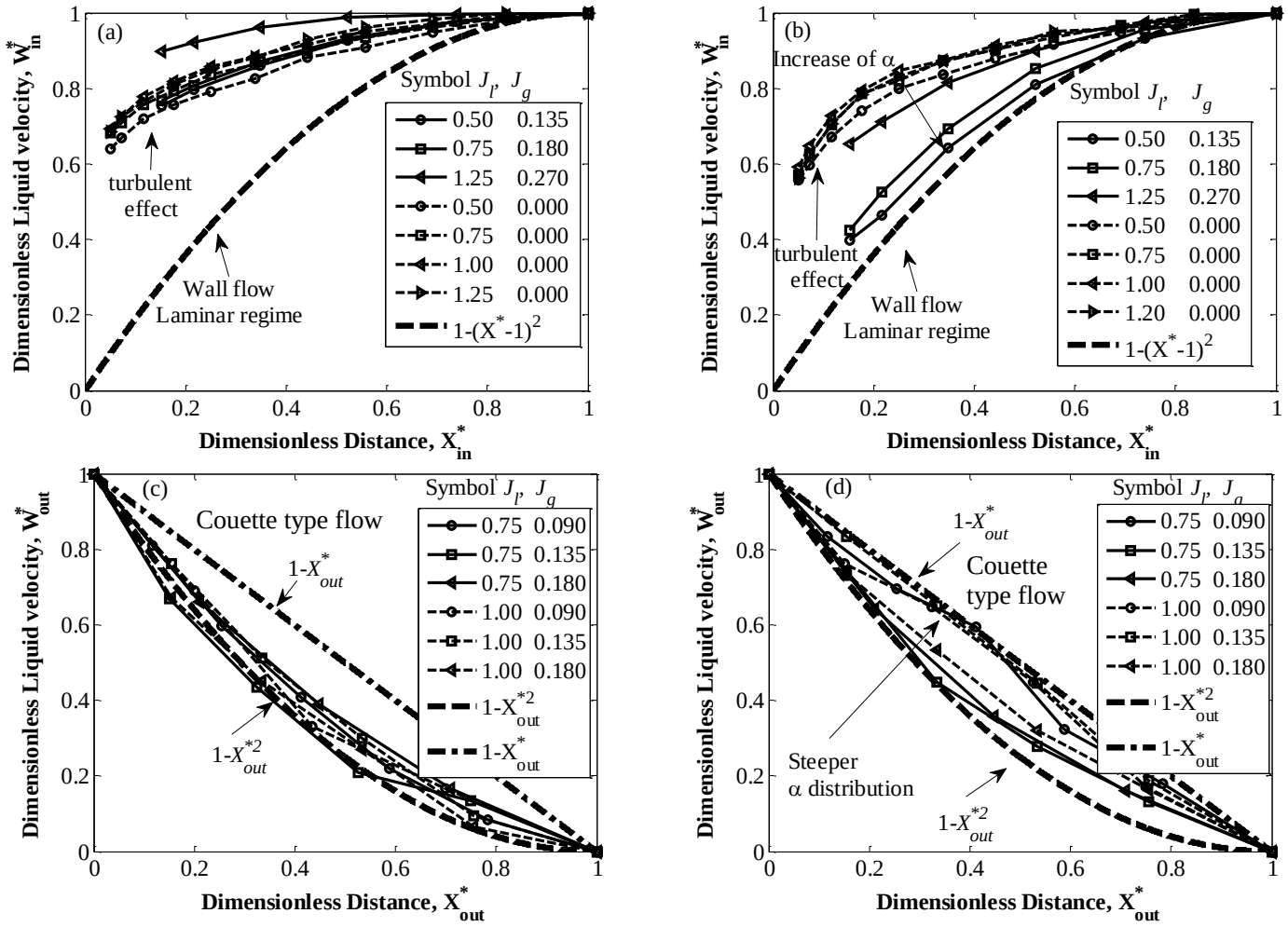

Fig. 5.9 Velocity characteristics in the inner layer along (a) the bisector line and (b) diagonal line; and in the outer layer (c) along the bisector line and (d) the diagonal line. The mean void fraction could be approximated as $\alpha_{gm}=J_g/(J_g+J_l)$.

5.7 Numerical validation of the liquid phase velocity

In this section, the numerical validation of the liquid phase velocity profile was carried out based on the experimentally measured pressure drop and the void fraction distribution [5.1].

5.7.1 Numerical models

In order to obtain the lateral distribution of the axial liquid phase velocity W_l, the force balance equation in the axial direction is solved according to the formulation proposed by Ishii and Hibiki [5.11]. For the gas phase:

$$-\alpha_g \frac{dp}{dz} + \frac{\partial\left(\alpha_g \tau_{xz,g}\right)}{\partial x} + \frac{\partial\left(\alpha_g \tau_{yz,g}\right)}{\partial y} + \alpha_g \rho_g g + F_{DZ} = 0. \qquad (5.16)$$

For the liquid phase:

$$-\left(1-\alpha_g\right)\frac{dp}{dz} + \frac{\partial\left(\left(1-\alpha_g\right)\tau_{xz,l}\right)}{\partial x} + \frac{\partial\left(1-\alpha_g\right)\left(\alpha\tau_{yz,l}\right)}{\partial y} - F_{DZ} = 0, \qquad (5.17)$$

where dp/dz is the pressure gradient for the upward turbulent bubbly flow; $\tau_{xz,l}$, and $\tau_{xz,g}$ are the shear stress induced by the molecular and eddy viscosity for liquid phase and gas phase, respectively; F_{DZ} is the drag force due to the phase interaction; ρ_l and ρ_g are the liquid and gas density, respectively; g is gravity acceleration: -9.81m^2/s. By summing Eqs. (5.16) and Eq. (5.17) and neglecting the gas phase due to $\rho_g << \rho_l$,

$$-\frac{dp}{dz} + \frac{\partial\left(\left(1-\alpha_g\right)\tau_{xz,l}\right)}{\partial x} + \frac{\partial\left(\left(1-\alpha_g\right)\tau_{yz,l}\right)}{\partial y} - \left(1-\alpha_g\right)\rho_l g = 0.. \qquad (5.18)$$

Considering the geometrical symmetry, the governing equation on the bisector lines is:

$$-\frac{dp}{dz} + \frac{d\left(\left(1-\alpha_g\right)\tau_{sz}^{L}\right)}{ds} - \left(1-\alpha_g\right)\rho_l g = 0\,, \qquad (5.19)$$

where ds=dx or ds=dy for the bisector line vertical to y or x axis, respectively.

The one-equation turbulence model is used to express the liquid phase turbulent

Reynolds shear stress as $\tau_{sz,l}=\rho_l \nu_t \, dW_l/ds$ in terms of the eddy viscosity ν_t and the liquid phase velocity gradient dW_l/ds. The turbulence eddy viscosity ν_t is expressed in the form of $\nu_t = \sqrt{k} l_t$. k, l_t and $\sqrt{k}$ are the turbulent kinetic energy, the characteristic length scale and the velocity of turbulent structures for the upward turbulent bubbly flow, respectively. Substituting the Reynolds stress $\tau_{sz,l}$ to Eq. (5.19), it is obtained that

$$-\frac{dp}{dz}+\frac{d\left(\left(1-\alpha_g\right)\rho_l \sqrt{k} l_t \frac{dW_l}{ds}\right)}{ds}-\left(1-\alpha_g\right)\rho_l g = 0 . \qquad (5.20)$$

Eq. (5.20) was solved to get the liquid phase velocity profile W_l given by the experimental measured pressure gradient, the void fraction distribution and the turbulent kinetic energy. The flow continuity is maintained by setting the mean liquid flow rate.

For the upward turbulent bubbly flow, the turbulence could be induced by both the liquid shear and the bubbles relative motion. When the bubble-induced turbulence played a dominated role, the characteristic length scale l_t could depend on the bubble diameter D_B and also the bubble-bubble interval distance $l_{B\text{-}B}$ due to the interactions between the bubble-induced eddies. Here, the mean vertical bubble-bubble interval distance $l_{B\text{-}B}$ is chosen as the flow characteristic length scale l_t during solving Eq. (5.20). As shown in Fig. 5.10, $l_{B\text{-}B}$ could be estimated based on the mean bubble diameter D_B and the void fraction α_g as follows:

$$l_{B-B} = W_B T_L / \left(N_B - 1\right) \underset{N_B >> 1}{\approx} D_B \left(1-\alpha_g\right) / \alpha_g . \qquad (5.21)$$

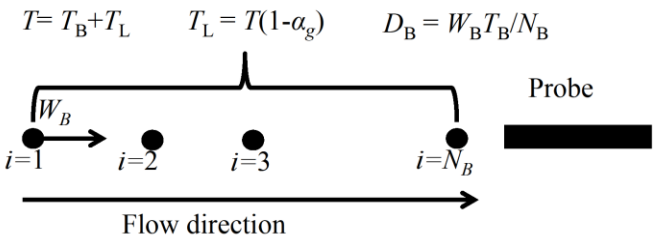

Fig. 5.10 Estimation of $l_{B\text{-}B}$ from the experiments. T, T_B and T_L are the total measuring time, bubbles passing time and liquid passing time, respetively. W_B is the mean bubble velocity.

5.7.2 Numerical results

Fig. 5.11 shows the comparison between the predicted axial liquid phase velocity W_l and the experimental measurement on the bisector line. It is observed that: (1) with the characteristic length scale of $l_{B\text{-}B}$, the liquid phase velocity profile W_l could be predicted very close to the experimental measurement especially in core region, indicating $l_{B\text{-}B}$ could be another suitable parameter to model the bubble-induced turbulence for the upward turbulent bubbly flow. However, it still needs further validations based on more experimental database. (2) As compared to the experimental data, the predicted velocity profile W_l shows the flow all in the outer layer where the flow was driven by shear. The lateral distribution of the mean viscous force τ_v calculated from the experiments confirms this point as shown in Fig. 5.12, since it is all negative.

The two assumptions are attributed for the disagreement with the experimental measurements, that is, neglecting the flow acceleration and the uniform pressure gradient distribution among the cross sections. However, in the experiments though the void fraction distribution firstly reached the developed status at $z = 4.5D_H$, the liquid-phase velocity distribution was not confirmed whether it reached the fully-developed status or still on the developing way at $z = 16D_H$ [5.1] since no lateral downstream measurements were carried out. If the velocity was still on the developing way, local flow acceleration term should be considered under the uniform pressure gradient distribution. Therefore, to improve the upward turbulent bubbly flow modeling in the noncircular ducts, it is necessary to establish the experimental database with better developed-flow status to validate current models. Moreover the experiments with the detailed flow developing process are also necessary to model the flow acceleration.

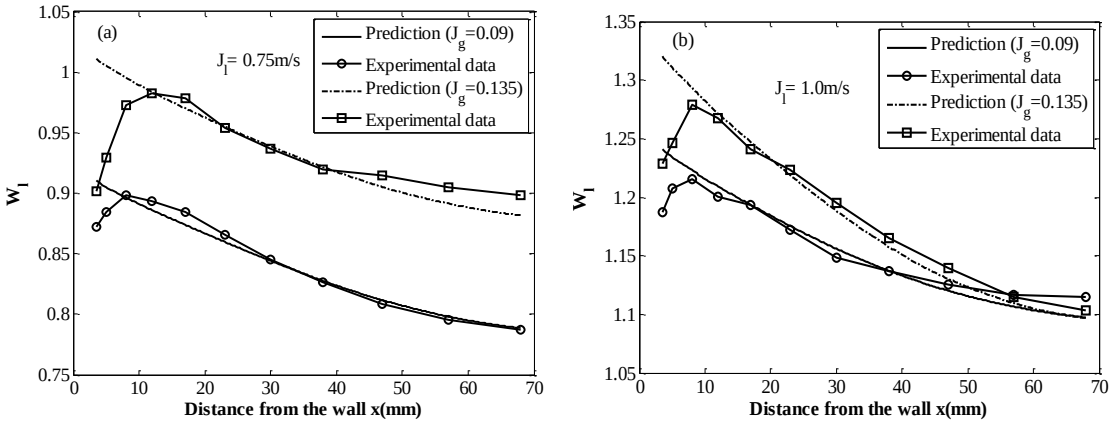

Fig. 5.11 Comparison between numerical predicted liquid phase velocity W_l and experimental measurement on the bisector line for (a) J_l =0.75*m/s* and (b) J_l =1.0*m/s*, respectively.

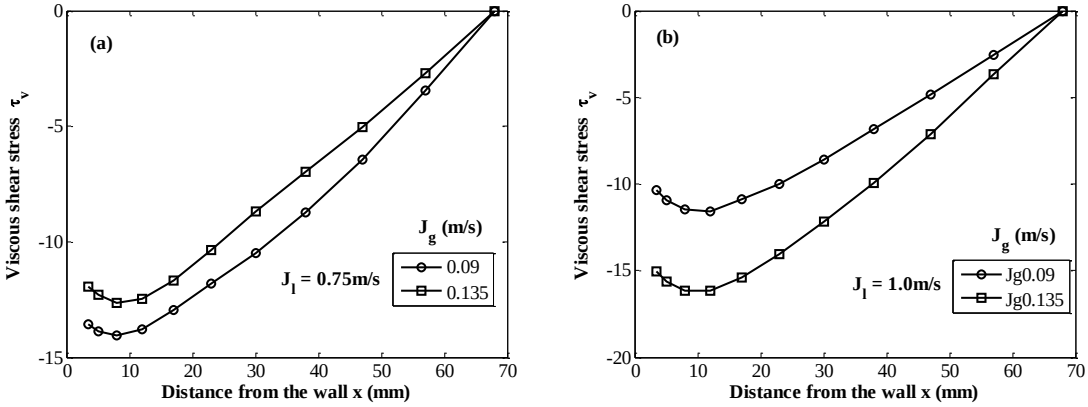

Fig. 5.12 Lateral distribution of mean viscous force τ_v based on the experimental measurements for (a) J_l =0.75*m/s* and (b) J_l =1.0*m/s*, respectively.

5.8 Summary and discussion

In this section, the formation of the typical M-shaped velocity profile of the upward turbulent bubbly flow in the large square duct was studied by considering the index of flow type, the formation conditions and the peak locations of the velocity profile. The following findings were obtained therein.

(1) Neglecting the fluid acceleration and secondary flow, the local net driving force F could be chosen as an index to show the flow type. Based on the sign of F the formation of the M-shaped or W-shaped velocity profile could be implied for the turbulent bubbly flow with the small and large void fractions respectively, which has been verified for the small void fraction cases.

(2) According to the sign of F, it was found that for the turbulent bubbly flow in the large square duct two layers with the different flow types could be formed between the wall and the duct center. For the small void fraction cases, two layers are the upward pressure driven flow near the wall, and the viscous shear driven flow in the core region. For the large void fraction cases, two layers are the upward pressure driven flow in the core region, and the viscous shear driven flow near the wall.

(3) According to the analysis on the conditions for the formation of the M-shaped velocity profile, the final flow type was determined by the lateral void fraction distribution and the wall drag resistance, where the duct geometry plays a dominated role on determining these two factors.

(4) The phenomenon of the M-shaped velocity profile in the large square duct could be attributed to the geometry effect (a large square duct) which owns not only stronger bubble gathering ability to the wall but also the smaller wall shear stress.

(5) As for the peak location of the velocity, based on the current knowledge it lies between the wall and that of sign changing point of F. However, the experimental measurements of the velocity profile showed an inconsistent

result.

(6) According to the flow characteristics, the two-layer model for the upward turbulent bubbly flow in the large square duct was suggested. The current numerical validation indicates that the bubble-bubble distance could be another important parameter to model the bubble-induced turbulence.

It is notable that the above analyses were carried out assuming the flow reached the developed status without the secondary flow and uniform pressure gradient in the cross section. Even though the experimental data at $z = 16D_H$ was used with better developed status according to the analysis in Section 4.2, there are no further measurements after $z = 16D_H$ to verify the flow reached the developed status or not. As is known, the secondary flow among the cross section is the typical characteristics for the single-phase turbulent in the noncircular ducts as compared to that in the circular pipes. Here this effect was assumed to be neglected because of the following reason. The experimental data of the lateral turbulent normal stresses (<*uu*> and <*vv*>) in [5.2] showed that more symmetric as compared with that of the single-phase flow due to the formation of the bubble layer near the wall and corner for the turbulent bubbly flow in the square duct. It indicated the horizontal secondary flow may be very weak and mainly exist in the region very near the corner; and the secondary flow could be neglected. However, since there is no direct experimental information about the horizontal convection and there may exist some error of the lateral normal turbulent stresses (<*uu*> and <*vv*>), it still needs further consideration about this assumption.

Besides, the analysis implied the W-shaped velocity profile for the large void fraction cases, the lack of the experimental data limited us the further validation. In addition, the inconsistence about the peak location might be attributed to the assumptions used. Therefore, in order to understand and develop the model of the turbulent bubbly flow in the large square duct, the further detailed measurements should be carried out with checking the flow developing status. The measurements of the secondary flow were also suggested for the modeling of the turbulent bubbly flow in the noncircular duct.

Reference

[5.1] Sun, H. M., 2014, Study on upward air-water two-phase flow characteristics in a vertical large square duct, Doctor Thesis, Kyoto University.

[5.2] Serizawa, A., Kataoka, I., Michiyoshi, I., 1975, Turbulence structure of air-water bubbly flow—II. local properties, Int. J. Multiphase Flow 2, 235–246.

[5.3] Theofanous, T. G., Sullivan, J., 1982, Turbulence in two-phase dispersed flows, J. Fluid Mechanics 116, 343-362.

[5.4] Wang, S., Lee, S., Jones, O., Lahey, R., 1987, 3-D turbulence structure and phase distribution measurements in bubbly two-phase flows, Int. J. Multiphase Flow 13, 327–343.

[5.5] Liu, T. J., Bankoff, S. G., 1993, Structure of air-water bubbly flow in a vertical pipe—I. liquid mean velocity and turbulence measurements, Int. J. Heat Mass Transfer 36, 1049–1060.

[5.6] Shawakat, M. E., Ching, C. Y., Shoukri, M., 2008, Bubble and liquid turbulence characteristics of bubbly flow in a large diameter vertical pipe, Int. J. Multiphase Flow 34, 767-785.

[5.7] Sun, X., Smith, T. R., Kim, S., Ishii, M., Uhle, J., 2003, Interfacial structure of air-water flow in a relatively large pipe. Exp. Fluids 34, 206-219.

[5.8] Lahey, Jr R. T., Bertodano, de M. L., Jones, Jr O. C., 1993, Phase distribution in complex geometry conduits, Nucl. Eng, Des. 141, 177-201.

[5.9] Lockhart, R. W., Martinelli, R. C., 1949, “Proposed Correlation of Data for Isothermal Two Phase Flow, Two Component Flow in Pipes,” Chem. Eng. Prog., 45, pp. 39–48.

[5.10] Hoagland, L. L., 1960, Fully Developed Turbulent Flow in Straight Rectangular Ducts - Secondary Flow, Its Cause and Effect on the Primary Flow, Ph.D. thesis, Department of Mechanical Engineering, MIT.

[5.11] Ishii, M., Hibiki, T., 2012, Thermo-Fluid Dynamics of Two-Phase Flow, Springer.

Chapter 6

Void fraction of the turbulent bubbly flow

6.1 Introduction

As mentioned previously, for the turbulent bubbly flow, the deformation and size of the bubble could significantly affect the bubbles' behavior as well as the associated momentum, heat and mass transfer processes. In the numerical predictions of the turbulent bubbly flow, they are essential to calculate the bubble drag and lift forces, which are two important forces to determine the fluid velocities, the phase distributions and so on [6.1-6.4]. So far, a number of studies have been carried out on the effects of the bubble's deformation and size on the drag and lift force coefficients, C_D and C_L, most of which were based on the single bubble experiments in different flow systems, especially in the stagnant and simple shear flow systems [6.5-6.10]. For the bubbly flow, the bubble size has long been an important measurement to understand the bubbly flow characteristics with the aid of the optical or electrical probe techniques [6.11-6.13]. Using the general optical and electrical probe techniques, the time-averaged chord length L_c of the bubbles could be measured, and indicate the characteristic axial size of the bubbles. Based on the spherical bubble assumption, the volume equivalent spherical bubble diameter (Sauter mean diameter: D_{SM}) was estimated by $D_{SM} = 1.5L_c$.

As for the measurement of the bubble's deformation, the flow visualization is an efficient way, and some correlations have been established based on the experiments of the single bubble or droplet in the infinite stagnant liquids or various conduits [6.5]. However, since the flow visualization fails for the bubbly flows due to the low visibility, there are few researches on the bubbles' deformation for the bubbly flow except under the low void fraction [6.14]. Currently, the numerical models of the bubbly flow mainly

consider the bubble deformation based on the single-bubble correlations [6.2, 6.8].

On the other hand, based on the double-sensor or multi-sensor probe, the interfacial area concentration (IAC) a_i , the void fraction α_g, the averaged chord length of the bubbles L_c could be measured for the bubbly flow simultaneously. Coupling the IAC with the local time-averaged void fraction α_g, the Sauter mean diameter D_{SM} could be given as follows:

$$D_{SM} = 6\alpha_g / a_i. \tag{6.1}$$

With these three variables, it is regarded here that the bubble deformation for the bubbly flow could be statistically reflected by combing the Sauter mean diameter D_{SM} and chord length L_c. In this chapter, the bubble deformation will be firstly studied in the turbulent bubbly flow including many bubbles based on the recently established experimental database by Sun [6.15]. After that, the numerical validation of the void fraction will be carried out based on the experimental measurements.

6.2 Bubble deformation

6.2.1 Definition of bubbles' statistical shape

To begin with, the time-averaged Sauter mean diameter D_{SM} and chord length L_c measured from the experiments were firstly shown in Figs. 6.1-6.3 as a database along the bisector, diagonal and the near wall lines, respectively. The current analysis was limited for the bubbles with the time-averaged D_{SM} ranging from 3.5*mm*~5.5*mm* and L_c ranging from 2.5*mm*~4.0*mm*. The following trends could be observed:

(1) When it gets close to the wall, L_c shows monotonously increase, but D_{SM} shows different tendency, indicating the effect of the bubble deformation changing from the duct center to the near wall region. Since the present study mainly considers the void fraction effects on the bubble deformation, the following comparisons will be mainly carried out in the core region and neglecting the wall effects.

(2) D_{SM} doesn't change with increase of the gas flow rate or the void fraction,

but L_c clearly increases. According to the definition of L_c, the characteristic length of the bubbles in the axial direction could be represented by L_c even for the different bubble shapes [6.16]. Therefore, for the bubbly flow the change of L_c under the same D_{SM} implies the change of the bubble deformation statistically, which will be analyzed in this section.

To investigate the bubble deformation for the bubbly flow, the shape factor of the bubbles is defined and examined in this part. From the flow visualization for different flow conditions, the bubbles could be assumed to be the ellipsoidal shape with circular plane vertical to the axial direction from the statistical point of view, as shown in Fig. 6.4. D_V and D_H are defined as the dimensions in the axial and horizontal directions, respectively. Liu and Clark [6.16-6.17] have carried out a series of studies on the relation between the chord length and the axial dimension of the bubbles for the different shapes. Assuming a spherical or ellipsoidal bubble, D_V could be calculated as D_V=1.5L_c if there were enough bubbles penetrated by the sensor.

So far, by a four-sensor optical probe, the void fraction, the IAC and the chord length were measured. Assuming to the bubbles to be spherical, D_{SM} could be calculated. Similarly, assuming the bubbles to be statistically ellipsoids, it is possible to calculate the bubble deformation based on D_V=1.5L_c as follows.

Firstly, the shape of the bubbles is defined as the aspect ratio E between the bubble horizontal and axial dimensions,

$$E = D_H / D_V , \tag{6.2}$$

Based on E, the volume V_B and the surface area S_B could be calculated by

$$V_B = \frac{\pi D_H^2 D_V}{6} = \frac{\pi E^2 D_V^3}{6} , \tag{6.3}$$

$$\text{and} \quad S_B = \frac{\pi D_V^2 E^2}{2} \sqrt{1 + \tfrac{2}{3E} + \tfrac{7}{3E^2}} . \tag{6.4}$$

Then, the bubble deformation could be obtained by

$$\frac{6V_B}{D_V S_B} = \frac{2}{\sqrt{1+\frac{2}{3E}+\frac{7}{3E^2}}} \,. \tag{6.5}$$

According to the definition of D_{SM} ($=\frac{6V_B}{S_B}=\frac{6\alpha}{a_i}$) and substituting $D_V = 1.5L_c$, Eq. (6.5) can be rearranged as

$$r \equiv \frac{D_{SM}}{1.5L_c} = \frac{2}{\sqrt{1+\frac{2}{3E}+\frac{7}{3E^2}}}. \tag{6.6}$$

With D_{SM} and L_c, E could be shown by the ratio between D_{SM} and L_C measured by the four-sensor optical probe. After solving Eq. (6.6), it could be obtained as

$$E = \frac{2r^2 + \sqrt{340r^2 - 84r^4}}{\left(24 - 6r^2\right)}. \tag{6.7}$$

The relation between E and D_{SM}/L_C was plotted in Fig. 6.5. If D_{SM}/L_C is larger than 1.5, it indicates $E>1$ which corresponds to the statistical oblate bubbles. If D_{SM}/L_C equals to 1.5, it indicates $E=1$ which corresponds to the statistical spherical bubbles. Otherwise, it indicates the statistical prolate bubbles. Therefore, the statistical bubble shape could be summarized based on D_{SM}/L_C as

$$\frac{D_{SM}}{L_c} = \begin{cases} >1.5 & \text{For oblate} \\ =1.5 & \text{For spherical} \\ <1.5 & \text{For prolate} \end{cases} \tag{6.8}$$

In the following section, D_{SM}/L_c will be examined to show the bubble statistical deformation.

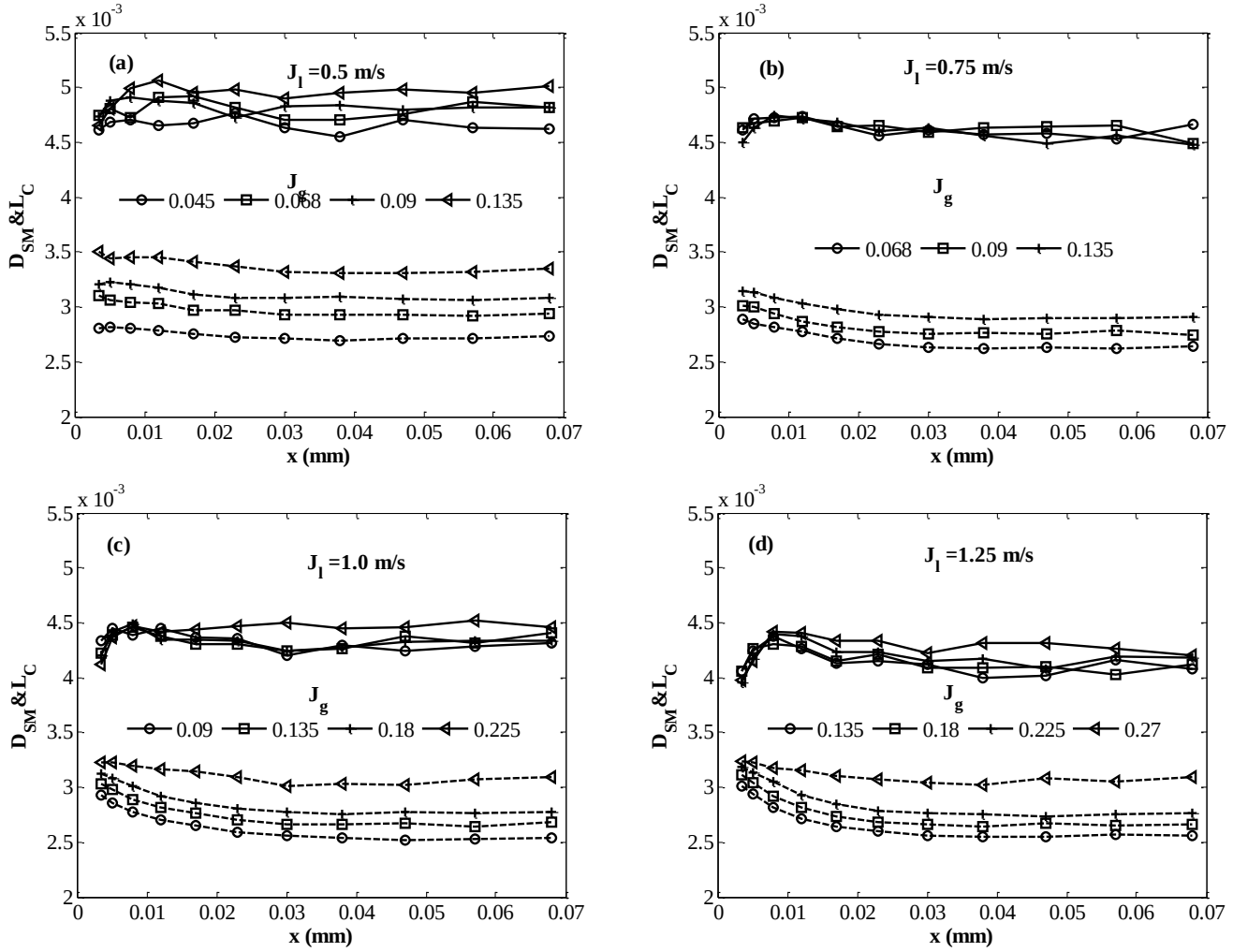

Fig. 6.1 Distributions of the Sauter mean diameter D_{SM} and the chord length L_c *a*long the bisector line under different flow conditions :(a) J_l =0.5*m/s*; (b) J_l =0.75*m/s*; (c) J_l =1.0*m/s*; (d) J_l =1.25*m/s*. The solid and dashed lines show D_{SM}, and L_c respectively.

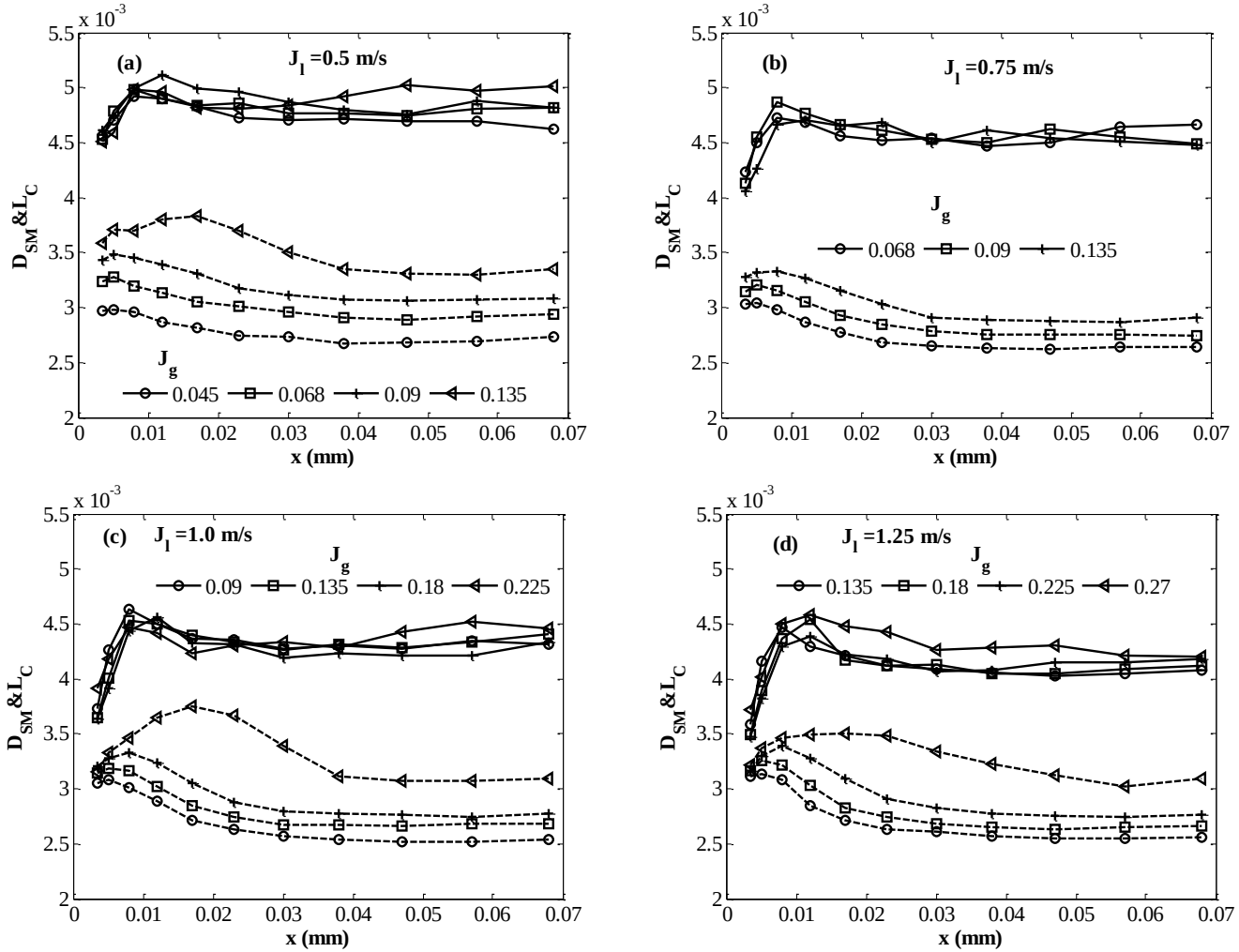

Fig. 6.2 Distributions of the Sauter mean diameter D_{SM} and the chord length L_c *a*long the diagonal line under different flow conditions :(a) J_l =0.5*m/s*; (b) J_l =0.75*m/s*; (c) J_l =1.0*m/s*; (d) J_l =1.25*m/s*. The solid and dashed lines show D_{SM}, and L_c respectively.

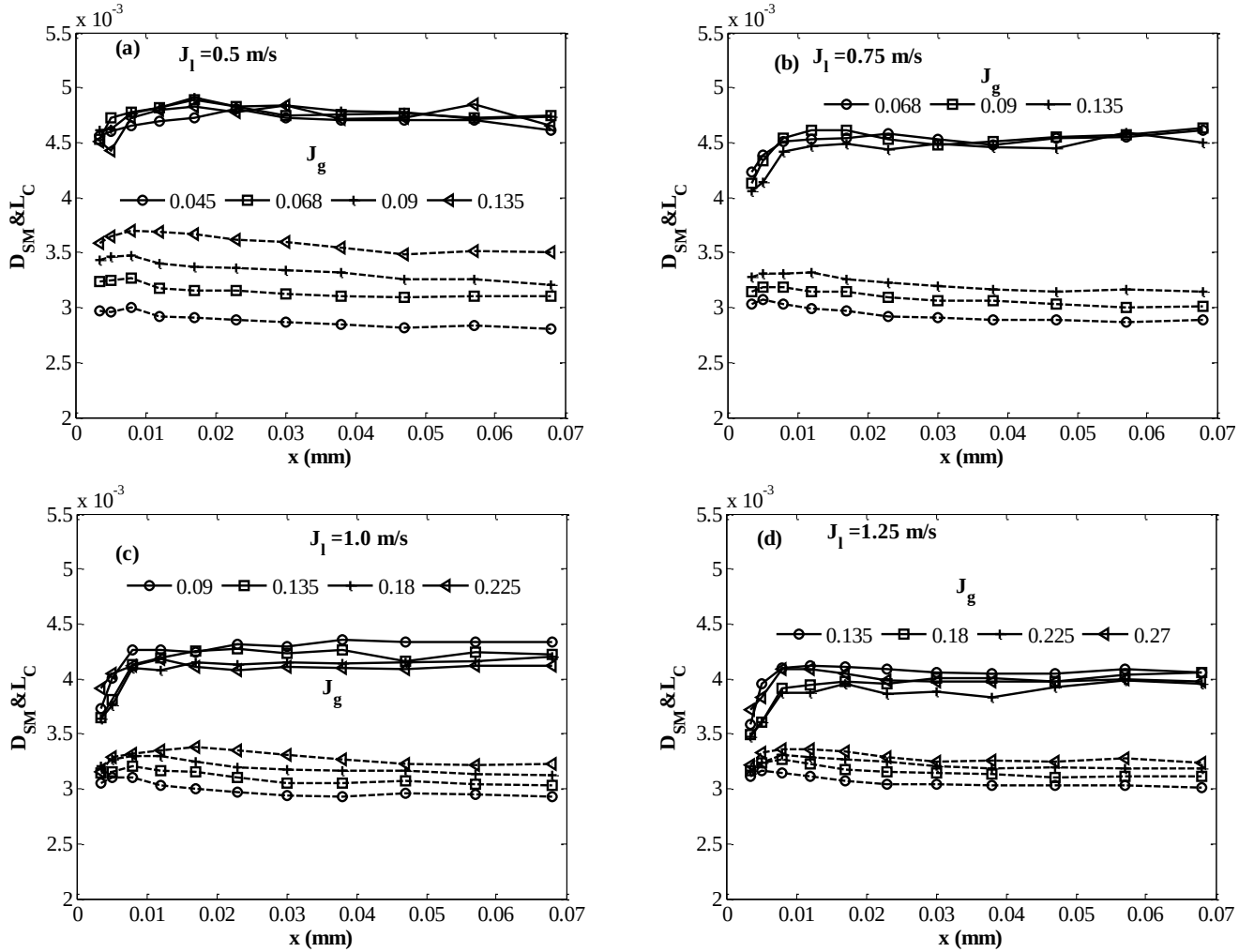

Fig. 6.3 Distributions of the Sauter mean diameter D_{SM} and the chord length L_c *a*long the near-wall line under different flow conditions :(a) J_l =0.5*m/s*; (b) J_l =0.75*m/s*; (c) J_l =1.0*m/s*; (d) J_l =1.25*m/s*. The solid and dashed lines show D_{SM}, and L_c respectively.

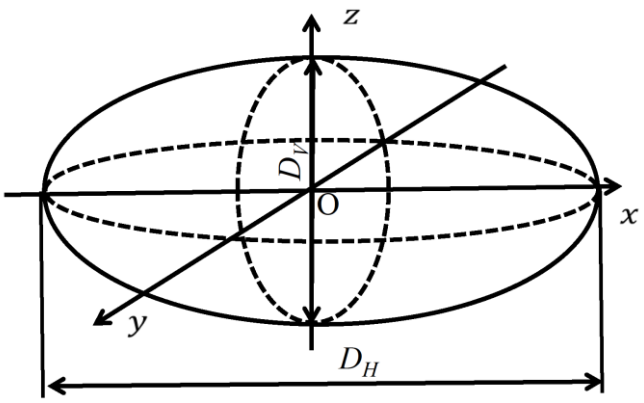

Fig. 6.4 Schematic diagram of the ellipsoidal bubble shape.

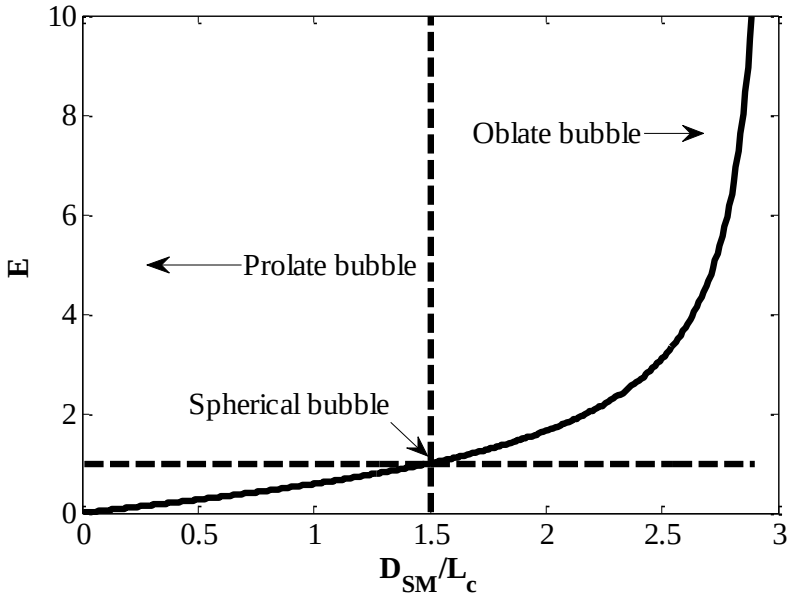

Fig. 6.5 Aspect ratio E vs. the ratio D_{SM}/L_c for the ellipsoidal bubbles.

6.2.2 Distribution of bubbles' shape factor

Together with the void fraction distributions, Figs. 6.6-6.8 show D_{SM}/L_c for different flow conditions along the bisector, the diagonal and the near-wall lines, respectively. It is observed as follows:

(1) D_{SM}/L_c decreases when it gets close to the wall, and for the low void fraction cases, D_{SM}/L_c is greater than 1.5 in the core region and sometimes less than 1.5 near the wall where there are high local void fraction and liquid shear. According to the definition of D_{SM}/L_c in Eq. (6.8), it means the bubbles statistically behave oblate in the core region, which is qualitatively in agreement with that observed in the single bubble or droplet experiments in the infinite liquids [6.5].

(2) However, increasing the void fraction, D_{SM}/L_c decreases in the whole area including both the core region and near the wall, indicating that the bubbles statistically behave more elongated. Especially for the largest void fraction case here, the bubbles show statistically prolate even in the core region, and the most prolate bubbles could be implied near the corner, which coincides with the prolate bubbles cluster observed by the flow visualization.

The above analysis indicates that for the bubbly flow with the different flow conditions the bubbles don't always behave oblate even in the core region. In addition, the existence of the many bubbles may affect the bubble deformation to deviate from the single bubble case. However, before considering the void fraction effects, it is necessary to examine whether the above observation is owing to the variation of the bubble size for the different flow conditions or not. In the following, whether and how the many bubbles affect the bubble deformation will be focused on.

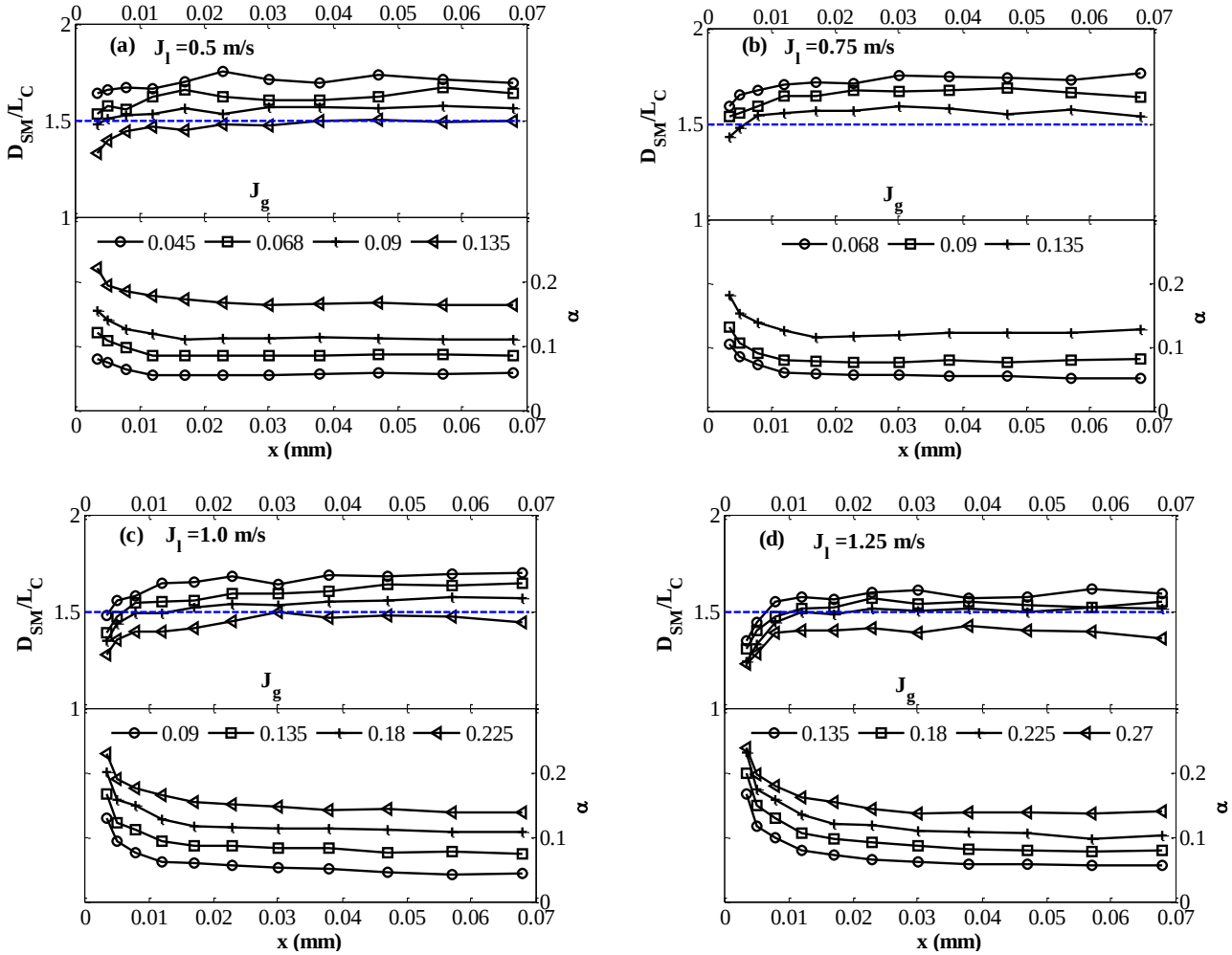

Fig. 6.6 Distributions of the ratio *r a*long the bisector line under different flow conditions: (a) J_l =0.5*m/s*; (b) J_l =0.75 *m/s*; (c) J_l =1.0 *m/s*; (d) J_l =1.25*m/s*.

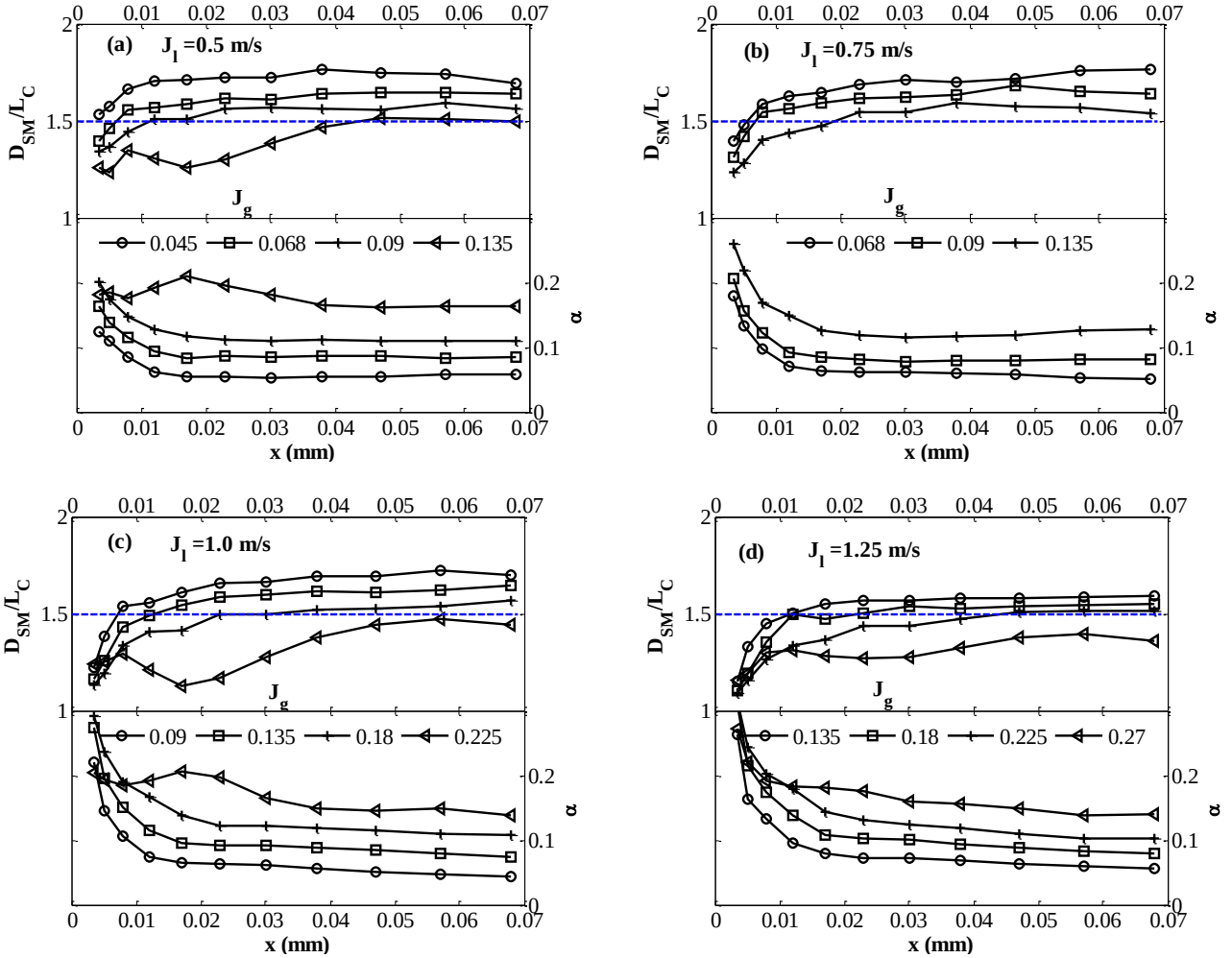

Fig. 6.7 Distributions of the ratio *r a*long the diagonal line under different flow conditions: (a) J_l =0.5*m/s*; (b) J_l =0.75*m/s*; (c) J_l =1.0*m/s*; (d) J_l =1.25*m/s*.

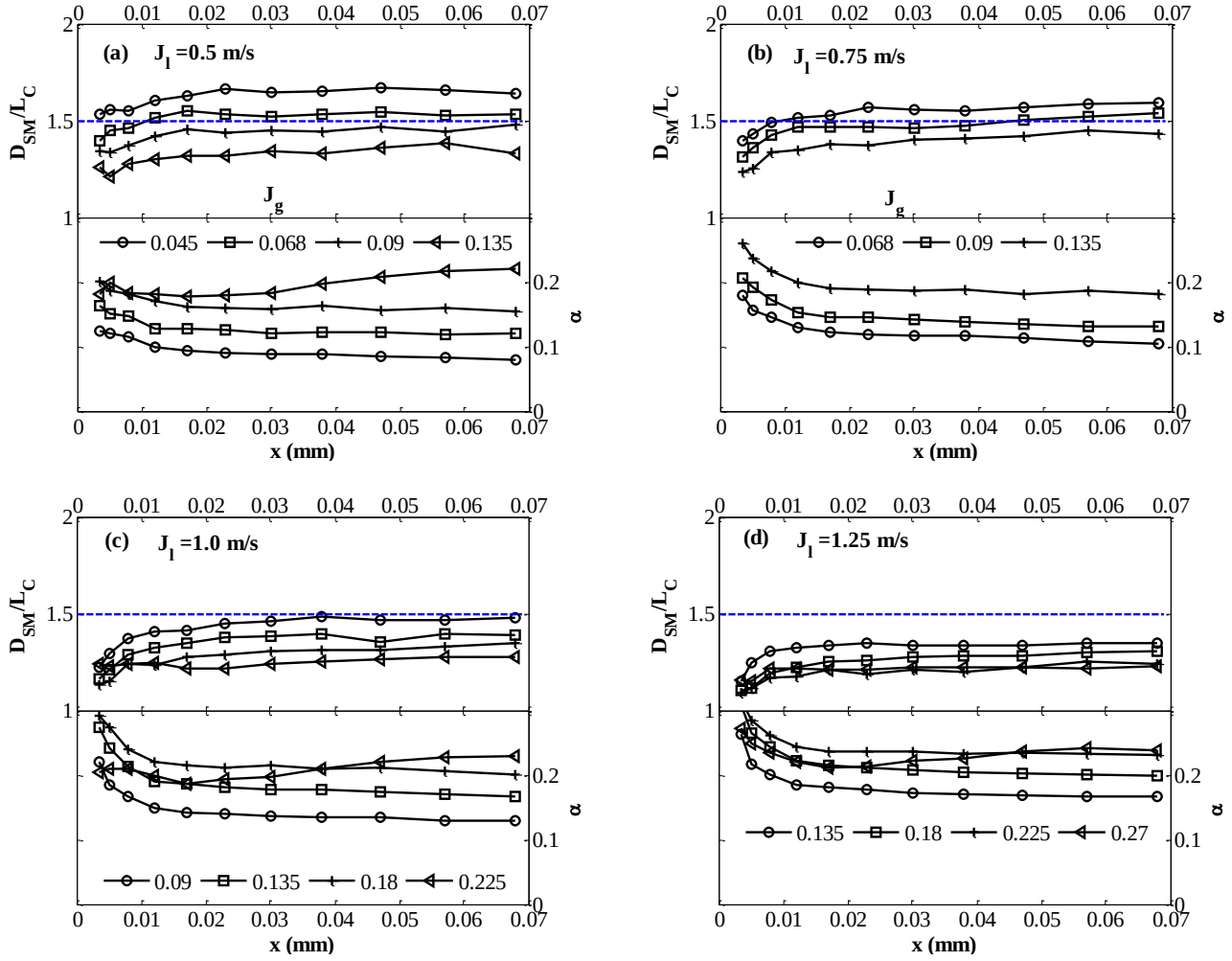

Fig. 6.8 Distributions of the ratio *r a*long the near-wall line under different flow conditions: (a) J_l =0.5*m/s*; (b) J_l =0.75*m/s*; (c) J_l =1.0*m/s*; (d) J_l =1.25*m/s*.

6.2.3 Void fraction effects on shape factor

6.2.3.1 Bubble deformation for single-bubble case

As for the bubble deformation, theoretically it is governed by the force balance on the bubbles from the continuous phase including the normal force, viscous shear stress, gravity and the surface tension. The previous researches of the bubble deformation in the single bubble or droplet experiments mainly considered the bubble deformation correlated based on the dimensionless numbers including Eo, M, Re and We, when it is dominated by different effects such as the surface tension, inertial or viscosity effects.

For the bubble deformation of the ellipsoidal bubbles, Clift *et al.* [6.5] recommended the correlation proposed by Wellek *et al.* [6.18] which analyzed photographs of rising drops of immiscible liquids in continuous liquid. Therein, for low M system with Eo < 40, the effect of Re is not important and the bubble deformation E_0 for the single bubble could be estimated by

$$E_0 = \frac{D_H}{D_V} = \left(1 + 0.163 Eo^{0.757}\right), \tag{6.9}$$

$$\text{or } D_H = D_{SM} E_0^{1/3}. \tag{6.10}$$

This correlation has been well validated based on the single-bubble experiments [6.5, 6.19]. Currently, it is usually adopted in the two-fluid or multi-fluid model to calculate the lift force coefficient C_L which is related with the bubbles deformation and is also crucial to the phase prediction of the numerical models [6.19]. Here, the bubble size effect on the bubble deformation will be examined based on the above single bubble correlation. By substituting Eq. (6.9) to Eq. (6.2) to eliminate the bubble size effect, it is obtained that

$$R \equiv E_\alpha / E_0 = \begin{cases} < 1, & \text{other effects make the bubble more prolate;} \\ = 1, & \text{the same as the single bubble case;} \\ > 1, & \text{other effects make the bubble more oblate.} \end{cases} \tag{6.11}$$

Here, E_α is the statistical aspect ratio of the bubbles for the bubbly flow case. Figs. 6.9-6.11 show the distribution of E_α/E_0 along the bisector, the diagonal and the near-wall lines, respectively. Based on the previous assumption and after eliminating bubble size effect, it is observed that for the bubbly flow, the bubble deformation E_α was over-predicted based on the single bubble correlation. Besides, with the increase of void fraction, it deviates more from the single bubble correlation. Therefore, for the bubbly flow, the correlation of the bubble deformation may need further correction considering the void fraction effects.

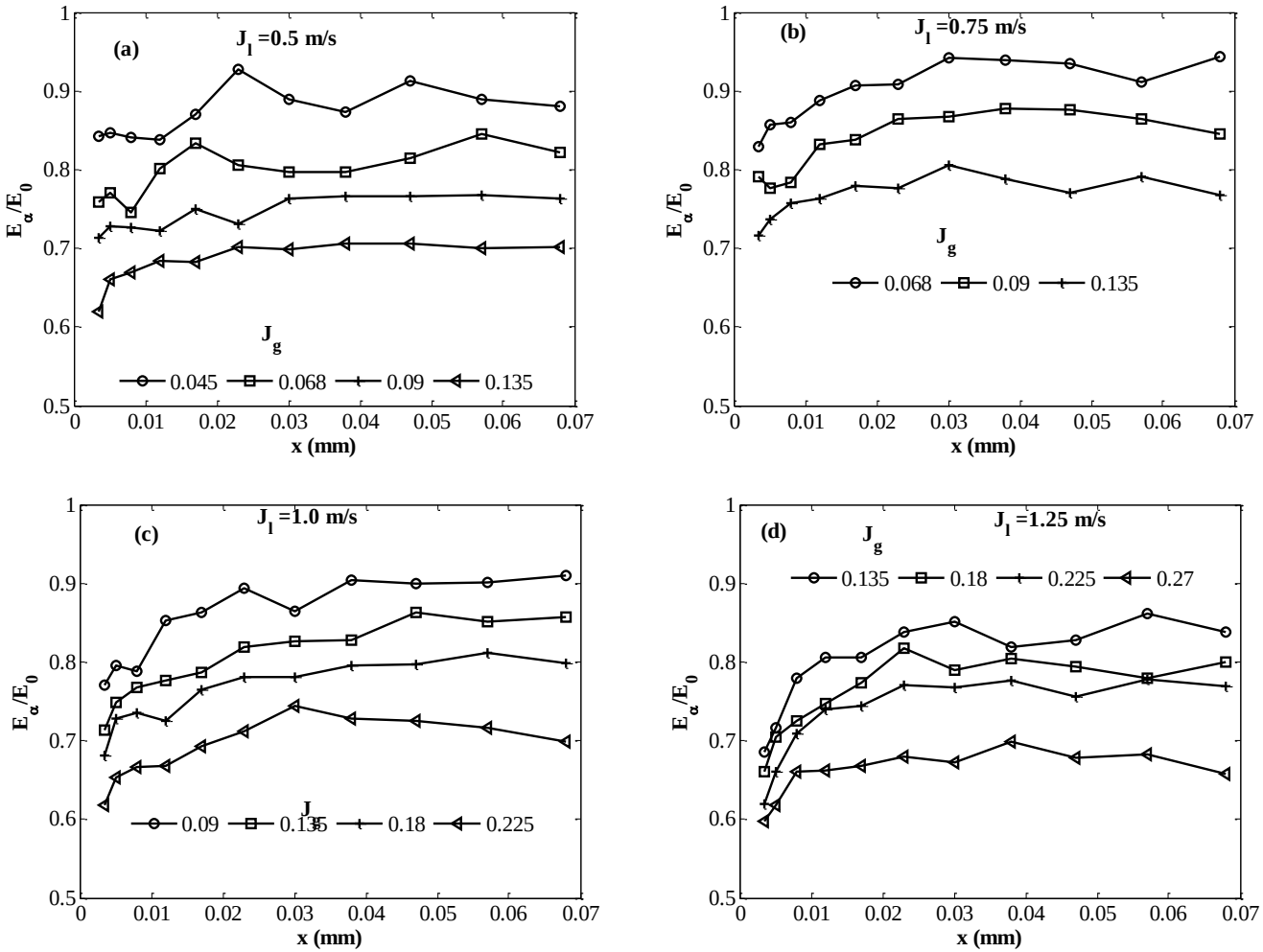

Fig. 6.9 Distributions of the ratio E_α/E_0 along the bisector line under different flow conditions: (a) J_l =0.5*m/s*; (b) J_l =0.75*m/s*; (c) J_l =1.0*m/s*; (d) J_l =1.25*m/s*.

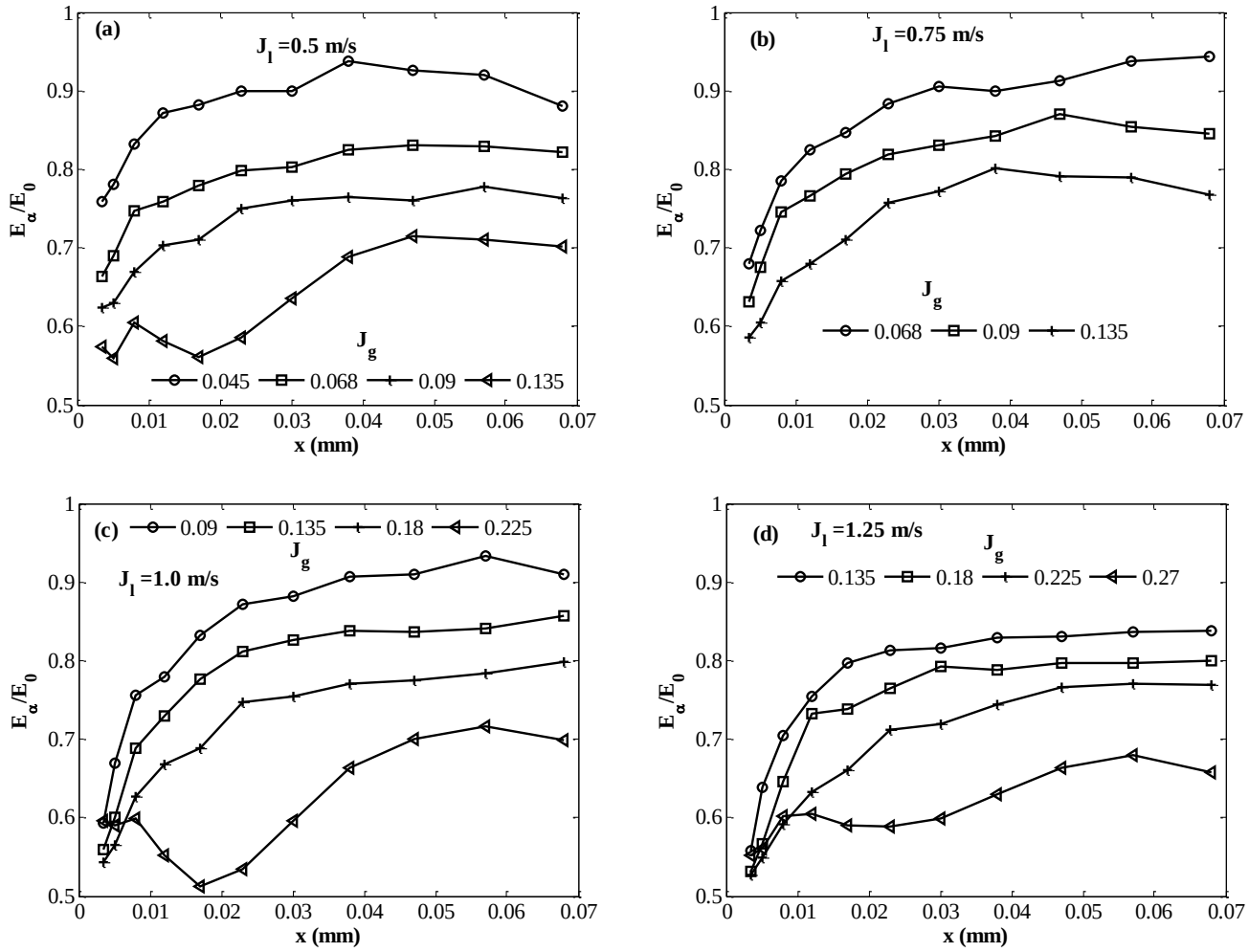

Fig. 6.10 Distributions of the ratio E_α/E_0 along the diagonal line under different flow conditions: (a) J_l =0.5*m/s*; (b) J_l =0.75*m/s*; (c) J_l =1.0*m/s*; (d) J_l =1.25*m/s*.

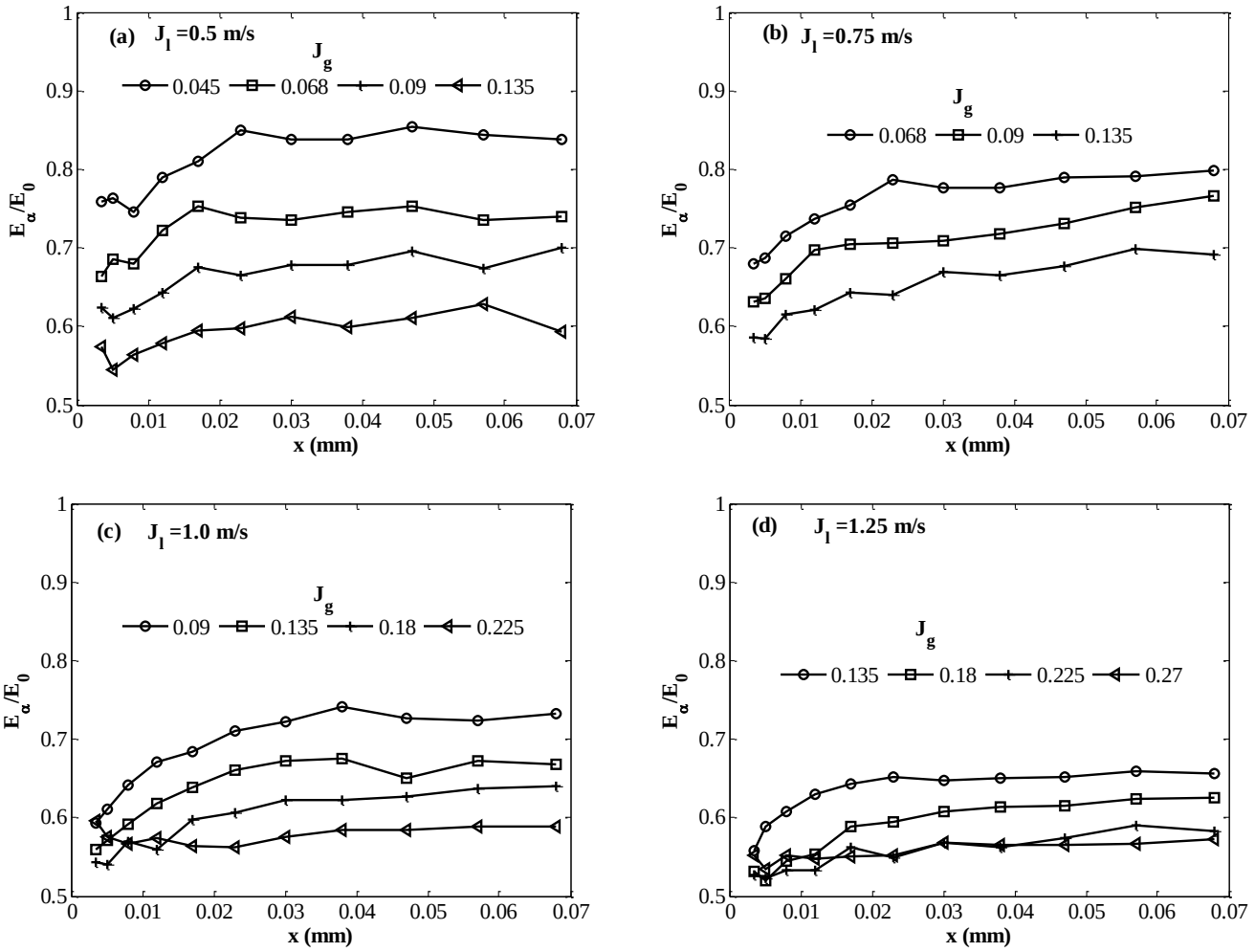

Fig. 6.11 Distributions of the ratio E_α/E_0 along the near-wall line under different flow conditions: (a) J_l =0.5*m/s*; (b) J_l =0.75*m/s*; (c) J_l =1.0*m/s*; (d) J_l =1.25*m/s*.

6.2.3.2 Correction on the multi-bubble effect

As compared to the single bubble case with the similar bubble size, the introduction of the many bubbles may change the force balance exerted on the bubbles which dominates the bubble deformation. One effect of the many bubbles is to statistically decrease the relative velocity V_R due to the increase of the mixture viscosity μ_m or drag on the bubbles [6.20-6.21]. Assuming the simple similarity between the single bubble system and bubbly flow system, the decrease of V_R and increase of μ_m could modify the bubble deformation by decreasing the inertial effects and increasing viscous effects respectively. The above two effects could be reflected by the Reynolds number. In the present study, the void fraction effect on the statistical bubble deformation was considered according to Re in the following form,

$$E_\alpha = E_0 \cdot f\left(\frac{\mathrm{Re}_\alpha}{\mathrm{Re}_S}\right) = E_0 \cdot f\left(\frac{V_{R\alpha}}{V_{RS}}\right), \tag{6.12}$$

where $\mathrm{Re}_\alpha = \rho_l V_{R\alpha} D_{SM}/\mu_l$ and $\mathrm{Re}_S = \rho_l V_{RS} D_{SM}/\mu_l$ are Reynolds numbers for the bubbly flow case with the void fraction α and for the single bubble case, respectively; and $V_{R\alpha}$ and V_{RS} are the relative velocities between the bubbles and liquid phase for the bubbly flow case and single bubble case, respectively.

Based on the assumption of the similarity between the single bubble system and bubbly flow system, Ishii and Zuber [6.20] proposed the following relative velocity $V_{R\alpha}$,

$$V_{R\alpha} = V_{RS}(1-\alpha)^{1.75}, \tag{6.13}$$

According to the measurements of the buoyancy-driven bubbly flow, Garnier *et al.* [6.21] proposed the following relation between $V_{R\alpha}$ and α,

$$V_{R\alpha} = V_{RS}\left(1-\alpha^{1/3}\right). \tag{6.14}$$

In the present study, Eq. (6.13) is chosen. Substituting Eq. (6.13) to Eq. (6.12) and after rearranging, it is obtained that

$$E_\alpha = E_S \cdot f(1-\alpha). \tag{6.15}$$

To identify the function $f(1-\alpha)$, Fig. 6.12 shows the relation between E_α/E_S and $(1-\alpha)$ by collecting the experimental data under the different flow conditions. A clear tendency of the void fraction effect on the bubble deformation was shown and the function $f(1-\alpha)$ is obtained as follows,

$$f(1-\alpha) \approx (1-\alpha)^{2.3}. \tag{6.16}$$

For the single bubble case $\alpha=0$, the above Eq. (6.15) becomes Eq. (6.9) which keeps the consistency.

Replacing E_S in Eq. (6.9) by E_α in Eq. (6.15), therefore for the bubbly flow, the statistical horizontal dimension of the bubbles in Eq. (6.9) could be calculated by,

$$D_H \approx D_{SM}\left(1+0.163\mathrm{Eo}^{0.757}\right)^{1/3}(1-\alpha)^{0.767}. \tag{6.17}$$

6.2.4 Bubble size validation

Figs. 6.13 and 6.14 show the comparisons among the statistical horizontal dimensions of the bubbles calculated from the experimental data $D_{H.exp}$, D_{HS} calculated based on Eq. (6.9) and $D_{H\alpha}$ calculated based on Eq. (6.17). It indicates that with E_S, the bubble deformations for the bubbly flow are all over-predicted, but with E_α the bubble deformation for the bubbly flow could be predicted much better. Therefore, Eq. (6.17) is recommended to calculate the statistical horizontal dimension D_H for the bubbly flow. However, it is notable that the above correlation Eqs. (6.15)-(6.17) was validated only for the limited range of the bubble size around 3.5*mm*~5.5*mm* and the void fraction around 5%~30%. For the bubbly flow with the different range of the bubble size and void fraction, it still needs further validation and consideration based on more experimental data in the future.

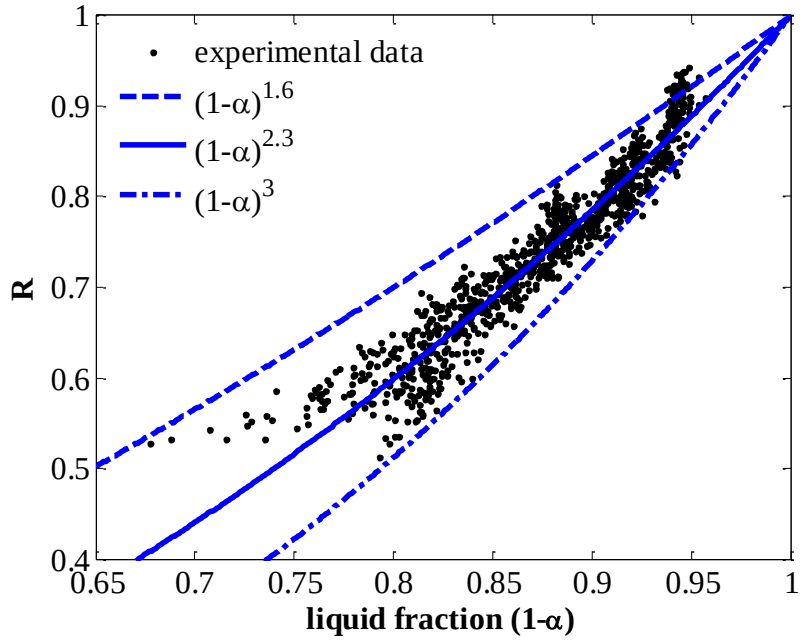

Fig. 6.12 Ratio $R=E_\alpha/E_0$ vs. the liquid fraction (1-α) under all the tested flow conditions.

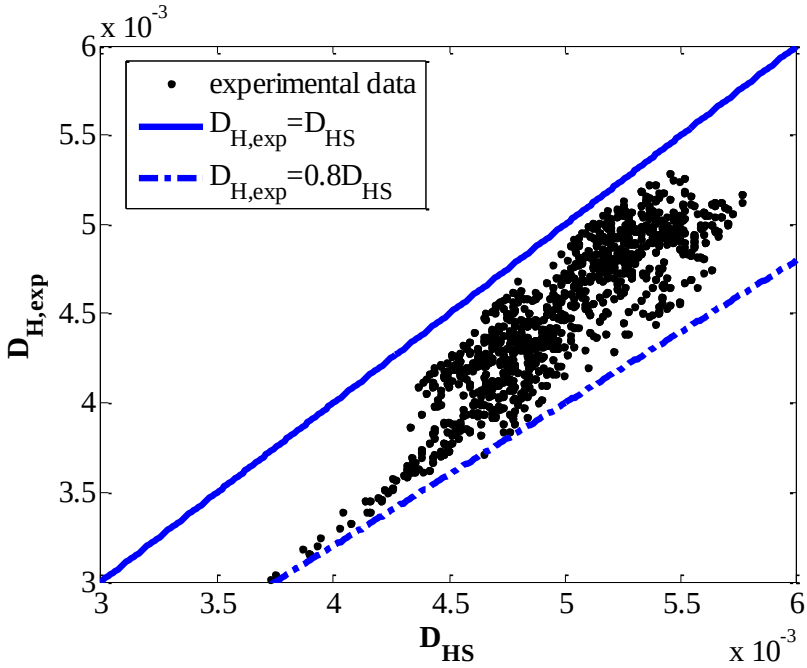

Fig. 6.13 $D_{H.exp}$ vs. D_{HS} under all the tested flow conditions.

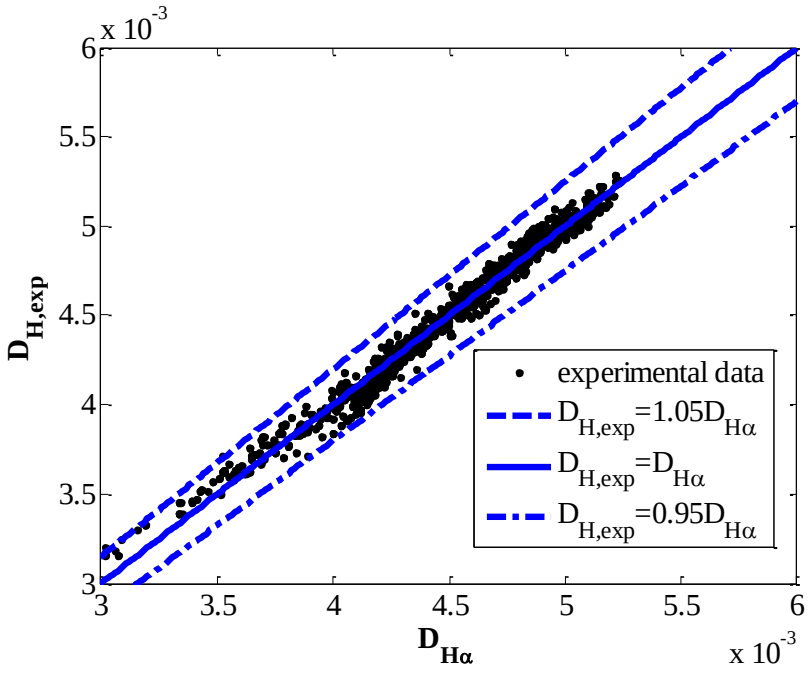

Fig. 6.14 $D_{H.exp}$ vs. $D_{H\alpha}$ under all the tested flow conditions.

6.3 Numerical validation of the void fraction

In this section, the numerical validation of the lateral distribution of the void fraction will be carried out based on two-fluid model and the experimentally measured turbulent intensities and the liquid-phase velocity distributions [6.15].

6.3.1 Numerical models

As shown in Chapter 5, in order to validate the liquid-phase velocity distribution the force balance in the axial direction was solved based on the mixing length theory to model the turbulent Reynolds shear stress. In this chapter, the force balance equation in the horizontal direction will be solved in order to obtain the lateral distribution of the void fraction following the method used in the small circular pipe [6.22]. Firstly, assuming the fully developed flow status and neglecting the secondary flow effect, the force balance in the horizontal direction is shown for the liquid and gas phases, respectively. For the gas phase:

$$-\alpha\frac{\partial P}{\partial X}+\frac{\partial\left(\alpha\boldsymbol{\tau}_{xx}^{G}\right)}{\partial X}+\frac{\partial\left(\alpha\boldsymbol{\tau}_{xy}^{G}\right)}{\partial Y}+\mathbf{M}_{Lx}=0\,, \tag{6.18}$$

$$-\alpha\frac{\partial P}{\partial Y}+\frac{\partial\left(\alpha\boldsymbol{\tau}_{xy}^{G}\right)}{\partial X}+\frac{\partial\left(\alpha\boldsymbol{\tau}_{yy}^{G}\right)}{\partial Y}+\mathbf{M}_{Ly}=0\,. \tag{6.19}$$

For the liquid phase:

$$-(1-\alpha)\frac{\partial P}{\partial X}+\frac{\partial\left((1-\alpha)\boldsymbol{\tau}_{xx}^{L}\right)}{\partial X}+\frac{\partial\left((1-\alpha)\boldsymbol{\tau}_{xy}^{L}\right)}{\partial Y}-\mathbf{M}_{Lx}=0\,, \tag{6.20}$$

$$-(1-\alpha)\frac{\partial P}{\partial Y}+\frac{\partial\left((1-\alpha)\boldsymbol{\tau}_{xy}^{L}\right)}{\partial X}+\frac{\partial\left((1-\alpha)\boldsymbol{\tau}_{yy}^{L}\right)}{\partial Y}-\mathbf{M}_{Ly}=0\,, \tag{6.21}$$

where $\mathbf{M}_{Lx}$ and $\mathbf{M}_{Ly}$ are the lift forces in X and Y directions, respectively. Eliminating the pressure gradient by $(6.18)\times(1-\alpha)-(6.20)\times\alpha$ and $(6.19)\times(1-\alpha)-(6.21)\times\alpha$ and neglecting the turbulent stress of the gas phase due to $\rho_G/\rho_L<<1$, we have

$$\frac{\partial\left((1-\alpha)\boldsymbol{\tau}_{xx}^{L}\right)}{\partial X}+\frac{\partial\left((1-\alpha)\boldsymbol{\tau}_{xy}^{L}\right)}{\partial Y}-\frac{\mathbf{M}_{Lx}}{\alpha}=0\,, \tag{6.22}$$

$$\frac{\partial\left((1-\alpha)\boldsymbol{\tau}_{xy}^{L}\right)}{\partial X}+\frac{\partial\left((1-\alpha)\boldsymbol{\tau}_{yy}^{L}\right)}{\partial Y}-\frac{\mathbf{M}_{Ly}}{\alpha}=0\,. \tag{6.23}$$

With the above assumptions, the local void fraction distribution is determined by the balance between the lateral turbulence dispersion force and the lift force. The lateral turbulence dispersion is closely related to turbulence anisotropy which will be considered in Chapter 7. Currently, the experimental measurements of the lateral turbulence will be adopted.

Considering the geometrical symmetry, on the bisector and diagonal lines, Eqs. (6.22) and (6.23) could be simplified as follows:

$$\frac{d\left((1-\alpha)\boldsymbol{\tau}_{xx}^{L}\right)}{dX}-\frac{\mathbf{M}_{Lx}}{\alpha}=0\ \Rightarrow\ \frac{d(1-\alpha)}{dX}+F(X)(1-\alpha)=G(X) \tag{6.24}$$

where $F(X)=\dfrac{d\overline{uu}}{\overline{uu}dX}$ and $G(X)=\dfrac{C_L W_R dW_L}{\overline{uu}dX}$.

By solving Eq. (6.24) the lateral void fraction distribution could be obtained as

$$\begin{aligned}\alpha(X) &= 1\text{-}\left\{(1\text{-}\alpha_{\mathrm{Gc}})+\int_0^X G(y'')\exp\left(\int_0^{y''}F(y')dy'\right)dy''\right\}\exp\left(-\int_0^X F(y')dy'\right)\\ &= 1\text{-}\left\{(1\text{-}\alpha_{\mathrm{Gc}})+\frac{C_L W_R}{\overline{uu}_{Lc}}(W_L-W_{LC})\right\}\left(\frac{\overline{uu}_{Lc}}{\overline{uu}}\right)\end{aligned} \tag{6.25}$$

where α_{gc}, W_{LC} and $\overline{uu}_{Lc}$ are the void fraction, liquid phase velocity, the normal turbulent intensities at the duct center.

To solve Eq. (6.25), the lateral distributions of the liquid phase velocity and the normal turbulent intensities are required in addition to α_{gc} according to the experimental databases. It is notable that in [6.15], the experimental measurements were carried out based on the coordinate parallel with the wall direction. Here, during solving Eq. (6.25) along the diagonal line, the relation about the turbulent normal components shown Fig. 6.15 is adopted.

The relative velocity W_R is determined by the following correlation

$$W_R=\sqrt{\frac{4d(\rho_l-\rho_g)}{3\rho_l g}}. \tag{6.26}$$

As for the lift coefficient C_L, Tomiyama's correlation [6.8] was used and therein the bubble horizontal dimension D_H was considered by $D_{H0}=D_{SM}\left(1+0.163Eo^{0.757}\right)^{1/3}$ and $D_{H\alpha}=D_{SM}\left(1+0.163Eo^{0.757}\right)^{1/3}(1-\alpha)^{0.767}$, respectively.

6.3.2 Numerical results

Firstly, Figs. 6.16-6.18 show the comparison of the lateral void fraction distribution predicted by Eq. (6.25) and measured experiments at z=16D_H along the bisector and diagonal lines respectively. From these figures, it could be observed that:

(1) The predictions of the void fractions are in well consistent with the

experimental measurements for the cases (J_l =0.75*m/s*, J_g =0.09*m/s*, J_l =0.75*m/s*, J_g =0.135*m/s* and J_l =1.0*m/s*, J_g =0.135*m/s*). However, for the other cases, the prediction showed quite different behaviors.

(2) Based on the current experimental data, the choice of the bubble horizontal dimension slightly modified the prediction of the void fraction.

The following characteristics are considered to be responsible of the above observations. (1) According the developing status as analyzed in Fig. 4.9 of Chapter 4, for the cases (J_l =0.75*m/s*, J_g =0.09*m/s*, J_l =0.75*m/s*, J_g =0.135*m/s* and J_l =1.0*m/s*, J_g =0.135*m/s*), the flow showed better developed status at the location z=16D_H. However, for the other cases the liquid phase velocity was not either lifted up for the low void fraction cases or entered the third developing stage for the large void fraction cases, which deviates from the assumptions of Eq. (6.25). (2) The current bubble size is around 3.5*mm*~5.5*mm*, among which there is little effect of D_{H0} or $D_{H\alpha}$ on the lift coefficients C_L.

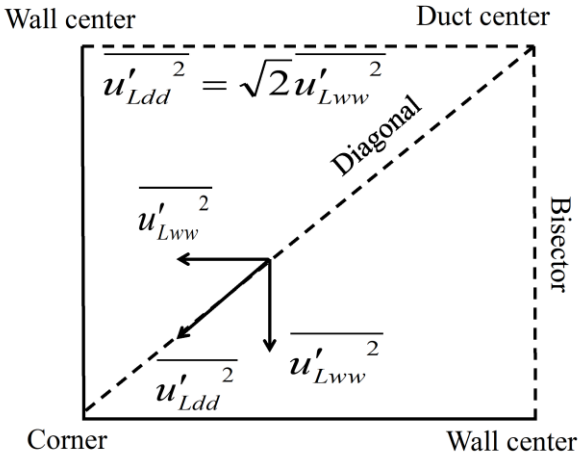

Fig. 6.15 Schematic diagram of the turbulent components along the diagonal line.

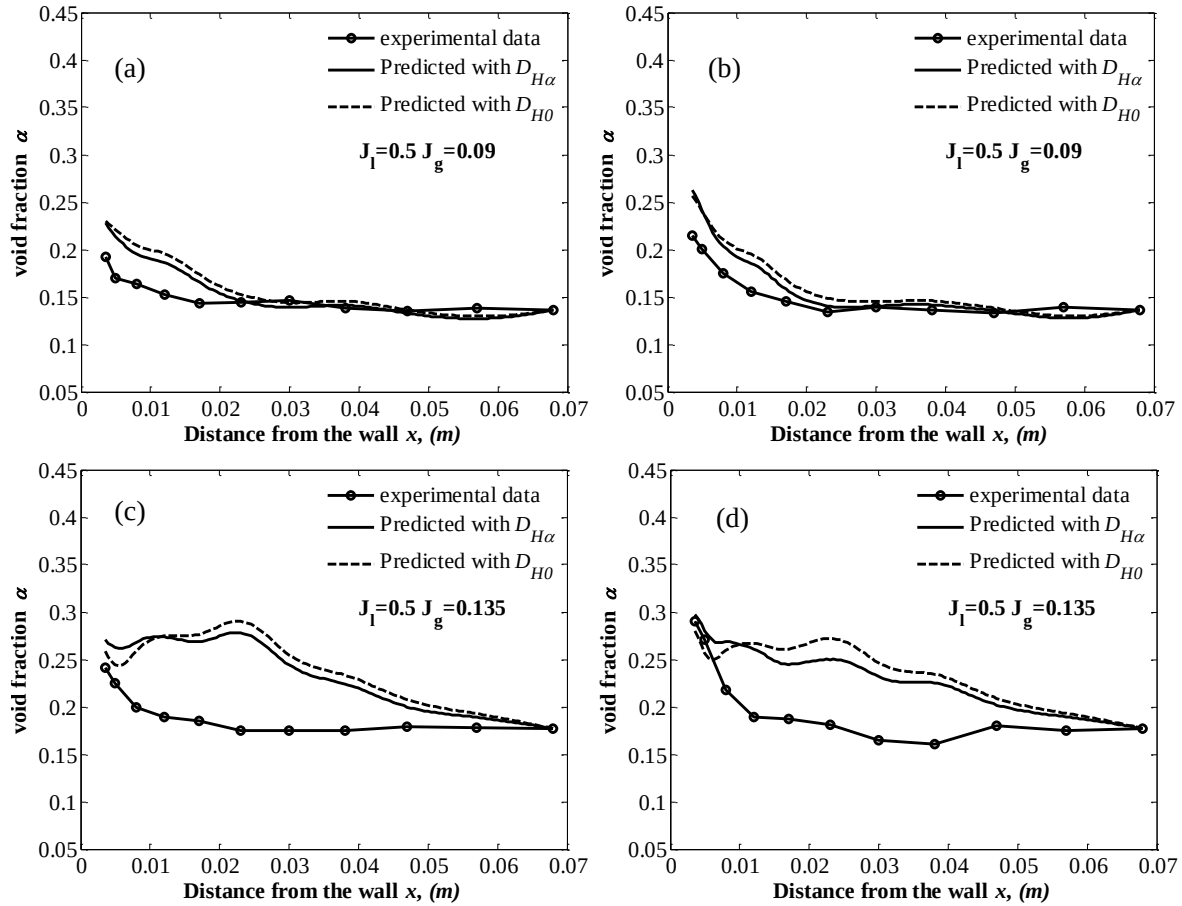

Fig. 6.16 Comparison between numerical predicted void fraction α and experimental measurement for J_l =0.5m/s at z=16D_H:
with J_g =0.09m/s (a) along the bisector line; (b) along the diagonal line;
with J_g =0.135m/s (c) along the bisector line; (d) along the diagonal line.

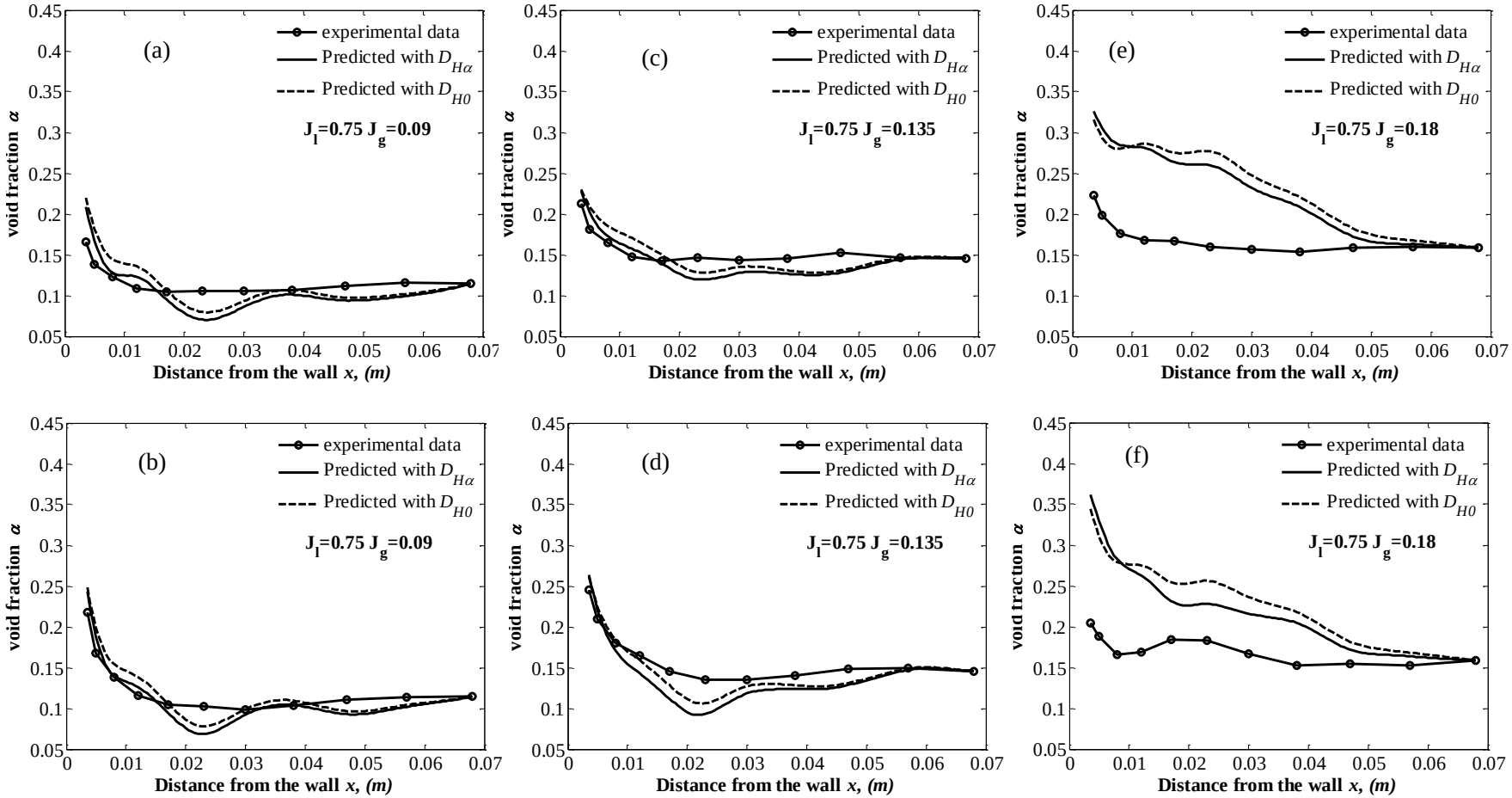

Fig. 6.17 Comparison between numerical predicted void fraction α and experimental measurement for J_l =0.75*m/s* at z=16D_H: with J_g =0.09*m/s* (a) along the bisector line; (b) along the diagonal line; with J_g =0.135*m/s* (c) along the bisector line; (d) along the diagonal line; with J_g =0.18*m/s* (e) along the bisector line; (f) along the diagonal line.

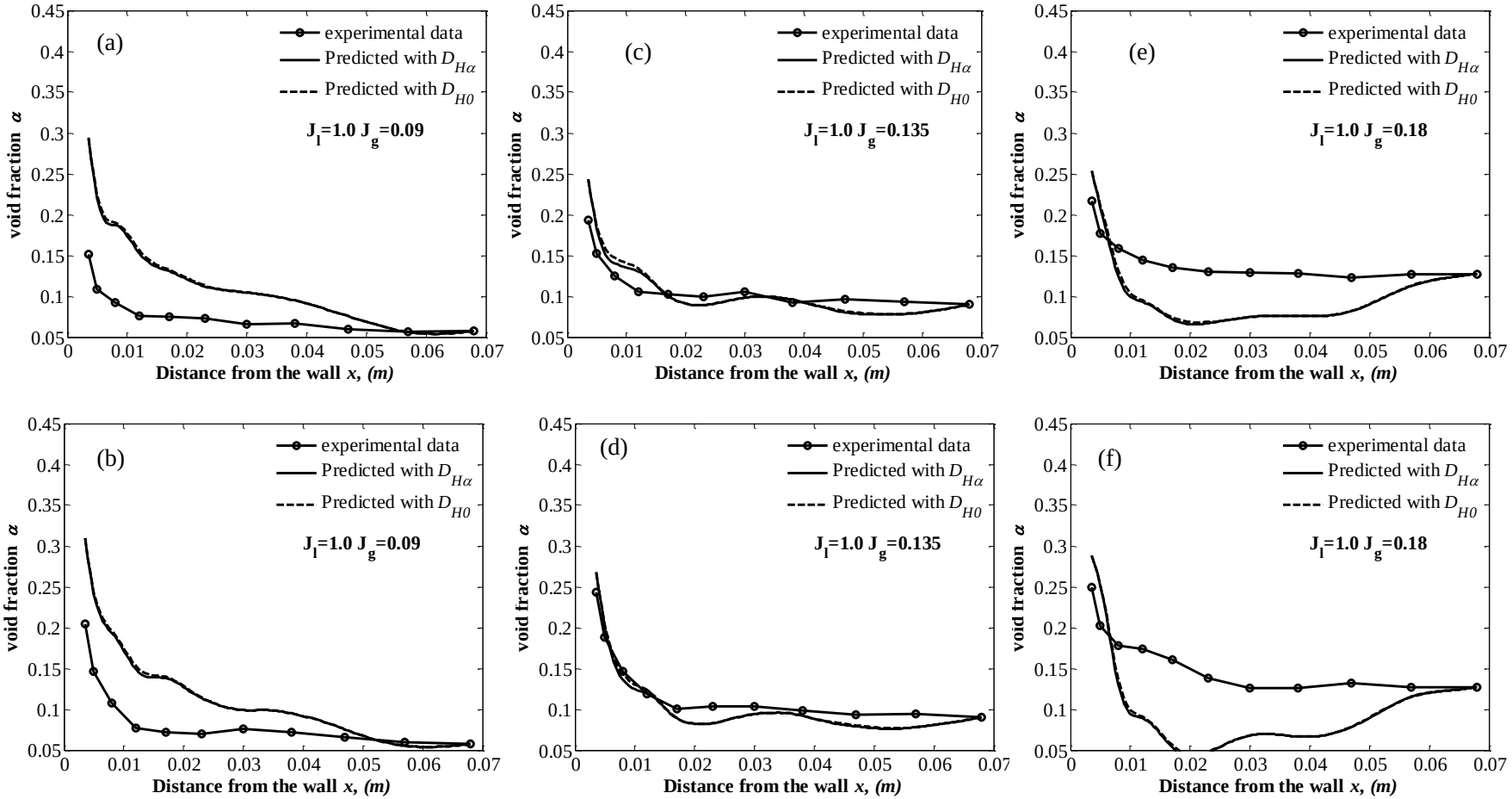

Fig. 6.18 Comparison between numerical predicted void fraction α and experimental measurement for J_l =1.00*m/s* at z=16D_H: with J_g =0.09*m/s* (a) along the bisector line; (b) along the diagonal line; with J_g =0.135*m/s* (c) along the bisector line; (d) along the diagonal line; with J_g =0.18*m/s* (e) along the bisector line; (f) along the diagonal line.

6.4 Summary and Discussion

In this chapter, the void fraction effect on the bubble deformation was firstly studied. Numerical validation of the void fraction was then carried out based on the experimental results. The following findings were obtained:

(1) For the bubbly flow, the existence of the many bubbles could affect the statistical bubbles' deformation. Compared to the single-bubble case, the bubbles behaved more prolate with the increase of the void fraction.

(2) Considering the void fraction effect, a new correlation for the statistical bubble deformation were proposed and validated combining the bubble size and void fraction.

(3) The numerical validation showed that only for the cases with the better-developed flow, the predictions of the void fractions were in well consistent with the experimental measurements.

It is notable that the analysis on the void fraction effect on the bubble deformation was based on some assumptions such as all the ellipsoidal bubble shape and enough bubble number during the measurements. Since the measurements were carried out in the large duct, the wall effect was also neglected. Whether these assumptions are suitable or not still needs further validation based on more experimental data in the future. In addition, currently the new correlation of the bubble deformation was proposed and validated for the mean bubble size around 3.5mm~5.5mm and the limited void fraction range. For the wider range of the bubble size and flow conditions, it still needs further study in the future. The numerical work further suggests the importance of knowing the developing status for the modeling of the turbulent bubbly flow.

Reference

[6.1] Ishii, M., Hibiki, T., Thermo-Fluid Dynamics of Two-phase flow, Second edition, 2010, Springer.

[6.2] Tomiyama, A., Shimada, N., 2001, A numerical method for bubbly flow simulation based on a many-fluid model, Trans. ASME, J. of Pressure Vessel Tech. 23, 510-516.

[6.3] Bunner, B., Tryggvason, G., 2003, Effect of bubble deformation on the properties of bubbly flows, J. Fluid Mech. 495, 77–118.

[6.4] Lu, J. C., Tryggvason, G., 2008, Effect of bubble deformability in turbulent bubbly upflow in a vertical channel, Phys. Fluids 20, 040701.

[6.5] Clift, R., Grace, J.R., Weber M.E., 1972, Bubbles, drops, and particles, Science.

[6.6] Tomiyama, A., Kataoka, I., Zun, I., and Sakaguchi T, 1998, Drag coefficients of single air bubbles under normal and micro gravity conditions, JSME Int. J., Ser. B 41, 472

[6.7] Magnaudet, J., Eames, I., 2000, The motion of high-Reynolds number bubbles in homogeneous flows, Annual Rev. Fluid Mech. 32, 659-708.

[6.8] Tomiyama, A., Tamai, H., Zun, I., Hosokawa, S., 2002, Transverse migration of single bubbles in simple shear flows, Chem. Eng. Sci. 57, 1849-1858.

[6.9] Legendre, D., 2007, On the relation between the drag and the vorticity produced on a clean bubble, Phys. Fluids 19, 018102.

[6.10] Rastello, M., Mari´e, J. L., Lance, M., 2011, Drag and lift forces on clean spherical and ellipsoidal bubbles in a solid body rotating flow, J. Fluid Mech. 682, 434.

[6.11] Serizawa, A., Kataoka, I., Michiyoshi, I., 1975, Turbulence structures of air-water bubbly flow-I. measuring techniques, Int. J. Multiphase Flow 2, 221-233.

[6.12] Liu, T. J., 1993, Bubble size and entrance effects on void development in a vertical channel, Int. J. Multiphase Flow 19, 99-113.

[6.13] Liu, T. G., Bankoff, S. G., 1993, Structure of air-water bubbly flow in a vertical pipe—II. Void fraction, bubble velocity and bubble size distribution, Int. J. Heat and Mass Transfer 36, 1061–1072.

[6.14] Fujiwara, A., Danmoto, Y., Hishida, K., Maeda, M., 2004, Bubble deformation and flow structure measured by double shadow images and PIV/LIF, Exp. Fluids 36, 157–165.

[6.15] Sun, H. M., 2014, Study on upward air-water two-phase turbulent flow characteristics in a vertical large square duct, Doctor Thesis, Kyoto University.

[6.16] Clark, N. N., Turton R, 1988, Chord length distributions related to bubble size distributions in manyphase flows, Int. J. Multiphase Flow 14, 413-424.

[6.17] Liu, W., Clark, N. N., 1995, Relationships between distributions of chord length and distributions of bubble sizes including their statistical parameters, Int. J. Multiphase Flow 21, 1073-1089.

[6.18] Wellek, R. M., Agrawal, A. K., Skelland, A, H, P, 1966, Shape of liquid drops moving in liquid media, AIChE J. 12, 854-862.

[6.19] Tomiyama, A., Celata, G. P., Hosokawa, S., Yoshida, S., 2002, Terminal velocity of single bubbles in surface tension force dominant regime, Int. J. Multiphase Flow 28, 1497-1519.

[6.20] Ishii, M., Zuber, N., 1979, Drag coefficient and relative velocity in bubbly, droplet or particulate flows, AIChE J. 25, 843-855.

[6.21] Garnier, C., Lance, M., Mariém J. L., 2002, Measurement of local flow characteristics in buoyancy-driven bubbly flow at high void fraction, Experimental Therm. Fluid Sci. 26, 811-815.

[6.22] Wang, S., Lee, S., Jones, O., Lahey, Jr R. T., 1987, 3-D turbulence structure and phase distribution measurements in bubbly two-phase flows, Int. J. Multiphase Flow 13, 327–343.

Chapter 7

Turbulence modulation of the turbulent bubbly flow

7.1 Introduction

As compared with the single-phase turbulent flow, for the turbulent bubbly flow the presence of the bubbles will modulate the turbulence characteristics by the following mechanisms: (1) Altering the shear-induced turbulence by modifying mean flow properties such as the mean shear rate; (2) Inducing additional pseudo turbulence by agitating the flow such as wake structure behind the bubbles; (3) Interacting with the existing shear-induced eddies by being captured or colliding; (4) Inducing additional interaction between bubble-induced and shear-induced eddies. Due to the above mechanisms, the turbulence modulation such as turbulence enhancement or suppression occurs in the turbulent bubbly flow, which has been partially discussed in [7.1].

Though several studies on the turbulence modulation [7.2-7.13] have been carried out for the turbulent bubbly flow, the understanding and modeling are still unsatisfactory so far. In this Chapter, the turbulence modulation of the upward turbulent bubbly flow will be further studied based on the recently established experimental database. It will aim at understanding the following questions:

(1) How much turbulent energy was induced by the bubbles?

(2) How does the interaction between the bubble-induced turbulence and the wall-induced turbulence behave?

(3) What is the property of the bubble-induced turbulence such as the turbulence anisotropy?

(4) How to model the bubble induced turbulence considering the above properties?

7.2 Turbulent kinetic energy

For the turbulent bubbly flow in the ducts, the turbulence generation includes the wall-induced turbulence t_{kw} which is the main mechanism for the single-phase turbulent flow and the bubble-induced turbulence t_{kb}. Several studies [7.3-7.4, 7.8-7.11] have been conducted to model the bubble-induced turbulence by comparing the turbulence with and without the bubbles. The theoretical analysis could be found in [7.4, 7.11], which estimated the bubble-induced turbulence based on the potential theory [7.4] and based on the mean flow velocity and the wall shear stress [7.11], respectively. The uniform bubbly flow experiments in [7.9] showed that below the critical void fraction α_c of the order of 1%, the bubble-induced pseudo turbulence could be well estimated by the potential flow model, and above the critical void fraction α_c, the turbulence was strongly amplified by the hydrodynamic interactions between the bubbles and also the background turbulence. The DNS study [7.14] showed a large difference from the prediction by potential flow model.

This part focuses on the question of how much turbulent energy could be induced by the bubbles. The turbulence databases shown in Chapter 2 will be adopted. For the turbulent bubbly flow in the ducts, the wall-induced turbulence t_{kw} and the bubble-induced turbulence t_{kb} are coupled with each other. Therefore, the knowledge of both the solely wall-induced turbulence and the solely bubble-induced turbulence are required to understand the final turbulent characteristics therein. For the solely wall-induced turbulence, numerous researchers has been carried out for the single-phase flow, based on which we reached a comprehensive understanding. However, for the solely bubble-induced turbulence, there are still very few studies except the experiments by Lance and Bataille about the uniform bubbly flow for the lower void fractions lower than 3% [7.9]. For cases with larger void fraction, the solely bubble-induced turbulence is different due to the stronger effect of the bubble-bubble interaction. To quantify the solely bubble-induced turbulence for a wider range of void fraction, the recently established experimental database of the bubbly flow in the ducts will be used and

analyzed in the following. Firstly the comparison between the bubble-induced turbulence t_{kb} and wall-induced turbulence t_{kw} will be carried out to understand the role of the bubble-induced turbulence. After that, the relations between the bubble-induced turbulence t_{kb}, the void fraction α and wall-induced turbulence t_{kw} will be considered. Finally, the interaction between bubble-induced turbulence and wall induced turbulence will be discussed based on their relations.

The role of the bubble-induced turbulence here is considered by the ratio of the turbulent kinetic energies between the turbulent bubbly flow t_{kt} and the single-phase flow t_{ks} under the same flow rate according to existed data, which were shown in Figs. 7.1-7.5 for the circular pipes with small and large diameter and also the noncircular ducts. Larger ratio t_{kt} / t_{ks} indicates stronger role of the bubble-induced turbulence. Here, generally two-sets of the cases with closer liquid flow rates are given for simplicity and comparison. Similar tendency could be found for the other cases. As shown from Figs. 7.1-7.5, the following trends could be obtained:

(i) Void fraction and liquid flow rate effect

The ratio t_{kt} / t_{ks} increases with the increase of the void fraction for the same liquid flow rate, and shows larger for cases with the smaller liquid flow rate for the similar void fraction. It is easy to understand this observation because of the increase of the bubble-induced turbulence with increasing the void fraction and the decrease of the wall-induced turbulence with decreasing the liquid flow rate.

(ii) Turbulence enhancement or reduction

Generally, the ratio t_{kt} / t_{ks} is greater than 1 especially in the duct center of the large duct indicating the turbulence enhancement by the bubbles, except several cases in the small circular pipe with very small gas flow rate and high liquid flow rate where the turbulence reduction could be observed in the near wall region such as J_l=1.03*m/s* and $X\%$=0.0085 in Serizawa's experimental database [7.2-7.3]. The turbulence reduction under these cases was discussed in [7.8] and will be considered later in this chapter.

(iii) Lateral distribution

Except two cases under J_l=0.491m/s in Hibiki's experimental database [7.15] which were in the transition regime, generally the ratio t_{kt} / t_{ks} for the turbulent bubbly flow decrease from the duct center to the wall even with much higher void fraction near the wall. It indicates the bubble-induced turbulence played a dominated role in the duct center as compared with the near wall region. The exception of the two cases mentioned above might be attributed to the bubble coalescence and breakup which induced another mechanism for the turbulence generation and will not be considered here.

(iv) Geometry effect

Fig. 7.6(a) summarizes the ratio $<ww>_{tc}/<ww>_{sc}$ of the axial turbulent intensity for the turbulent bubbly flow in the duct center $<ww>_{tc}$ to that of the single-phase turbulence $<ww>_{sc}$ for different flow conditions and ducts. It shows the larger ratio t_{kt}/t_{ks} could be observed for the larger duct size D_H. Fig. 7.6(b) shows the contour lines for the flow conditions J_l and J_g under which the ratio $<ww>_{tc}/<ww>_{sc}$ is around 5 and 25, respectively. Here the flow conditions on the contour lines were summarized and interpolated from the corresponding references for different ducts. It was found that the contour lines for the small circular pipes from Hibiki's database [7.15] lie in the upper region of that for the large ducts from Shakwat's [7.13] and Sun's database [7.16]. For the Serizawa's database [7.2] in the small circular pipe, the critical conditions for $<ww>_{tc}/<ww>_{sc} \approx$ 25 were not reached even in the slug regime. It means that under the same flow condition, the ratio $<ww>_{tc}/<ww>_{sc}$ in the larger ducts is larger than that in the small ducts. For example, for the case of J_l ≈1.0m/s and J_g≈0.1m/s as shown in Fig.7.6(b), $<ww>_{tc}/<ww>_{sc}$ ≈10 in the large ducts while $<ww>_{tc}/<ww>_{sc}$ ≈5 in the small ducts. Therefore, the bubble-induced turbulence played a more dominate role in the larger ducts especially in the core region. The following two factors might be responsible for this observation (a) more space for the bubble's horizontal deformation and wake development behind the bubbles for the large ducts which induced stronger turbulence; (b) less effect from the wall-induced turbulence for the large ducts.

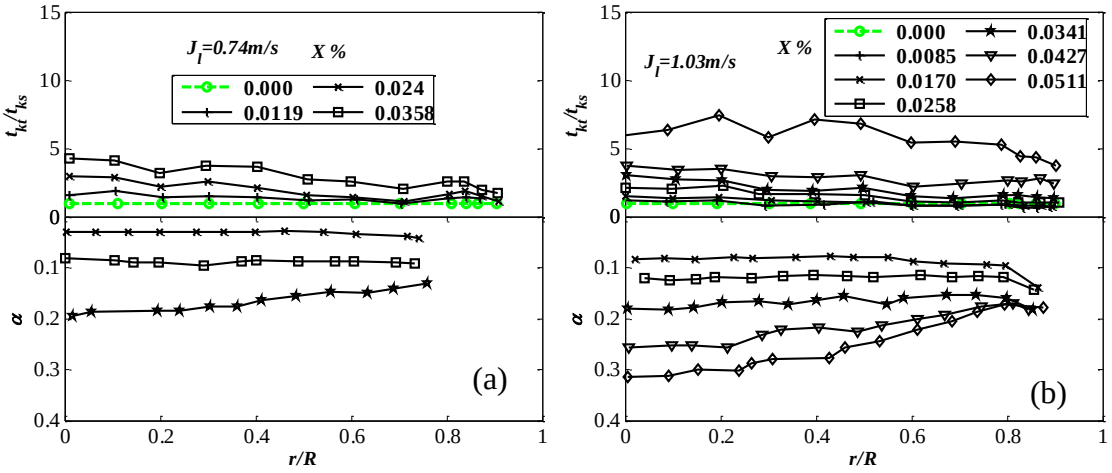

Fig. 7.1 Lateral distributions of the ratio of the turbulent kinetic energies between t_{kt} and t_{ks} in the small circular pipe with D_H=60mm based on Serizawa's experimental database under (a) J_l =0.74m/s and (b) J_l =1.03m/s [7.2].

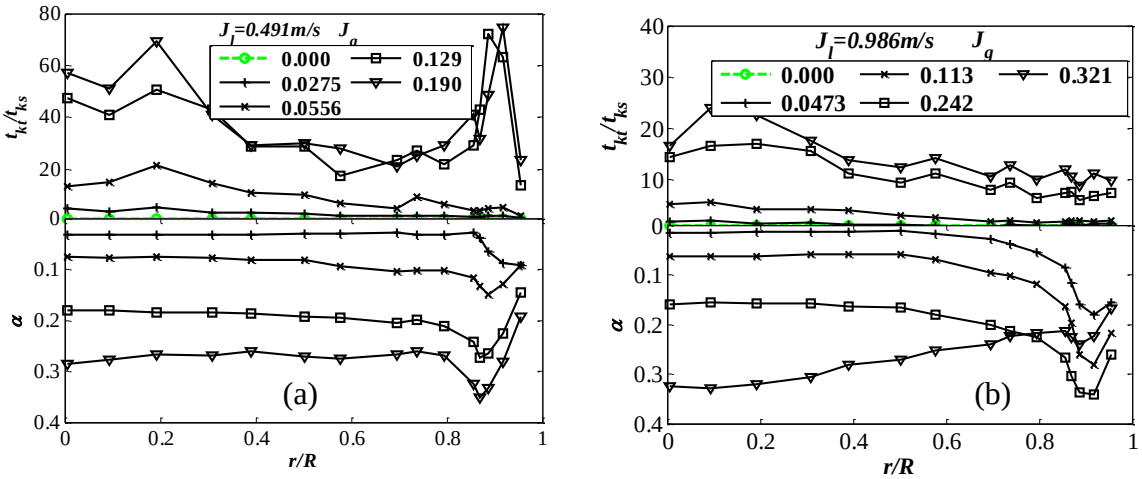

Fig. 7.2 Lateral distributions of the ratio of the turbulent kinetic energies between t_{kt} and t_{ks} in the small circular pipe with D_H=50.8mm based on Hibiki's experimental database: under (a) J_l =0.491m/s and (b) J_l =0.986m/s [7.15].

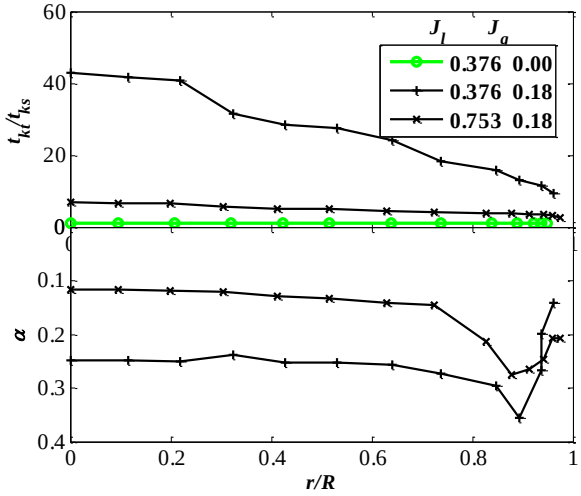

Fig. 7.3 Lateral distributions of the ratio of the turbulent kinetic energies between t_{kt} and t_{ks} in the small circular pipe with D_H=60*mm* based on Liu's experimental database [7.7].

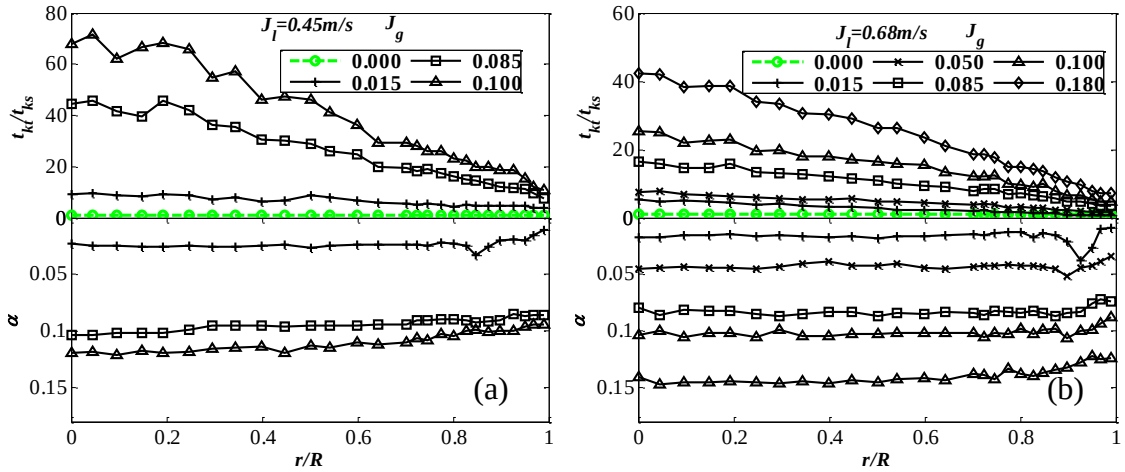

Fig. 7.4 Lateral distributions of the ratio of the turbulent kinetic energies between t_{kt} and t_{ks} in the large circular pipe with D_H=200*mm* based on Shakwat's experimental database under (a) J_l =0.45*m/s* and (b) J_l =0.68*m/s* [7.13].

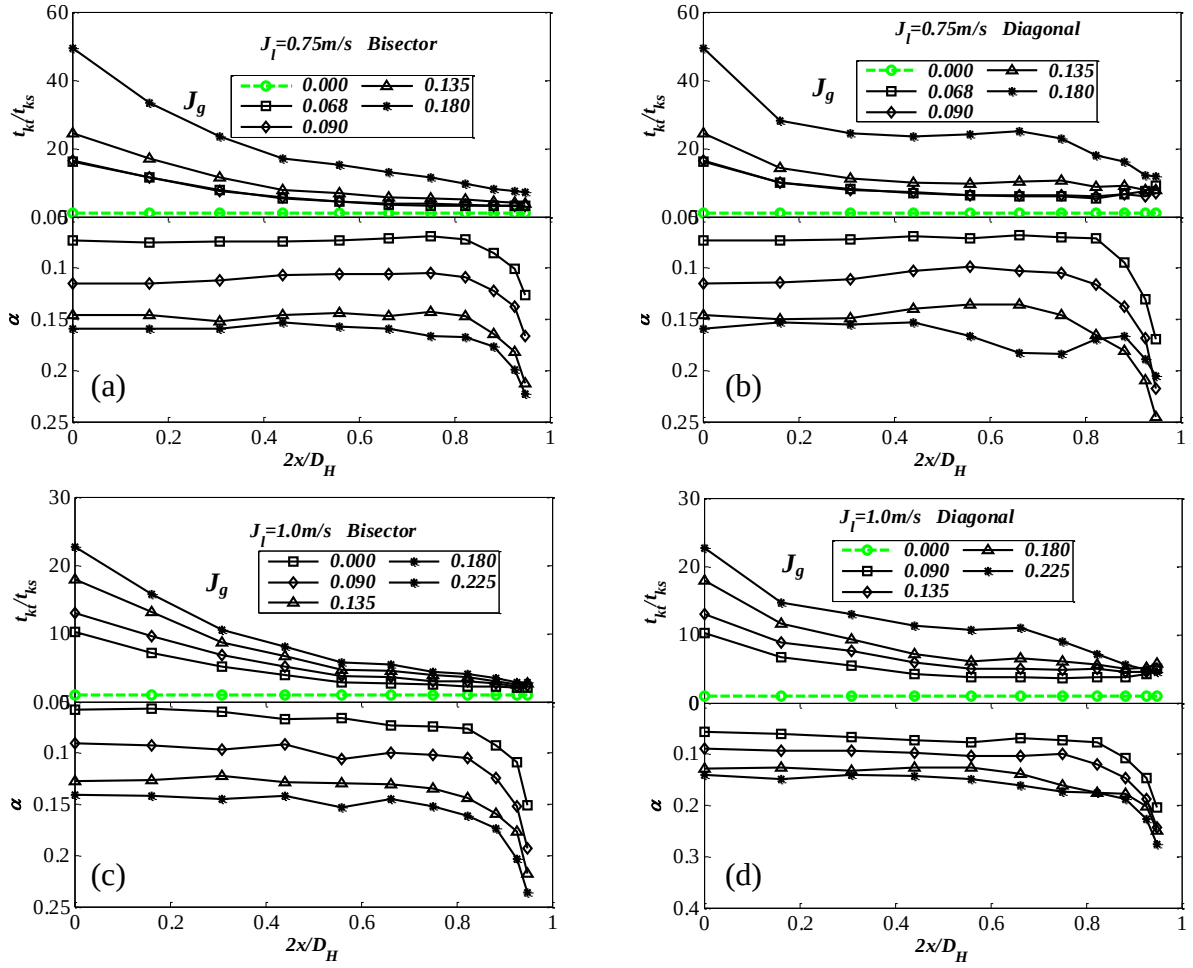

Fig. 7.5 Lateral distributions of the ratio of the turbulent kinetic energies between t_{kt} and t_{ks} in the large circular pipe with D_H=136mm based on Sun's experimental database: under J_l =0.75m/s (a) along the bisector line; (b) along the diagonal line; under J_l =1.0m/s (c) along the bisector line; (b) along the diagonal line [7.16].

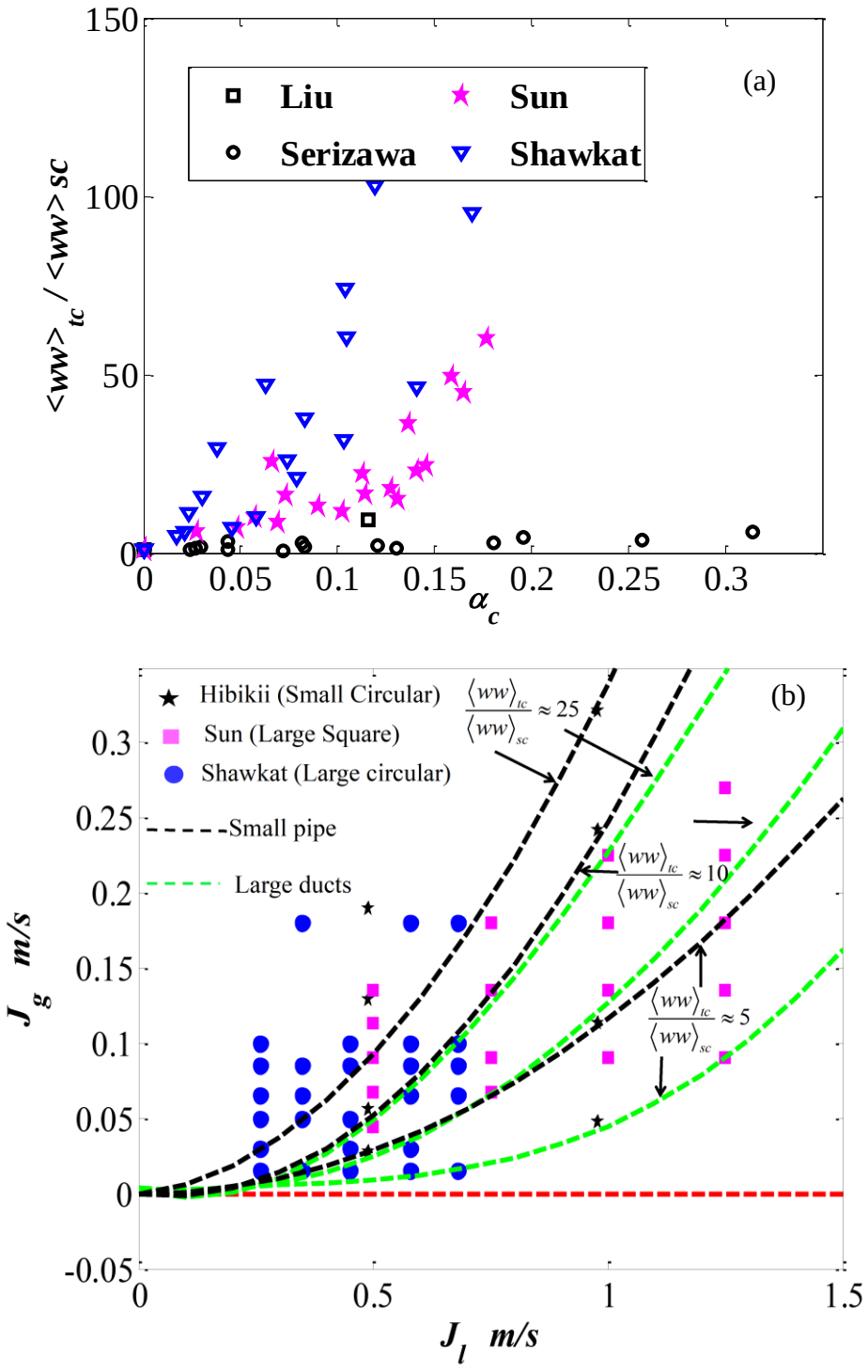

Fig. 7.6 (a) The relation between the ratio $<ww>_{tc}/<ww>_{sc}$ and the local void fraction α in the duct center for different ducts; (b) The contour lines for the flow conditions J_l and J_g when $<ww>_{tc}/<ww>_{sc} \approx 5, 10, 25$.

7.2.1 Bubble-induced turbulence at the duct center

Based on the above analysis, in the following the turbulent intensities in the duct center will be mainly considered and analyzed especially in the large ducts where the bubble-induced turbulence dominates the local turbulence in order to quantify and model the bubble-induced turbulence. Here, we consider the turbulence in the duct center as the solely bubble-induced turbulence since therein the shear-induced turbulence is very weak due to the flat liquid phase velocity profile or small liquid phase velocity shear. In addition, we also neglect the horizontal diffusion and convective effect which are extremely weak in the core region. In other words, the turbulence in the core region was mainly induced because of the bubble agitation.

Fig. 7.7 shows the relation between the axial turbulent intensities $<ww>_c$ and the local void fraction α in the duct center based on the above experimental databases. Besides, three correlations for the bubble-induced turbulence were also shown in Fig. 7.7, which are $0.2\alpha W_r^2$ proposed by [7.9, 7.11] based on the potential theory and experimental results for α < 1%, αW_r^2 proposed by [7.14] by fitting their DNS results for α<24%, and $0.72\alpha^{1.6}$ proposed by [7.5] by fitting their experimental results including the near wall region for α>1.3%. W_r is the relative velocity between the bubbles and liquid phase and W_r=0.23*m/s* (the terminal velocity) in the above correlations. As shown from Fig. 7.7(a), the following trends could be obtained:

(i) Duct geometry effect

Under the same void fraction, the bubble-induced turbulence is stronger in the large ducts as compared to that in the small circular pipes. The discrepancy increases with the increase of the void fraction. Similarly it could also be attributed to the suppression of the bubble's horizontal deformation and wake development in the small circular pipes.

(ii) Liquid flow rate effect

The turbulence for the turbulent bubbly flow in the large ducts shows much more scattered than that in the small circular pipes. The scattering in the large ducts was found to be related with different liquid flow rates, which is consistent with [7.9]. Fig.7.7 (b) shows the ratio $<ww>/W_l$ for the above cases. It was found that after dividing by the local liquid velocity W_l or Reynolds number Re_l, the scattering could be significantly improved especially in the large duct. In addition, based on $<ww>/W_l$ the dependence of the turbulence on the duct size could be clearly shown especially for the cases with α>5%. The deviation for further higher void fraction could be attributed to that the flow was in the transition regime where bubble-coalescence is needed to be considered. The ratio $<ww>/W_l$ shows linear almost linear increase with the void fraction α, where the slope should be determined by the duct size D_H, the bubble size D_B, the bubble deformation E, and the relative velocity of the bubbles W_r. However, how it relates to these parameters, it still needs further study in the future.

(iii) Correlation validation of $0.2\alpha W_r^2$

Generally, the bubble-induced turbulence is larger than the predictions by $0.2\alpha W_r^2$ especially in the large ducts, which indicates the important role of the wake behind the bubbles to the turbulence generation. However, in the small circular pipe, the discrepancy between the potential theory and experimental measurements is apparently smaller than that in the larger ducts. It is noticed that in the two-fluid models proposed by Lahey [7.17], Bertodano *et al.* [7.18], Politano *et al.* [7.19], and Hosokawa and Tomiyama [7.20], the bubble-induced turbulence was predicted by this potential theory and validated based on the experimental database in the small ducts. The predictions therein were basically in consistent with the experimental measurements. However, for the large pipes the prediction shows larger discrepancy, and the discrepancy increases with the void fraction α. Therefore, the new model considering the bubble-induced wake and bubble deformation is required for the turbulent bubbly flow in the large ducts for more accurate turbulence prediction therein.

(iv) Correlation validation of αW_r^2

The turbulence because of the wake behind bubbles was included in the correlation αW_r^2 [7.14] by fitting their DNS results with tens of the bubbles in a limited domain. The prediction shows larger than the experimental measurements in the small circular pipes but still smaller than that in the larger circular and noncircular ducts, which might be attributed to the limited bubble number and computational domain.

(v) Correlation validation of $0.72\alpha^{1.6}$

The correlation $0.72\alpha^{1.6}$ was proposed in [7.5] by directly extracting the wall-induced single-phase turbulence from the total turbulence of the turbulent bubbly flow even the whole flow region. Though the prediction shows closer to the experimental results in the large ducts, it is lack of the physical considerations and the scattering phenomenon of the turbulence for different liquid flow rates could not be predicted.

In addition, all the above correlations are independent of the bubble size and deformation which played important roles in the bubble-induced turbulence. It made the predictions deviate more from the experimental measurements in the large ducts.

In [7.21], based on the plausible assumption that all the energy lost because of the drag resistance $\mathbf{F}_L^{\text{drag}}$ on the bubbles was converted to the turbulent kinetic energy in the bubble wake, the additional source term S_L^B in the liquid phase turbulent kinetic energy t_k transport equation was proposed for the bubbles contribution as follows:

$$S_L^B = \mathbf{F}_L^{\text{drag}} \cdot \mathbf{V}_r \,. \tag{7.1}$$

However, it is notable that for the turbulent bubbly flow the work done by the drag force $\mathbf{F}_L^{\text{drag}}$ contributes not only to the turbulent kinetic energy t_k but also the mean kinetic energy t_M, where the total energy in the flow is $t_{\text{total}} = t_{\text{M}} + t_{\text{k}}$. Hence, in this way the double computation of the mean energy occurs in the governing equations

of the bubbly flow. This was mentioned and discussed by Yokomine *et al.* for the turbulent flow with the dispersed solid particles [7.22]. Therein the double computation was extracted from the source term by modifying the drag coefficient as follows:

$$C_D^W = C_D - C_{D,Stokes} \tag{7.2}$$

where $C_{D,Stokes}$ is the drag coefficient for the dispersed particles based on the Stokes flow.

In the following, this method proposed by Yokomine *et al.* [7.22] will be adopted. For simplicity, the energy balance for the liquid phase turbulence kinetic energy only at the duct center will only be considered where the shear contribution, and horizontal diffusion and convection could be neglected. Therein, the turbulent kinetic energy t_{kc} was determined by the local bubble contribution S_L^B and dissipation rate ε_L as follows.

$$S_L^B - \varepsilon_L = \mathbf{F}_L^{\text{drag}} \cdot \mathbf{V}_r - \varepsilon_L = 0. \tag{7.3}$$

For the turbulent bubbly flow, the dissipation rate ε_L is not only related with the eddy dissipation due to viscosity ε_υ similar to the single-phase turbulent flow but also the dispersed bubbles ε_B due to the bubble deformation, the capture of the bubbles by eddies and also the collisions between the bubbles and eddies. The contribution of the dispersed particles to the dissipation rate ε_L is related with the characteristic length and time of both the dispersed bubbles and eddies, which was discussed in [7.22]. However, the case with the large light particles such as large bubbles was not considered in detail because of its complexity such as the deformability, which still needs further studies in the future. Here, as an initial step the dissipation rate ε_L will be considered based on the effective viscosity υ_t in which for the turbulent bubbly flow the bubble contribution is needed to be considered:

$$\varepsilon_L = C_\mu \frac{t_k^2}{\upsilon_t} \tag{7.4}$$

where C_μ is the constant and around 0.09 for the single-phase turbulent flow.

Substituting Eq. (7.4) into Eq. (7.3), it is obtained that

$$t_k = \sqrt{\frac{\upsilon_t}{C_\mu}\mathbf{F}_L^{\text{drag}} \cdot \mathbf{V}_r} \ . \tag{7.5}$$

At the duct center, the eddy viscosity υ_t induced by the bubbles is considered by the model proposed by Sato and Sadatomi [7.23],

$$\upsilon_t = \alpha C_{\mu b} D_B w_{r\infty} \tag{7.6}$$

Substituting Eqs. (1.4), (7.2) and (7.6) into Eq. (7.5), the turbulent kinetic energy t_k in the liquid phase could be determined as follows:

$$t_k = \alpha |W_r|^2 \sqrt{\frac{C_D - C_{D,Stokes}}{C_\mu} C_{\mu b}} \tag{7.7}$$

where $C_{D,Stokes}$ was determined by $C_{D,\text{Stokes}} = 24/\text{Re}$; C_μ is chosen to be 0.09 similar to the single-phase turbulent flow; $C_{\mu b}$ is chosen to be 0.6; the correlation proposed by Tomiyama *et al.* [7.24] was used to determine drag coefficients as

$$C_D = \max\left[\min\left(\left[\frac{24}{\text{Re}_B}\left(1 + 0.15\,\text{Re}_B^{0.687}\right), \frac{72}{\text{Re}_B} \right] \right), \frac{8}{3}\frac{\text{Eo}}{\text{Eo}+4} \right] \frac{1}{(1-\alpha)^{0.5}} \ .$$

Fig. 7.8 shows the turbulent kinetic energy t_k based on Eq. (7.7) for different bubble diameters, from which better prediction of t_k could be obtained for the turbulent bubbly flow in the large ducts. Hence, Eq. (7.7) is suggested for the turbulent bubbly flow in the large ducts. However, the effect of the bubble deformation still needs further consideration in the future.

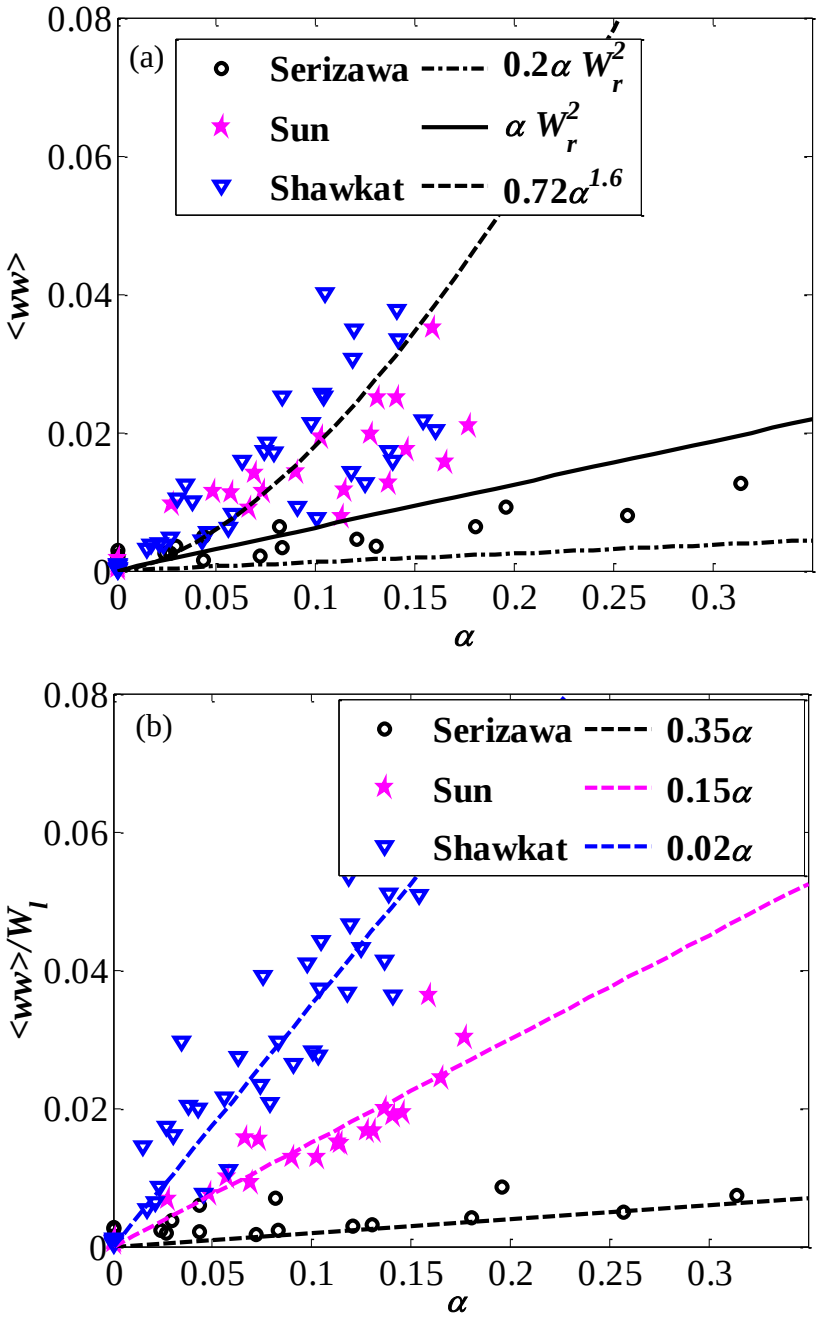

Fig. 7.7 (a) The axial turbulent intensities <*ww*> vs. the local void fraction α in the duct center; (b) <*ww*>/W_l vs. the local void fraction α in the duct center.

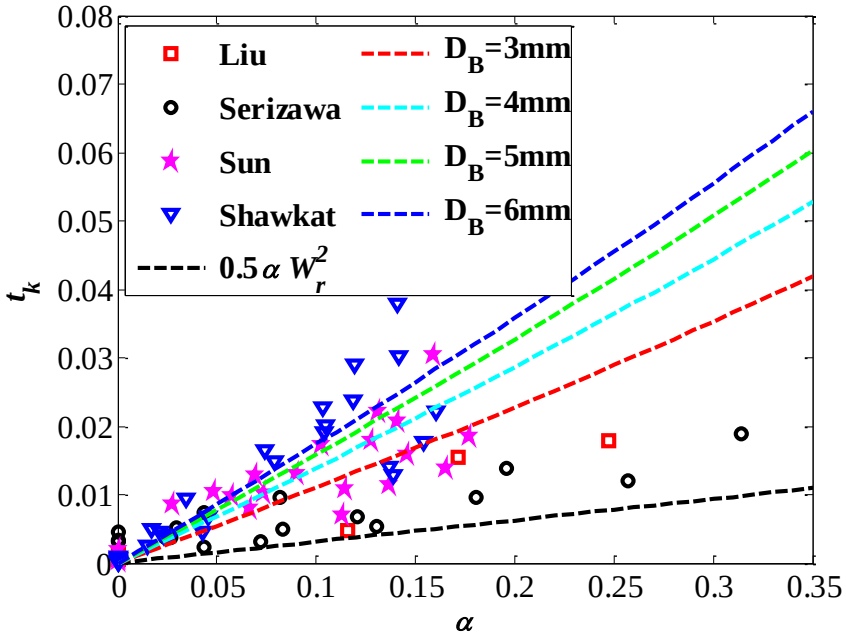

Fig. 7.8 Comparison the experimental data of the turbulent kinetic energy t_k of the liquid phase with the new correlation Eq. (7.7) for different bubble diameter at the duct center.

7.2.2 Bubble-induced and wall-induced turbulence interaction

In the near wall region, the turbulence in the liquid phase includes the wall-induced and bubble-induced. To investigate the bubble-induced turbulence, the wall-induced contribution is necessary to be extracted. However, near the wall the wall-induced turbulence could be strongly modified by the bubbles, thus it might be not suitable to directly extract the wall-induced single-phase turbulence from the total turbulence of the turbulent bubbly flow. In other words, it is very difficult to directly investigate the bubble-induced turbulence in the near wall region. In the present study, the bubble-induced turbulence and wall-induced turbulence will be investigated near the wall in an indirect way hereafter.

7.2.2.1 Wall effect on bubble-induced turbulence

As discussed in Section 7.2.1, the turbulence in the duct center could be considered solely induced by bubbles. Firstly, the ratio of the local turbulent kinetic energy t_{kt} to that in the duct center t_{kt}^{c} will be analyzed and shown in Figs. 7.9-7.13 for the circular pipes with small and large diameter and also the noncircular ducts based on the existed experimental databases. The following trends could be observed:

(1) From Figs. 7.9-7.13, except two cases under J_l=0.491m/s from Hibiki's experimental databases [7.15] in the transition regime, generally the ratio t_{kt} / t_{kt}^{c} for the single-phase turbulent flow is much larger than that for the turbulent bubbly flow even with higher void fraction near the wall, i.e.

$$\frac{t_{kw}^{S,w}}{t_{kw}^{S,c}} > \frac{t_{kw}^{B,w}+t_{kb}^{B,w}}{t_{kw}^{B,c}+t_{kb}^{B,c}} \approx \frac{t_{kw}^{B,w}+t_{kb}^{B,w}}{t_{kb}^{B,c}}. \tag{7.8}$$

where $t_{kw}^{S,w}$ and $t_{kw}^{S,c}$ are the wall-induced turbulence near the wall and in the duct center for the single-phase turbulent flow; $t_{kw}^{B,w}$ and $t_{kw}^{B,c}$ are the wall-induced turbulence near the wall and in the duct center for the turbulent bubbly flow; $t_{kb}^{B,w}$ and $t_{kb}^{B,c}$ are the bubble-induced turbulence near the wall and in the duct center for the

turbulent bubbly flow. The exceptions in the small circular pipes mentioned above might be attributed to the bubble coalescence and breakup which induced another mechanism for the turbulence generation, which will not be considered here.

Rearranging Eq. (7.7), it could be obtained that

$$\frac{t_{kw}^{B,w}}{t_{kw}^{S,w}} < \frac{t_{kb}^{B,c}}{t_{kw}^{S,c}}, \tag{7.9}$$

indicating that for the turbulent bubbly flow the modification of the wall-induced turbulence is much less than that in the duct center. In addition, from Eq. (7.8) we also have

$$\frac{t_{kw}^{B,w} + t_{kb}^{B,w}}{t_{kb}^{B,c}} \geq \frac{t_{kb}^{B,w}}{t_{kb}^{B,c}}. \tag{7.10}$$

Based on Eq. (7.10), the wall effect on the bubble-induced turbulence could be considered. Due to the non-uniform void fraction distribution, we need to know how much is the bubble-induced turbulence in the absence of the wall before in order to consider the wall effect on the bubble-induced turbulence, which will be considered by the proposed correlation Eq. (7.8) and the linear relation with the void fraction, i.e.,

$$\frac{t_{kb}^{B,w}}{t_{kb}^{B,c}} = \frac{\alpha_w}{\alpha_c}. \tag{7.11}$$

Substituting Eq. (7.11) to Eq. (7.10), it should be

$$\frac{t_{kw}^{B,w} + t_{kb}^{B,w}}{t_{kb}^{B,c}} \geq \frac{\alpha_w}{\alpha_c}. \tag{7.12}$$

Fig. 7.14 shows the comparison between the left and right hands of Eq. (7.11) based on Sun's experimental database. In contrast, it is observed that

$$\frac{t_{kb}^{B,w}}{t_{kb}^{B,c}} \leq \frac{t_{kw}^{B,w} + t_{kb}^{B,w}}{t_{kb}^{B,c}} \leq \frac{\alpha_w}{\alpha_c}, \tag{7.13}$$

indicating that comparing to the core region under the same void fraction the

bubble-induced turbulence is reduced by the wall effect. The following two mechanisms could be considered to be responsible for this observation: (a) the wall effect elongates the bubble shape; (b) the wall suppressed the bubble wake development.

The scattering in Fig. 7.14 is due to the different liquid flow rates, i.e.,

$$\frac{t_{kw}^{B,w}+t_{kb}^{B,w}}{t_{kb}^{B,c}}=F\left(\frac{\alpha_w}{\alpha_c},J_l\right). \tag{7.14}$$

Considering $F\left(\alpha_w/\alpha_c,J_l\right)=H\left(\alpha_c\right)$ as shown in Fig. 7.15(a), Fig. 7.15(b) shows comparison between $\left(t_{kw}^{B,w}+t_{kb}^{B,w}\right)/t_{kb}^{B,c}$ and α_c, in which the scattering was significantly improved. Besides, it was found that $\left(t_{kw}^{B,w}+t_{kb}^{B,w}\right)/t_{kb}^{B,c}$ linearly decreases with the increase of α_c, indicating the turbulence near the wall could be predicted by the following correlation:

$$t_{kb}^{B,w}\approx t_{kb}^{B,c}H\left(\alpha_c\right). \tag{7.15}$$

$H\left(\alpha_c\right)$ shows the suppression of the bubble-induced turbulence and is related with duct geometry and the local void fraction. It still needs further researches and verification for different cases in the future.

From Figs. 7.9-7.13, it was also observed that for the single-phase turbulent flow the ratio t_{kt}/t_{kt}^{c} is always larger than 1, since the turbulence is mainly generated near the wall and decayed to the duct center. However, it is not always true for the turbulent bubbly flow even for the cases with higher void fraction near the wall, i.e.,

$$\frac{t_{kw}^{S,w}}{t_{kw}^{S,c}}>1>\frac{t_{kw}^{B,w}+t_{kb}^{B,w}}{t_{kw}^{B,c}+t_{kb}^{B,c}}\approx\frac{t_{kw}^{B,w}+t_{kb}^{B,w}}{t_{kb}^{B,c}}\quad\text{or}\quad t_{kb}^{B,c}\left(\alpha_c\right)>t_{kw}^{B,w}+t_{kb}^{B,w}\left(\alpha_w\right). \tag{7.16}$$

For the turbulent bubbly flow in the large ducts as shown in Figs. 7.12-7.13 where the void fraction shows a flatter distribution, this tendency could be obviously observed and further confirms wall suppression of the bubble-induced turbulence. In the small circular pipe, increasing the void fraction when the near wall turbulence was dominated by the bubbles, this phenomenon could be observed as shown in Fig. 7.11.

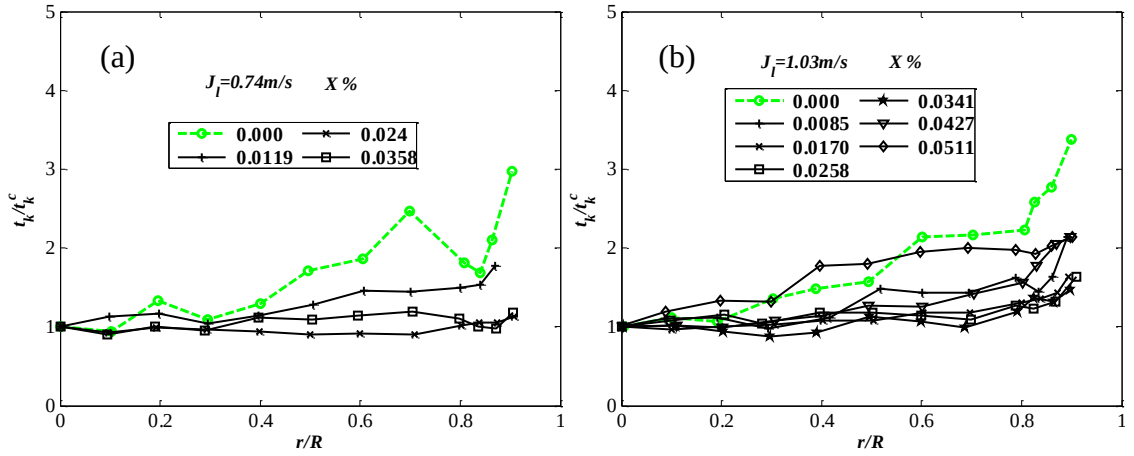

Fig. 7.9 Lateral distributions of the ratio of the local turbulent kinetic energy t_{kt} to that in the duct center t_{kt}^c in the small circular pipe with D_H=60*mm* based on Serizawa's experimental database: under (a) J_l =0.74*m/s* and (b) J_l =1.03*m/s* [7.2].

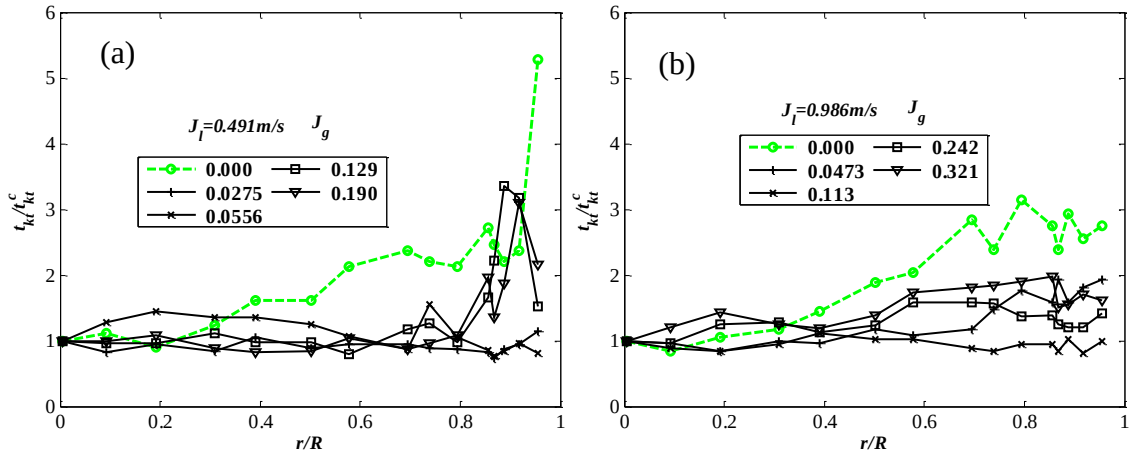

Fig. 7.10 Lateral distributions of the ratio of the local turbulent kinetic energy t_{kt} to that in the duct center t_{kt}^c in the small circular pipe with D_H=50.8*mm* under (a) J_l =0.491*m/s* and (b) J_l =0.986*m/s* based on Hibiki's experimental database [7.15].

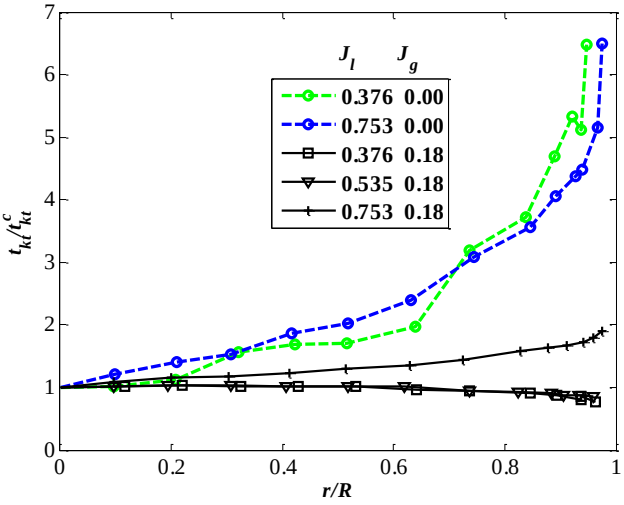

Fig. 7.11 Lateral distributions of the ratio of the local turbulent kinetic energy t_{kt} to that in the duct center t_{kt}^c in the small circular pipe with D_H=60*mm* based on Liu's experimental database [7.7].

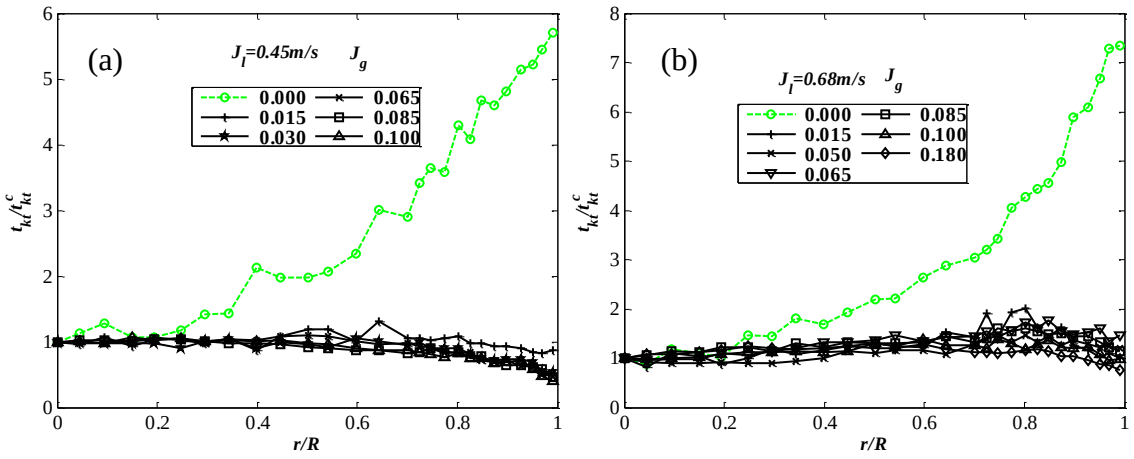

Fig. 7.12 Lateral distributions of the ratio of the local turbulent kinetic energy t_{kt} to that in the duct center t_{kt}^c in the large circular pipe with D_H=200*mm* under (a) J_l =0.45*m/s* and (b) J_l =0.68*m/s* based on Shakwat's experimental database [7.13].

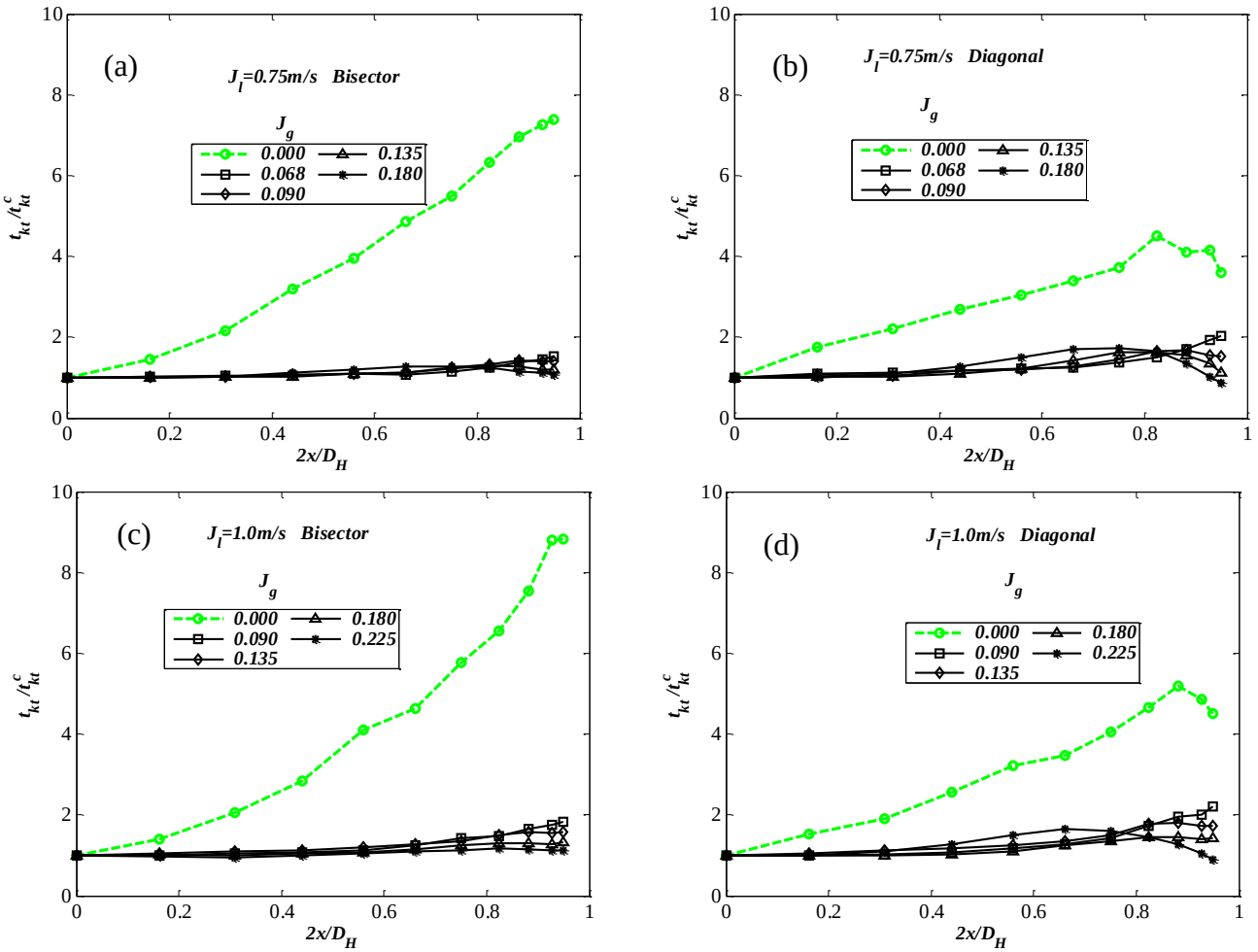

Fig. 7.13 Lateral distributions of the ratio of the local turbulent kinetic energy t_{kt} to that in the duct center t_{kt}^c in the large noncircular pipe with D_H=136mm based on Sun's experimental database: under J_l =0.75m/s (a) along the bisector line; (b) along the diagonal line; under J_l =1.0m/s (c) along the bisector line; (b) along the diagonal line [7.16].

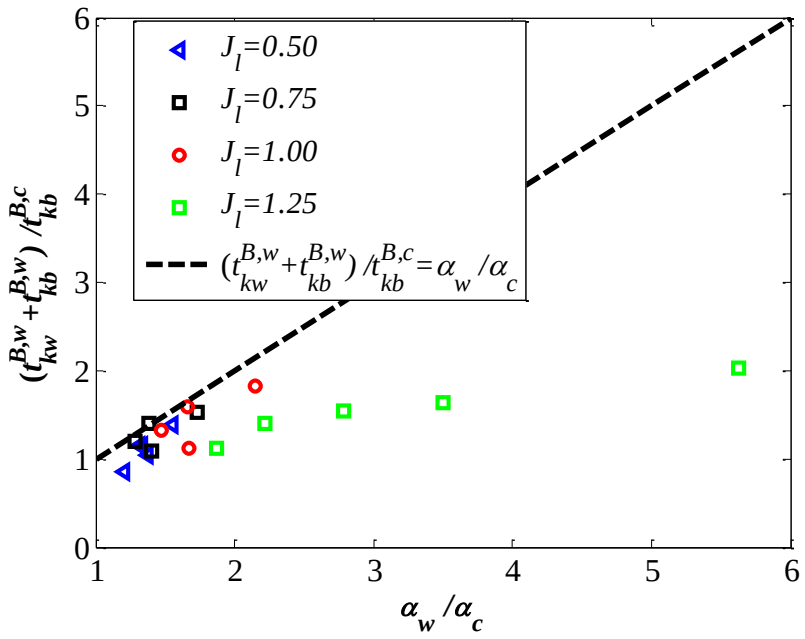

Fig. 7.14 Comparison between $\left(t_{kw}^{B,w}+t_{kb}^{B,w}\right)/t_{kb}^{B,c}$ and α_w/α_c based on Sun's experimental database [7.16].

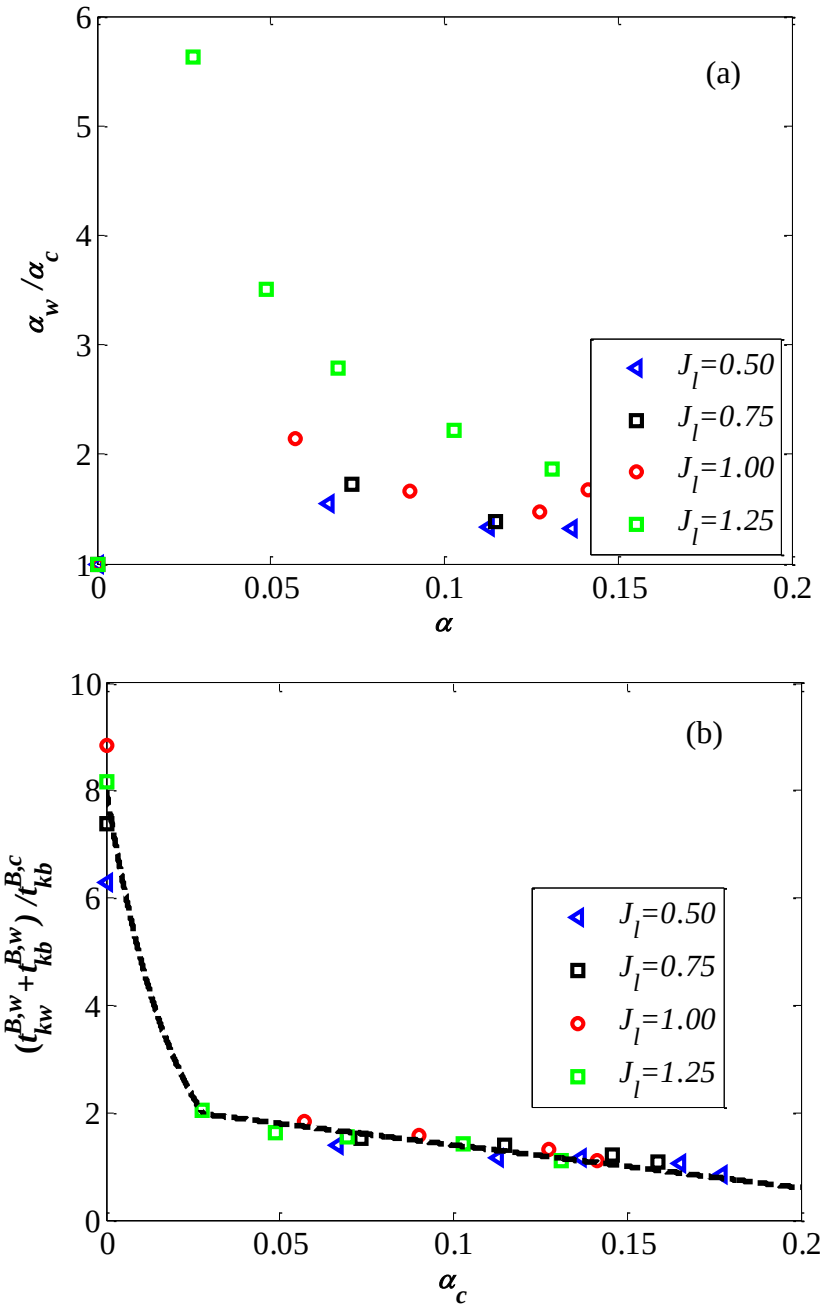

Fig. 7.15 (a) Relation between α_w / α_c and α_c; (b) Relation between $\left(t_{kw}^{B,w}+t_{kb}^{B,w}\right)/t_{kb}^{B,c}$ and α_c based on Sun's experimental database [7.16].

7.2.2.2 Bubble effect on wall-induced turbulence

It is difficult to consider the bubble effect on wall-induced turbulence near the wall coupling with the modification of the bubble-induced turbulence by the wall effect. As compared to the single-phase turbulent flow, generally the turbulence in the liquid phase increases with the void fraction for the turbulent bubbly flow, the tendency of which is shown in Fig. 7.16. For cases with low void fraction, the turbulence reduction in the liquid phase was found as compared to the single-phase turbulent flow [7.8]. Fig.7.17 shows the experimental conditions under which turbulence reduction in the liquid phase was observed. Hereafter, a simple criterion for turbulent reduction will be considered in the turbulent bubbly flow.

For the case with the turbulence reduction in the liquid phase, we have

$$t_{kw}^{B,w} + t_{kb}^{B,w}\left(\alpha_w\right) < t_{kw}^{S,w}. \tag{7.17}$$

As for the bubble-induced turbulence, though it was suppressed by the wall effect, it should be stronger than that the pseudo-turbulence based on the potential theory, i.e.,

$$t_{kb}^{B,w}\left(\alpha_w\right) > \frac{1}{2}\alpha_w W_R^2. \tag{7.18}$$

Substituting Eq. (7.18) to Eq. (7.17), we have

$$t_{kw}^{B,w} < t_{kw}^{S,w} - \frac{1}{2}\alpha_w W_R^2. \tag{7.19}$$

Based on Eq. (7.19), the critical void fraction near the wall could be obtained as $\alpha_{calc} = 2t_{kw}^{S,w}/W_R^2$. It indicates that the turbulent enhancement will occur if $\alpha_w > 2t_{kw}^{S,w}/W_R^2$ and the turbulent reduction is only possible to occur if $\alpha_w < 2t_{kw}^{S,w}/W_R^2$. Fig.7.18 shows comparison the experimental measured void fraction and the calculated void fraction based on $\alpha_{calc} = 2t_{kw}^{S,w}/W_R^2$ near the wall for the cases including turbulence enhancement and reduction. Since it is lack of the experimental database of

the void fraction and near wall turbulence, only the data from Shakwat *et al.* [7.13] and Sun [7.16] were shown, based on which the above consideration was confirmed. Moreover, it explains the reason why the turbulence reduction could occur under higher void fraction for larger liquid flow rate but lower void fraction for smaller liquid flow rate.

As for the mechanism for the turbulence reduction near the wall under certain conditions, in [7.8] it was attributed to the following two effects due to the bubbles: (1) large velocity fluctuations gradient near the bubble interface which increases the turbulent energy dissipation; (2) energy dumping effect due to the bubble deformation. Here, another two mechanisms responsible for the reduction of the wall-induced turbulence in the turbulent bubbly flow are proposed as shown in Fig. 7.19.

(i) Flow acceleration laminarization

As shown in Fig. 7.19(a), due to the formation of the bubble layer near the wall, the liquid flow was confined between the wall and the bubble layer, which laminarized the flow due to the local flow acceleration due to the bubbles. However, it still needs further experimental measurement including the velocity and turbulence in the inner layer to confirm the above points.

(ii) Suppression of "bursting event" of the coherent structures

For the single-phase flow, the turbulence generation is mainly due to the "bursting event" of the coherent structures near the wall as shown in shown in Fig. 7.19(b). However, the presence of the bubbles whose size is on the similar order of the coherent structures broke these structures, thus suppressed the source of the wall-induced turbulence.

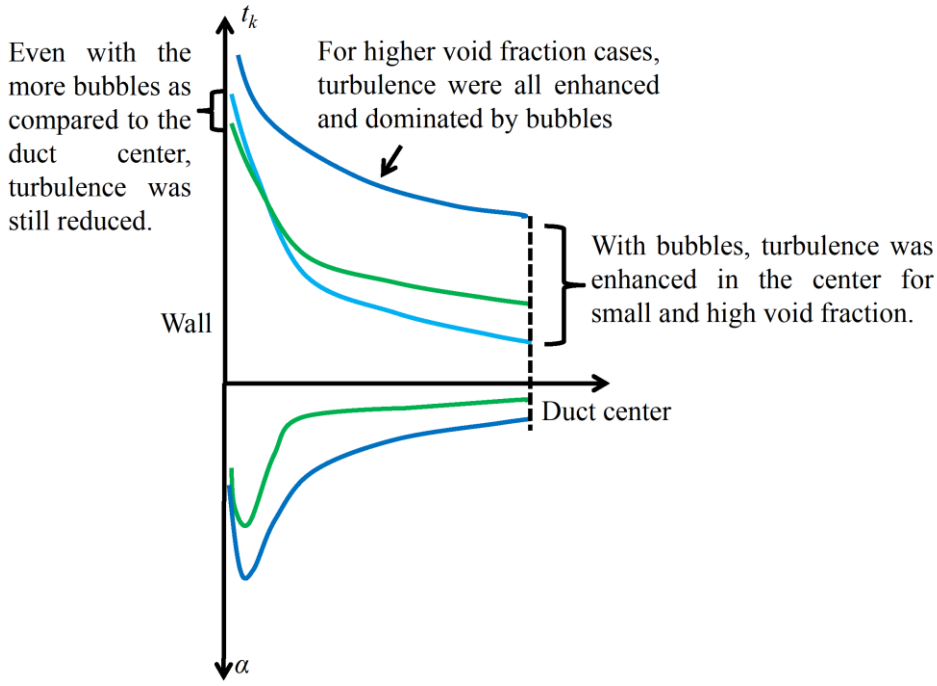

Fig. 7.16 Schematic diagram of the relation between the turbulence in the liquid phase and the void fraction for the turbulent bubbly flow.

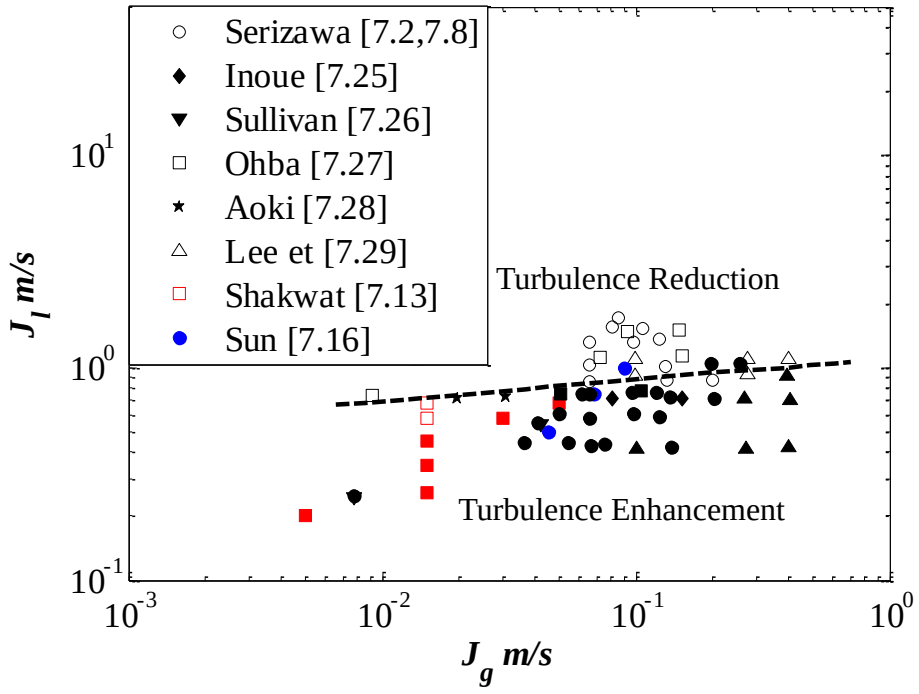

Fig. 7.17 Experimental conditions with turbulence suppression and enhancement in the liquid phase from [7.8].

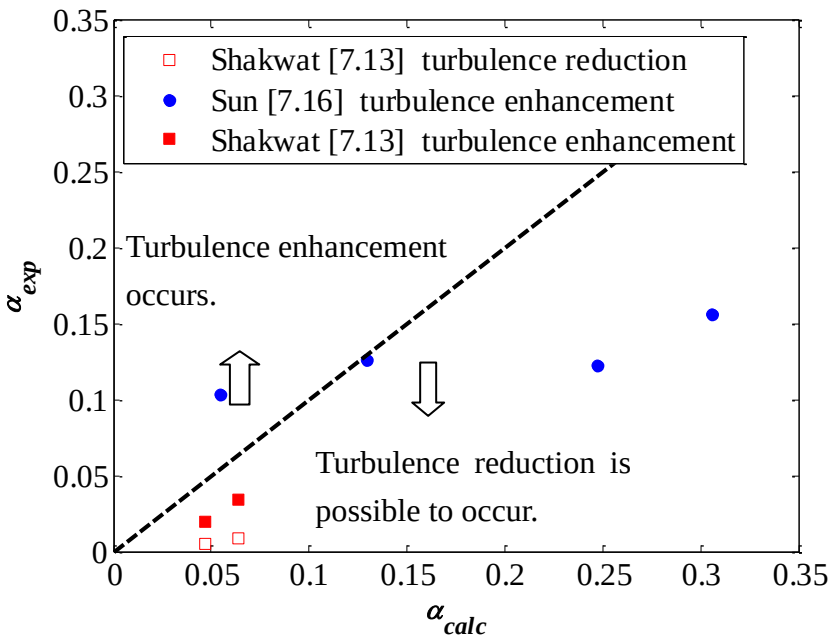

Fig. 7.18 Comparison the experimental measured void fraction and the calculated void fraction based on $\alpha_{calc} = 2t_{kw}^{S,w} / W_R^2$ near the wall.

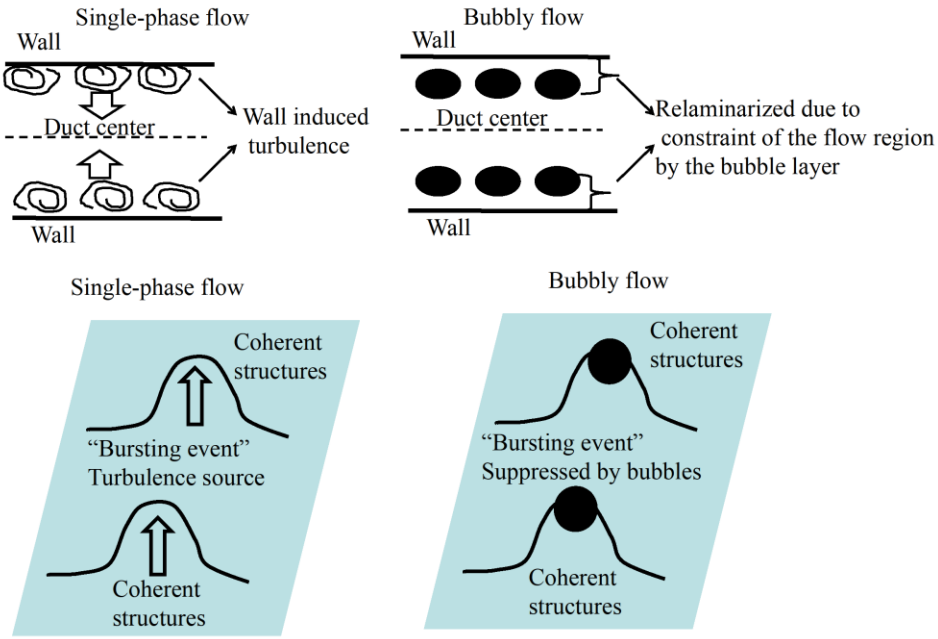

Fig. 7.19 Schematic diagram of the mechanism for the turbulence suppression.

7.3 Turbulence anisotropy in turbulent bubbly flow

As mentioned in Chapter 1, so far there are very few detailed discussions on the turbulence anisotropy of the turbulent bubbly flow, based on which the qualitative effects of the bubbles on the turbulence anisotropy are still contradictory [7.6, 7.9, 7.30-7.31]. Therefore, how the bubbles affect turbulence anisotropy and how to model turbulence anisotropy are still two open questions. This section is aimed at these two topics. Firstly, the bubble effects on turbulence anisotropy will be analyzed in the liquid phase based on the currently established database for bubbly flows in circular and noncircular ducts. According to the analysis, the suggestions on the future model of the turbulence anisotropy will be given then.

7.3.1 Bubble effects on turbulence anisotropy in liquid phase

Firstly, the turbulence anisotropy tensor **b** was defined to show the strength of turbulence anisotropy as follows:

$$\mathbf{b}=\begin{bmatrix} \overline{uu}/(2t_k)-1/3 & \overline{uv}/(2t_k) & \overline{uw}/(2t_k) \\ \overline{uv}/(2t_k) & \overline{vv}/(2t_k)-1/3 & \overline{vw}/(2t_k) \\ \overline{uw}/(2t_k) & \overline{vw}/(2t_k) & \overline{ww}/(2t_k)-1/3 \end{bmatrix}. \tag{7.20}$$

where $b_{11}+ b_{22}+ b_{33}=0$; for the isotropic turbulence, **b**=0. Here, the normal components b_{11}, b_{22}, and b_{33} will be focused on. The deviation from 0 shows the strength of the turbulence anisotropy.

Figs. 7.20-7.24 show b_{11}, b_{22}, and b_{33} calculated based on the current database for the circular pipes with small and large diameter and the noncircular ducts. The following trends could be observed:

(1) For the single-phase turbulent flow, the turbulence anisotropy increase from the duct center to the near wall region, due to the high velocity gradient and the wall suppression on the turbulent wall-normal

components in the near wall region.

(2) For the turbulent bubbly flow, as shown in Fig. 7.20 and Fig. 7.23, Serizawa's experiments [7.2] in the smaller circular pipes and Shakwat's experiments [7.13] with lower gas flow rates in the large circular pipe showed the introduction of the bubbles didn't alter the turbulent isotropy or made the turbulence more isotropic in the whole cross section. However, as shown in Fig. 7.21 and 7.22, experiments of Wang *et al.* [7.6] and Liu and Bankoff [7.7] in the smaller circular pipes showed that the presence of the bubbles made the turbulence more anisotropic in the core region but more isotropic in the near wall region. Similar results were also obtained for the turbulent bubbly flow in the large circular pipe based on Shakwat's experiments [7.13] with the higher gas flow rates and in the large non-circular duct based on Sun's experiments [7.16].

(3) For the cases as shown in Figs. 7.21-7.24 in which bubbles increased the turbulence anisotropy, in the core region the anisotropy tensor was found to reach a constant value to some extent. For example $b_{11} \approx 0.22$ and $b_{33} \approx -0.11$ where b_{11} and b_{33} are in the axial and lateral direction, respectively.

In order to understand the above observations and model the bubble effects on the turbulence anisotropy in liquid phase, it is necessary to discuss the following parameters' effects due to their crucial importance to the bubble-induced turbulence including: (a) void faction; (b) duct geometry; (c) bubble size; (d) bubble relative velocity; (e) bubble deformation.

Firstly, the void fraction effect is considered in the duct center, where the turbulence might be dominated by bubbles. Fig.7.25 shows the relation between the turbulence anisotropy tensor b_{11} and b_{33} and the local void fraction α in the duct center

for different ducts. Based on the potential theory [7.11], the anisotropy tensor of the bubble-induced turbulence is as follows and shown in Fig. 7.25 as a reference:

$$\mathbf{b} = \begin{bmatrix} -1/30 & 0 & 0 \\ 0 & -1/30 & 0 \\ 0 & 0 & 1/15 \end{bmatrix}. \tag{7.21}$$

For the turbulent bubbly flow in the large ducts based on Shakwat's [7.13] and Sun's [7.16] experiments, it could be obtained that the turbulence is more isotropic for the small void say less than 5% and the anisotropy tensor **b** was closer to the value predicted based on the potential theory in Eq. (7.20), which is in consistent with that observed by Lance [7.9]. For the higher void fraction, the turbulence is anisotropic and the anisotropy tensor **b** reaches a constant value independent of the void fraction.

For the turbulent bubbly flow in the small circular pipes, Serizawa's data showed more isotropic turbulence closer to the potential theory and was focused in the smaller void fraction range say less than 10%. However, Wang's [7.6] and Liu's [7.7] data in the small circular pipes showed more anisotropic turbulence similar to that in the large ducts, which were focused in the larger void fraction range larger than 10%.

Therefore, how the bubble affects the turbulence anisotropy is related with the void fraction, and the turbulence anisotropy increase with the void fraction to a constant value. The tendency of the void fraction effect on the turbulence anisotropic tensor **b** obtained here is inconsistent with that in Trygovasson's DNS [7.31] results for the solely bubble-induced turbulence. In [7.31], it showed the turbulence behaves more isotropic with increase of the void fraction by comparing the results for 2%, 6%, and 12%, which might be due to the reduction of the relative velocity with increase of void fraction.

In addition, how the bubble affects the turbulence anisotropy is also related with the duct geometry. As obtained from Fig. 7.25, the critical void fraction under which the turbulence anisotropy reached to the constant value is larger for the smaller pipes. It could be attributed to the strong wall effect therein.

Next, the bubble size effect is considered in the duct center as shown in Fig. 7.26. Since there was only few database of the turbulence together with the bubble size, the rough range of the bubble size was shown in Fig. 7.26. For the current database, the bubble size D_B was around 3*mm* in the small circular pipes, and 3~6*mm* in the large ducts. It was observed from the database of the large ducts, the turbulence was more isotropic for the smaller bubble size but more anisotropic for larger bubble size. It might also explain why the critical void fraction under which the turbulence anisotropy reached to the constant value is larger for the smaller pipes, which might be due to the smaller bubble size therein.

In summary, Figs. 7.25-7.26 indicate that in the core region when the local turbulence was dominated by the bubble-induced turbulence, under high void fraction and larger bubble size the turbulence will be more anisotropic and the anisotropy tensor reaches a constant value to some extent with $b_{11} \approx 0.22$ and $b_{33} \approx -0.11$.

As for the bubble relative velocity and the bubble deformation effects, since there is very few data to identify these effects on the turbulence anisotropy, in the following it is qualitatively considered. The turbulence anisotropy in the turbulent bubbly flow could be considered to be determined by the energy production among different direction by the bubbles. For higher relative velocity the bubble-induced turbulence will be stronger and more energy will be injected to the axial direction, which could make the turbulence more anisotropic. In addition, Trygovasson's DNSs [7.31] results showed that as compared to the spherical bubbles, the flow with deformed bubbles behaves more anisotropic because of the capture of the deformed bubbles in the formed bubble wake.

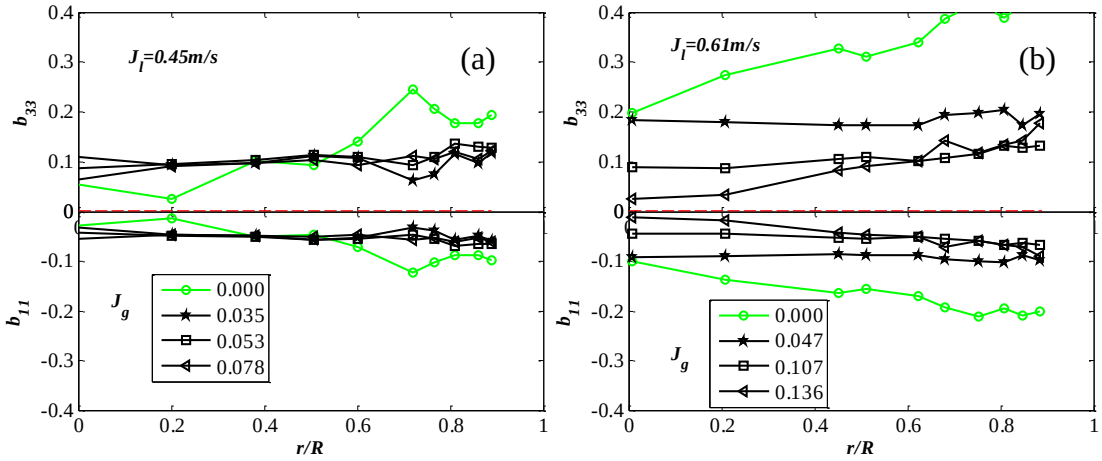

Fig. 7.20 Lateral distributions of the turbulence anisotropy tensor b_{11} and b_{33} in the small circular pipe with D_H=60*mm* based on Serizawa's experimental database: under (a) J_l =0.45*m/s* and (b) J_l =0.61*m/s* [7.2].

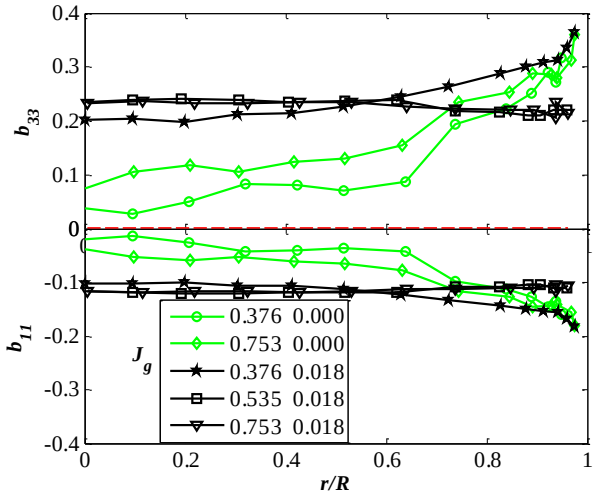

Fig. 7.21 Lateral distributions of the turbulence anisotropy tensor b_{11} and b_{33} in the small circular pipe with D_H=57.2*mm* based on Liu's experimental database [7.7].

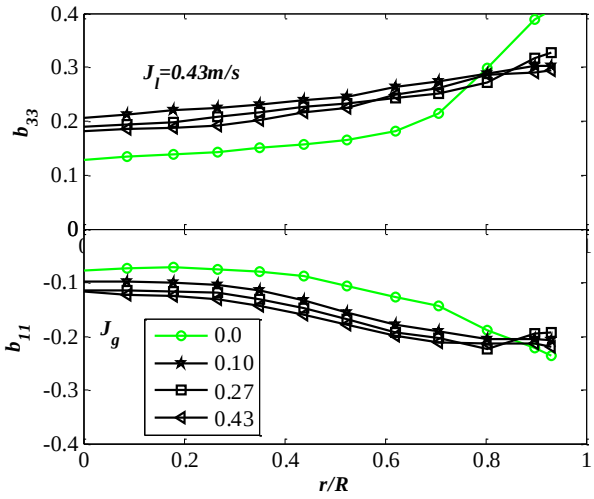

Fig. 7.22 Lateral distributions of the turbulence anisotropy tensor b_{11} and b_{33} in the small circular pipe with D_H=57.15*mm* based on Wang's experimental database [7.6].

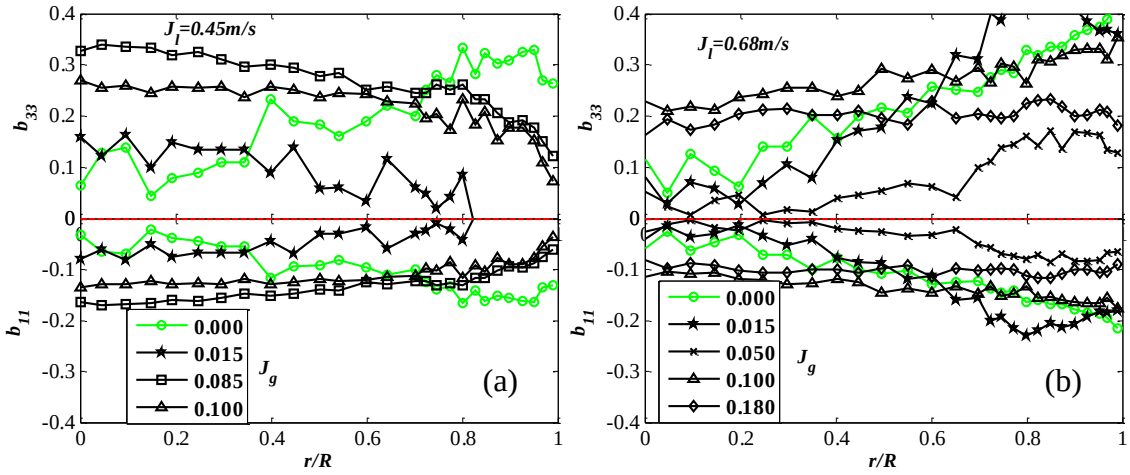

Fig. 7.23 Lateral distributions of the turbulence anisotropy tensor b_{11} and b_{33} in the large circular pipe with D_H=200*mm* based on Shakwat's experimental database: under (a) J_l =0.45*m/s* and (b) J_l =0.68*m/s* [7.13].

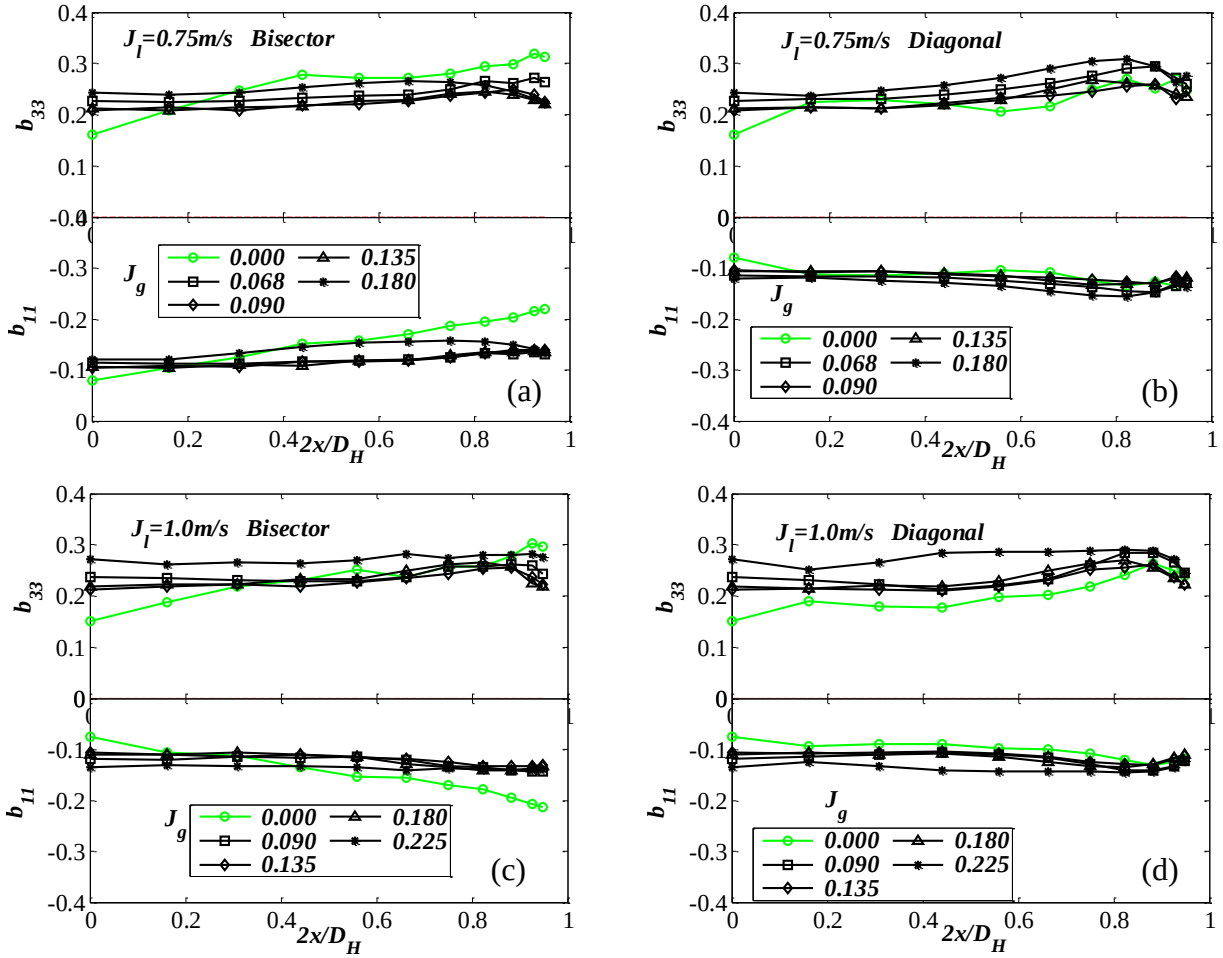

Fig. 7.24 Lateral distributions of the turbulence anisotropy tensor b_{11} and b_{33} in the large circular pipe with D_H=136*mm* based on Sun's experimental database: under J_l =0.75*m/s* (a) along the bisector line; (b) along the diagonal line; under J_l =1.0*m/s* (c) along the bisector line; (b) along the diagonal line [7.16].

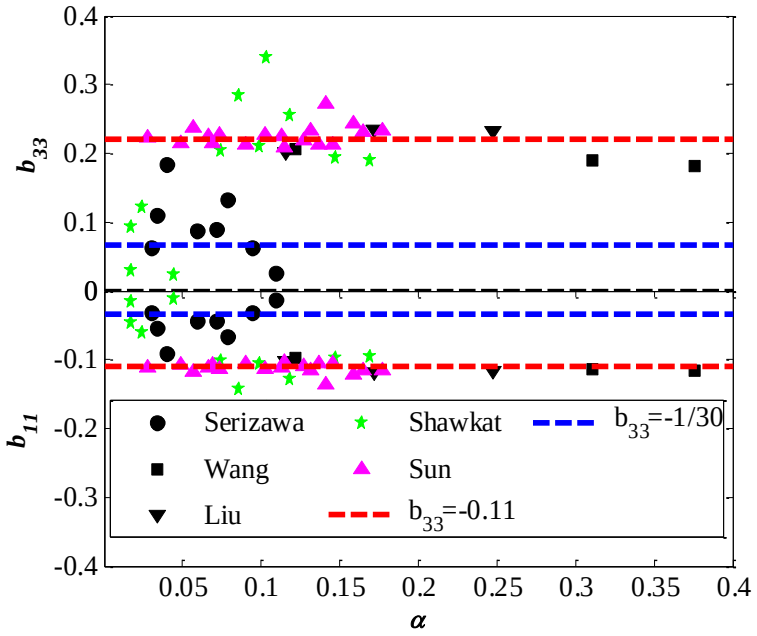

Fig. 7.25 The relation between the turbulence anisotropy tensor b_{11} and b_{33} and the local void fraction α in the duct center for different ducts. The black and green symbols indicate the results in the small circular pipes and the large ducts respectively.

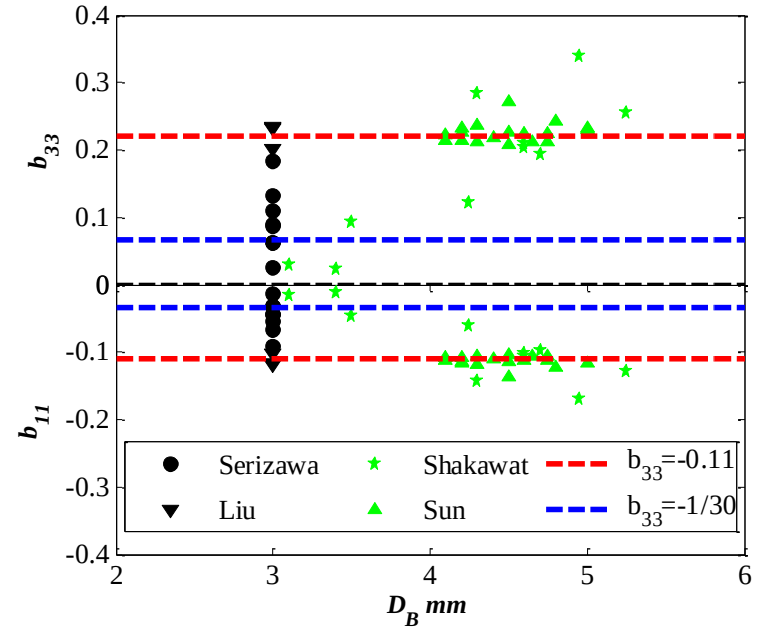

Fig. 7.26 The relation between the turbulence anisotropy tensor b_{11} and b_{33} and the local bubble size α in the duct center for different ducts. The black and green symbols indicate the results in the small circular pipes and the large ducts respectively.

7.3.2 Modeling of the anisotropic turbulent bubbly flow

In this section, we will focus on how to model the anisotropic turbulence in the liquid phase of the turbulent bubbly flow. Before this, the physical process of the turbulence anisotropy generation is considered for the turbulent bubbly flow as compared to that of the single-phase turbulent flow.

7.3.2.1 Turbulence anisotropy in the single-phase turbulent flow

Firstly, transport equation of the Reynolds stress is given in Eq. (7.22) and (7.23)

$$\frac{D\left\langle u_i u_j \right\rangle}{Dt} = \mathrm{P_{ij}} + \mathrm{D_{ij}} + \Phi_{\mathrm{ij}} - \frac{2}{3}\varepsilon\delta_{\mathrm{ij}} \tag{7.22}$$

where P_{ij} is the production term , $P_{ij} = \left\langle u_i u_k \right\rangle \frac{\partial U_j}{\partial x_k} + \left\langle u_j u_k \right\rangle \frac{\partial U_i}{\partial x_k}$; D_{ij} is the diffusion term, $D_{ij} = \frac{\partial T_{ijk}}{\partial x_k}$ with $T_{ijk} = \left\langle u_i u_j u_k \right\rangle + \upsilon \frac{\left\langle u_i u_j \right\rangle}{\partial x_k} + \left\langle u_i p' \right\rangle \delta_{jk} + \left\langle u_j p' \right\rangle \delta_{ik}$; Φ_{ij} is the redistribution term, $\Phi_{ij} = \left\langle p' \left(\frac{\partial u_i}{\partial x_j} + \frac{\partial u_j}{\partial x_i} \right) \right\rangle + \left(\frac{2}{3}\varepsilon\delta_{ij} - \varepsilon_{ij} \right)$; ε_{ij} is the dissipation rate of $\left\langle u_i u_j \right\rangle$, $\varepsilon_{ij} = 2\upsilon \left\langle \frac{\partial u_i}{\partial x_k} \frac{\partial u_j}{\partial x_k} \right\rangle$ and $\varepsilon = \left(\varepsilon_{11} + \varepsilon_{22} + \varepsilon_{33}\right)$.

For the single-phase turbulent flow, the production and redistribution term plays an important role in the turbulence anisotropy property. Models considering the slow term (return-to-isotropy) and fast term (rapid-distortion theory) have been proposed for the redistribution term, which is shown as follows:

$$\Phi_{\mathrm{ij}} = -C_R \frac{\varepsilon}{k} \left(\left\langle u_i u_j \right\rangle - \frac{2}{3} t_k \delta_{ij} \right) - C_2 \left(P_{ij} - \frac{2}{3} P \delta_{ij} \right) \tag{7.23}$$

where $P=P_{11}+P_{22}+P_{33}$; the first and second terms are Rotta's model for the slow term and isotropization of production (IP) model [7.32].

The turbulence anisotropy could be considered as the problem of the turbulent energy distribution among different components. As shown in Eq. (7.21) and Fig. 7.27(a) each turbulent component is determined by the energy balance among the production, diffusion, redistribution and dissipation. The production term due to Reynolds shear stress and the velocity shear causes the turbulence anisotropy, while the redistribution term due to the interaction between the pressure and strain rate of the velocity field returns the anisotropic turbulence to isotropic and counteracts the anisotropic production effect. Fig. 7.27(b) shows the schematic diagram of the generation of the turbulence anisotropy of the single-phase turbulent flow in the channel. In the near wall region, the turbulence behaves strongly anisotropic because of the wall suppressing effect on the normal turbulent components and the existence of the high velocity shear and Reynolds stress. While in the bulk region, the turbulence is much less anisotropic. For the region far enough from the wall, the turbulence might be considered as isotropic.

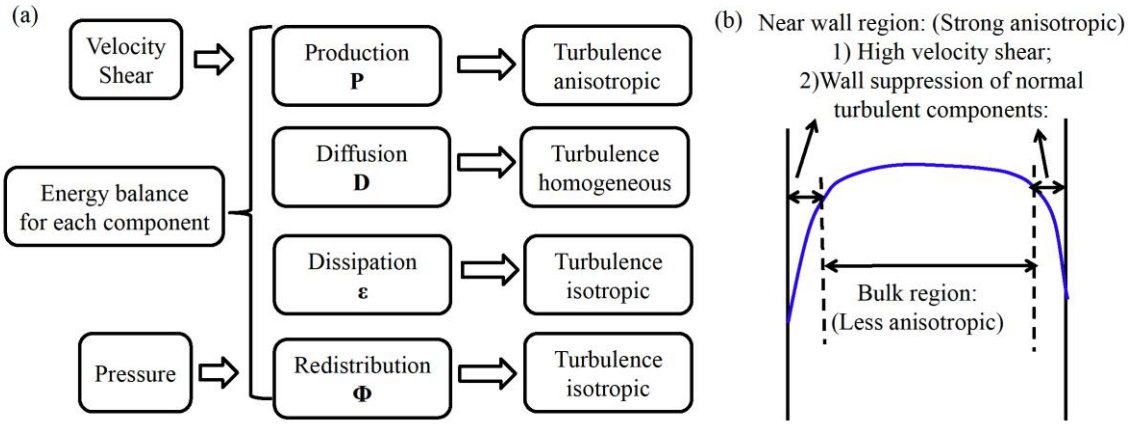

Fig. 7.27 (a) Contribution of each term in the energy balance to the turbulence anisotropy; (b) Schematic diagram of the generation of the turbulence anisotropy of the single-phase turbulent flow in channel.

7.3.2.2 Turbulence anisotropy for turbulent bubbly flow

As compared to the single-phase turbulent flow, the existence of the dispersed bubbles in the turbulent bubbly flow modifies the energy balance for each turbulent component as shown in Eq. (7.24) by introducing another mechanism of turbulence production, diffusion, redistribution and dissipation, which affected the turbulence anisotropy to some extent as discussed in Section 7.3.2.

$$\frac{D\left\langle u_i u_j \right\rangle}{Dt} = \left(P_{ij}^S + D_{ij}^S + \Phi_{ij}^S - \frac{2}{3}\varepsilon^S \delta_i \delta_j \right) + \frac{\alpha}{1-\alpha}\left(P_{ij}^B + D_{ij}^B + \Phi_{ij}^B - \frac{2}{3}\varepsilon^B \delta_i \delta_j \right), \qquad (7.24)$$

where P_{ij}^B, D_{ij}^B, Φ_{ij}^B, and ε^B are the turbulence production, diffusion, redistribution and dissipation terms due to bubbles.

Correspondingly, the generation mechanism of the turbulence anisotropy is different from that in the single-phase turbulent flow. To understand the anisotropic property of the turbulent bubbly flow and simplify the problem, the turbulence will be considered in the area where the local turbulence is dominated by bubbles and the shear-induced turbulence and anisotropy could be neglected such as the core region or in the uniform flow. Therein, Eq. (7.24) could be simplified as

$$\frac{D\left\langle u_i u_j \right\rangle}{Dt} = \left(\Phi_{ij}^{Slow} - \frac{2}{3}\varepsilon^S \delta_i \delta_j \right) + \frac{\alpha}{1-\alpha}\left(P_{ij}^B + \Phi_{ij}^B - \frac{2}{3}\varepsilon^B \delta_i \delta_j \right). \qquad (7.25)$$

Hereafter, the modeling of the terms related with the dispersed bubbles will be considered.

In order to model the anisotropic turbulence property, the turbulence induced by bubbles is considered to mimic the grid-induced turbulence as shown in Fig. 7.28, which is often adopted to the study of the isotropic turbulence for single-phase turbulent flow [7.32]. Therein, the turbulence was firstly induced by the wake behind the grid and grid shear, and then return to isotropy during the turbulence decay with time. Similar to

that in the grid-generated turbulence, Fig. 7.29 shows the schematic diagram of turbulence generation process with the dispersed bubbles in the core region, where the bubbly flow was firstly simplified in the form of column like the grids. Similarly, the turbulence is considered at the measured points as shown in Fig. 7.29. Similar to the grids in the single-phase turbulence, there exits wake behind the bubbles and velocity shear between the bubbles for the turbulent bubbly flow. Within the measuring time ΔT in the liquid phase it might experience two periods i.e., (1) inside the bubble wake when the turbulence T_w was produced and developed and (2) outside the bubble wake when the turbulence decays T_D and returns to isotropic. The process of the turbulence anisotropy could be considered as the turbulence anisotropy generates in the first period and then decays in the second period until the next bubble comes. Therefore, the final turbulence anisotropy in the experimental measurements was strongly related with ΔT and the ratio between T_w and ΔT, which determines the turbulence property and the effect of return-to-isotropy. The above parameters could be considered as follows:

$$\Delta T = \frac{l_{B-B}}{W_B} = \frac{L_c(1-\alpha)}{\alpha W_B}, \tag{7.26}$$

$$T_W = \frac{L_w}{W_B} = \frac{f(\mathrm{Re}_B)D_B}{W_B}, \tag{7.27}$$

$$\frac{T_W}{\Delta T} = \frac{f(\mathrm{Re}_B)\alpha}{(1-\alpha)}, \tag{7.28}$$

where $l_{B\text{-}B}$ is the vertical distance between the bubbles and was obtained in Eq. 5.21; l_w is the wake length of the bubble, which is related with the bubble size D_B and bubble Reynolds number Re_B.

As obtained from Eq. (7.28), $T_w/\Delta T$ increases with that of the void fraction. It explains why for the turbulent bubbly flow with very low void fraction, the measured turbulence behaves more isotropic because of the stronger effect of the return-to-isotropy. In addition, $T_w/\Delta T$ increases with that of bubble size. It explains why

for the turbulent bubbly flow with small bubble size, the measured turbulence behaves more isotropic because of the more isotropic turbulence generated by bubbles initially.

Therefore, during the derivation of the anisotropic turbulence model for the turbulent bubbly flow, the above process is suggested to be considered in the turbulence production term in the future work based on the understanding of the turbulence anisotropy inside the bubble wake.

$$P_{ij}^{B} = A_{ij}^{B} P^{B} \quad \text{and} \quad A_{ij}^{B} = F_{ij}\left(\frac{f\left(\mathrm{Re}_{B}\right)\alpha}{1-\alpha}\right). \tag{7.29}$$

As for the other two terms Φ_{ij}^{B} and ε^{B}, it is much more complicated and is suggested to be considered as follows in the future model. The introduction of the moving bubbles could be considered as the additional wall-echo effect which suppresses the lateral turbulence and increases the turbulence anisotropy. As for the dissipation induced by bubbles, it is suggested to be reflected in the A_{ij}^{B} in the future model, i.e., considering the net turbulence production term due to the bubbles.

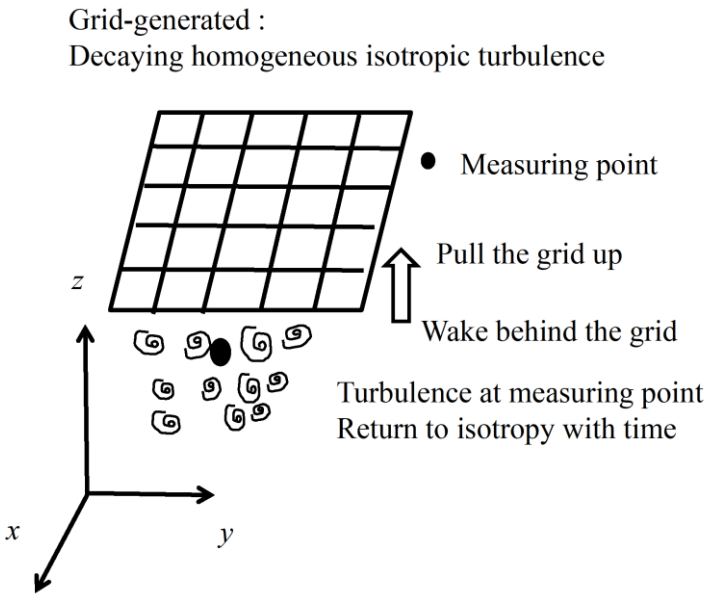

Fig. 7.28 Schematic diagram of grid-generated decaying homogeneous isotropic turbulence.

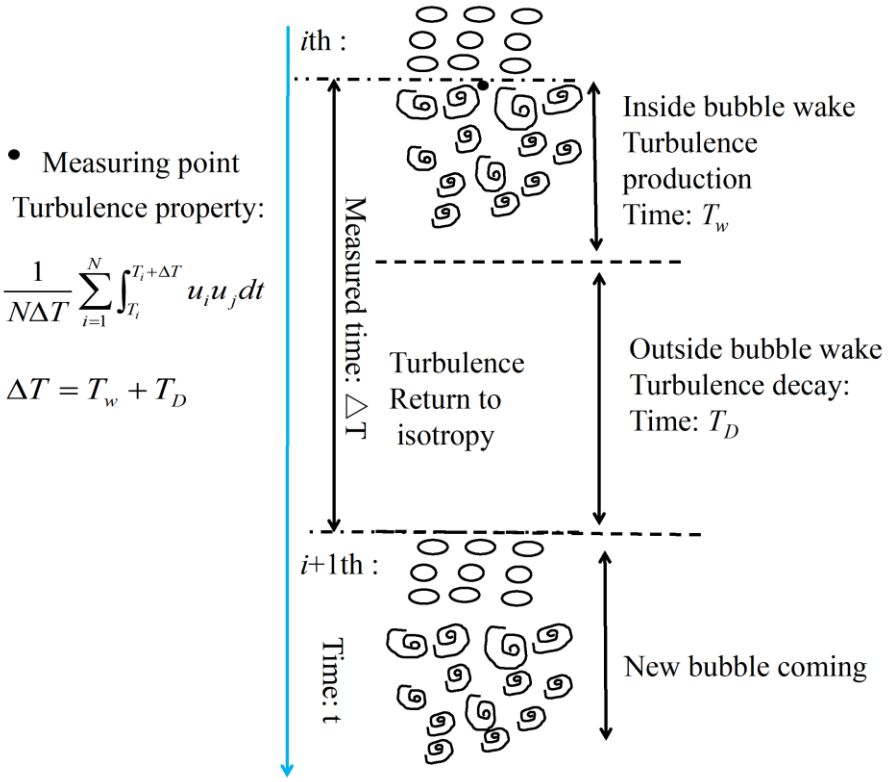

Fig. 7.29 Schematic diagram of turbulence generation of the turbulent bubbly flow in the core region where the turbulence is dominated by bubbles.

7.4 Summary and discussion

In this Chapter, the turbulence modulation of the turbulent bubbly flow was studied based on the recently established experimental database including the turbulent kinetic energy and turbulence anisotropy. The following findings were obtained:

(1) In order to quantify the solely bubble-induced turbulence in a wider range of void fraction, the turbulence was investigated in the duct center where it was dominated by the bubbles. It was found that the relation between the turbulence and the void fraction was affected by the duct geometry. Comparing to the small circular pipes the stronger turbulence could be induced in the large ducts. In addition, the turbulence in the small circular pipe was found to be closer to prediction of the potential theory. In the large ducts, the turbulence model needs to be modified to get better prediction.

(2) The present study on the interaction between bubble-induced turbulence and wall-induced turbulence indicates that comparing to the core region, the bubble-induced turbulence under the same void fraction was reduced by the wall effect, which made the turbulence more homogeneous in the turbulent bubbly flow. In addition, the turbulence reduction due to existence of the bubbles was discussed to consider the bubble-effect on wall-induced turbulence. The acceleration laminarization and suppression of the “bursting events” of the coherent structures in the near wall region were proposed as the mechanisms responsible for the turbulence reduction therein.

(3) The present study on the turbulence anisotropy indicates that the existence of the bubbles could affect the turbulence anisotropy such as causing the turbulence more anisotropic in the duct core region but more isotropic in the near wall region. How the turbulence anisotropy is affected by bubbles is related with the void fraction, duct geometry, and bubble size. Under higher void fraction or larger bubble size, the turbulence anisotropy tensor was found to be more anisotropic and reach a constant value to some extent.

It is notable that since the database for the liquid phase turbulence is very limited so far, the present analysis was only carried out for several databases. Therefore, it still needs further validation of the above observations based on new turbulence database for the turbulent bubbly flow especially in the large ducts to consider the solely bubble-induced turbulence in the future. In addition, for the anisotropic turbulent model, more databases about the bubble and bubble-induced wake are also required.

Reference

[7.1] Hosokawa, S., Tomiyama, A., 2010, Effect of bubbles on turbulent flows in vertical channels, 7th International Conference on Multiphase flow. FL USA.

[7.2] Serizawa, A., 1974, Fluid dynamics characteristics of two-phase flow, Doctor Thesis, Kyoto University.

[7.3] Serizawa, A., Kataoka, I., Michiyoshi, I., 1975, Turbulence structure of air-water bubbly flow—II. local properties, Int. J. Multiphase Flow 2, 235–246.

[7.4] Theofanous, T. G., Sullivan, J., 1982, Turbulence in two-phase dispersed flows, J. Fluid Mechanics 116, 343-362.

[7.5] Michiyoshi, I., Serizawa, A., 1986, Turbulence in two-phase bubble flow, Nucl. Eng. Des. 95, 253-267

[7.6] Wang, S., Lee, S., Jones, O., Lahey, Jr R. T., 1987, 3-D turbulence structure and phase distribution measurements in bubbly two-phase flows, Int. J. Multiphase Flow 13, 327–343.

[7.7] Liu, T.J., Bankoff, S.G., 1993, Structure of air-water bubbly flow in a vertical pipe—I. liquid mean velocity and turbulence measurements, Int. J. Heat Mass Transfer 36, 1049–1060.

[7.8] Serizawa, A., Kataoka, I., 1990, Turbulence suppression in bubbly two-phase flow, Nucl. Eng. Des. 122, 1–16.

[7.9] Lance, M. , Bataille, J., 1991, Turbulence in the liquid phase of a uniform bubbly air-water flow, J. Fluid Mech., 222, 95-118.

[7.10] Lance, M., Bataille, J., 1991, Homogeneous turbulence in bubbly flows, J. Fluids, Eng., 113, 295-300.

[7.11] Wijngaarden, van L., 1998, On pseudo turbulence, Theoret. Comput. Fluid Dynamics 10, 449-458.

[7.12] Shawakat, M. E., Ching, C. Y., Shoukri, M., 2007, On the liquid turbulence energy spectra in two-phase bubbly flow in a large diameter vertical pipe, Int. J. Multiphase Flow 33, 300-316.

[7.13] Shawakat, M. E., Ching, C. Y., Shoukri, M., 2008, Bubble and liquid turbulence characteristics of bubbly flow in a large diameter vertical pipe, Int. J. Multiphase Flow 34, 767-785.

[7.14] Bunner, B., Tryggvason, G., 2002, Dynamics of homogeneous bubbly flows Part 2: velocity fluctuations, J. Fluid Mech. 466, 53-84.

[7.15] Hibiki, T., Ishii, M., Z. Xiao, 2001, Axial interfacial area transport of vertical bubbly flows, Int. J. Heat Mass Transfer 44, 1869-1888.

[7.16] Sun, H. M., 2014, Study on upward air-water two-phase flow characteristics in a vertical large square duct, Doctor Thesis, Kyoto University.

[7.17] Lahey Jr. R.T., 1990, The analysis of phase separation and phase distribution phenomena using two-fluid models, Nucl. Eng. Des. 122, 17-40.

[7.18] Bertodano, Lopez M., Lahey, Jr. R.T., Jones, O. C., 1994, Phase distribution in bubbly two-phase flow in vertical ducts, Int. J. Multiphase Flow 20, 805-818.

[7.19] Politano M. S., Carrica P. M., Converti J., 2003, A model for turbulent polydispers two-phase flow in vertical channels, Int. J. Multiphase Flow 19, 1153-1182.

[7.20] Hosokawa, S., Tomiyama, A., 2009, Multi-fluid simulation of turbulent bubbly pipe flows, Chem. Eng. Sci. 64, 5308-5318.

[7.21] Rzehak, R., Krepper, E., 2013, Bubble-induced turbulence: Comparison of CFD models, Nucl. Eng. Des. 258, 57-65.

[7.22] Yokomine, T., Shimizu, A., 1995, Prediction of turbulence modulation by using k-ε model for gas-solid flows, Advances in Multiphase Flow 191-199.

[7.23] Sato, Y., Sadatomi, M., 1981, Momentum and heat transfer in two-phase bubble flow—I. Theory, Int. J. Multiphase Flow 7, 167-177.

[7.24] Tomiyama, A., Tamai, H., Zun, I., Hosokawa, S., 2002, Transverse migration of single bubbles in simple shear flows, Chem. Eng. Sci. 57, 1849-1858.

[7.25] Inoue, A., Koga, T., Yaegashi, H., 1976, Void fraction, bubble and liquid velocity profiles in a vertical pipe, Trans. Japan Soc. Mech. Eng. 42, 2521-2531.

[7.26] Sullivan, J. P., Houze, R. N., Buenger, D. E., Theofanous, T. J., 1978, Turbulence in two-phase flows, Proc. 2nd CSNI Specialist Meeting, Paris,

583-608

[7.27] Ohba, K., Yuhara, T., 1982, Study on vertical bubble flow using laser Doppler measurement, Trans. Japan Soc. Mech. Eng. 48, 78-85

[7.28] Aoki, S., 1982, Eddy diffusivity of momentum in bubbly flow, M.S. Thesis, Kyoto University.

[7.29] Lee, S. G., 1986, Turbulence modeling in bubbly two-phase flow, PhD Thesis, RPI

[7.30] Bolotnov, Igor A., 2013, Influence of bubbles on the turbulence anisotropy, J. Fluids Eng. 135, 051301.

[7.31] Bunner, B., Tryggvason, G., 2003, Effect of bubble deformation on the properties of bubbly flows, J. Fluid Mech. 495, 77-118.

[7.32] Pope, S. B., 2000, Turbulent flows, Cambridge University Press.

Chapter 8

Conclusions

8.1 Summary of dissertation

Io order to improve the understanding and modeling of the turbulent bubbly flow especially in the large square duct, the present dissertation contains three parts. Firstly, the state-of-the-art of the upward turbulent bubbly flow was reviewed in Chapter 1 and the existing database was collected in Chapter 2. In second part, the numerical evaluation of the existing models was carried out based on the experimental databases in the large square duct. The third part was contributed to improving the understanding of the flow characteristics and the physical processes therein including the flow developing processes, the axial velocities of the liquid phase, the bubble deformation and the turbulence modulation in the liquid phase. The main achievements in each part could be summarized as follows:

1) Numerical evaluation (Chap. 3)

It indicates the existed model might not be suitable for the turbulent bubbly flow in the large noncircular ducts because of the different physical processes therein as compared to that in the small circular pipes. The detailed analyses of the physical process of the turbulent bubbly flow in the large noncircular ducts are suggested to improve the model therein.

2) Flow developing process (Chap. 4)

During the developing of turbulent bubbly flow, there exist at least two stages which are forming the bubble layer and the velocity developing based on the formed bubble layer. During the bubble layer formation at the first stage, the length required to

form the bubble layer was considered and found to be less than that required to develop the liquid phase boundary layer with the similar thickness. At the second stage, the length required to lift up the liquid phase velocity near the wall was analyzed, and the criterion to judge the flow developing status was suggested.

3) Axial velocity in the liquid phase (Chap. 5)

For the turbulent bubbly flow in the large square duct, the formation of the typical M-shaped velocity profile was noticed and studied by considering the index of flow type, the formation conditions, the peak locations of the velocity profile and velocity characteristics. Therein, two layers with the different flow types were observed and analyzed between the wall and the duct center, which are the pressure driven and shear driven flows. The formation of the M-shaped velocity profile was found to be determined the duct geometry which dominates the lateral void fraction distribution and the wall drag resistance. Based on the flow characteristics of the turbulent bubbly flow in the large square duct, two-layer model and analysis was suggested to improve the understanding and modeling therein.

4) Bubble deformation (Chap. 6)

The void fraction effect on the bubble deformation for the turbulent bubbly flow was found which showed that the bubbles behaved more prolate with the increase of the void fraction as compared to the single-bubble case. A new correlation for the statistical bubble deformation was proposed and validated combining the bubble size and void fraction to consider the void fraction effect. Numerical validation of the void fraction showed that only for the cases with better developed status, the predictions of the void fractions were in well consistent with the experimental measurements. It indicates the importance of knowing developing status to model the turbulent bubbly flow.

5) Turbulence modulation in the liquid phase (Chap. 7)

The quantification of the solely bubble-induced turbulence in a wider range of void fraction was carried out by focusing the turbulence in the duct center. The relation

between the turbulence and the void fraction was found to be affected by the duct geometry. As compared to the small circular pipes the stronger turbulence could be induced in the large ducts. The interaction between bubble-induced turbulence and wall-induced turbulence was considered by comparing the turbulence in the core region and near wall region. It indicates that as compared to the core region, the bubble-induced turbulence could be reduced by the wall effect. The mechanisms of the turbulence reduction of the turbulent bubbly flow were proposed which are the flow acceleration laminarization and suppression of the coherent structures in the near wall region. The investigation of the turbulence anisotropy indicates that the introduction of the bubbles could affect the turbulence anisotropy such as causing the turbulence more anisotropic in the duct core region but more isotropic in the near wall region. However, how the turbulence anisotropy is affected by bubbles was found to be related with the void fraction, duct geometry, and bubble size.

8.2 Recommendation for future work

1) To understand the flow developing process

There are several interesting observations during the developing of the turbulent bubbly flow such as two-stage developing and the almost constant thickness of the bubble layer δ_B. In addition, the understanding of the developing status is also important for the flow modeling. However, the current database is still limited to understand the detailed developing process of the turbulent bubbly flow. Therefore, the boundary layer flow type is suggested for the bubbly flow.

2) To understand the secondary flow

Currently, the secondary flow effect in the turbulent bubbly flow was neglected by considering the experimental data of the lateral turbulent normal stresses. So far there is no direct experimental information about it, which is suggested in the future work.

3) To understand the bubble deformation

Currently, the void fraction effect on the bubble deformation was considered for the mean bubble size around 3.5*mm*~5.5*mm* and limited void fraction range. For the wider range of the bubble size and flow conditions, it still needs further study in the future.

4) To understand the turbulence modulation

The mechanisms here proposed for the turbulence reduction of the turbulent bubbly flow still needs further experimental measurements including the velocity and turbulence in the near wall region to confirm.

Nomenclature

Latin

a_i	Interfacial area concentration
A	Dimensionless parameter to show flow developing status
$\mathbf{A}_S$	Anisotropy matrix related with shear-induced turbulence
$\mathbf{A}_B$	Anisotropy matrix related with bubble-induced turbulence
$\mathbf{b}$	Turbulence anisotropy tensor
C_ε	Model constants in τ-ε model of the turbulent bubbly flow
$C_{\varepsilon 1}$	Model constants in τ-ε model of the turbulent bubbly flow
$C_{\varepsilon 2}$	Model constants in τ-ε model of the turbulent bubbly flow
$C_{\varepsilon \mathrm{B}}$	Model constants in τ-ε model of the turbulent bubbly flow
$C_{\mu l}$	Model constants related with shear-induced eddy viscosity
$C_{\mu b}$	Model constants related with bubble-induced eddy viscosity
C_L	Lift force coefficient
C_T	Turbulent dispersion force coefficient
C_{VM}	Virtual mass force coefficient
D_B	Bubble size
D_H	Duct hydraulic radius
D_{HB}	Maximum horizontal bubble dimension
$\mathbf{D}$	Diffusion term Reynolds stress transportation
D_{max}	Maximum bubble size
D_{SM}	Sauter mean diameter
D_V	Axial bubble dimension
E	Bubble aspect ratio or bubble deformation
E_α	Bubble aspect ratio for bubbly flow

E_S	Bubble aspect ratio obtained by single-bubble correlation
Eo	Eötvös number based on D_{SM}
$\mathrm{Eo_H}$	Eötvös number based on D_{HB}
f_b	Bubble frequency
f_l	Friction factor
F	Local net driving force
$\mathbf{g}$	Gradational acceleration vector
J_k	Superficial velocity of phase-k
k	Turbulent kinetic energy
k_{Ba}	Asymptotic value of bubble-induced turbulent kinetic energy
l_e	Characteristic length of the most energetic eddy
l_s	Mixing length of shear-induced turbulence
l_b	Mixing length of bubble-induced turbulence
$l_{B\text{-}B}$	Vertical bubble-bubble interval
l_w	Length of the bubble wake
L_B	Length from the inlet to form bubble layer δ_B
L_c	Chord length
$L_{\delta l}$	Length from the inlet to form liquid-phase boundary layer δ_l
L_p	Length required
M	Morton number
$\mathbf{M}_{ik}$	Interfacial force exerted on phase-k
$\mathbf{M}_{ik}^{\ d}$	Interfacial drag force exerted on phase-k
$\mathbf{M}_{ik}^{\ L}$	Lift force exerted on phase-k
$\mathbf{M}_{ik}^{\ nd}$	Interfacial non-drag force exerted on phase-k
$\mathbf{M}_{ik}^{\ P}$	Interfacial term due to pressure exerted on phase-k
$\mathbf{M}_{ik}^{\ S}$	Interfacial term due to shear stress exerted on phase-k
$\mathbf{M}_{ik}^{\ T}$	Turbulent dispersion force exerted on phase-k

$\mathbf{M}_{ik}^{V}$	Virtual mass force exerted on phase-*k*
$\mathbf{M}_{ik}^{W}$	Wall force exerted on phase-*k*
$\mathbf{M}_{wk}$	Wall shear force exerted on phase-*k*
p_k	Pressure field in phase-*k*
$\mathbf{P}$	Production tensor in Reynolds stress transportation
P	P=trace ($\mathbf{P}$)/2
Re	Reynolds number
$\mathbf{S}_i$	Interfacial tensor in turbulent kinetic energy transportation
S_i	S_i=trace ($\mathbf{S}$)/2
S_B	Surface area of the bubble
t_e	Characteristic time of the eddy
t_k	Turbulent kinetic energy in Chapter 7
T_D	Time period of the bubble wake decay
T_w	Time period of the bubble wake
We	Weber number
$\mathbf{v}_k$	Fluctuating velocity vector in phase-*k*
$\overline{\mathbf{v}_k\mathbf{v}_k}$	Reynolds stress tensor in phase-*k*
$\overline{\mathbf{V}}_k$	Phase averaged velocity vector in phase-*k*
$\boldsymbol{V}_k$	Instantaneous velocity vector in phase-*k*: $\boldsymbol{V}_k = \overline{\mathbf{V}}_k + \mathbf{v}_k$
$\boldsymbol{V}_T$	Terminal velocity
$\boldsymbol{V}_R$	Relative velocity between bubble and liquid phase
V_B	Volume of the bubble
W_k	Axial velocity of phase-*k*
W_{lm}	Maximum of Axial liquid-phase velocity
W^*	Dimensionless velocity
x	Coordinate component, horizontal direction
X^*	Dimensionless location

x_p	Location of the liquid-phase velocity peak
y	Coordinate component, horizontal direction
z	Coordinate component, flow direction

Greek

α_k	Void fraction of phase-k
χ	Mass quality
δ_l	Thickness of the liquid phase boundary layer
δ_B	Thickness of the bubble layer
ε	Dissipation rate of the turbulent kinetic energy
$\boldsymbol{\varepsilon}$	Dissipation term Reynolds stress transportation
$\boldsymbol{\Phi}$	Redistribution term Reynolds stress transportation
γ	Ratio between maximum void fraction and that in duct center
μ_k	Dynamic viscosity of phase-k
υ_b	Eddy viscosity due to bubbles
υ_s	Eddy viscosity due to shear-induced turbulence
σ	Surface tension between liquid and gas phase
σ_ε	Model constants in k-ε model
ρ_k	Density of phase-k
$\boldsymbol{\tau}_B$	Bubble-induced Reynolds stress tensor in liquid phase
$\boldsymbol{\tau}_k$	Shear stress tensor in phase-k
$\boldsymbol{\tau}_k^T$	Turbulent Reynolds stress tensor in phase-k

Superscript

B	Bubbly flow
c	In the duct center
S	Single-phase flow

w	Near the wall

Subscript

0	Single-bubble cases
α	Bubbly flow cases
b or *B*	Bubble-induced
c	Duct center
i	Interface-induced
in	Insider the bubble layer
k	Phase number
g	Gas phase
l or *L*	Liquid phase
m	Mean value
out	Outside the bubble layer
s or *S*	Shear-induced
t	Two-phase flow
w or *W*	Wall-induced

duct center

S	Single-phase flow
w	Near the wall

Subscript

0	Single-bubble cases
α	Bubbly flow cases
b or *B*	Bubble-induced

c	Duct center
i	Interface-induced
in	Insider the bubble layer
k	Phase number
g	Gas phase
l or *L*	Liquid phase
m	Mean value
out	Outside the bubble layer
s or *S*	Shear-induced
t	Two-phase flow
w or *W*	Wall-induced